Julius Maximilian University Würzburg

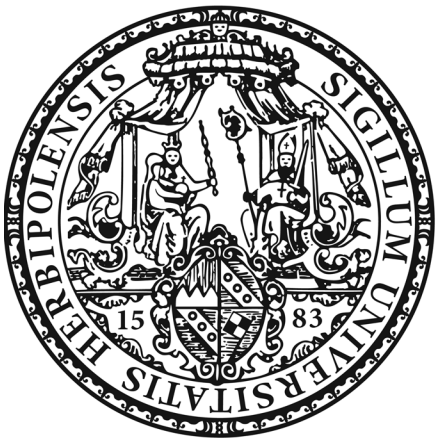

Establishment of an infection model of the human intestinal epithelium to study host and pathogen determinants during the *Salmonella* Typhimurium infection process

Etablierung eines Infektionsmodells des menschlichen Darmepithels zur Untersuchung von Wirts- und Erregerdeterminanten während des *Salmonella* Typhimurium-Infektionsprozesses

Doctoral thesis for a doctoral degree

at the Graduate School of Life Sciences,

Julius-Maximilians-Universität Würzburg,

Section: Biomedicine

submitted by

Thomas Däullary

from

München (Germany)

Würzburg, 2022

Submitted on: _____

Office stamp

Members of the Thesis Committee

Chairperson:	Prof. Dr. Thomas Dandekar
Primary Supervisor:	PD Dr. Marco Metzger
Supervisor (Second):	Prof. Dr. Cynthia Mira Sharma
Supervisor (Third):	Jun. Prof. Dr. Alexander Westermann
Supervisor (Fourth):	Dr. Daniela Zdzieblo

Table of contents

Abstract

According to the WHO, foodborne derived enteric infections are a global disease burden and often manifest in diseases that can potentially reach life threatening levels, especially in developing countries. These diseases are caused by a variety of enteric pathogens and affect the gastrointestinal tract, from the gastric to the intestinal to the rectal tissue. Although the complex mucosal structure of these organs is usually well prepared to defend the body against harmful agents, specialised pathogens such as *Salmonella enterica* can overcome the intestinal defence mechanism. After ingestion, *Salmonella* are capable of colonising the gut and establishing their proliferative niche, thereby leading to inflammatory processes and tissue damage of the host epithelium. In order to understand these processes, the scientific community in the last decades mostly used cell line based *in vitro* approaches or *in vivo* animal studies. Although these approaches provide fundamental insights into the interactions between bacteria and host cells, they have limited applicability to human pathology. Therefore, tissue engineered primary based approaches are important for modern infection research. They exhibit the human complexity better than traditional cell lines and can mimic human-obligate processes in contrast to animal studies.

Therefore, in this study a tissue engineered human primary model of the small intestinal epithelium was established for the application of enteric infection research with the exemplary pathogen *Salmonella* Typhimurium.

To this purpose, adult stem cell derived intestinal organoids were used as a primary human cell source to generate monolayers on biological or synthetic scaffolds in a Transwell®-like setting. These tissue models of the intestinal epithelium were examined for their comparability to the native tissue in terms of morphology, morphometry and barrier function. Further, the gene expression profiles of organotypical mucins, tight junction-associated proteins and claudins were investigated. Overall, the biological scaffold-based tissue models showed higher similarity to the native tissue - among others in morphometry and polarisation. Therefore, these models were further characterised on cellular and structural level. Ultrastructural analysis demonstrated the establishment of characteristic microvilli and tight-junction connections between individual epithelial cells. Furthermore, the expression pattern of typical intestinal epithelial protein was addressed and showed *in vivo*-like localisation. Interested in the cell type composition, single cell transcriptomic profiling revealed distinct cell types including proliferative cells and stem cells, progenitors, cellular entities of the absorptive lineage, Enterocytes and Microfold-like cells. Cells of the secretory lineage were also annotated, but

without distinct canonical gene expression patterns. With the organotypical polarisation, protein expression, structural features and the heterogeneous cell composition including the rare Microfold-like cells, the biological scaffold-based tissue model of the intestinal epithelium demonstrates key requisites needed for infection studies with *Salmonella*.

In a second part of this study, a suitable infection protocol of the epithelial tissue model with *Salmonella* Typhimurium was established, followed by the examination of key features of the infection process. *Salmonella* adhered to the epithelial microvilli and induced typical membrane ruffling during invasion; interestingly the individual steps of invasion could be observed. After invasion, time course analysis showed that *Salmonella* resided and proliferated intracellularly, while simultaneously migrating from the apical to the basolateral side of the infected cell. Furthermore, the bacterial morphology changed to a filamentous phenotype; especially when the models have been analysed at late time points after infection. The epithelial cells on the other side released the cytokines Interleukin 8 and Tumour Necrosis Factor α upon bacterial infection in a time-dependent manner. Taken together, *Salmonella* infection of the intestinal epithelial tissue model recapitulates important steps of the infection process as described in the literature, and hence demonstrates a valid *in vitro* platform for the investigation of the *Salmonella* infection process in the human context.

During the infection process, intracellular *Salmonella* populations varied in their bacterial number, which could be attributed to increased intracellular proliferation and demonstrated thereby a heterogeneous behaviour of *Salmonella* in individual cells. Furthermore, by the application of single cell transcriptomic profiling, the upregulation of *Olfactomedin-4* (*OLFM4*) gene expression was detected; OLFM4 is a protein involved in various functions including cell immunity as well as proliferating signalling pathways and is often used as intestinal stem cell marker. This *OLFM4* upregulation was time-dependent, restricted to *Salmonella* infected cells and seemed to increase with bacterial mass. Investigating the *OLFM4* regulatory mechanism, nuclear factor κB induced upregulation could be excluded, whereas inhibition of the Notch signalling led to a decrease of OLFM4 gene and protein expression. Furthermore, Notch inhibition resulted in decreased filamentous *Salmonella* formation. Taken together, by the use of the introduced primary epithelial tissue model, a heterogeneous intracellular bacterial behaviour was observed and a so far overlooked host cell response – the expression of *OLFM4* by individual infected cells – could be identified; although *Salmonella* Typhimurium is one of the best-studied enteric pathogenic bacteria. This proves the applicability of the introduced tissue model in enteric infection research as well as the importance of new approaches in order to decipher host-pathogen interactions with higher relevance to the host.

Zusammenfassung

Nach Angaben der WHO stellen lebensmittelbedingte Darminfektionen eine globale Krankheitslast dar und äußern sich häufig in Krankheiten, die potenziell lebensbedrohliche Ausmaße annehmen können, insbesondere in Entwicklungsländern. Diese Krankheiten werden durch eine Vielzahl von enterischen Erregern verursacht und betreffen den Magen-Darm-Trakt, vom Magen über den Darm bis zum Enddarm. Obwohl die komplexe Schleimhautstruktur dieser Organe in der Regel gut darauf vorbereitet ist, den Körper vor schädlichen Reagenzien zu schützen, können spezialisierte Erreger wie *Salmonella enterica* den Abwehrmechanismus des Darms überwinden. Nach der Nahrungsaufnahme sind Salmonellen in der Lage, den Darm zu kolonisieren und ihre proliferative Nische zu etablieren, was letztlich zu entzündlichen Prozessen und Gewebeschäden des Wirtsepithels führt. Um diese Prozesse zu verstehen, hat die Wissenschaft in den letzten Jahrzehnten hauptsächlich auf Krebslinien basierende *in vitro*-Ansätze oder *in vivo*-Tierstudien verwendet. Obwohl diese Ansätze grundlegende Erkenntnisse über die Wechselwirkungen zwischen Bakterien und Wirtszellen lieferten, sind sie nur begrenzt auf die Pathologie des Menschen übertragbar. Daher sind Tissue engineering und primärzellbasierte Ansätze für die moderne Infektionsforschung wichtig. Sie spiegeln die menschliche Komplexität besser wider als Ansätze mit Krebszellen und können im Gegensatz zu Tierversuchen human-obligate Prozesse nachbilden.

Daher wurde in dieser Studie ein tissue engineered humanes Primärmodell des Dünndarmepithels für die Anwendung in der enterischen Infektionsforschung am Beispiel des Erregers *Salmonella* Typhimurium etabliert.

Zu diesem Zweck wurden aus adulten Stammzellen gewonnene Darmorganoide als primäre humane Zellquelle verwendet, um 2D-Monolayer auf biologischen oder synthetischen Trägestrukturen in einer Transwell®-ähnlichen Umgebung zu erzeugen. Die so erzeugten Gewebemodelle des Darmepithels wurden auf ihre Vergleichbarkeit mit dem nativen Gewebe in Bezug auf Morphologie, Morphometrie und Barrierefunktion untersucht. Weiterhin wurde die Genexpression von organtypischen Muzinen, Tight Junction-assoziierten Proteinen und Claudinen sowie das Expressionsmuster der Tight Junction-Proteine untersucht. Insgesamt wiesen die auf biologischen Matrizes basierenden Gewebemodelle eine größere Ähnlichkeit mit dem nativen Gewebe auf - unter anderem in Bezug auf Morphometrie und Polarisation -, weshalb diese Modelle auf zellulärer und struktureller Ebene tiefgehender charakterisiert wurden. Die ultrastrukturelle Analyse zeigte die Ausbildung charakteristischer Mikrovilli und Tight-Junction-Verbindungen zwischen einzelnen Epithelzellen. Darüber hinaus wurden die

Expressionsmuster typischer Darmepithelproteine untersucht, die eine *in vivo* ähnliche Lokalisation aufwiesen. Im Hinblick auf die Zelltypenzusammensetzung ergab die Analyse des Transkriptoms auf Einzel-Zell-Ebene definierte Zelltypen. Dies waren Zellen mit proliferativem Profil, Stammzellen und Vorläuferzellen, und Zellen der absorptiven Linie, Enterozyten und Microfold-Zellen. Zellen der sekretorischen Linie wurden ebenfalls annotiert, jedoch ohne eindeutige kanonische Genexpression. Mit der organotypischen Polarisierung, der Proteinexpression, den strukturellen Merkmalen und der heterogenen Zellzusammensetzung, einschließlich der seltenen Microfold-Zellen, weist das auf einer biologischen Matrix basierende Gewebemodell des Darmepithels die wichtigsten Voraussetzungen für Infektionsstudien mit Salmonellen auf.

Im zweiten Teil dieser Studie wurde ein geeignetes Infektionsprotokoll für das Epithelgewebemodell mit *Salmonella* Typhimurium erstellt, gefolgt von der Untersuchung der wichtigsten Merkmale des Infektionsprozesses. *Salmonella* hafteten an den epithelialen Mikrovilli und verursachten während der Invasion das typische Membran-Kräuseln; interessanterweise konnten die Schritte der Invasion einzeln beobachtet werden. Nach der Invasion zeigte die Zeitverlaufsanalyse der Infektion, dass die Salmonellen intrazellulär lokalisierten und replizierten, während sie gleichzeitig von der apikalen zur basolateralen Seite der infizierten Zelle migrierten. Darüber hinaus veränderte sich die Morphologie der Bakterien in der Spätphase der Infektion zu einem filamentösen Phänotyp. Die Epithelzellen auf der anderen Seite setzten nach der bakteriellen Infektion zeitabhängig die Zytokine Interleukin 8 und Tumor-Nekrose-Faktor-α frei. Insgesamt rekapituliert die Salmonelleninfektion des intestinalen Epithelgewebemodells wichtige Schritte des Infektionsprozesses, wie sie in der Literatur beschrieben sind und stellt somit eine valide *in vitro* Plattform für die Untersuchung des Salmonelleninfektionsprozesses in einem menschlichen Kontext dar.

Interessanterweise variierten die intrazellulären Salmonellenpopulationen während des Infektionsprozesses in ihrer Bakterienzahl, was auf eine erhöhte intrazelluläre Proliferation zurückgeführt werden konnte und somit ein heterogenes Verhalten der Salmonellen in einzelnen Zellen demonstriert. Darüber hinaus wurde durch die Anwendung von Einzel-Zell-Transkriptom-Analysen die Hochregulierung der Genexpression von *Olfactomedin-4* (OLFM4) nachgewiesen; OLFM4 ist ein Protein mit verschiedenen Funktionen, darunter Prozesse der Zellimmunität sowie proliferierende Signalwege, und es wird häufig als Darmstammzellmarker verwendet. Diese *OLFM4*-Hochregulierung war zeitabhängig, auf mit *Salmonella* infizierten Zellen beschränkt und schien mit der intrazellulären Bakterienmasse zuzunehmen. Bei der Untersuchung der *OLFM4*-Regulationsmechanismen konnte eine nuclear

factor κB-induzierte Hochregulierung ausgeschlossen werden, während die Hemmung der Notch-Signalübertragung zu einem Rückgang der OLFM4-Gen- und Proteinexpression führte. Darüber hinaus führte die Hemmung von Notch zu einer verminderten Bildung von filamentösen *Salmonella*. Insgesamt konnte durch die Verwendung des hier eingeführten primären Epithelgewebemodells ein heterogenes intrazelluläres bakterielles Verhalten beobachtet und eine bisher übersehene Wirtszellantwort - die Expression von OLFM4 durch einzelne infizierte Zellen - bei einem der am besten untersuchten enterischen Pathogene identifiziert werden. Dies beweist die Anwendbarkeit des vorgestellten Gewebemodells in der enterischen Infektionsforschung sowie die Bedeutung neuer Ansätze zur Entschlüsselung von Wirt-Pathogen-Interaktionen mit höherer Relevanz für den Wirt.

1 Introduction

1.1 The global burden of infectious diseases

With the emergence of SARS-CoV-2 in 2019, a new pathogen conquered the world in a short time period and demonstrated excessively the impact of an infectious disease on the global human society. Infectious diseases are still one of the major causes of death in a global perspective, although fundamental technological and medical innovations have helped in the treatment or avoidance of infectious diseases, for instance the discovery of antibiotics by Alexander Fleming in the 1930s. In 2019, the global burden report stated in total 26.13 billion incidences, with 420.39 million Disability-Adjusted Life Years (DALY) and 7.86 million deaths (Roser et al., 2021) that were connected to infections with microorganisms, including bacteria, viruses, fungi and parasites (Figure 1). Enteric infections alone made up 23.03 % and 96.8 million DALY in 2019 and of those a large proportion were caused by *Salmonella*-associated infections (Figure 1).

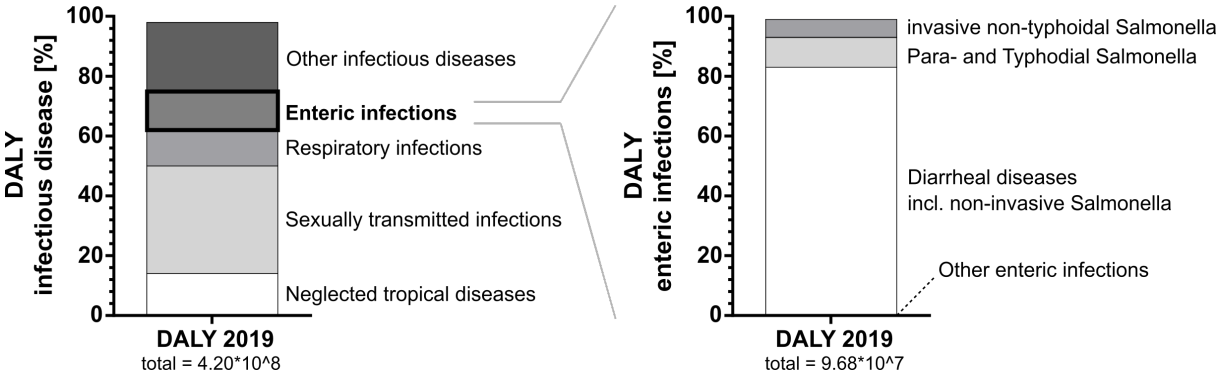

Figure 1. The Global Disability-Adjusted Life Years of infectious diseases including enteric infections of 2019. Percentile distribution of global Disability-Adjusted Life Years (DALY) of infectious diseases (**left**) and enteric infections (**right**) according to the Global Burden of Disease Collaborative Network (Roser et al., 2021).

1.2 The pathophysiology of enteric infections

In general, the course of an enteric infection starts with the ingestion of contaminated material, in most cases food or water (Kirk et al., 2015). After passing the mouth and oesophagus, enteric pathogens are adapted to survive and withstand the antimicrobial environments in the gastrointestinal tract, especially the harsh low pH milieu of the gastric compartment. Some pathogens actively neutralise the pH extra- or intracellularly, others such as *Salmonella* depend on the food structure for protection (Smith, 2003; Waterman and Small, 1998). After entry into the intestine, the environmental conditions change in favour of the pathogens, mainly due to a mild pH and a nutrient-rich environment. Depending on the species, the different

microorganisms can colonize specific intestinal regions. Under physiological conditions, the small intestinal mucosa is covered with a simple layer of mucus that protects the epithelial cells by physical separation as well as provides lubrication towards the luminal content (Figure 2 A). The bile in the lumen is further colonised with beneficial prokaryotes, the intestinal microbiome, whose abundance increases distally from the small to the large intestine (see 1.4). Under pathogenic conditions, this structured hierarchy is lost, resulting in the typical symptoms of enteric infections, such as diarrhoea, nausea, and abdominal pain.

In a simplified and generalised view, the infectious process can be described as followed: the pathogen enters the intestinal section and starts proliferation and colonisation; eventually by secretion of specific toxins or factors, the mucus layer is destabilised, resulting in direct epithelial contact of the pathogens and commensals (Figure 2 B). By that, the pathogens are able to adhere to and ultimately invade the epithelial barrier by their respective mechanisms, leading in most cases to initiation of inflammatory processes and to activation of the innate immune system. These processes eventually lead to barrier and tissue damage, finally resulting in the characteristic symptoms (Figure 2 C) (Rogers et al., 2022).

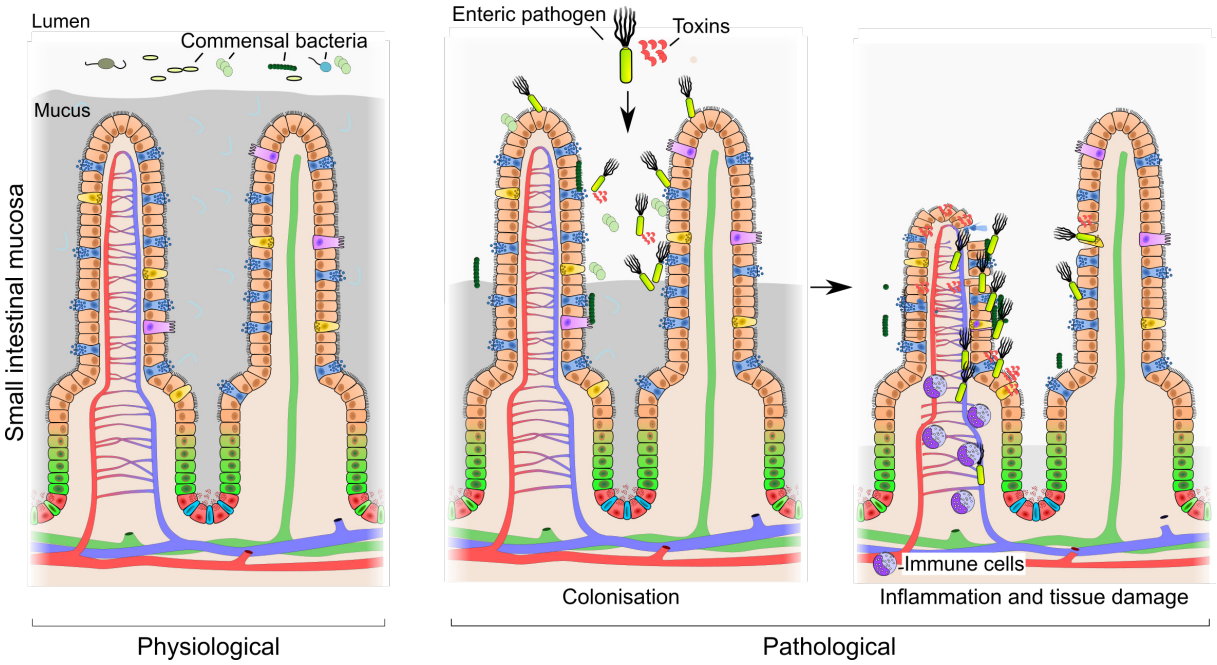

Figure 2. The process of enteric infections. A simplified and generalised schematic depiction of the infection process by enteric pathogens. Under healthy conditions, the small intestinal mucosa is covered with a layer of mucus that separates the luminal content including commensal bacteria from the cellular compartments (**left**). Upon arrival of an enteric pathogen, they start colonising the luminal and mucosal parts, which eventually leads to an inconsistent mucus layer. Thereby, the pathogens and prokaryotes of the microbiome are enabled to directly contact the epithelial cells (**middle**). The pathogens can subsequently adhere and invade the mucosal tissue, leading to the initiation of inflammatory processes and ultimately tissue damage (**right**). Schematics were prepared according to Rogers, Mileto, and Lyras 2022.

1.3 The human gastrointestinal tract

Enteric pathogens are specialised microbes capable of infecting the gastrointestinal (GI) tract. The GI tract comprises multiple individual organ systems, promoting and mediating the absorption of nutrients and liquids along with food digestion. It is composed of the upper and lower GI tract; former includes the mouth, oesophagus, stomach and small intestine (SI); the latter include the colon, rectum and anus. Each organ performs specialised actions to fulfil the overall function of nutrient uptake. In general, the ingested food moves luminally along the GI tract with the help of smooth muscle peristaltic activity; it enables an adequate contact time and thereby absorption of nutrients by specialized uptake mechanisms of the epithelial surface. In particular, the digestion begins already with ingestion of food through the mouth and initial mechanical and enzymatic breakdown, followed by highly coordinated oesophageal peristalsis driving the ingested content into the gastric compartment. In the stomach, the ingested content is exposed to harsh environmental conditions characterized by a low pH, where enzymatic digestion processes the food to chime. After bypassing the pyloric sphincter, the chime reaches the SI, where digestive processes decompose larger proteins, fats and carbohydrates. Accessory organs, such the pancreas, liver and gallbladder support these processes. In the large intestine (LI) most of the water of the luminal content is recovered and a large number of commensal bacteria - the microbiome - supports further digestion processes. Finally, the luminal content is released by the rectum via the anus (Greenwood-Van Meerveld et al., 2017).

1.3.1 The small intestine

The SI connects the stomach and the large intestine with a length of 6-7m and fulfils various tasks, besides chime digestion and processing, namely nutrient absorption and transportation (Volk and Lacy, 2017). It is further a supportive part of the immune system with a specialised anatomy and structure (Mowat and Agace, 2014). The SI is compartmentalized into the proximal duodenum, connecting jejunum and distal ileum, each with its own region-specific functionalisation (Figure 3).

The human duodenum (*duodenum digitorum*) includes a distance of 25 cm (roughly the width of twelve finger, hence the name) with a tube diameter of 2.5 cm, connected distal to the stomach (Cronin et al., 2010). It represents the transition of the gastric to the intestinal part and is therefore confronted with harsh acidic conditions in the stomach. For neutralisation and digestion, submucosal glands - the *glandulae submucosae* (Brunner glands) - secrete mucus, bicarbonate and enzymatic precursors, while mixing the chime (Drenckhahn and Benninghoff,

2008). Furthermore, the pancreas supports with secretion of digestive enzymes into the duodenal lumen. The duodenum is thus the central site of enzymatic food digestion and hence prepares the chime for nutrient absorption in the distal intestinal compartments.

The jejunal part of the SI (*jejunum*) is designed for extensive absorption of the digested luminal content. For that, the surface area is extended compared to duodenum and distal ileum by an increased number of *plicae circularis* and finger-like shaped villi (Cronin et al., 2010; Drenckhahn and Benninghoff, 2008; Smith and Morton, 2010) (see 1.3.1.2.). By that, the passive transport of carbohydrates and active transport of amino acids, glucose, small peptides and others is facilitated and controlled.

The distal part of the SI represents the *ileum*, which transits terminally into the cecum and colon. Here, the ileal epithelium absorbs remaining nutrients with specialisation for vitamin B12 or bile salts (Collins et al., 2021). Furthermore, the ileum exhibits immunological-relevant features by the presence of gut-associated lymphoid tissue, such as Peyer's Patches (PP). The PPs are increasingly found in the distal ileal region, but are also present in the duodenum and jejunum (Cornes, 1965). They are covered by follicle-associated epithelium (FAE) and are specialised structures with close proximity to the immune system (Neutra et al., 2001). Their main function is the uptake and transport of luminal antigens (including microbial peptides) and the presentation to residing immune cells, which is mainly mediated by Microfold cells (M-cells) (Kanaya et al., 2018; Kelsall and Strober, 1996; Kraehenbuhl and Neutra, 2000).

1.3.1.1 The structure of the small intestine

Structurally, the SI is a hollow tube consisting of several layers with multifaceted purposes (Figure 3) (Däullary et al., 2020; Rumsey, 2005). Although there are structural differences and specialties in the various sections of the SI, the general composition is the same. The first layer, separating the SI from the peritoneal space, is the *tunica serosa*. It consists of a mesothelium (*lamina epithelialis serosae*) and connective tissue (*lamina propria serosae*), which is contains with small vessels and nerves and passes to the *tela subserosa.* Adjacent is the *tunica muscularis* - a muscular layer - composed of a thin outer longitudinal and a thicker inner circular smooth muscle fibre layer; the first stretches the intestinal tube, the latter constricts it, thereby propagating the chime in the distal direction. The following layer is the *tela submucosa*, a vascularised layer of connective tissue rich in various collagen subunits and laminins (Berger et al., 2020). It connects the *tunica muscularis* with the *mucosa* and supports the latter with arteries, veins, lymphatic vessels and nerve fibres. The innermost layer, the *mucosa*, composes

three layers: the *lamina muscularis*, *lamina propria* and the mucosal epithelium. The first one, the *lamina muscularis,* ensures the mixing of the luminal chime due to small local contractions. The *lamina propria* consists of connective tissue, which is loosely arranged and populated with residing immune cells. Furthermore, it is embedded with micro vessels, vascular and lymphatic, and the submucosal plexus. It thereby supports the overlying epithelium with oxygen and mediates the circulation of absorbed nutrients. The final cellular layer exposed to the luminal content is the epithelium, a layer of specialised cells lining the inner surface of the hollow SI tube (Däullary et al., 2020; Rumsey, 2005).

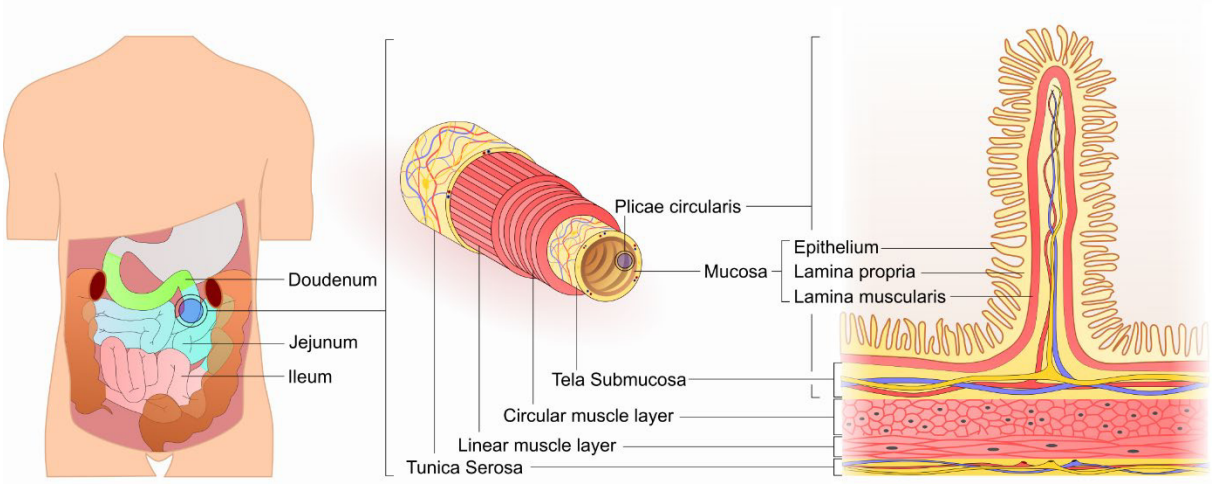

Figure 3. Structure of the small intestine. Schematic depiction of the small intestine. The small intestine, divided in duodenum, jejunum and ileum (**left**), represents a hollow tube connecting the stomach with the large intestine. The tube consists of several layers (from basolateral to luminal): the vascularised *tunica serosa*, layers with linear longitudinal as well as circular muscle fibres, the vascularised *tela submucosa* and the terminal mucosa (**middle and right**). The mucosa in turn is composed of the *lamina muscularis*, the *lamina propria* and the epithelium, which is the outer layer and in contact with the luminal content (**right**). Schematic adapted from Däullary et al. 2020.

The main function of nutrient and liquid uptake by the intestinal tract is mediated by active transport or passive but facilitated diffusion mechanisms. One important factor is the surface area over which transport or diffusion can occur: the larger the surface the higher the uptake per time. The uptake efficiency of the intestinal mucosa is increased by an enlargement of the surface area via multiple factors: first by invaginations of the mucosa into the lumen, so called *plicae circularis* (Figure 3 C), second by further invaginations on the *plicae circularis*, the *villi intestinali* or villus (Figure 3 D), and third via the formation of microvilli at the cellular surface mainly by Enterocytes (Figure 3 F). Formerly, the intestinal surface was thought to be the area of a tennis court, around 230 – 400m^2 (Macdonald and Monteleone, 2005; Niess and Reinecker, 2006), but recent calculations rather state 32m^2 as valid estimation of the human gastrointestinal

tract (Helander and Fändriks, 2014). The SI contributes with 30m^2 to the total area and shows the highest surface extension in relation to the length (Helander and Fändriks, 2014).

1.3.1.2 The small intestinal epithelium

The intestinal epithelium is the last cellular layer and barrier, which separates the luminal content from the inside of the body and represents therefore a boundary tissue to the host-external environment. It is composed of a monolayer of cells, which are columnar in shape, highly polarized and tightly connected and consists of various types of cells, each with specialised and unique functions. It secretes digestive enzymes, antimicrobial peptides and defensive mucus with simultaneous selective absorption of water, amino acids, lipids, fatty acids and carbohydrates (Goodman, 2010; Nicholl et al., 1985). In addition, it establishes a physical and chemical barrier against the luminal content such as enteric pathogens or harmful environmental substances. It therefore plays a multifunctional role in balancing absorption or uptake of essential substances and protection against potential hazards. In order to fulfil these purposes, it holds a divers set of structural morphological, cellular and physical features (Figure 4) (Bonis et al., 2021; Däullary et al., 2020). The SI epithelium is compartmentalised into two functional regions: the crypt and the villus region.

The crypt niche represents the proliferative compartment by harbouring the stem cell (SC) niche with intestinal SCs (ISC) and transit amplifying (TA) cells (Barker, 2013). The villus region on the other site consists mainly of terminally differentiated non-proliferative cell types, which perform the multiple distinct functions of the IE. At the tip of the villus region, the epithelial cells loose cell-cell contacts and are subsequently shed off into the lumen; this controlled process is a programmed cell death, named anoikis (Frisch and Francis, 1994). This natural loss of cells is compensated by the highly regenerative potential of cells residing in the crypt niche. Here, active cycling ISCs undergo asymmetric cell division, where one daughter cells retains SC characteristics residing in the SC niche and the second one becomes an absorptive or secretory progenitor cell (Goulas et al., 2012; van der Flier and Clevers, 2009). Absorptive progenitors, also called transit amplifying (TA) cells, or secretory progenitors migrate from the transit-amplifying zone of the crypt niche towards the villus tip region. During the migration process, the progenitors undergo differentiation into the various intestinal cell types of the epithelium (Enterocytes, Goblet cells, Enteroendocrine (EE) cells, etc.). Although the migration process is thought to be rather passive, recent evidence showed active migratory forces (Krndija et al., 2019). According to this process, the small ISC population provides the cell source for

regeneration and homeostatic balance of the SI epithelium, which exhibits a cell turn-over of 3-5 days (Darwich et al., 2014).

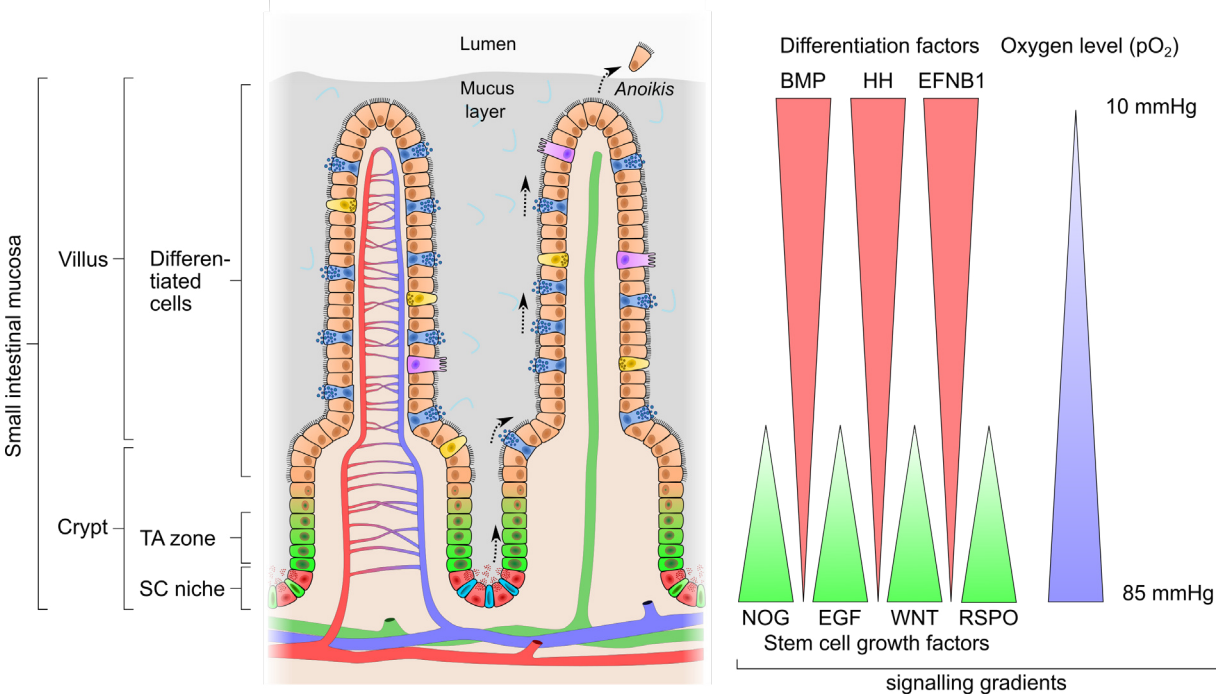

Figure 4. The small intestinal mucosa and important signalling gradients. Schematic depiction of the small intestinal (SI) mucosa including various signalling gradients. (**Left)** The SI epithelium is functionally compartmentalised into crypt and villus regions with the first containing the stem cell (SC) niche and the proliferative transit amplifying (TA) zone and the second containing the differentiated cell types. The highly proliferative crypt niche generates progenitor cells that migrate towards the villus tip and undergo differentiation into the various cell types. On the terminal tip of the villus, the differentiated cells lose cell-cell contact and are shed into the lumen, a programmed cell death process called anoikis. (**Right**) The maintenance of the SC niche as well as the processes of differentiation are among others mediated via several signalling gradients: SC growth factors (e.g. Noggin (NOG), epithelial growth factor (EGF), Wnt3A (Wnt), R-Spondin (RSPO)) are enriched in the SC niche whereas differentiation factors (bone morphogenic protein (BMP), hedgehog (HH), ephrin b1 (EFNB1) are enriched at the villus region. These gradients are opposing and some act as agonist/antagonist. In addition, the level of oxygen is higher in the SC niche and lower at the villus region. Schematic adapted from Däullary et al. 2020.

1.3.1.3 The cell types of the small intestinal epithelium

The intestinal epithelium consists of a variety of different cell types, each exhibiting a distinct set of features to maintain tissue integrity and functionality (Figure 5):

Intestinal stem cells

The ISC population is responsible for tissue homeostasis and regenerative potential after tissue damage. Two types of adult ISCs are located at the bottom of the SC niche: the fast cycling leucine-rich repeat-containing G-protein coupled receptor 5 positive (LGR5+) ISCs and the slow cycling +4 label retaining ISCs (Barker, 2013; Barker et al., 2012, 2007; Potten and Loeffler, 1990), which are thought to act as quiescent and reserve ISC population (Tian et al., 2011). Further, polycomb complex protein 1 (BMI1)+ ISCs were described as additional ISC population, but whether +4 and BMI1+ ISCs represent the same population is under debate.

Collectively, ISCs represent a heterogeneous and dynamic population regarding proliferation and location with long term-self-renewal capacity (Ritsma et al., 2014).

Progenitor cells

After asymmetrical ISC division, one daughter cell starts migrating into the TA-zone with subsequent further cell division. These cells are classified into absorptive or secretory progenitors, depending on their priming for terminal differentiation towards the respective cell lineage. The absorptive progenitors are also called transit amplifying cells and show a high proliferative profile (Bonis et al., 2021); they are further characterised among others by the expression of *HES1* (Bjerknes et al., 2012; Takahashi and Shiraishi, 2020). The secretory progenitors; however, exhibit a low proliferative profile and express among others the transcription factor ATOH1 (Basak et al., 2014; Gracz et al., 2018; Van Es et al., 2012). However, whether a single population of multipotent secretory progenitors exists is still under debate, as a recent study demonstrated Paneth and EE cell development directly from stem cells in contrast to Goblet cells (Böttcher et al., 2021). The fate of the progenitor cells is mostly determined by Notch and Wnt signalling: after stem cell division, the progenitor cells experience high Wnt and low Notch signals leading to a secretory progenitor fate or low Wnt and high Notch signals leading to an absorptive progenitor fate (Sancho et al., 2015). In more detail, when Notch signalling is absent, HES1 is inactive and ATOH1 is active, inducing progenitor fate and simultaneously Notch ligand expression (Kim et al., 2014a; Lo et al., 2017); this process leads to increased Notch signalling in surrounding cells, thereby inducing development towards the absorptive progenitor fate, while repressing the secretory fate by lateral inhibition (Sancho et al., 2015).

The majority of cells in the IE are differentiated cell types and are classified as absorptive or secretory cells, according to their main function (Figure 5):

Absorptive – Enterocytes and Microfold cells

The most abundant cell type are the absorptive Enterocytes. They are responsible for nutrient, water and ions uptake and transcytosis from the lumen into the body (Bonis et al., 2021; Andreas E. Moor et al., 2018). This process is facilitated by microvilli formation on the apical cell surface, which increases the surface area. After cell fate determination of the progenitor, Enterocytes undergo progressive maturation during their migration to the villus tip (Andreas E. Moor et al., 2018). The second absorptive cell type are M-cells, an overall rare cell type with localised enrichment in FAE. Their major role lies in luminal antigen sampling and presentation to the immune system. In contrast to Enterocytes, M-cells lack microvilli formation, instead

they are characterised by the name giving small microfolds on the apical surface (Kucharzik et al., 1998). Similar to Enterocytes, M-cells undergo several maturation steps, which is mainly driven by Receptor Activator of NF-κB Ligand (RANKL) signalling (Mabbott et al., 2013; Nakamura et al., 2018a). Interestingly, absorptive cells can transdifferentiate to M-cells when exposed to RANKL and this process can be actively induced by *Salmonella* Typhimurium (Knoop et al., 2009; Tahoun et al., 2012). These bacteria seem to highjack the sampling function of M-cells to overcome the epithelial barrier for successful infection (see chapter 1.5.2 for more details).

Secretory – EE cells, Paneth cells, Goblet cells and Tuft cells

The secretory progenitors give rise to a broad spectrum of secretory cell types with each serving a distinct function: Enteroendocrine (EE) cells, Paneth cells, Goblet cells and Tuft cells (Figure 5) (Bonis et al., 2021). EE cells are rare chemosensory cells that mainly produce hormones and coordinate thereby the intestinal function with the whole organism. The further subtypes of EE are classified depending on their respective hormonal or secreted product (Beumer et al., 2020). Goblet cells secrete mucus that form a protective layer on top of the epithelium and are the most abundant secretory cells. So called Sentinel Goblet cells reside at the crypt opening and induce mucus release of lower crypt Goblet cells upon detection of bacterial products (Birchenough et al., 2016). Paneth cells can secrete antimicrobial products for the protection of neighbouring cells as wells as important regulatory factors, such as Wnt3A (Date and Sato, 2015). They therefore play an important role in defence and homeostasis, especially as they are located in direct contact to the ISCs. By providing Notch signalling they ultimately control the stemness in the crypt niche (Yin et al., 2013). Tuft cells are the rarest cells in the IE with a prevalence of 0.4 %; their main function is the sensing of helminths and protozoa and the subsequent induction of the inflammatory response (Bonis et al., 2021).

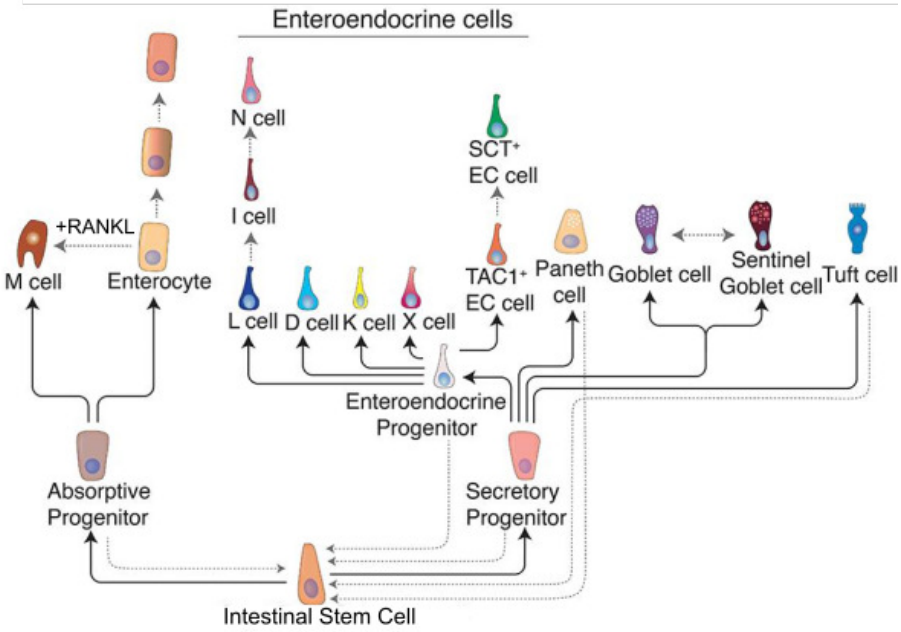

Figure 5. Intestinal cell types and their lineage development. Schematic depiction of the various intestinal cell types and the respective lineage development. By asymmetrical cell division, the intestinal stem cell give rise to either absorptive or secretory progenitor cells. The absorptive progenitor (also transit-amplifying cells) differentiate to Enterocytes or Microfold cells (M cell) depending on the factor RANKL. The secretory progenitor differentiates either to EE progenitors, which further differentiate to several subtypes of EE cells, or to Paneth cells, or to Goblet cells, which can transdifferentiate to Sentinel Goblet cells, or to Tuft cells. Absorptive and EE progenitors, Paneth and Tuft cells can dedifferentiate to stem cells. Schematic adapted from Bonis, Rossell, and Gehart 2021.

1.3.1.4 Signalling and cell lineage determination in the small intestinal epithelium

Intestinal cell development and definition of cell type identity are tightly controlled processes. For instance, the establishment of growth factor gradients contributes to the maintenance of the ISC niche as well as to the controlled differentiation of functional cell types. The growth factors Wnt3A (WNT3a), Noggin (NOG), epithelial growth factor (EGF), and R-Spondin (RSPO) are essential for the ISC population and high in concentration in the crypt niche with decreasing concentration towards the villus region (Farin et al., 2016; Wang et al., 2018). The complex interplay and regulation of stemness by these factors enables stable localised homeostasis, with Wnt signalling as most important. Active Wnt signalling is critical for the maintenance of the ISC niche, as shown by loss of crypt and villus structure and terminal lethality by Dickkopf-1 (Dkk1) induced Wnt-signalling inhibition (Kuhnert et al., 2004). Inter alia, Wnt activation leads to stabilisation of β-catenin, which in favour activates downstream targets for stem cell identity and proliferation (Clevers and Nusse, 2012). In addition, the activity of the Wnt signalling is further increased by RSPO as it facilitates binding of WNT3a to the frizzled receptor (Mah et al., 2016). In addition to the Paneth cell population, also sub-epithelial mesenchymal telocytes actively contribute to the establishment of the WNT3a gradient (Shoshkes-Carmel et al., 2018). NOG, expressed mainly by mesenchymal cells underneath the crypts, inhibits BMP signalling

and thereby cell differentiation (see below) and EGF supports the ISC population by promoting proliferative pathways (Biteau and Jasper, 2011; He et al., 2004; Suzuki et al., 2010; Tan and Barker, 2014).

While WNT3a, NOG, RSPO and EGF concentrations decrease towards the villus region, the concentration of bone morphogenic proteins (BMPs), hedgehog protein (HH) and ephrin B1/B2/B3 (EPHB1/B2/B3) is higher in the villus region (Batlle et al., 2002; Haramis et al., 2004; Tan and Barker, 2014). By this gradient stemness of ISCs is restricted to the crypt niche, as BMPs directly supresses SMAD (Mothers against decapentaplegic homolog) mediated stem cell signature genes independent of Wnt signalling (Qi et al., 2017). Furthermore, these gradients are involved in induction of cell differentiation, directly and indirectly. For instance, BMPs signalling has been shown to be essential for further secretory cell lineage differentiation (Auclair et al., 2007). In contrast, EPHB signalling regulates Paneth cell localisation to the crypt niche by repulsive mechanisms, disclosing active sorting for individual cell types (Batlle et al., 2002). HH signalling mainly mediated by the IECs to the underlying mesenchyme regulates villus-crypt compartmentalisation, as shown by decreased structured villus-crypt axis during HH signalling interference (Madison et al., 2005; van Dop et al., 2009). Collectively, the signalling via Wnt, NOG and EGF seems to dominate the cell fate determination in comparison to BMP, HH or EPHB signalling (Beumer and Clevers, 2020).

Direct intercellular communication contributes as well to the IEC development in the crypt niche and the villus region. Active Notch signalling for instance regulates ISC homeostasis and regeneration (VanDussen et al., 2012). In detail, Paneth cells activate Notch1/2 signalling in neighbouring LGR5+ ISCs by the expression of Dll-1 and Dll-4, which in turn prevents differentiation and supports ISC identity by the induction of downstream target genes, such as Olfactomedin-4 (*OLFM4*) (Carulli et al., 2015; Engelmann and Massberg, 2012; Pellegrinet et al., 2011). However, Notch signalling is then lost during TA transition, but later stochastically restored during TA migration (Van Es et al., 2012). Notch reactivation by Dll-1 does not actively stimulate cell differentiation towards the absorptive lineage, but further Notch inhibition leads to ATOH1 activation and to secretory lineage development (Kim et al., 2014b; Lo et al., 2017; Van Es et al., 2012).

Interestingly, recent investigations in mechanical properties revealed that the geometry of the crypt niche attributes as well to the cell development and that the stiffness of the surrounding extra cellular matrix (ECM) plays a role as it regulates de novo crypt folding in 2D organoid layers (Gjorevski et al., 2022; Pérez-González et al., 2021). However, the geometry of the crypt

regulates rather Paneth cell development, rather than the individual ISC identity directly (Gjorevski et al., 2022).

Collectively, intestinal epithelium homeostasis, including maintenance of the crypt niche and the residing ISC, as well as the IE involves various chemical gradients, cellular interaction and mechanical stimuli and exhibits therefore complex networks and interplays.

1.3.1.5 The barriers of the small intestine

Acting as a barrier is a general important feature of epithelial tissues, as they finally separate the inner body from the environment, may it be the stratified, thick and stable skin epidermis or the simple monolayer SI epithelium (Madison, 2003). In the SI tract, the epithelial barrier can be further divided into a cellular and a non-cellular component: the first is mediated by the tightly connected and structured individual IECs and the latter by factors, which are secreted by the IECs, such as mucins and the resulting mucin layer (Ivanov, 2013; Mandel et al., 1993; Martini et al., 2017; McCauley and Guasch, 2015). At the same time, the epithelial barrier must be able to allow the transport of selected substances for nutrient or water absorption.

1.3.1.6 The mucus barrier

The first layer of defence in the GI tract is the mucus layer that covers the epithelial cells. It lubricates luminal content and acts a physical barrier against pathogens and other harmful agents. Although all organs of the GI are coated with mucus, the composition and distribution vary regionally. For example, the mucus layer of the SI is a single, discontinuous and relatively penetrable layer compared to that one of the colon, which is two-layered, continuous and highly viscous (Herath et al., 2020). There are two kinds of mucins: secreted gel forming mucin 2 (MUC2) and the transmembrane located variants including MUC1, MUC3, MUC4, MUC12, and MUC13 (Grondin et al., 2020). MUC2 is continuously secreted by the specialised secretory Goblet cells and forms the aqueous mucus layer overlaying the epithelium. The membrane-associated mucins contribute further to the glycocalyx formation, a protective layer of glycoprotein and glycolipids that is established on top of the microvilli of Enterocytes (Sun et al., 2020). Several enteric pathogens are specialised in adhering to these glycoproteins, for example *Salmonella* adhesion is facilitated by MUC1 (Li et al., 2019a). The mucus layer and glycocalyx plays therefore a critical role in physiological as well as pathophysiologic processes.

1.3.1.7 The cellular barrier

Cell-cell junction

The tight connection between individual IECs, which gives physical strength and prevents uncontrolled substance transition, is mainly exhibited by the establishment of the epithelial intercellular junction (EIJ) (Chelakkot et al., 2018). EIJ are composed of gap junctions (GJ), desmosomes, adherens junctions (AJ) and tight Junctions (TJ) (Green et al., 2019); GJs are located in basolateral regions between IECs, desmosomes in the middle region and AJs and TJs in the apicolateral region (Al-Ghadban et al., 2016; Citi, 2019; Orr et al., 2019). The TJ complex consists of two families of proteins: occludin and claudins, both members of the transmembrane protein superfamily, which form homo-dimeric complexes in the interstitial space between individual cell membranes (Citi, 2019; Van Itallie and Anderson, 2014). The claudin protein family members expressed in the human SI include claudin (CLDN) 1, 2, 3, 4, 5, 7, 8, 12 and 15 (Garcia et al., 2018). Occludin and claudins bind directly to the cytoplasmic adaptor proteins zonula occludens (ZO-1, -2, -3), which in turn are bound and connected to the actin cell skeleton (Fanning et al., 2012). ZOs are therefore closely localised to TJ proteins and indirectly connect the cell skeleton of neighbouring cells. The TJ complex is supported by the junctional adhesion molecules (JAM-1, -2, -3), members of the immunoglobulin superfamily, which localise at apical cell-cell contacts and interact with the TJ-associated proteins ZO-1 and ZO-2 (Hartmann et al., 2020). The TJ-complex and JAMs are therefore important for the appropriate barrier function of the small intestinal epithelium.

Cell polarisation

A characteristic feature of epithelial cells is the polarized cell status; thus, intestinal epithelial cells develop highly prismatic forms with apical-basolateral specific features, such as apical microvilli and basolateral integrin expression. The polarised status is important to maintain cellular functions, such as vesicle trafficking for transcellular nutrient transport, and is controlled by the epithelial polarity programme (EPP) (Rodriguez-Boulan and Macara, 2014). EPP includes the complex interaction of proteins of the partitioning defective (PAR) proteins, the Crumbs (CRB) and Scribble (SCRIB) proteins, which ultimately lead to a controlled organisation of cell organelles and intracellular trafficking. A key component are the cytoskeletal microtubules, which organise for example the intracellular trafficking as well as the Golgi apparatus and nucleus positioning at the basolateral side (Apodaca, 2001; Chabin-Brion et al., 2001; Gundersen and Worman, 2013). Hence, the nucleus position at the intracellular basolateral side of the cell is an indicator for successful cell polarisation. Furthermore, the establishment and interaction of the various EIJ proteins stabilise and

coordinate the cell polarisation. For instance, JAM-1 interacts and activates the PAR3-aPKC-PAR6 polarity protein complex and classical cadherins participates in the control of nucleus positioning (Dupin et al., 2009; Macara, 2004). In addition, TJ proteins are downregulated in epithelial-mesenchymal transition and JAM-1 promotes polarity maturation in hepatocytes (Chaffer et al., 2016; Iden et al., 2012), underlining the role of the EIJ in the development of cell polarisation.

1.4 Modelling enteric diseases

Enteric pathogens, such as STm, are especially adapted to overcome the gastrointestinal mucosa, a complex tissue that serves among others as barrier against invasion (Kolling et al., 2012). Structural as well as biological and physico-chemical characteristics are important for understanding enteropathogenic infection mechanisms and associated host responses. In the past decades, the main model systems to study enteric pathogens and *Salmonella* pathology were cell lines of cancerous background or immortalized cell lines derived from primary tissue used to establish *in vitro* models of the small intestine and further murine *in vivo* models. Together, these model systems have helped to decipher important principles of STm biology, infection and host cell responses (Collazo and Galán, 1997; Galan and Curtiss, 1989a; Ibarra et al., 2010). For example, the *Salmonella* type three secretion system (T3SS) and the *Salmonella* pathogenicity island (SPI) were identified with the help of the cancer cell lines Henle-407 and MDCK (Criss et al., 2001; Galan and Curtiss, 1989b). Furthermore, the Microfold-cell tropism of STm was first described in mouse models and chronic infections were investigated in mice (Gebert, 1997; B. Jones et al., 1994). However, these model systems come with their benefits and drawbacks: (1) In cell line-based research strategies, data reproducibility and ease of use are key advantages, next to the ability to precisely control experimental parameters. However, they represent only a simplified system lacking the cellular heterogeneity of the native tissue as well as important structural features, such as a correct tissue geometry. (2) On the other side, while animal models represent the complex system of a heterogeneous cell composition and tissue geometry, unfortunately they cannot adequately reproduce the physiology of the human gut due to species variances. For example, the pathogenesis of *Salmonella* infection is different between mice and men ((Keestra-Gounder et al., 2015); of note it can be overcome partly by the usage of humanized mice (Mian et al., 2010). Therefore, in modern infection research alternative tools such as Tissue Engineering-inspired, human-relevant *in vitro* models are required, which could bridge the gap between *in vivo* mouse models and cell line-based model systems.

In this context, it is particularly important to establish *in vitro* models of the intestinal epithelial layer, as it forms the first barrier with the help of epithelial tight junctions, mucus and antimicrobial peptides, thereby preventing the initial infection of the host. However, these *in vitro* systems need to mimic the complexity of the IE regarding structural and cellular features in order to represent the IE and its diverse functions properly.

1.5 The enteric pathogen *Salmonella enterica*

With 109.9 million reported cases of infection per year, *Salmonella* is one of the most common foodborne pathogens worldwide (GBD 2017 Non-Typhoidal Salmonella Invasive Disease Collaborators, 2019) and the research regarding the development of Salmonellosis has been conducted for almost a hundred years (Duncan, 1924). *Salmonella* are rod shape, Gram-negative, facultative anaerobic bacteria and members of the family of Enterobacteriaceae that are classified into over 2500 serovars based on their individual flagellar and surface antigenic composition (Brenner et al., 2000; Kauffmann, 1973). They are further classified based on the clinical manifestation during infection: 'typhoidal' serovars (e.g. *S. enterica* serovar Typhi or *S. enterica* serovar Paratyphi) cause systemic infection in humans with typhoid fever and 'non-typhoidal' serovars (NTS) (e.g. *S. enterica* serovar Typhimurium) infect a broader range of hosts and often cause self-limiting gastroenteritis without typhoid fever (Hohmann, 2001; House et al., 2001). The main environmental source of *Salmonella* infection are chicken eggs and dairy products, but it can also derive from other animal products or pets (Silva et al., 2011). After ingestion, the NTS strain *Salmonella enterica* serovar Typhimurium (STm) survives the acidic environment of the gastric tract by various escape strategies including adaption of the membrane composition or anti-acidic activities (Álvarez-Ordóñez et al., 2011). It then colonizes the human intestinal epithelium and triggers an inflammatory response, which ultimately leads to diarrhoea, potentially life threatening in third world countries. In addition, STm-induced gastroenteritis may cause serious complications, including sepsis and death in immunocompromised persons, the elderly, as well as young children (Feasey et al., 2012; Gilchrist et al., 2015). While STm infections are usually restricted to the intestinal epithelium, the pathogen is able to spread systemically under certain conditions and recurrent episodes can result in chronic infection, contributing to concomitant diseases such as gallbladder or colorectal cancer (Gunn et al., 2014; Keithlin et al., 2015; Lu et al., 2014; Scanu et al., 2015; Zha et al., 2019). Furthermore, due to the excessive usage of antibiotics, antimicrobial drug resistant strains of multiple pathogens are emerging in the past decades, leading to increased mortality rates in infected patients (Ventola, 2015). Also *Salmonella* strains are developing

antibiotic resistance and hence pose the risk of transmission of a multidrug resistant strain from animal to humans (Hyeon et al., 2011). As multidrug resistant pathogens are an increasing threat to the global health and economy, understanding of the bacterial pathogenesis and the bacteria-host interaction are needed to develop tailor-made drug development.

1.5.1 The *Salmonella* Typhimurium infection process

The STm infection and life cycle is a complex process with multiple steps and interconnections, as depicted in Figure 6. After STm bypassed the stomach, it enters the small intestine and starts replication in the lumen. For that, it prepares a beneficial environment by the induction of the inflammatory response; for instance the physiological release of tetrathionate during inflammatory processes nourishes STm and provides an advantage in growth over the intestinal microbiota (Müller et al., 2019; Stecher et al., 2007; Winter et al., 2010). When encountering the epithelial layer, STm invades a variety of cells of the mucosal barrier and can be found in non-phagocytic cells, such as Enterocytes and M-cells, and in phagocytic cells, such as macrophages, neutrophils, and dendritic cells (Figure 7) (Malik-Kale et al., 2011). After trespassing the epithelial barrier, STm can survive in the phagocytic immune cells and uses them for systemic dissemination (Larock et al., 2015; Leoni Swart and Hensel, 2012). Of note, the invasion of M-cells is thought to be the preferred infection route with the aim to invade the underlying macrophages (B. D. Jones et al., 1994).

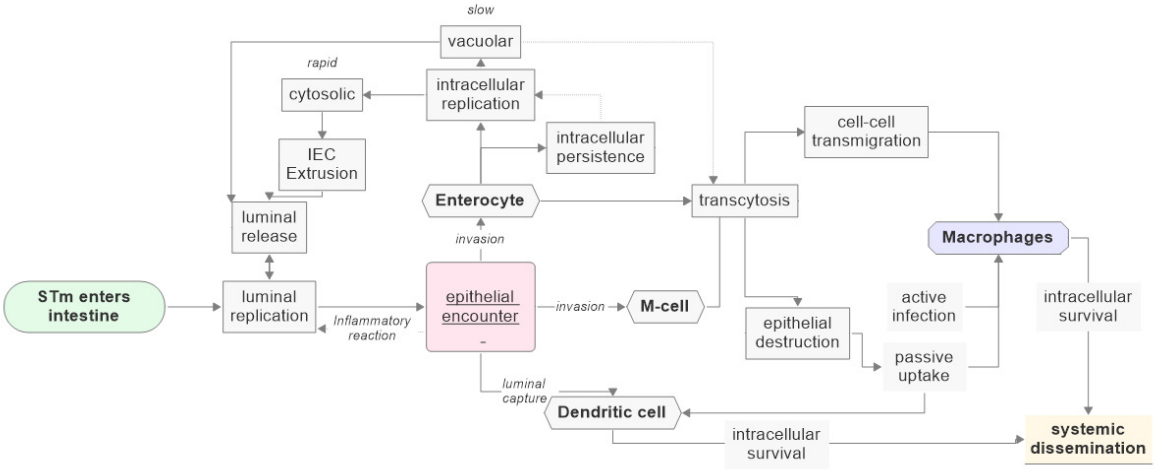

Figure 6. The *Salmonella* Typhimurium life cycle. Schematic depiction of the steps and interconnection of *Salmonella* Typhimurium during its intestinal life cycle according to Chong et al. 2021; Gog et al. 2012; Jones, Ghori, and Falkow 1994; Larock, Chaudhary, and Miller 2015; Leoni Swart and Hensel 2012; Malik-Kale et al. 2011).

1.5.2 The *Salmonella* infection route

In order to successfully adhere to, invade into and proliferate within the host cells, STm has developed a diverse set of molecular mechanisms. These so called virulence factors are encoded on the bacterial genome as at least 23 pathogenicity islands (SPIs) (Schultz et al., 2021). SPI-1 and SPI-2 are the most important in the infection cycle and encode the type three secretion systems (T3SS), a needle like protein cluster, which are used to translocate SPI-1 or -2 effector proteins into the host cytoplasm (Moest and Méresse, 2013). These effector proteins facilitate the bacterial uptake, intracellular survival, and bacterial release as well as control and partially regulate the host immune response (Schultz et al., 2021). For instance, the bacterial entry is mainly facilitated by the SPI-1 T3SS and SPI-1 effectors; thus, the cytoskeleton rearrangement is mediated via SPI-1 T3SS-applied effector SipA (Wang et al., 2016a; Zhou et al., 1999). After successful entry, the SPI-2 encoded effectors mainly regulate intracellular processes; for example, the SPI-2 encoded effectors SifA, SopD2, SseJ are translocated by the SPI-2 T3SS over the vacuole membrane in order to initiate the formation of *Salmonella* induced tubules (SITs) (Knuff-Janzen et al., 2020; Knuff and Finlay, 2017).

After the STm encounters the cellular surface, it adheres first with the help of flagella and type-1 fimbriae to glycosylated cell surface structures and then translocate effector proteins via the T3SS into the cell cytoplasm (Li et al., 2019b; Wagner and Hensel, 2011). These SPI-1 effectors initiate actin rearrangement, which leads to bacterial uptake into a vacuole (Galán and Zhou, 2000). From the SCV, SPI-2 effectors are released into the cytoplasm and inhibit the fusion with lysosomes, leading to maturation of the early SCV to late SCV. Some STm populations escape the early SCV and proliferate rapidly in the cell cytoplasm, whereas others form inactive and persisting populations in late SCVs (Castanheira and García-Del Portillo, 2017). The main proportion of SCV; however, migrated to the Golgi apparatus and the nucleus via dynein interaction and the microtubule network (Fang and Méresse, 2021). In the periphery of the nucleus, SPI-2 effectors further initiate the formation of SIT - highly dynamic, endosomal and elongated, membrane tubules-, which are thought to facilitate nutrient supply (Knuff and Finlay, 2017). Inside the SIT, STm proliferates rapidly and SCVs are shed to the cellular membrane for bacterial release.

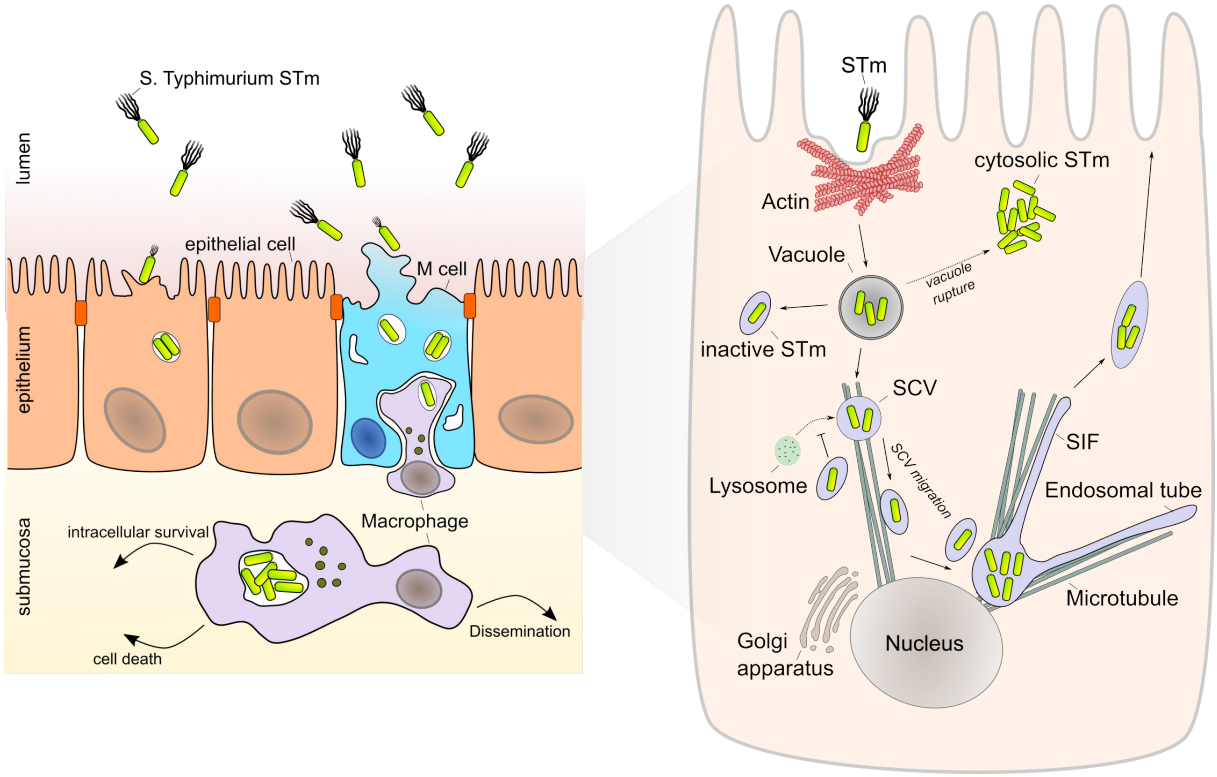

Figure 7. The *Salmonella* Typhimurium mucosal infection route. Left Schematic depiction of the *Salmonella* Typhimurium (STm) encounter of epithelial cells from the luminal side. *Salmonella* invade a variety of epithelial cells as well as specialised microfold ells; in both they proliferate and multiply. After trespassing the cellular barrier, they translocate to underlying macrophages, where they intracellularly survive and either lead to cell death or disseminate throughout the body. **Right** After successful attachment, STm injects *Salmonella* Pathogenicity Island (SPI)-1 effectors via Type Three Secretion Systems (T3SS) into the host-cell cytoplasm, which induce rearrangement of the Actin cytoskeleton and lead to bacterial uptake into the *Salmonella* containing vacuole (SCV). Some STm can escape the SCV and proliferate rapidly in the cytosol, whereas others remain inactive and do not progress. STm in the SCV inhibit actively the fusion with lysosomes as protective measure and migrate via the microtubule network towards the Golgi apparatus and the nucleus. In the nuclear periphery the formation of *Salmonella* induced filaments (SIF) is initiated, which serve as proliferative niche with increased nutrient supply. From SIF newly formed SCVs are shed to the cell membrane and STm can be released. (Larock et al., 2015; Schultz et al., 2021). Schematics were prepared according to Larock, Chaudhary, and Miller 2015 and the Marc Erhardt lab.

Of note, the STm pathobiology can be viewed as an example for co-evolutionary development: the bacteria adapt to a broad range of host cell defence functions and vice versa. For instance after the infection of Enterocytes, STm can escape the SCV and rapidly replicate in the host cytosol (Castanheira and García-Del Portillo, 2017), which in turn leads to extrusion of the Enterocyte by non-canonical activation of the inflammasome as an indirect protective measure (Knodler et al., 2014a, 2010; Sellin et al., 2014). However, these superinfected cells burst in the lumen and release intracellular STm, which then are capable of infecting surrounding cells (Chong et al., 2021). It means that the STm uses the initial defence mechanism for further spreading and hence its survival.

Although the infection route of STm is a well-studied process, some of the phenomena are still under debate. One example is the heterogeneity of the different intracellular STm populations and their relevance *in vivo*. On the one site, SITs were so far only observed in *in vitro* systems,

but are used as an explanation for the high abundance of medium infected cells *in vivo* (Knuff and Finlay, 2017). On the other side, the rapidly replicating cytosolic STm population were just recently identified as a supply for reinfection after the highly infected epithelial cells are shed (Chong et al., 2021), but were long thought to be *in vitro* artefacts. Furthermore, these populations can also vary between infected cell types and species-dependent mechanisms are likely to influence this process as well. This highlights the fact that parts of the STm biology - especially regarding bacterial interaction with the host cell - remain to be discovered, particularly in the context of complex model systems and human physiology.

1.6 Tissue engineering of the intestinal epithelium

The IE plays an important role in infectious diseases and is therefore of particular interest for basic and applied research. It is the entrance point for pathogens or maleficent substances, it can act as a barrier for certain therapeutics or nutrients, and it can be the area for chronic inflammatory diseases, such as colitis ulcerosa. Therefore, i*n vitro* modelling of the intestinal epithelium is an important aspect of biotechnology.

1.6.1 Cell line based *in vitro* model systems

In the past, cell line-based culture systems were widely used and fundamental insights were obtained in gastrointestinal biology. For instance, the adenocarcinomas cell lines, Caco-2 and HT29, are two of the most commonly used *in vitro* models of the human small intestinal epithelium (Fedi et al., 2021). Caco-2 cells spontaneously differentiate into a dense epithelial barrier composed of polarized Enterocyte-like cells with a brush border membrane under standard 2D monolayer culture conditions (Meunier et al., 1995). They express digestive enzymes comparable to the native SI (Engle et al., 1998); however, the tight junction protein expression profile resembles the colonic tissue. Nevertheless, Caco-2 monolayer cultures are commonly used for transport or absorption studies, mainly when cultured in the Transwell® system (Chen et al., 2016).

In contrast to Caco-2, the colon cancer-derived HT29 cell line resembles undifferentiated cells that cannot form a dense barrier. While Caco-2 cells develop an Enterocyte-like phenotype, HT29 cell cultures establish a goblet cell-specific phenotype (Chantret et al., 1988). The mucus-secreting goblet cell-like phenotype can be stabilised by sub-culturing HT29 cells in the

presence of methotrexate (HT29-MTX), which enables the HT29-MTX cell line for investigation of the intestinal mucus layer (Chantret et al., 1988; Jochems et al., 2018).

Caco-2 and HT29-MTX cells are often grown in co-cultures, due to their specific phenotype and functional properties. The co-culture systems exhibit a monolayer of absorbing Enterocyte-like cells with interspaced mucin-secreting goblet cells (Ferraretto et al., 2018). By integrating additional cell types, such as fibroblasts, enteric glia or immune cells, the co-culture models can be further improved (Ferraretto et al., 2018; Kämpfer et al., 2017). However, Caco-2 and HT29 cells are both derived from colon tissue, but are also widely used as substitute for small intestinal research.

Cancer cell line based models are valuable tools for SI research and have led to important fundamental findings. However, because of several aspects these models face limitations regarding their relevance in representing the human pathophysiology: (1) they do not represent all cellular subtypes of the native organ, (2) their cancerous identity inherently represents diseased tissue, and (3) they potentially exhibit artificial gene and protein expression profiles. On the other hand, the advantages are inter alia the cost-efficiency, the standardisation and the reproducibility of cell line-based *in vitro* model systems.

1.6.2 Primary cell-based model system

In addition to cell line based approaches, primary cell based approaches have become more and more popular in the recent years. Formerly, explantation of intestinal tissue (*ex vivo* approaches) already improved the translatability of the obtained observations to patients or phenotypes, but were limited in reproducibility or standardisation. Further, availability and costs hamper the usage in common laboratories. Advances in cell culture methodology enabled the application of primary cells in basic and applied research in an easier and more available manner.

Two large technology steps facilitate todays work with primary intestinal cells: adult stem cells (ASC) derived intestinal organoids and pluripotent/embryonic stem cells (PSC/ESC). PSC cells are often reprogrammed primary human fibroblasts, whereas ESC are inherently pluripotent cells, but must be isolated from primary foetal tissue (Liang and Zhang, 2012; Liu et al., 2019); both can be actively guided into various cell lineages by complex differentiation protocols (McCracken et al., 2014; Spence et al., 2011). ASCs on the other hand are multipotent cell populations that are involved in homeostasis and repair and their differentiation spectrum is limited to respective tissue (Brunet et al., 2022). When cultivated in a 3D ECM-like hydrogel

together with specific growth factors, certain ASC types can form organoids, a 3D multicellular structure that reassembles the spatial and cellular composition of a specific organ (Sato et al., 2011; Zhao et al., 2022). ASC-derived organoids dependent on the stem cell and renewal capacity of the adult organ. For ASC-derived intestinal organoids, the LGR5+ stem cell containing crypt compartments are isolated from the donor tissue and embedded in the 3D ECM-like environment. By the addition of WNT3a, NOG, EGF, and RSPO, these stem cells form stable homeostatic organoids (Figure 8) (Sato et al., 2009; Sato and Clevers, 2013).

Both recapitulate the organogenesis of the desired tissue *in vitro* under specific and controlled growth conditions (Liu et al., 2019; Takahashi et al., 2007). However, the main differences between PSC/ESC and ASC-derived intestinal organoids is the presence of mesenchymal cell types in PSC/ESC derived organoids (Min et al., 2020).

Organoid technology has revolutionised *in vitro* cell model systems, as it is now possible to cultivate human primary cells similarly to cell lines for long-term experiments and in a reproducible manner with the additional 3D feature.

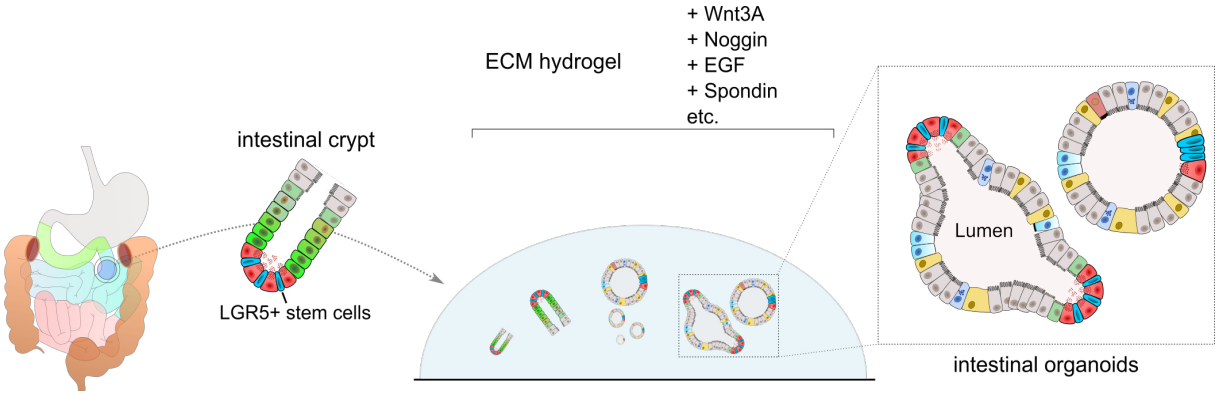

Figure 8. ASC-derived organoid establishment. When intestinal crypts containing LGR5+ stem cells are embedded in an ECM-like hydrogel and cultivated with essential growth factors (WNT3a, Noggin, EGF, Spondin), mimicking the intestinal niche, they form intestinal organoids with the luminal compartment facing inwards and multi-cell type composition. Schematic prepared according the Rahmani et al. 2019

1.6.3 Application of organoids in infection studies

One major drawback of the organoids - especially in infectious disease research - is their inversed polarisation, meaning the apical site of the cell is facing the inner part of the organoid (Aguilar et al., 2021). In that regards, enteric pathogens physiologically encounter first the apical side of cells, penetrate or transcytose the epithelial barrier and then reach the basolateral and stromal side of the epithelium. In organoids, the accessibility of the luminal compartment and hence the “natural” environment is restricted by (1) the surrounding ECM and (2) the

epithelial cell layer. In order to circumvent these restrictions, several valuable approaches were developed that can be separated in two larger ideas: (1) application in 3D leaving the organoid intact and (2) application in 2D by breaking the organoid 3D structure and reseeding them as 2D layers (Figure 9) (Aguilar et al., 2021).

For the first approach, reagents can be applied by microinjection into the lumen (Forbester et al., 2015; Hill and Spence, 2017) or the organoids can be fragmented (Scanu et al., 2015), thereby exposing the inner luminal compartment to the reagent. Both methods are time consuming, labour-intensive and involve mechanical injury to the tissue. As an alternative, the organoid polarity can be inverted by simply removing the ECM and culturing them in suspension, leading finally to apical-out organoids with an accessible apical side (Co et al., 2019). This method so far comprises a low efficiency of the polarity reversal and difficulties in standardization.

In the second approach, the cells are expanded as organoids in an intermediate step and then reseeded as fragments on an appropriate 2D surface (Aguilar et al., 2022, 2021; Breau et al., 2022). The cells establish a 2D monolayer, but usually require an ECM-like coating, such as Matrigel®, collagen, or gelatine coatings for cell attachment and proliferation, in order to sustain carrier-mediated transporter expression and to maintain cellular morphology or permeability characteristics (Behrens and Kissel, 2003). When seeded in a Transwell®-like system, these monolayer systems even recapitulate an accessible luminal and basolateral compartment; they have been successfully established for mouse, human, and porcine intestinal epithelial cells (IEC) (Altay et al., 2019; Hoffmann et al., 2021; Roodsant et al., 2020). Furthermore, it is possible to co-culture the monolayers with cells of the innate immune system in a tissue-like geometry, meaning the correct apical-basolateral orientation of the IECs together with immune cells on the basolateral side (Noel et al., 2017a). These characteristics allow transport, transcytosis and absorption studies and are therefore valuable tools (Däullary et al., 2020).

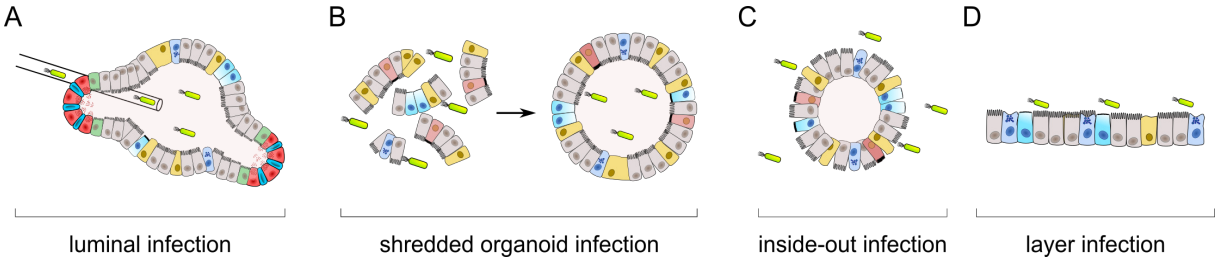

Figure 9. Methods for organoids in infection studies. Schematic depiction of methods for infection of organoids or organoid-derived layers. Pathogens can be applied in various ways: to the luminal compartment of the organoid via microinjection (**A**), to fragments with subsequent organoid regrowth (**B**), to the apical side of organoids with inverted polarity (inside out) (**C**), to the apical side of organoid-derived 2D layers. Schematic prepared according to Aguilar et al. 2021.

1.6.4 Scaffold and matrices for organoid-derived monolayers

The compartmentalization of the SI mucosa in luminal and basolateral compartments is an important feature when mimicking the native tissue in *in vitro* model systems. Therefore, compartmentalised organoid-derived monolayer systems can be generated by application of the cells onto a scaffold or matrix in a Transwell®-like manner. The current Transwell®-like approaches are mostly based on commercially available synthetic matrices, including polyester (PE), polycarbonate (PC) or polyethylene terephthalate (PET) based thin membranes. The membranes usually include defined holes allowing liquid exchange between the two compartments and the standardized production procedure leads to high reproducibility and defined characteristics (Kannaiyan et al., 2016). Of note, recent technical developments allow the production of fibre based synthetical scaffolds with the possibility to easily adjust pore size, stiffness and elasticity (Weigel et al., 2022). An alternative to synthetic approaches are biological scaffolds (=bioscaffolds); these include matrices that are derived from allogenic or xenogeneic native tissue in the form of decellularised tissue structures or hydrogels. For that, the tissue is explanted and extensively washed with cell lysing reagents, thereby removing the host cells entirely but sustaining the biomimetic tissue characteristics (Andrée et al., 2013). Afterwards, the decellularised tissue can be directly used for seeding cells or further processed to a liquid hydrogel that is cast as a cell supporting structure (McCrary et al., 2020). In particular, decellularised small intestinal submucosa (SIS) tissue was used by Schweinlin et al. and by Meran et al. to generate small intestinal tissue models with ASC-derived organoids (Meran et al., 2020; Schweinlin et al., 2016) and Kim et al. generated tissue-specific hydrogel from small intestinal tissue for 3D organoid culture as an alternative to Matrigel® (Kim et al., 2022).

In comparison to biological scaffold, the synthetic scaffolds are cheap, accessible and standardized, whereas decellularised biological matrices exhibit high expense in production and often lack standardization (Kannaiyan et al., 2016; Kitano et al., 2017). However, the standardized synthetic matrices usually require additional coating procedures, in order to achieve adequate cell attachment and behaviour (Pagel and Beck-Sickinger, 2017; Zhang et al., 2009). Furthermore, the synthetic membrane might influence diffusion and distribution of biological or chemical compounds, as it represents an additional artificial barrier, and the proper physical features such as the structural geometry or the biomechanical elasticity of the native ECM is often not represented (Kannaiyan et al., 2016). Recent studies emphasized the importance of those biomechanical cues mediated by the ECM (Berger et al., 2020; Gjorevski et al., 2022; Pérez-González et al., 2021); they are transmitted via the cell skeleton in individual

cells, thereby regulating cell morphology, differentiation and identity and are hence important features for correct cellular behaviour. Unlike synthetic ones, the bioscaffolds inherently resemble the native protein composition of ECM and mimic the physical parameters; they provide eventually the correct 3D geometry as well as the elasticity/stiffness of the native tissue (McCrary et al., 2020).

Bioscaffolds as well as synthetic scaffolds are currently used in combination with organoid-derived monolayers for small intestinal tissue engineering (Meran et al., 2020; Moorefield et al., 2018; Roodsant et al., 2020; Schweinlin et al., 2016). In the context of enteric infectious disease research, it is especially important that these model systems resemble the native tissue to the best extent. In that regard, impaired cellular morphology was demonstrated when cells were grown on a synthetic PET membrane as they exhibited reduced cellular polarisation in comparison to cells of the native tissue (Pusch et al., 2011). Therefore, an evaluation of primary cell-based *in vitro* tissue models of the small intestinal epithelium with regards to biological or synthetic scaffolds is needed, especially for applications in enteric infectious research.

2 Aim of the study

In recent years, fundamental research regarding gut biology in general and the intestinal epithelium in detail was conducted on behalf of primary ASC-based organoid technology as well as traditional cell line-based approaches. The findings of Sato et al. in 2009 especially allowed progress in the research field of IECs development and characterisation of cellular entities focusing in particular on intestinal stem cells (Sato et al., 2009). However, although revolutionizing this research field, organoid technology still comes with drawbacks, in particular in infectious disease research. Therefore, methods were developed to overcome the limitations of the organoid technology, such as inverting intestinal organoid polarisation or growing organoids as 2D monolayers in Transwell®-like set ups (Co et al., 2019; Moon et al., 2014). Biological scaffolds derived from decellularised tissue, such as the SIS, have been shown to be valuable solutions as they provide the *in vivo* microniche in an *in vitro* system with potential transplantation applications as shown by Schweinlin et al. in 2016 and Meran et al. in 2020 (Meran et al., 2020; Padhi and Nain, 2020; Schweinlin et al., 2016). Before applying a complex tissue model in infectious disease research, it is essential to characterise the applied system and its resemblance to the native tissue. For that, all tissue engineered model systems need validation to see if they simulate the original tissue in structural, functional and cellular components and can thus recapitulate further the infection process.

Thus, the aim of the first part of the present study was the in-depth characterisation of the formerly developed hITM-SIS regarding its bio-comparability and tissue analogy. Therefore, structural, cellular and functional aspects of the hITM-SIS were investigated for, whether they resemble tissue characteristics of the native IE and how a biological (SIS) versus a synthetic scaffold (PET) influences these aspects in a Transwell®-like *in vitro* system. For that, the cellular morphometry and barrier features of the tissue models were examined. Furthermore, the cellular composition as well as structural features of the hITM-SIS were characterised for the first time with cutting-edge technologies (scRNA sequencing).

The aim of the second part of the present study was to develop a human STm infection tissue model, which can be applied in fundamental research in the cellular pathogenesis of STm infection, and to investigate the STm dynamics during the infection process. Therefore, the resemblance of STm infection key steps, such as bacterial invasion, intracellular replication and establishment of the ST niche, was examined in the hITM-SIS upon infection. Next, the cellular pathogenesis of STm was investigated with focus on STm dynamics and on the host-cell response by an in-depth transcriptomic approach.

3 Material and Methods

3.1 Material

3.1.1 Equipment

Table 1: List of applied technical equipment and devices.

Equipment/Device	Manufacturer
Blocking Station TES Valida	MEDITE
Cell Incubator (37 °C, 5 % CO_2)	Heraeus
Centrifuge Multifuge X3R	Thermo Fisher Scientific
Centrifuge 5417R	Eppendorf
Confocal microscope TCS SP8	Leica Microsystems
Embedding Station Microm STP 120	Thermo Fisher Scientific
Flow Cytometer BD Accuri C6 Plus	BD Biosciences
Freezer -20 °C	Liebherr
Freezer -80 °C	Thermo Scientific
Infinite 200 PRO NanoQuant Microplate Reader	Tecan Group AG
Liquid Nitrogen Storage Tank MVE 815 P190	German cryo
Microscope BZ9000 E BIOREVO System	KEYENCE Deutschland GmbH
PCR Thermocycler	SensoQuest
CFX 96 Touch™ Real-Time PCR Detection System	Bio-Rad
Sliding Microtome RM 2255	Leica
TissueLyser LT	Qiagen
FACS Aria 3	BD Biosciences
Scanning Electrone Microscope JSM-7500F	JEOL
Transmission Electrone Microscope JEM-2100	JEOL
2100 Bioanalyzer	Agilent
Accu-Jet Pro Pipettor	Brand
Aspiration Device: VacuBoy	Integra Biosciences
QubitTM 4.0 Fluorometer	ThermoFisher
ChromiumTM Controller	10x Genomics
Water bath	Lauda
NextSeq 500 sequencer	Illu mina
Mantis Microfluidic Liquid Handler	Formulatrix

3.1.2 Software

Table 2: List of applied software.

Software	Version	Source
FlowJo	10.6.1	FlowJo
Graphpad Prism	6.04	GraphPad Software Inc.
ImageJ (Fijii)	1.51s	NIH USA
LAS-X	V1.6	Leica
Mendeley	1.19.18	Mendeley
IMARIS	8.4.2	Oxford Instruments
FCAP array	v3	BD Biosciences

3.1.3 Consumable material

Table 3: List of disposable materials.

Disposable materials	Manufacturer
Cell Culture Multiwell Plates: 6 well, 12 well, 24 well, 96 well	TPP
Cell strainer: EASYstrainer™ 40 µm sterile	Greiner BioOne
Cell strainer: Pep-preparation Filters 30 µm	Miltenyi Biontech
Centrifuge Tube PP CentriStar 15 ml	Corning
Centrifuge Tubes: 15 ml, 50 ml	Greiner BioOne
Cover Slips for Object Slides: 24 x 60 mm	Menzel Glaser
Cryo Tubes: 1.8 ml	Greiner BioOne
Disposable Pipettes: 5 ml, 10 ml, 25 ml, 50 ml	Greiner BioOne
Disposal Bags	Hartenstein
Embedding Cassettes	Klinipath
Embedding Filter Paper	Labonord
Microtome Disposable Blades: Type A35	pfm Medical
Nitrile gloves	Hartmann
Object Slides: PolysineTM (25 x75 x1 mm) Superfrost Plus	 Thermo Fisher Scientific Thermo Fisher Scientific
Parafilm®, M	Carl Roth
Pasteur Pipettes	Brand
Petri Dishes: 145 x20 mm	Greiner BioOne

PET-Cell culture Transwells (0.4 µm poresize)	Greiner BioOne
Pipette Filter Tips: 0.5-10 µL, 10-100 µL, 100-1250 µL	Nerbe Plus
QIAshredder spin column	Qiagen
Reaction Tubes: 0.5 ml, 1.5 ml, 2.0 ml	Sarstedt
Scalpel Blades, rounded	Bayha
Sterile Filter: Diameter 50 mm, Pore Size 0.2 µm	Sartorius Biotech
Super PAP Pen Liquid Blocker	Science Services
Syringes: 5 ml, 10 ml, 20 ml, 50 ml	BD Biosciences

Table 4: List of laboratory materials.

Laboratory materials	**Manufacturer**
Beakers: 1 l, 250 ml	Schott
Cell crowns	Chair of Tissue Engineering and Regenerative Medicine, Wuerzburg
Centrifuge Tubes Rack	NeoLab
Cold Protection Gloves	VWR
Freezing container Mr. Frosty	ThermoFisher Scientific
Funnel	Hartenstein
Glass Pipettes: 5 ml, 10 ml, 25 ml	Brand
Hemocytometer Neubauer Improved	Hartenstein
Laboratory Bottle: 1 l, 250 ml, 100 ml, 50 ml	Schott
Magnetic Stirring Bar	Hartenstein
Magnetic Stirring Bar Retriever	Hartenstein
Object Slide Racks: Glass, Stainless Steel	Mercateo
Protective Goggles	NeoLab
Reaction Tubes Rack	NeoLab
Scalpel	Bayha
SIS scaffold	Chair of Tissue Engineering and Regenerative Medicine, Wuerzburg
Spatula	VWR
Spoon Spatula	Hartenstein

Stainless Steel Casting Molds for Embedding Tissue 24 x37 x9 mm	Labonord
Sterile Filter (Attachment for Laboratory Bottles)	Hartenstein

3.1.4 Commercial kits

Table 5: List of commercial kits used in this work.

Kit	Manufacturer
10X Single 3' Reagent kit v3.1	10x Genomics
Click-iT™ Plus EdU flow cytometry Assay Kit	Thermo Fisher Scientific
CytoTox 96® Non-Radioactive Cytotoxicity Assay	Promega
ERCC RNA Spike-Ins Mix1	Invitrogen
High Sensitivity DNA kit	Agilent
iScript™ cDNA Synthesis Kit	BioRad
Nextera® XT	Illu mina
RNeasy Micro Kit	Qiagen
SMART-seq2 V4 kit	Takara
TotalSeq™	Biolegend
Venor®GeM Classic Mycoplasma detection kit	minerva Biolabs
Human Inflammatory Cytokine Cytometric Bead Array (CBA) - I Kit	BD BioSciences

3.1.5 Chemicals

Table 6: List of applied chemicals and solutions.

Chemical/Solution	Manufacturer	Catalogue #
[Leu^{15}]-Gastrin	Sigma-Aldrich	G9145
A83-01	Tocris Bioscience	1939
Advanced Dulbecco's Modified Eagle Medium F12 (DMEM) 1X (NEAA, NaPy)	ThermoFisher Scientific	12634028
Alcianblue 1 % (pH 2.0)	Morphisto	10126.00500
AMPure XP beads	Beckman Coulter	A63882
AntiAnti	ThermoFisher Scientific	15240-062 (100x)

Antibody dilution solution	DCS Innovative Diagnostic-Systems	
B27 Supplement	ThermoFisher Scientific	12587010
Basic FGF (human)	Peprotech	100-18B
Bovine Albumin	MP Biomedicals	0219989925
Cell Staining Buffer	Biolegend	420201
DAPI FluoromountG™	Invitrogen	SBA010020
Descosept	Dr. Schuhmacher	
Dimethyl sulfoxide (DMSO)	SigmaAldrich	D243850 ML
Donkey Serum	SigmaAldrich	D966310 ML
Dulbecco's Phosphate Buffered Saline w/o Ca^{2+} and Mg^{2+} (PBS-)	SigmaAldrich	D8537
Dulbecco's Phosphate Buffered Saline with Ca^{2+} and Mg^{2+} (PBS^{+})	SigmaAldrich	D8662
EDTA	SigmaAldrich	E5134
Entellan	Merck	10177.01000
Ethanol, absolute	Carl Roth	9065.2
Ethanol, denatured (96 %)	Carl Roth	T171.2
Fetal Calf Serum	Lonza	8SBO16
GlutaMAX-I (100x)	ThermoFisher Scientific	35050-061
Hepes	SigmaAldrich	H3662-1MBioreagent
HistoGel™	Thermo Scientific	HG-4000-012
hR-Spondin 1	Peprotech	120-38-500UG
human Epidermal Growth Factor (hEGF)	Peprotech	AF-100-15-500UG
iScript™ Reverse Transcription Supermix	BioRad	1708840
JAG-1 (Notch Ligand)	AnaSpec Inc.	AS-61298
LY2157299	CaymanChemicalCompany	15312
Lysisbuffer	Takara	635013
Matrigel Matrix Growth Factor Reduced (GFR) phenol red free	Corning	356231

N2 Supplement	ThermoFisher Scientific	17502048
N-Acetylcystein	Sigma-Aldrich	A9165-5G
Nicotinamid	Sigma-Aldrich	N0636-100G
Nuclear fast red 0.1 %	Morphisto	10264,00500
Paraffin	Carl Roth	6642.6
Paraformaldehyde (PFA)	AppliChem	A3813,1000
Phalloidin-iFluor 555 Conjugate	abcam	ab176756
Phalloidin-iFluor 647 Conjugate	abcam	ab176759
Rec Murine Noggin	Peprotech	250-38-1MG
RNAprotect Tissue Reagent	QIAGEN	1018087
Roticlear Histofix®	Carl Roth	P087
SB202190	Absource Diagnostics	S1077-0100
SsoFast EvaGreen Supermix	Biorad	172-5201
SYTOX Deep Red Fluorescence Nucleic Acid Stain for fixed/dead cells	ThermoFisher Scientific	S11380
TritonX 100	Carl Roth	3051.2
TruStain FcXTM FcBlocking	Biolegend	422301
Trypan Blue, 0.4 %	SigmaAldrich	T8154100 ML
TrypLE Express	ThermoFisher Scientific	12605-010
Tween20	VWR	8.22184.0500
Ultrapure Water	Millipore	
WST-1	Sigma-Aldrich	11644807001
Xylene	Carl Roth	9713.3
Y-27632 (ROCK inhibitor)	Tocris Bioscience	1254/10
β-Mercaptoethanol	Carl Roth	4227.1

3.1.6 Cell culture media

The L-WRN conditioned medium and the WNT3a conditioned medium used for cell culture were produced in house using the cell lines L-Wnt-3A and L-WRN (see table 14).

Table 7: Composition of organoid crypt medium.

Concentration	Crypt medium
100 %	Basal medium (DMEM F12 Advanced)

1x	B27
1x	N2
1 mM	N-acetylcystein
1x	AntiAnti
10 mM	HEPES
2 mM	GlutaMax-I

Table 8: Composition of proliferation medium used for organoid and tissue model culture.

Concentration	**Proliferation medium**	
75 %	L-WRN conditioned medium	
25 %	crypt medium	
500 nM	A-83	
50 ng/ ml	hEGF	
10 mM	Nicotinamid	
10 nM	Leu-Gastrin	
500 nM	LY2157299	
10 µM	SB202190	
0,75 %	AntiAnti	
10 µM	Y-27632	Only after passaging
1 µM	JAG-1	Only after passaging

Table 9: Composition of differentiation medium used for organoid and hITM culture.

Concentration	**Differentiation medium**	
25 %	WNT3a conditioned medium	
75 %	crypt medium	
500 nM	A-83	
50 ng/ ml	hEGF	
10 nM	Leu-Gastrin	
500 nM	LY2157299	
100 ng/ ml	mNoggin	
500 ng/ ml	hR-Spondin	

3.1.7 DNA oligos

Table 10: List of qPCR primer and sequences.

Name	Sequence
mucin 2	5'-AGGATCTGAAGAAGTGTGTCACTG-3' 5'-TAATGGAACAGATGTTGAAGTGCT-3'
Villin	5'-GCAGCATTACCTGCTCTACGTT-3' 5'-GCTTGATAAGCTGATGCTGTAATTT-3'
Lysozyme	5'-CCGCTACTGGTGTAATGATGG-3' 5'-CATCAGCGATGTTATCTTGCAG-3'
mucin 1	5'-AGCTTCTACTCTGGTGCACAA-3' 5'-GGTGGCTGGGAATTGAGA-3'
OLFM4	5'-ACT GTC CGA ATT GAC ATC ATG G -3' 5'- TTC TGA GCT TCC ACC AAA ACT C - 3'
Ef1α	5′-AGGTGATTATCCTGAACCATCC-3′ 5′-AAAGGTGGATAGTCTGAGAAGC-3′

Table 11: List of DNA-sequences for HCR-FISH Probes of OLFM4

Pair		Sequence (5'-3')
OLFM4-P1	odd	gTCCCTgCCTCTATATCTTTctataatactccaacagtctccca
	even	tagcaaatcatccagtgtgttgtacTTCCACTCAACTTTAACCCg
OLFM4-P2	odd	gTCCCTgCCTCTATATCTTTgtgttgtacatgttgacgtacatgt
	even	gtcaggttaactctggcaatattccTTCCACTCAACTTTAACCCg
OLFM4-P3	odd	gTCCCTgCCTCTATATCTTTacatggatgaggactagtcattggg
	even	tccaggcatggaagaattagtggtgTTCCACTCAACTTTAACCCg
OLFM4-P4	odd	tcaagacaaatgtcctagatctctaTTCCACTCAACTTTAACCCg
	even	gTCCCTgCCTCTATATCTTTgtggtagaactatgcacctaaacat
OLFM4-P5	odd	acagaagcacatcacatacaccagcTTCCACTCAACTTTAACCCg
	even	gTCCCTgCCTCTATATCTTTggtttccaactactgcactgattaa
OLFM4-P6	odd	accatgaaggcgttagaagcagatgTTCCACTCAACTTTAACCCg
	even	gTCCCTgCCTCTATATCTTTttatactgcttggtataccaagtgt
OLFM4-P7	odd	gattacgacggatattattggcaaaTTCCACTCAACTTTAACCCg
	even	gTCCCTgCCTCTATATCTTTtgtgctaacgacactgagtttgaga
OLFM4-P8	odd	acctctcaagagaacccttagtagaTTCCACTCAACTTTAACCCg
	even	gTCCCTgCCTCTATATCTTTatctctagatcctgtaaacagaact

3.1.8 Antibodies

Table 12: List of primary antibodies used in this study.

Antigen	Host	Clonality	Manufacturer/ Cat. #	Applied dilution
mucin 2	rabbit	polyclonal	Abcam/ 76774	1:100
mucin 1	rabbit	monoclonal	Abcam/109185	1:100
Lysozyme	goat	polyclonal	SantaCruz/ sc27958	1:100
Villin	goat	polyclonal	SantaCruz/ sc7672	1:100
Occludin	mouse	monoclonal	Thermo Fisher / 33-1500	1:100
ZO-1	rabbit	polyclonal	Ptglab/ 21773-1-AP	1:100
LPS		monoclonal	Abcam /	1:300
OLFM4	rabbit	monoclonal	Cell Signaling / D1E4M	1:250
p65 NfkB	rabbit	monoclonal	Cell Signaling / D14E12	1:100

Table 13: List of secondary antibodies used in this study.

Antigen	Host	Conjugated Fluorochrome	Manufacturer/ Cat #
Rabbit	Donkey	Alexa Fluor 647	Invitrogen / A-31573
Rabbit	Donkey	Alexa Fluor 555	Invitrogen / A-31572
Mouse	Donkey	Alexa Fluor 555	Invitrogen / A-31571
Goat	Donkey	Alexa Fluor 647	Invitrogen / A-21447

3.1.9 Cell lines and organoids

Table 14: List of applied cell lines and organoids.

Line	Source	Catalogue #	Note
L-Wnt-3A	ATCC	CRL-2647™	
L-WRN	ATCC	CRL-3276™	

Human intestinal organoids 15-09	Chair of Tissue Engineering and Regenerative Medicine, Würzburg		Female, 26 years

3.1.10 Bacterial strains

Table 15: List of applied bacterial strains and their features

Name	Strain	Source	Specification	Marker	Note
STm-GFP	S. Typhimurium SL1344	IMIB, AG Vogel	Ptet-GFP	Str^R Cm^R	wt, constitutively expressing GFP
STm-rep	S. Typhimurium SL1344	IMIB, AG Vogel	pAW-18	Str^R Amp^R	wt, constitutively expressing mCherry, Arabinose inducible GFP

3.2 Methods

3.2.1 Cell and bacterial culture

3.2.1.1 Cell culture

Cell culture was performed under sterile conditions by using a laminar flow cabinet. Cells were cultivated and maintained in a humidified incubator at 37 °C, 95 % humidity, 5 % CO_2. Applied media and media compositions are listed in chapter 3.1.6. Mycoplasma tests were regularly performed with the Venor®GeM Classic kit.

3.2.1.2 Organoids - ethics approval for human tissue biopsies

Crypts were isolated from Human jejunal biopsies that were obtained from obese patients undergoing gastric bypass surgery at the University Hospital Würzburg, surgery unit of PD Dr. med. C. Jurowich. Informed written consent was obtained beforehand. The use of human tissue was approved by the Institutional Ethics Committee on human research of the Julius-Maximilians University Würzburg (approval number: 280/18-sc). (Däullary et al., 2022, in review)

3.2.1.3 Organoids - crypt isolation for organoid establishment

Small intestinal organoids were established from healthy donor biopsy tissue material as previously described (Sato et al., 2009; Schweinlin et al., 2016). In detail, a ~2 cm^2 piece of small intestinal biopsy material was acquired during surgery and stored in HBSS on ice for up to 4h until further processing. For crypt isolation, first the underlying muscle layer was removed mechanically via a pair of scissors. Next, the mucosal and the villus regions were partly removed by scrapping with sterile glass slides. Afterwards, the crypt containing epithelial tissue was washed once in ice-cold HBSS and subsequently incubated in HBSS supplemented with 0,5mM EDTA for 30 min under shaking conditions at 4 °C. After EDTA treatment, the tissue was washed once with ice-cold HBSS and transferred to a 50 ml tube containing 10 ml ice-cold HBSS, followed by mechanical shaking of the tube for ~1 min (= fraction 1). Subsequently, the tissue was transferred to a fresh 50 ml tube containing 10 ml ice-cold HBSS and the shaking procedure was repeated (= fraction 2). After an additional repeat of that process (= fraction 3), the tissue was removed and crypt number was determined in each of the fractions

microscopically. Fractions with the lowest number of single cells and villus fragments but containing the highest number of crypts were pooled and centrifuged at 350 g for 3 min at RT. Crypts were resuspended in proliferation medium containing JAG-1 (1 µM) and Y-27632 (10 µM) to a final concentration of 100 crypts/ µl and were subsequently mixed with an equal volume of Matrigel®. The crypt-media-Matrigel® suspension was applied in prewarmed 6 well cell culture plates as 10 µl droplets forming domes. After solidification of the droplets for 15 min at 37 °C, 1,5 ml proliferation medium containing JAG-1 and Y-27632 was added per individual 6 well and plates were incubated at 37 °C, 95 % humidity, 5 % CO_2. After 48h, the formation of organoids was detectable that were further cultivated and processed as mentioned in 3.2.1.4.

3.2.1.4 Organoids - cultivation of intestinal organoids

Organoid passaging was performed every 4-5 days depending on organoid size and distribution. For intestinal organoid passaging, Matrigel®:media droplets containing organoids were detached from the 6 well plate by resuspension in the cultivation media, followed by transfer of the suspension into 15 ml non-adhesive tubes containing 1 ml cold PBS-. After centrifugation at 350 g for 3 min at RT, the supernatant was discarded and remaining organoids were enzymatically dissociated into either single cells or clusters of diverse sizes. To this, organoids were resuspended carefully in TrypLE® and were incubated at 37 °C for up to 10 min with resuspension steps every 3 min. Single cell or cluster formation was observed microscopically. TrypLE® activity was inhibited upon completed dissociation by 10-x dilution with cold basal media. Cells were centrifuged at 450 g, 3 min RT, resuspended in basal media and cell number was determined using TrypanBlue counterstaining and a Neubaur counting chamber. After additional centrifugation at 450 g for 3 min at RT, the cell concentration was adjusted with cold proliferation medium containing JAG-1 (1 µM) and Y-27632 (10 µM) and mixed with Matrigel® at a 1:1 ratio. Subsequently, the cell-media-Matrigel® suspension was applied on prewarmed cell culture plates as 10 µl droplet forming domes and the plate was incubated at 37 °C, 95 % humidity, 5 % CO2 for 15 min for Matrigel® solidification. Afterwards domes were submerged in proliferation medium containing JAG-1 (1 µM) and Y-27632 (10 µM) for 48h. Media was changed every 48h-72h.

3.2.1.5 Organoids - Cryopreservation of intestinal organoids

For cryopreservation, small intestinal organoids were detached from the cell culture plate and washed once with basal media to remove excessive Matrigel. Organoids were resuspended in 90 % FCS + 10 % DMSO and were frozen at -80 °C in a freezing container. After 24h, frozen organoid samples were transferred to -170 °C liquid nitrogen tank for long-term storage. For thawing of frozen organoids, the frozen cell suspensions were quickly thawed at 37 °C and transferred immediately to a 15 ml tube with 9 ml prewarmed basal media. After centrifugation with 350 g for 3 min at RT, organoids were washed once with basal media, followed by another centrifugation step. Finally, the supernatant was discarded and the organoids were cultured as described in section 3.2.1.4.

3.2.1.6 Bacterial culture

Bacteria were grown on Lennox broth (LB)-Agar plates and in LB liquid with or without their respective antibiotics (Chloramphenicol: 100 µg/ ml; Ampicillin: 50 µg/ ml), incubated at 37 °C. For infection experiments, two STm strains were applied (Table 15): (1) the constitutively GFP expressing Wild-type derivative of the STm strain SL1344 (JVS-3858 (Papenfort et al., 2009)), further called STm, and (2) the constitutively mCherry expressing STm proliferation reporter strain (=STm-rep) NCTC 12023 carrying a fluorescence dilution plasmid pFCcGi (JVS-11424 (Helaine et al., 2010; Stapels et al., 2018)), which contains an Arabinose inducible GFP cassette.

3.2.2 Intestinal tissue model preparation

Tissue models were generated using either a biological small intestinal submucosa (SIS) matrix or synthetic PET-membranes. SIS scaffolds were prepared in house from the porcine small intestine, assembled in cell crowns in a Transwell®-like setting (Figure 10). PET membranes were commercially purchased in Transwell®-like settings.

3.2.2.1 SIS based tissue models (hITM-SIS)

Preparation of SIS

According to the German law and institutional guidelines, animal research was performed and approved by the Ethics Committee of the District of Unterfranken, Würzburg, Germany (approval number 55.2-2532-2-256). The biological matrix (SIS; small intestinal submucosa)

was prepared from jejunal segments that were explanted from young pigs (~20 kg; age: 6-8 weeks; weight: provided by Niedermayer, Dettelbach, Germany). According to previously published protocols chemical decellularization was performed on the explanted jejunal segments (Jannasch et al., 2015; Pusch et al., 2011). In short, small intestinal tissue (jejunal and ileal) free of peyers patches was explanted from euthanized piglets with subsequent mechanical removal of the mucosal layer. Mucosa-free tissue was decellularised via several incubation and washing procedures. After final gamma sterilisation, the SIS pieces were stored in sterile PBS- until use.

Assembly of SIS and cell crown

In order to establish a compartmentalised SIS based tissue model, the decellularised SIS scaffold is fixed between two plastic cylinders (Figure 10), further referred to as cell crowns. For that, the SIS was spread on a sterile petri dish and the intestinal tube was opened by removing a ~1mm broad piece, resulting in a sheet of tissue. The sheet was turned with the basolateral site facing upwards and the overlaying serosa layer was removed. Subsequently, the tissue was turned to the luminal site facing upwards and the remaining mucosa was carefully removed. Then, the inner part of the cell crown was placed on the luminal site and the underlying SIS was cut with ~1cm^2 area with the inner cell crown in the middle. The overlapping SIS was stretched and attached to the outer wall of the inner cell crown part. The inner cell crown part, including the SIS tissue piece, was transferred carefully into the outer cell crown part, thereby fixing the SIS tissue between the plastic cylinders with the luminal site facing upwards. The SIS equipped cell crowns were transferred to a 24well cell culture plate, filled with 300 µl apical and 900 µl basolateral basal media and stored at 37 °C, 95 % humidity, 5 % CO_2, for minimum 2h until cell seeding.

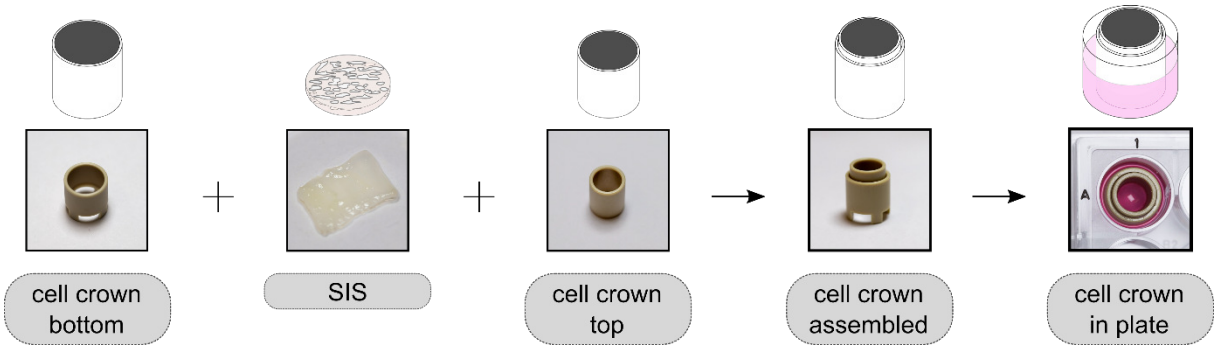

Figure 10. Cell crown assembly. Schematic depiction of the stepwise cell crown assembly.

3.2.2.2 PET based tissue models (hITM-PET)

Before IEC seeding, PET membranes were coated with Matrigel®, in order to increase cell attachment. For this purpose, cold basal medium was mixed with Matrigel® in a ratio of 1:20 and 100 µl were pipetted into the apical compartment of a PET transwell. After incubation for 15 min at RT, the remaining liquid was discarded and the PET membranes were seeded with IECs.

3.2.2.3 Tissue model cell seeding and cultivation

Prior to cell seeding on SIS or PET scaffolds, IECs were cultivated as organoids for 3-5 days in Matrigel® as described in chapter 3.2.1.4. Organoids were dissociated into cell clusters or single cells as described. The cell concentration was adjusted to 4000 cells/ µl in proliferation medium containing JAG-1 (1 µM) and Y-27632 (10 µM). 100 µl of the cell suspension (= 400.000 cells) was applied on the apical site of the SIS or PET matrix and placed for 30 min on 37 °C, 95 % humidity, 5 % CO_2 in order to facilitate attachment of the IECs to the scaffold. After attachment, apically 300 µl and basolaterally 800 µl of proliferation medium containing JAG-1 and Y-27632 was carefully applied. In the following proliferation phase, media was changed every 2-3 days to proliferation medium without JAG-1 (1 µM) and Y-27632 (10 µM). The confluence of the cell layer was examined microscopically and via transepithelial electrical resistance values (TEER) measurements. After reaching confluence (confluent cell layer and >30 Ω*cm^2 TEER), differentiation media was applied with further cultivation of 4 days. At day 4 of differentiation, tissue models were infected and/or further processed for analysis.

3.2.3 Tissue model infection with *Salmonella* Typhimurium

Pre-infection, bacteria were plated on Lennox broth (LB)-Agar plates with appropriate antibiotics and incubated at 37 °C for up to 24h. The next day, a single colony was picked, transferred to 5 ml LB medium and incubated at 37 °C under constant agitation at 220 rpm overnight (= day culture).

For infection, the day culture was diluted 1:100 in LB medium and incubated at 37 °C at 220 rpm agitation for ~3.5h (= infection culture) until reaching an OD_{600} of 2.0. Next, 500 µl of the infection culture was pelleted at 12000 g for 3 min at RT and resuspended in 1000 µl of Crypt medium (= Stock infection culture). According to the applied multiplicity of infection (MOI), the stock infection culture was diluted in 300 µl Crypt medium (= Infection medium; MOI5:

1:150, MOI10: 1:75, MOI100: 1:7.5) and added to the apical compartment of the hITM. The basolateral compartment was filled with 900 µl Crypt medium. After STm application, hITMs were centrifuged at 250 g for 10 min at RT for synchronised infection and incubated for 1h at 37 °C, 95 % humidity, 5 % CO_2 to allow bacterial adhesion and cellular invasion. Subsequently, the media of the apical and basolateral compartment was exchanged with Crypt medium + 50mg/ ml Gentamicin (=HG) followed by incubation for 30 min at 37 °C, 95 % humidity, 5 % CO_2 for inactivation of the extracellular bacteria. Then, the high Gentamicin medium in the apical and basolateral compartment was replaced with Crypt medium + 10mg/ ml Gentamicin (=LG) and incubated at 37 °C, 95 % humidity, 5 % CO_2 for up to 24h.

3.2.4 Tissue model processing - dissociation into single cells

For single cell analysis and FACS, the cells from hITM-SIS were detached from the scaffold and dissociated into single cells. For that, models were first washed once with PBS- + 1mM EDTA and then prewarmed Accutase (400 µl apical, 1000 µl basolateral) was applied for 10 min at 37 °C, 95 % humidity, 5 % CO_2. Cells were then mechanically detached from the SIS by thorough resuspension with a 1000-µl pipette in the apical compartment. The cell suspension was transferred to a 2-ml reaction tube containing the same amount of Accutase. The models were dissected and the respective SIS was transferred to the same reaction tube. The reaction vessel containing the cells and SIS was incubated in a thermoblock (Thermo Fisher) at 37 °C and shaking at 1000 rpm for 10 min.. Afterwards the cell suspension was thoroughly resuspended and the SIS removed. The cell suspension was centrifuged at 500 g for 3 min at RT. The cell pellet was washed twice with ice-cold PBS- and stored on ice until further processing.

3.2.5 Tissue model processing - fixation

SIS and PET based tissue models were fixed prior to histochemical or immunofluorescence analysis. Therefore, the models were washed once with PBS- and covered with 4 % PFA solution for 1-4h at RT for fixation. After fixation, models were stored in PBS- or 70 % EtOH at 4 °C until further processing.

3.2.6 Tissue model processing - RNA isolation and cDNA synthesis

For RNA isolation, tissue models were washed once with PBS-, carefully disassembled and the SIS scaffold directly frozen at -80 °C. PET based tissue models were frozen at -80 °C without disassembling. RNA was isolated using the RNeasy Micro Kit (Quiagen) or peqGold RNA isolation kit (VWR) according to the manufacturer's protocols. To obtain RNA by cell disruption, the SIS or the PET-based tissue model was transferred to a reaction tube containing RLT buffer + 20 % β-mercaptoethanol and lysed by vortexing for 1 min. RNA were isolated by Column based RNA purification technique and stored at -80 °C until further processing.

cDNA synthesis was conducted with iScript™ cDNA Synthesis Kit (BioRad) according to the manufacturer's protocol. In short, cDNA was generated by incubation of RNA with Reverse Transcriptase in a thermocycler according to the following protocol: 5 min at 25 °C, 30 min at 42 °C, 5 min at 85 °C and hold at 4 °C. The cDNA was either directly used for PCR or stored at -80 °C until further processing.

3.2.7 Analytics - transepithelial electrical resistance (TEER)

To verify the confluence and barrier integrity of the human small intestinal tissue models, transepithelial electrical resistance (TEER) was measured by applying a chopstick electrode with an alternating voltage at a frequency of 12.5 Hz. During individual measurements, the electrode was placed on three different sides of the models and the TEER values were calculated by averaging and subtracting the resistance measured in a cell-free control sample.

3.2.8 Analytics - permeability assay

For measuring the passive permeability of the hITM, a FITC Dextran solution was prepared first. To this aim, particles with an average molecular weight of 4 kD or 40 kD were dissolved in basal medium at a concentration of 10 µM. Next, molecular fragments were removed using Amicon® Ultra Centrifugal filters with a threshold of 3 kD or 30 kD, respectively. Upon centrifugation, the medium containing the respective particle was collected and refilled with basal medium to the initial volume (= FITC-basal medium).

After preparation of the FITC Dextran solution, the apical compartment of the hITM was filled with FITC-basal medium and incubated at 37 °C, 95 % humidity, 5 % CO_2. After 1 hour, samples of 50 µl were collected from the basal compartment and transferred to a black-bottomed 96-well plate, filled up to a total volume of 200 µl with medium, and fluorescence intensity was measured at an excitation wavelength of 495 nm and an emission wavelength at 520 nm using an Infinite M200 Plate Reader. The percentile amount of substance was calculated in comparison to the stock solution.

3.2.9 Analytics - lactate dehydrogenase assay

Lactate dehydrogenase release, as a measure of cell death, was determined in tissue model supernatants (SN) collected from the apical compartment of the hITM via the CytoTox 96® Non-Radioactive Cytotoxicity Assay (Promega) according to the manufacturer's protocol. In short, SN were mixed with reconstituted Substrate Mix and incubated at RT in the dark for 30 min. The reaction was stopped by adding Stop Solution and the absorbance was determined at 490nm with the Infinite 200 PRO NanoQuant Microplate Reader (Tecan Group Inc.).

3.2.10 Analytics - cytokine release assay

For the analysis of released cytokines from the infected hITM, a cytometric bead array (CBA) for inflammatory cytokines (IL-1β, IL-12p70, IL-6, IL-8, TNFα, IL-10) was performed with the Human Inflammatory Cytokine Cytometric Bead Array (CBA) - I Kit (BD BioSciences). For that, supernatants (SN) were collected from the apical and the basolateral compartment of the tissue models, centrifuged at 13.000 g for 3 min at 4 °C and directly frozen at -20 °C for long term storage. CBA was applied according to the manufacturer's protocol with ½ of the recommended reaction Volume. In short, SN were incubated with beads capturing the specific cytokines, which were further detected by a second fluorescently labelled antibody via flow cytometry. Based on the fluorescent signal and a titration curve, the concentration of the respective cytokines was calculated via the software FCAP array v3.

3.2.11 Histology - Paraffin embedding and preparation of histological sections

Paraffin embedding

After fixation, samples were embedded in paraffin for long-term storage and sectioning. Therefore, the tissue samples were transferred to a pre-wetted filter paper and put in an embedding cassette. The prepared embedding cassettes were paraffinised in a paraffin-embedding device according to the settings in Table 16.

Table 16: Paraffin embedding protocol

Step	Solution	Time [h]
Removal of PFA	dH_2O	2
Dehydration	50 % EtOH	1
	70 % EtOH	1
	90 % EtOH	1
	96 % EtOH	1
	Isopropanol I	1
	Isopropanol II	1
	Isopropanol/Xylene (1:2)	1
Removal of alcohol	Xylol I	1
	Xylol II	1
Paraffinisation	Paraffin I	3
	Paraffin II	3

Paraffin sectioning

Prior to sectioning, the samples were blocked in paraffin. Therefore, the samples were transferred into metal cassettes, filled with paraffin and solidified at RT overnight. The blocked samples were sectioned via a microtome (Leica) into 5 µm sections and the sections were transferred to glass slides and dried at 37 °C overnight.

Deparaffinisation and rehydration

Prior to stainings, samples were deparaffinized and rehydrated. Shortly, paraffin sections on glass slides were incubated at 60 °C for at least 15 min. Remaining paraffin was removed by sample rehydration according to the protocol shown in Table 17.

Table 17: Deparaffinisation and rehydration of paraffin embedded sections.

Reagent	Time
Xylol I	10 min
Xylol II	10 min
96 % EtOH I	Dip 3x
96 % EtOH II	Dip 3x
70 % EtOH	Dip 3x
50 % EtOH	Dip 3x
dH_2O	

3.2.12 Histology - Alcian blue staining of histological sections

For visualisation of acidic glycoproteins Alcian blue staining with nuclear fast red solution counterstaining was applied. Therefore, after rehydration, sections were first incubated in 3 % acetic acid for 3 min at RT, followed by incubation in 1 % Alcian blue solution for 30 min at RT. Slides were washed in H_2O and incubated in nuclear fast red solution for 5 min, RT to counterstain the cell nuclei and cytoplasm. After a washing step in dH_2O, samples were dehydrated according to the protocol shown in Table 18. Afterwards, samples were mounted with Entellan and covered with a #1.5 cover slip.

Table 18: Dehydration protocol

Reagent	Time
70 % EtOH	Dip 2x
96 % EtOH	2 min
Isopropanol I	5 min
Isopropanol II	5 min

Xylol I	5 min
Xylol II	5 min

3.2.13 Histology - Immunofluorescence labelling of histological sections

In order to visualize protein expression, immunofluorescence staining was applied. Therefore, rehydrated sections were incubated for 20 min in 1x Citric buffer at 100 °C in order to retrieve antigens from paraffin masking. Afterwards, the individual tissue sections on the glass slide were encircled with a fat pen and slides were washed carefully by dipping into PBS- + 0.2 % Tween 20 (PBS-T). Next, sections were permeabilized by incubation for 5 min with PBS- + 0.02 % Triton-X at RT, washed once with PBS-T and were subsequently incubated for 20 min, RT in PBS- + 5 % Donkey Serum. For that, each individual encircled sections were covered with ~100 µl Blocking Solution. After blocking, the individual sections were incubated with the respective primary antibody overnight at 4 °C. The next day, samples were washed three times with PBS-T before secondary antibodies were applied for 1-2h at RT in the dark. After performing three washing steps with PBS-T at RT, samples were covered with Fluoromount-G + DAPI (for DNA visualisation), mounted with a coverslip and stored at 4 °C in the dark until imaging.

3.2.14 Immunofluorescence labelling of whole mount samples

Whole-mount staining of tissue models was performed on PFA-fixed samples. For this purpose, the samples were either cut in half or quartered and transferred to a 48-well plate. All steps were conducted in solution in individual wells of a 24 well plate and samples were kept wet at all time. Importantly, the specimens were marked with a specific cutting pattern to identify the apical/basolateral orientation.

For antibody staining, samples were first permeabilized and blocked in Permeabilisation and Blocking solution (PBS + 0.2 % Triton X-100 + 5 % Donkey serum) for 30 min on a shaker at RT, followed by a washing step with PBS-T (3 min, RT, shaking). Respective primary antibodies were applied in 300 µl volume overnight at 4 °C under shaking conditions. Afterwards, samples were washed three times with PBS-T for 5 min each and were subsequently incubated with the secondary antibody for 1-2h at RT on a shaker. Samples were washed two times following incubation in a solution composed of fluorescently labelled Phalloidin (1:5000) and DAPI (1 mg/ ml, 1:10 000) diluted in PBS-T for 20 min at RT under shaking conditions. After an additional two washing steps with PBS-T, specimens were

transferred to glass slides with the apical side facing upwards, mounted with Fluoromount G (without DAPI), and sealed with a cover slip (#1.5). Glass slides were stored at 4 °C in the dark until imaging.

3.2.15 Hybridisation chain reaction – fluorescence *in situ* hybridisation (HCR-FISH)

HCR-FISH is a qualitative and quantitative technology to visualize RNA molecules, which can be interpreted as gene expression. In brief, sequence specific primary DNA are designed for the RNA of a gene of interest. Two neighbouring probes, each carrying a half of the initiator sequence (= split-initiator), bind to the RNA in close proximity, thereby generating the full initiator sequence. The secondary probe is connected to a fluorophore and can bind to the initiator sequence, which leads to conformational change and opening of the initiator sequence on the secondary probe. Here the next secondary probe can bind, which leads to stoichiometric amplification of the signal (Choi et al., 2018).

Probes design for HCR-FISH

Probes were designed by Tobias Krammer (working group of Dr. Antoine-Emmanuel Saliba, Helmholtz Institute for RNA-based Infection, Würzburg, Germany). In detail, DNA probes for HCR-FISH were designed as previously described (Choi et al., 2018). 25-nucleotide (nt) sequences of each gene were extracted. One probe consists of a pair of two 25-nt long oligos (25-nt encoding region, 2-nt spacer, and 18-nt initiator region) separated by a 2-nt gap. The oligo pairs were selected to have a Tm difference of < 5 °C. In addition, probe sequences were required to have a GC content within the 40 – 60 % range. The NCBI database was used to look up mRNA sequences. Any probe sequence that contained five or more consecutive bases of the same kind was dropped. To ensure specificity, an NCBI BLAST query was run on each probe against the human transcriptome. BLAST hits on sequences other than the target gene with a 15-nt match were considered off-targets. For each gene, eight encoding probe pairs were designed. The probes applied for OLFM4 are listed in Table 11.

HCR-FISH - Whole mount staining

HCR-FISH staining was performed with the Molecular Instruments HCR-FISH kit using the manufacturer's adapted staining protocol for chicken embryos. In detail, samples were permeabilized after fixation in 70 % EtOH for at least 12h and were then stored in 70 % EtOH up to 4 weeks. After storage, the models were disassembled, cut into appropriate pieces (halves or quarters), and stained in 48well cell culture plates. Samples were washed first with PBS-T, secondly with 50 % PBS-T and 50 % 5x SSC-T and finally with 5x SSC-T only. Each washing

step was performed for 5 min on ice. For the detection phase, the samples were equilibrated in hybridisation buffer for 30 min at 37 °C. Next, 5 pmol of the probe pool set was added to the hybridisation buffer and samples were incubated for 12h at 37 °C. Afterwards, samples were washed three times for 10 min at 37 °C using Probe wash buffer and were subsequently incubated two times for 5 min in 5x SSC-T at RT. For the amplification phase, samples were equilibrated by incubation in Amplification buffer for 30 min at RT (Pre-amplification). In the meantime, 15 pmol of each hairpin (h1 and h2 of B3-AF594) were separately prepared by heating at 95 °C for 90 seconds and cooling to RT for 30 min in the dark. Afterwards, the hairpin solution was prepared by mixing 15 pmol of h1 and 15 pmol of h2 in 150 µl of Amplification buffer. The Pre-amplification buffer was removed, the hairpin solution was added and specimens were incubated at RT for 16h without light exposure. After incubation, the samples were washed three times with 5x SSC-T at RT and stored at 4 °C until further processing. For consecutive antibody staining, the samples were washed 1x with 50 % PBS-T and 50 % 5x SSC-T and finally with PBS-T only, each for 1 min at 4 °C. Subsequently, the samples were blocked with 5 % Donkey serum in PBS- for 10 min and washed in PBS-T for 1 min at 4 °C. The respective antibody was applied for 2h at RT. Afterwards, samples were washed three times for 5 min with PBS-T and incubated with secondary antibody for 1h at RT, followed by two washing steps with PBS-T for 5 min each. For visualisation of cell nuclei, the samples were stained for 15 min with DAPI (1 mg/ml, 1:10000) diluted in PBS-T and subsequently washed in PBS-T for 10 min at RT. Samples were mounted onto a glass slide, as described in 0. Prepared glass slides were stored at 4 °C in the dark until imaging.

HCR-FISH - flow cytometry (Flow-FISH)

For flow cytometry of HCR-FISH-stained cells, HCR-FISH staining was applied on suspension cells according to the adjusted manufacturer's protocol for Mammalian Cells in Suspension. In detail, single cells from the hITM were obtained as described in 3.2.4, fixated in 4 % PFA for 1h at RT and washed once with PBS-. Cells were stored in 70 % EtOH at 4 °C until further processing.

For cell staining, approximately $4x10^5$ cells were applied and centrifuged at 500 g for 3 min at 4 °C. Cells were washed twice with PBS-T and resuspended in 150 µl Hybridisation buffer, followed by incubation for 30 min at 37 °C. For detection, 5 pmol of the probe pool set diluted in 100 µl prewarmed Hybridisation buffer was added directly to the cell pellet. Cells were carefully resuspended and incubated at 37 °C overnight. The next day, prewarmed 300 µl Probe wash buffer was directly added and the cell suspension was centrifuged at 500 g for 3 min at RT. Cells were then incubated for 10 min in 300 µl prewarmed Probe wash buffer at 37 °C.

Afterwards, the supernatant was discarded after centrifugation at 500 g for 3 min at RT. This washing step was repeated once and the cells were resuspended and incubated for 5 min in 500 µl 5x SSC-T. For the amplification phase, the cells were centrifuged at 500 g for 3 min at RT and resuspended in 150 µl Amplification buffer for 30 min at RT. In the meantime, 15 pmol of each hairpin (B3-h1-AF546 and B3-h2-AF546) were separately prepared by heating at 95 °C for 90 seconds and subsequent cooling to RT for 30 min in the dark. Afterwards, the hairpin solution was prepared by mixing 15 pmol of h1 and 15 pmol of h2 in 150 µl of Amplification buffer. The hairpin solution was then added to the cells which were incubated at RT for 16h in the dark. Subsequently, 500 µl of 5x SSC-T were added to the cell suspension and the SN was discarded after centrifugation at 500 g for 3 min at RT. This washing step was repeated three times. Finally, cells were resuspended in PBS- and directly analysed via flow cytometry.

3.2.16 Flow cytometry and fluorescence activated cell sorting

Single cells were generated by model dissociation as described under 3.2.4 with additional filtering of the cell suspension through a 30 µm cell strainer. Flow cytometry (FC) and fluorescence activated cell sorting (FACS) was conducted with a FACS Aria III at the Rudolf Virchow Centre by Fabian Imdahl (working group of Dr. Antoine-Emmanuel Saliba, Helmholtz Institute for RNA-based Infection, Würzburg, Germany). Flow cytometric analysis and cell sorting was performed with an 85 µm nozzle and a medium flow rate; for single cell sorting the highest fidelity settings were applied. Single cell sorting was performed into 96well plates at 4 °C containing lysis buffer with subsequent storage at -80 °C. Bulk sorting for single cell imaging was performed with a low flow rate into 1.5 ml reaction tubes containing 4 % PFA. Cell populations were determined based on the gating strategies in Figure 11. First, single cells were gated by doublet discrimination via the Forward Scatter (FSC) and Sideward Scatter (SSC) (Figure 11 A). Bystander and infected cells were determined on behalf of the GFP signal emitted by GFP expressing STm (STm-GFP; Figure 11 B) or on behalf of the mCherry-signal emitted by the mCherry expressing reporter strain (STm-rep; not shown). Gating for HCR-FlowFISH of *OLFM4* was performed in unstained, uninfected samples and then determined for bystander and infected cells (Figure 11 C). The infected cell population was classified into three different clusters (H: High; M: Medium; L: Low) according to the intensity of the GFP- (Figure 11 D) or mCherry-signal (not shown).

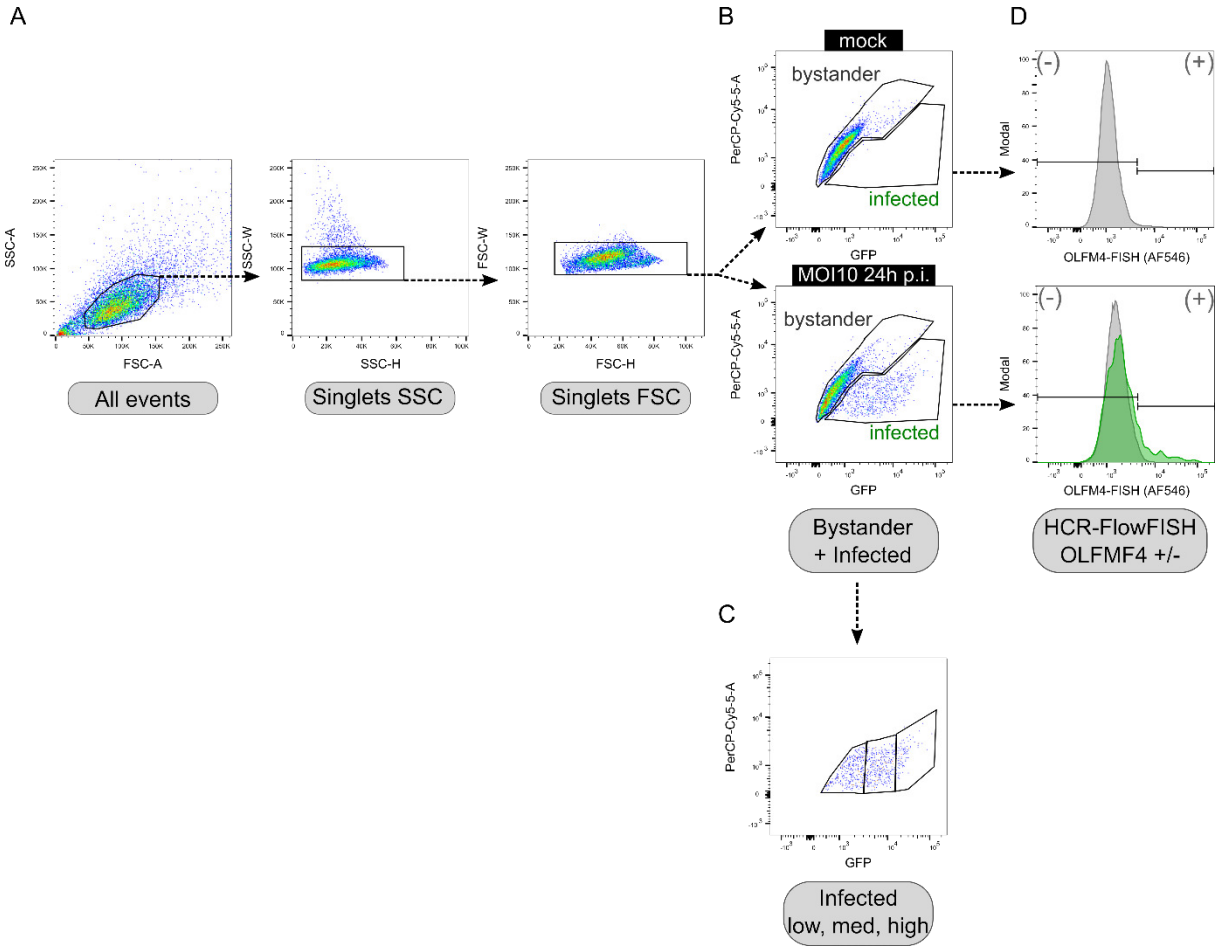

Figure 11. Gating strategy for uninfected and infected IECs. A Doublet cell discrimination. **B** Determination of infected and bystander cells. **C** Determination of low medium high infected cells. **D** Determination for HCR-FlowFISH for *OLFM4*.

3.2.17 Single cell transcriptomics

For single cell transcriptomic analysis, single cell RNA sequencing (scRNA-seq) was applied. For that, a single cell suspension from the hITM was prepared as described in 3.2.4 and further processed for scRNA-seq by Fabian Imdahl (working group of Dr. Antoine-Emmanuel Saliba, Helmholtz Institute for RNA-based Infection, Würzburg, Germany).

3.2.17.1 10x Genomics Chromium single-cell RNA-seq

In the Drop-Seq approach, single cells are separated and compartmentalized in high throughput via microfluidics into oil-droplets each containing one single cell diluted in lysis buffer and one microbead covered with barcoded primers. Inside this droplet, the cell is lysed and the thereby released RNA binds to the enclosed microbead. The RNA-microbead complex is then isolated and the bound RNA is reverse-transcribed to cDNA that is next PCR-amplified followed by

addition of sequencing adapters for subsequent library preparation and next generation sequencing (Macosko et al., 2015).

The cells of two tissue models (technical replicates) were hashtagged according to the manufacturer's protocol for TotalSeq^{TM}-A with TotalSeq-A antibodies followed by cell hashing using the 10X Single 3' Reagent kit v3.1. For Fc-blocking, approximately 4x10^5 cells per sample were resuspended in 100 µl Cell Staining Buffer plus 5 µl Human TruStain FcXTM FcBlocking and incubated at 4 °C for 10 min Afterwards, 1 µg of a unique TotalSeq^{TM}-Antibody was added to each sample and incubated at 4 °C for 30 min. Subsequently, the cells were washed three times with 1 ml Cell Staining Buffer and centrifuged for 5 min at 350 g at 4 °C. Finally, the cells were resuspended in PBS- and passed through a 40 µm cell strainer. The cell concentration was determined using a Neubauer Hemacytometer and adjusted to 1000 cells per µl with PBS-. The hashtagged cells were pooled in the same ratio and approximately 20,000 cells were loaded into the Chromium^{TM} Controller for droplet-based cell separation, cell lysis and barcoding. The following reverse transcription, cDNA amplification and the preparation of gene expression libraries was performed via the 10x Single Cell 3' reaction kit v3.1 according to the manufacturer's protocol. Preparation of the hashtag libraries was performed according to the cell hashing protocol for 10x Single Cell 3' Reagent Kit v3.1. The incubation and amplification steps were conducted with the SimpliAmp Thermal Cycler. Library quantification and quality control was evaluated using a Qubit^{TM} 4.0 Fluorometer and a 2100 Bioanalyzer with High Sensitivity DNA kit. Sequencing was performed on a NextSeq 500 sequencer.

3.2.17.2 SMART-seq

In the SMART-seq2 approach, single cells are separated before cell lysis via FACS. Cells are lysed in presence of dNTPs and oligo(dT)-primers containing universal anchor sequences, which bind to the Poly-A-tail of mRNAs. After addition of the reverse transcriptase, the cDNA is PCR-amplified, the sequencing library is prepared and next generation sequencing is applied (Picelli et al., 2014).

STm infected IECs were FACS-sorted directly into a 48 well plate each well containing 2.6 µl of Lysisbuffer (0.26 µl 10x Lysisbuffer, 0.03 µl RNase inhibitor (40 U/ µl) and 2.31 µl nuclease free H_2O). Cell sorting was performed on a BD FACS Aria III. After sorting, the plate was centrifuged to assure that the locates at the well bottom and the frozen at -80 °C until library preparation.

Libraries were prepared via the SMART-seq2 V4 kit using ¼ of the recommended volumes of the manufacturer's manual (Picelli et al., 2014). Afterwards, the ERCC RNA Spike-Ins Mix1 was added to each library at a dilution of 1:2,000,000. Briefly, for each library, 0.3 µl CDS primer and 0.2 µl ERCC RNA Spike-In Mix 1 were supplemented and incubated at 72 °C for 3 min in a Thermal Cycler. For reverse transcription, 1 µl 5x Ultra Low First-Strand Buffer, 0.25 µl SMART-Seq v4 Oligonucleotide (48 µM), 0.125 µl RNase Inhibitor (40U/ µl), and 0.5 µl SMARTScribe Reverse Transcriptase were prepared as mastermix. To each library, 1.9 µl of RT mix was added and first incubated at 42 °C for 90 min. Subsequently, the reaction mixture was incubated at 70 °C for 10 min. Finally, the reaction mix was cooled down to 4 °C for further storage. For cDNA amplification, 6.25 µl 2X SeqAmp PCR Buffer, 0.25 µl PCR Primer II A, 0.25 µl SeqAmp DNA Polymerase, and 0.75 µl Nuclease-Free water were mixed and 7.5 µl was added to each library. Afterwards, the plate was transferred to a thermal cycler and the amplification program (Table 19) was applied.

Table 19: Thermocycler program for amplification Smart-seq2 v4 amplification.

Time	**Temperature**	
1 min	95 °C	22x
10 sec	98 °C	
30 sec	65 °C	
3 min	68 °C	
10 min	72 °C	
∞	4 °C	

Library preparation steps were conducted via the Mantis Microfluidic Liquid Handler. Amplified libraries were cleaned via 12.8 µl AMPure XP beads and 0.3 µl 10X Lysisbuffer. The cDNA was eluted in nuclease free water. For quality control, cleaned libraries were evaluated using the Qubit™ and a 2100 Bioanalyzer. Libraries with lower concentration as 0.8 ng/ µl of cDNA or showing an inappropriate Bioanalyzer trace were excluded from further processing. Remaining libraries were diluted with Nuclease free water to a final concentration of 0.4 ng/ µl and applied in the Nextera XT library preparation protocol. Quality control was applied to the tagmented libraries and they were subsequently pooled according to their individual molarity. Finally, the pool was sequenced with a 75bp paired-end high output kit using the NextSeq 500 platform.

3.2.18 Gene expression analysis via qPCR

During quantitative real time PCR, cDNA is amplified and monitored after each synthesis cycle by fluorescence signals, the measured signal reflecting the amount of amplified product. This process allows the analysis of corresponding mRNA transcription levels under various conditions, using the housekeeping gene EF1α for normalization. The reaction mix was composed according to Table 20:

Table 20: Reaction mix for qPCR

Reagent	Volume
SsoFast EvaGreen Supermix	10 µl
Primer forward (400 nM)	2 µl
Primer reverse (400 nM)	2 µl
cDNA (25-50 ng)	1-2 µl
ddH2O (add up to final volume)	x µl
Total volume	20 µl

Each sample was measured in duplicates in the CFX 96 Touch™ Real-Time PCR Detection System (BioRad), using the 2-step PCR protocol in Table 21:

Table 21: Thermocycler protocol for qPCR

Step	Temperature	Time	Cycles
Initial denaturation	95 °C	30 sec	1x
Denaturation	95 °C	5 sec	40x
Annealing and extension	60 °C	5 sec	
Melt curve acquisition	95 °C	10 sec	1x
	60 °C	5 sec	1x
	95 °C	5 sec	1x

3.2.19 Gene expression analysis via High-throughput qPCR chip

Gene expression analysis via high-throughput qPCR barrier chip was performed as previously reported (Gerhartl et al., 2020; Krasemann et al., 2022; Lin et al., 2020; Ramme et al., 2019). In detail, 20 µl cDNA was produced from 250 ng RNA using the High-Capacity cDNA Reverse Transcriptase Kit (Thermo Fisher Scientific). After pre-amplification of the targets, the high-throughput qPCR chip was performed with the pre-amplified cDNA in 96x96 chips using the using the Biomark™ system (Fluidigm®). This was performed in the group of Dr. Prof. Winfried Neuhaus (Austrian Institute of Technology, Vienna, Austria).

3.2.20 Brightfield microscopy

The BZ-9000 light microscope equipped with 2x, 4x, 10x, 20x or 40x magnification objectives was used for light microscopy. In particular, the histological sections of the Alcian Blue stainings were imaged with the default settings with white balance correction in the Brightfield acquisition mode. For stitched images, the merge mode was applied during imaging and the merged images were assembled by the BZ-II Analyser software. Finally, the obtained images were processed for white balance correction and the Scale bar was inserted with ImageJ.

3.2.21 Widefield fluorescent microscopy

The BZ-9000 light microscope equipped with 2x, 4x, 10x, 20x or 40x magnification objectives was used for widefield fluorescent microscopy of fluorescently stained histological sections. In detail, images were acquired using the fluorescent mode with the filters for Cy5 (excitation: 620/60 nm), TRITC (excitation: 545/25 nm), and GFP (excitation: 470/40 nm) and the following camera settings: gain +10, adjusted black balance, adjusted exposure time. The obtained images were further processed for brightness/contrast balancing and the Scale bar was inserted with ImageJ. For corresponding samples the same setting was applied.

3.2.22 Confocal fluorescent microscopy

The LEICA TCS SP8 confocal microscope with the LASX software was used for confocal imaging of fluorescently labelled samples. Images were acquired with 40x (immersion: water) or 63x (immersion: oil) objectives with laser and detector settings according to Table 22 and with the following scanner settings: resolution 1024x1024, scanner speed 400 or 600 Hz, frame averaging 1-4, z-stack size 0.4 µm – 1µm, pinhole size 1.0 AU. Images were further processed with the build-in LAS X 3D Visualisation software. Corresponding samples were obtained and processed with the same settings.

Table 22: Laser and detector settings for confocal microscopy

Channel (detected fluorophore)	Laser wavelength [nm]	Detector (gain in %)	Detector range [nm]
#1 (DAPI)	405	HyD (100-150)	430-460
#2 (GFP and AF488)	488	HyD (100-120)	495-520
#3 (mCherry and AF555)	561	HyD (100-130)	600-620

#4 (AF594)	561	HyD (200-220)	600-620
#5 (AF647)	633	HyD (80-120)	660-680

3.2.23 Electron microscopy

For scanning electron microscopy (SEM) and transmission-electron microscopy (TEM), tissue models were first washed with 1x PBS- before fixation overnight at 4 °C in 0.1 M phosphate buffer pH 7.4 (9.46 g/L Na_2HPO4, 9,078 g/L KH_2PO_4 in ddH2O) containing 6.25 % glutaraldehyde (VWR). Fixed samples were washed five times in 0.1 M phosphate buffer before sample preparation for SEM/TEM and imaging was carried in cooperation with Daniela Bunsen and Prof. Christian Stigloher (Central Microscopy Department, University of Würzburg, Würzburg, Germany).

Transmission electron microscopy

For TEM, the samples were washed in 50 mM Cacodylate Buffer (pH 7.2, Roth) and further fixed with 2 % buffered OsO_4 (ScienceServices). They were then contrasted with 0.5 % watery Uranyl Acetate (Merck) and finally embedded in Epon (Serva) after EtOH based dehydration. Cross-sections with 65nm thickness were generated from Epon embedded samples and contrasted with 2 % Uranyl Acetate in EtOH and Reynolds stain (REYNOLDS, 1963). TEM imaging was performed on a JEM-2100 (JEOL Ltd.) with 200 kV using a TVIPS TemCam F416 for image registration.

Scanning electron microscopy

For SEM, the samples were dehydrated with acetone and further dried via critical point drying. Before imaging 10–20 nm gold/palladium (80/20) were applied on the sample in an argon bath using a BAL-TEC SCD 005 Sputter Coater (Leica Mikrosysteme). SEM imaging was performed on a JEOL JSM-7500F scanning electron microscope (JEOL Ltd.).

3.2.24 Bioinformatical analysis - cell height measurement

Cell height measurements were performed on cross-section views of z-stack confocal images that were representatives of whole tissue samples. In short, a defined grid of 9 x 9 fields was applied on the field of view (FOV). At the cross points of the grid lines, the cellular height was determined by measuring the distance between the apical and the basolateral F-actin signal of individual cells. The cell height measurements were performed via Fiji (v1.51s) (Däullary et al., 2022, in review).

3.2.25 Bioinformatical analysis - bacterial migration measurement

The bacterial migration distance within the hITM-SIS was measured by automated batch analysis that was performed with IMARIS (v8.4.2) on representative z-stack images. First, a threshold for the determination of the apical F-actin signal was set via the "Surface" function of IMARIS. Secondly, the centers of STm-expressing GFP signals were defined by the "Spot" function and bacterial migration was determined as distance between the defined GFP spot and the apical F-actin signal by applying the "Signal to Distance transformation" function (Däullary et al., 2022, in review).

3.2.26 Bioinformatical analysis - HCR-FISH intensity measurement

OLFM4 intensity was determined with Fiji (v1.51s) as follows: first, z-stacks of hITM-SIS images were projected as sum of all stacks combining the signal of all focal planes, secondly the mean OLFM4 HCR-FISH signal intensity in the FOV was measured, third the number of nuclei per FOV were determined based on the DAPI signal. The OLFM4 intensity was calculated as $OLFM4\ int\ =\ OLFM4\ mean\ intensity\ /\ number\ of\ nuclei$ (Däullary et al., 2022, in review).

3.2.27 Bioinformatical analysis -single cell RNA sequencing data analysis

The analysis was conducted by Oliver Dietrich (working group of Dr. Antoine-Emmanuel Saliba, Helmholtz Institute for RNA-based Infection, Würzburg, Germany). FASTQ files were aligned and counted using the CellRanger count pipeline against the GRCh38 human genome reference as well as the TotalSeqA Hashtags 1 and 2. The count matrix was imported into R for analysis using the Seurat framework. All R scripts used in the analysis process are available at https://github.com/saliba-lab/tissue-model-human-intestine.git. Briefly, the count matrix was split between counts for hashtags and gene expression. Hashtags were assigned by using count thresholds to distinguish replicates (Hashtag 1, 30; Hashtag 2, 50). Unstained (negative) and double positive (doublet) cells were removed. Gene expression counts were normalized (log1pCP10k), 5000 highly variable genes were selected and 45 principle components (PCs) were computed for UMAP projection, SNN graph (k=10, type=rank), and leiden clustering (resolution_parameter=1.2, n_iterations=5). Differential gene expression was assessed using scran::findMarkers(block=Replicate, pval.type=some). Visualizations were created with custom code using the ggplot2, dplyr, tidyr, and pheatmap packages. The versions of all

installed packages are specified in conda Y ML files in the GitHub repository (envs/default.y ml) (Däullary et al., 2022, in review).

3.2.28 Bioinformatical analysis - statistics

Statistical analysis was performed via GraphPad Prism (v6.02) with unpaired t-test, ordinary one-way ANOVA with Tukey's multiple comparison tests, two-way ANOVA with Tukey's multiple comparison tests, and Mann-Whitney-U test. All statistical tests were performed with a 95 % confidence interval. P-values < 0.05 were considered as significant, whereas P-values > 0.05 and < 1 were considered as trend. Significances are indicated as asterisks in the figures with the following nomenclature: ****= $P \leq 0.0001$, ***= $P \leq 0.001$, **= $P \leq 0.01$, *= $P \leq 0.05$. Not significant differences are not especially indicated.

3.2.29 Applied Software

IMARIS (8.9.2)

3D image analysis was performed with IMARIS (Version 8.9.2), kindly provided by Prof. Manfred Heckmann (Institute of Physiology, Department of Physiology – Neurophysiology, University of Würzburg, Würzburg, Germany). For image analysis, the built-in tools Surface, Spots and Filaments were applied. Suitable parameters for each tool were established based on one exemplary image and subsequently applied as automated batch analysis.

ImageJ (1.51s)

2D image processing and analysis was performed with Fiji (v 1.51s).

LAS X 3D Visualisation

3D projection of immunofluorescent images was generated by the Leica LAS X 3D Visualisation plugin for LAS X. For corresponding images, the same settings for signal intensity, threshold, and opacity were applied.

GraphPad Prism (6.02)

Statistical analysis and graph preparation was performed with GraphPad Prism (6.02).

R (4.2.2)

Bioinformatical analysis of the scRNA sequencing data was performed with R (4.2.2) by Oliver Dietrich (working group of Dr. Antoine-Emmanuel Saliba, Helmholtz Institute for RNA-based Infection, Würzburg, Germany).

Inkscape (1.0.2-2)

The open source software Inkscape was used for figure preparation, including line arts as well as graph and image alignment.

4 Results

4.1 Organoid-derived human IECs mimic morphological, structural and cellular features of the intestinal epithelium on an organ-specific bioscaffold

4.1.1 IECs display *in vivo*-like morphological and morphometrical features when cultured on a decellularised intestinal submucosa scaffold

In order to model the small intestinal epithelium with the aim of reassembling the native tissue, human intestinal epithelial cells (IECs) derived from human intestinal ASC-derived organoids of primary origin were applied in a Transwell®-like cell culture system. For cell attachment and as supportive structure, a decellularised porcine SIS was used as bioscaffold in comparison to a commercially available synthetic PET membrane.

For the setup of the human intestinal epithelial tissue model (hITM), primary intestinal organoids were enzymatically dissociated to obtain single cells and fragments followed by seeding apically on either the SIS (hITM-SIS) or PET (hITM-PET). With the aim to generate an intestinal model with a high *in vitro-in vivo* correlation, the established hITM based on the SIS or the PET membrane were investigated in several stages with regard to characteristic properties of the native tissue. First, the ability of forming a confluent cell monolayer was evaluated by comparing the macrostructure and cellular morphology of IECs grown on the SIS or the PET in comparison to the native tissue. Cytohistological analysis via Alcian blue staining, which in addition indicates glycosylated proteins (e.g. mucins), demonstrated the characteristic compartmentalisation into villus and crypt domains for the native small intestine (Figure 12 B1) as well as an epithelial monolayer composed of polarised columnar cells, individual cells with cytoplasmic mucins, and mucin inclusion bodies (Figure 12 B2). The IECs of the hITM-SIS and hITM-PET established a monolayer on the apical surface of the respective scaffold (Figure 12 C and D) as well, thereby reproducing the native feature *in vitro*. Furthermore, the monolayers of both models were confluent over the entire matrix with a uniform cellular distribution (Figure 12 C1, C2, C3 and D1, D2, D3). Of note, IECs on the SIS seemed to have a more pronounced cell density, columnar polarisation and cell height in comparison to the hITM-PET (Figure 12 C4 and 1 D4), thereby closer mimicking the native tissue features in regards of cellular morphology.

Referring to mucins, a key hallmark of the native intestinal epithelium, the native intestinal tissue displayed intensive indications for acidic mucin production and secretion (Figure 12 B2).

The monolayer of the hITM-SIS showed indications of a small apical mucin layer as well as signs depicting mucin inclusion bodies (Figure 12 C4). In contrast, the monolayer of the hITM-PET shows less to none indications for released mucins and further seemed to contain a reduced amount of mucin inclusion bodies. Additionally, while the hITM-SIS displayed a thin layer of mucins on the apical region, potentially membrane-bound, such a layer was mostly absent in the hITM-PET and only slightly visible in the native tissue. Overall mucin layer/secretion/inclusion bodies were most pronounced in the native tissue, less pronounced by the hITM-SIS and least pronounced by the hITM-PET.

To gain further insights into cellular polarisation characteristics of the hITM-SIS and the hITM-PET, distinct morphometrical features (cell height and relative nuclear positioning) were determined based on filamentous actin (F-actin) cytoskeleton and DNA staining as well as the expression of polarisation-related genes. When available, observations were compared with data from native tissue analysis or literature data. As shown in figure 1E, the cell height of individual IECs was significantly increased in the hITM-SIS (201 cells) compared to the hITM-PET (200 cells). In detail, the mean cell height of IECs cultured on the SIS was 40.82 µm (± 4.91 µm) and on the PET 17.35 µm (± 2.46 µm). Literature data specify the cell height of native IECs of the small intestine with 37 µm (± 3.00 µm) (Crowe and Marsh, 1993) (Figure 12 E), which indicates that IECs of the hITM-SIS showed a higher *in vivo* similarity than IECs of the hITM-PET regarding cell morphometry. Similarly, the mean distance of the nucleus position to the apical surface of IECs was significantly increased when cultured on the SIS (- 17.91 µm ± 6.07 µm; 2379 cells analysed in total) compared to cells grown on the PET (- 4.92 µm ± 1.34 µm; 709 cells analysed in total) (Figure 12 F), indicating a higher polarisation degree of IECs grown on the hITM-SIS. Furthermore, the expression of polarisation-related genes such as *JAM 1* and *JAM3*, was elevated in cells of the hITM-SIS compared to cells obtained from the hITM-PET (Figure 12 G).

To investigate differential mucin expression profiles in more detail, transcript levels for a defined set of mucins (secreted, membrane and cytoplasmic) were determined via qPCR microarray analysis (Figure 12 H), performed by the group of Prof. Dr. Winfried Neuhaus (Austrian Institute of Technology, Vienna, Austria). Together, the data show that cells cultured on the SIS tended to express membrane-associated mucins to a higher degree compared to cells from the hITM-PET (Figure 12 H right). In detail, gene expression levels were increased for *MUC1A*, *MUC1B*, *MUC3a*, *MUC4*, *MUC12* and *MUC17*. In contrast, the *MUC13* gene

expression value was not increased. Further, no gene expression was detected for *MUC2*, a secreted and gel-forming mucin, on the hITM-SIS or the hITM-PET.

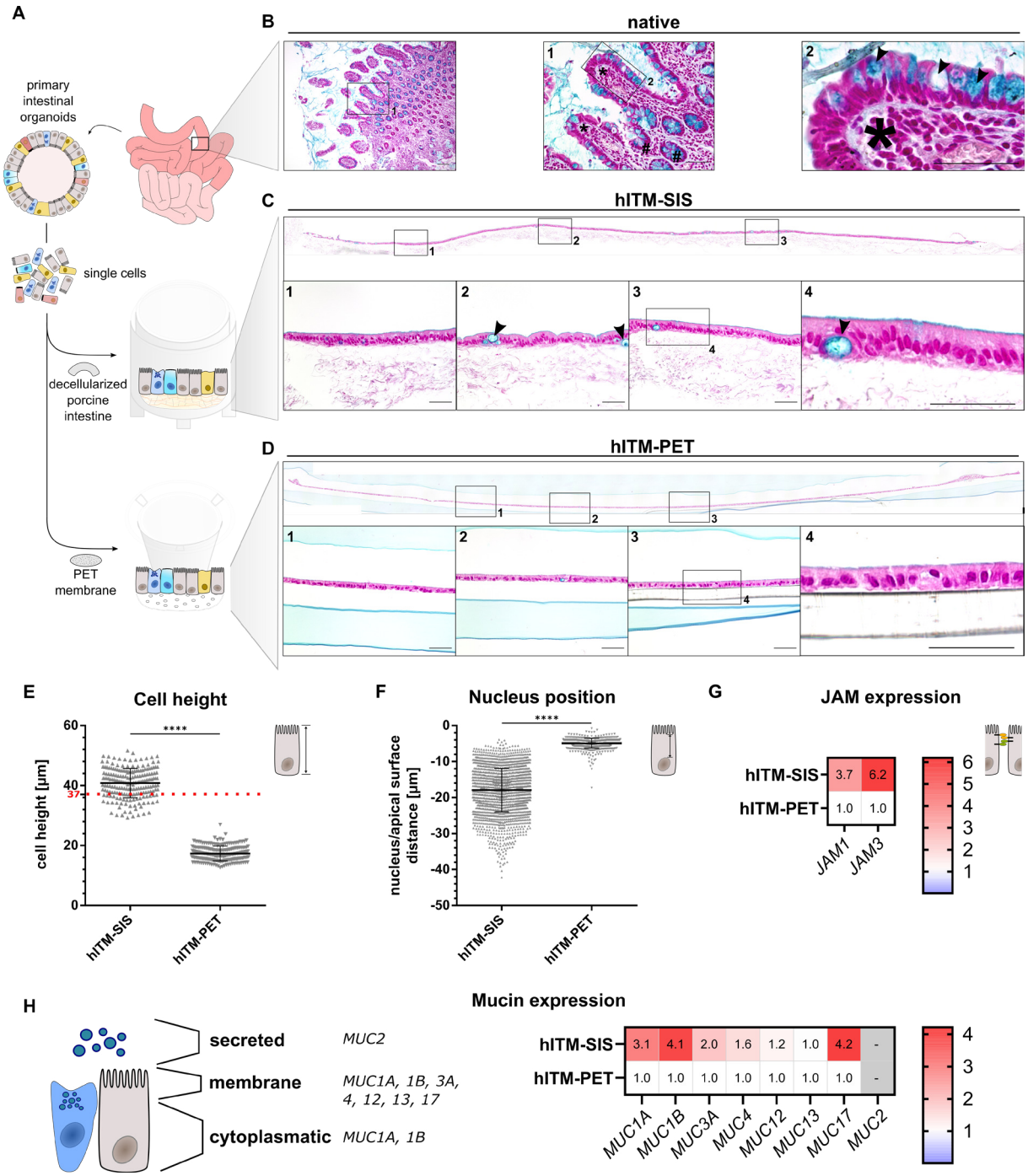

Figure 12. IECs display *in vivo*-like morphological and morphometric features when cultured on the biological matrix SIS and express characteristic mucins. A Schematic experimental workflow of the hITM-SIS preparation. **B** Representative microscopy pictures of the histochemical Alcian blue stainings of the native human small intestinal epithelium (n=1), the hITM-SIS (**C**, n=3) and the hITM-PET (**D**, n=3). Blue colour indicates glycosylated proteins, typically mucins, whereas deep purple indicates nuclei and light purple cell cytoplasm. **B1** Magnification of the native tissue with indicated villus (*) and crypt domains (#). **B2** Magnification of the villus region with columnar epithelial cells, mucus filled cells and mucin inclusion bodies (arrowhead). **C1** - **C4** Magnification of the hITM-SIS displaying the epithelial cell layer with tightly packed, polarised columnar cells, an apical mucin layer, a cell with a mucin inclusion body (arrow head) and the underlying SIS bioscaffold. **D1** - **D4** Magnification of the hITM-PET showing the epithelial cell layer with epithelial columnar cells and the underlying synthetic PET membrane. **E** Cell height of 201 cells of the hITM-SIS or 200 cells of the hITM–PET models (n=2). The red dotted line represents mean value of native intestinal cells (37 µm; (Crowe and Marsh, 1993). **F** Distance of the nucleus position in relation to the apical surface in IECs of the hITM-SIS (2379 cells) or the hITM–PET (709 cells) (n=2). **G** Heat map of *JAM1*

and *JAM3* gene expression levels of hITM-SIS cells, normalised to hITM-PET cells (n=1). **H left** Schematic depiction of localisation and/or secretion of *MUC1A, 1B, 3A,4,12,13,17,2* (Grondin et al., 2020; Pelaseyed and Hansson, 2020). **H right** Heat map of indicated mucin gene expression levels of hITM-SIS cells, normalised to hITM-PET cells (n=1). Significance was calculated by unpaired t-test for E and F with ********= P ≤ 0.0001. Non-significant P-values are not displayed. SB = 50 µm. (Däullary et al., 2022, in review). **Abbreviations**: F-actin: filamentous actin, hITM: human intestinal tissue model, SIS: small intestinal submucosa, PET: Polyethylenterephthalat, *MUC*: mucin, *JAM*: Junctional adhesion molecule. (Däullary et al., 2022, in review)

4.1.2 IECs develop a characteristic tight-junction expression profile on the biological scaffold and build a functional epithelial barrier

In addition to morphometric parameters, the epithelial barrier of the hITM-SIS and the hITM-PET was investigated. In detail, the protein and gene expression patterns of characteristic Tight Junction (TJ) proteins were analysed by immunohistochemistry (IHC) and qPCR microarray analysis. Barrier integrity was further evaluated by measuring the transepithelial electrical resistance (TEER) and functionality was investigated by classical transport assays to determine the permeability of the epithelium to small sized particles.

In order to characterize the intestinal barrier of the hITM-SIS and the hITM-PET in detail, both model variants were examined for the protein expression of two major TJ proteins, ZO-1 and occludin, via IHC. As shown in figure 2A, similar expression patterns for ZO-1 and occludin were observed at the intercellular borders of the IECs in the hITM-SIS and the hITM-PET. In detail, ZO-1 and occludin localised and concentrated in the apical region of the cell layers between individual IECs resulting in an uneven but characteristic honeycomb-like pattern. However, as indicated by the IHC signals, cytoplasmic ZO-1 seemed to be more abundant in the hITM-SIS (Figure 13 A right), whereas occludin appeared to be expressed at comparable levels in the hITM-SIS and the hITM-PET (Figure 13 A mid).

Subsequent gene expression profiling of TJ and -associated proteins by qPCR microarray analysis was performed in the group of Prof. Dr. Winfried Neuhaus (Austrian Institute of Technology, Vienna, Austria). It revealed increased gene expression values for *ZO-1, ZO-2, ZO-3*, *Tricellulin (TRIC*, also *MARVELD2*) and *Desmoglein3 (DSG3)* in cells of hITM-SIS compared to cells of the hITM-PET (Figure 13 B). The expression of *occludin (OCLN)* was comparable for cells of the hITM-SIS and the hITM-PET, confirming the observations made by IHC analysis shown in figure 2 A. Further, gene expression levels of claudin (CLDN) superfamily members were either increased or decreased in the hITM-SIS compared to the hITM-PET. In detail, gene expression values were increased for *CLDN4, 6, 7, 12, 15, 22, 23, 24*, whereas gene expression levels were decreased for *CLDN9*, *11*, *20*, *25* in cells cultured on the SIS compared to cells derived from the hITM-PET (Figure 13 C). Conclusively, TJ and -

associated proteins seemed to be expressed to a higher degree in IECs of the hITM-SIS compared to hITM-PET models.

To further validate the epithelial barrier on a functional level, barrier integrity was assessed by TEER measurement (Figure 13 D) and FITC-Dextran permeability assay (Figure 13 E). In detail, the hITM-SIS showed a TEER value of 58.69 (± 5.89) $\Omega*cm^2$. In contrast, analyses of the hITM-PET revealed a TEER value of 412.20 (± 24.41) $\Omega*cm^2$. Given a TEER value of 50-100 $\Omega*cm^2$,reported for the native small intestine (Srinivasan et al., 2015), the TEER value of the hITM-SIS approximated the native condition, whereas the hITM-PET exceeded this value by multiple times. Further, the paracellular diffusion of small molecules determined by a permeability assay for 40kDa FITC-Dextran was investigated as an additional functional measure of barrier integrity. As shown in figure 2 E, the mean FITC-Dextran permeability was higher for the hITM-SIS (6.35 % (± 2.11)) compared to the hITM-PET (0.21 % (± 0.02)). This indicates a weaker barrier to medium sized molecules of the hITM-SIS compared to the hITM-PET.

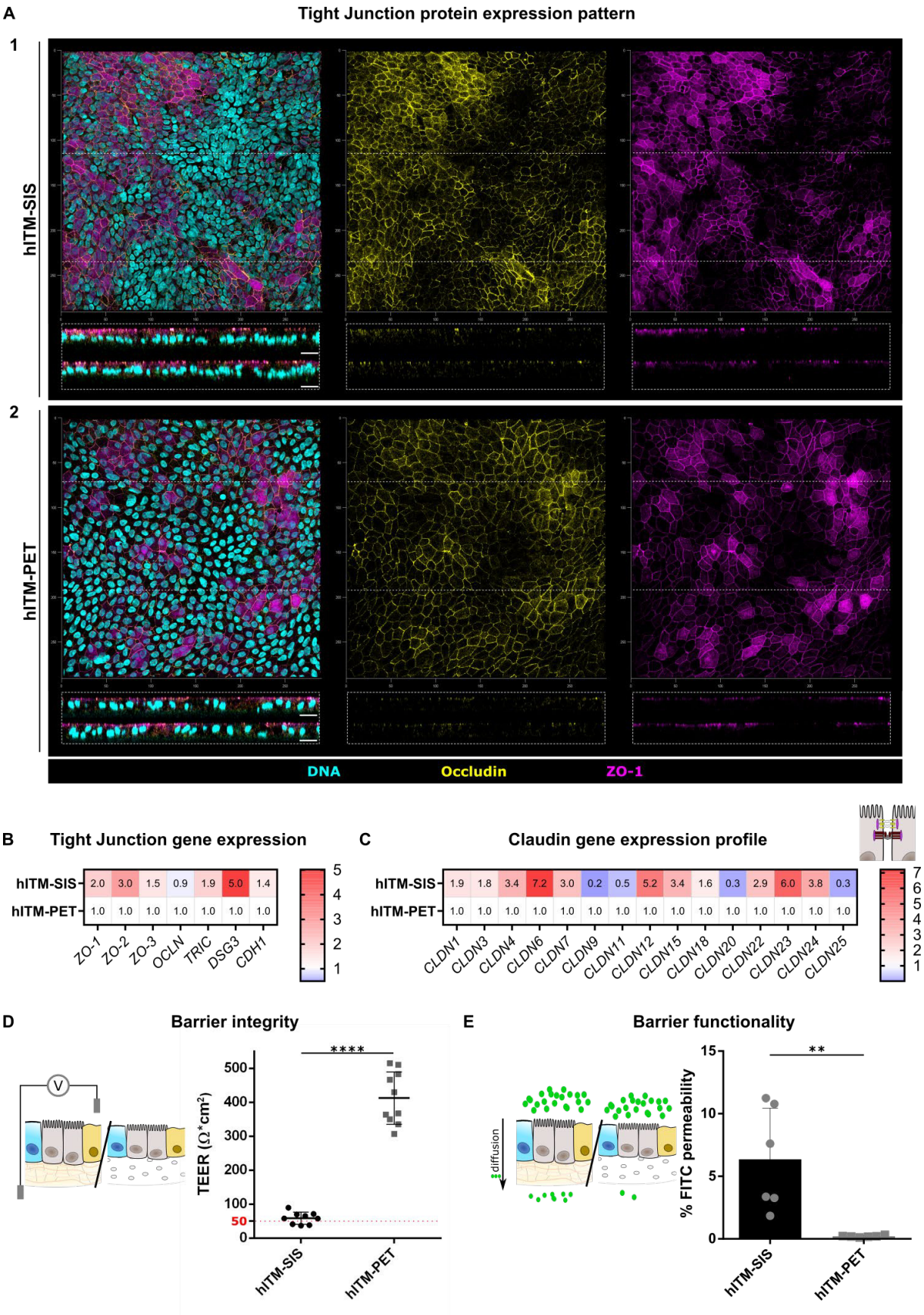

Figure 13. IECs hITM-SIS and-PET demonstrated typical intestinal epithelial barrier features, with variances in tight junction gene expression and barrier function. A Top view of IHC-staining of hITM-SIS (**A1**) and hITM-PET (**A2**) with DAPI (cyan), occludin (yellow) and ZO-1 (magenta) with representative orthogonal view underneath (n=3), showing typical and similar occludin and ZO-1 expression patterns. **B** Heat map displaying the gene expression profile of characteristic Tight-Junction-associated proteins of hITM-SIS, normalised to hITM-PET (n=1). **C** Heat map displaying the gene expression of

claudins of hITM-SIS, normalised to hITM-PET (n=1). **D** Schematic depiction of TEER measurement and TEER-values of hITM-SIS and hITM-PET models (n=2). Red line indicates *in vivo* measurements of 50-100 Ω*cm^2 according to Srinivasan et al., 2015. **E** Schematic depiction of FITC-Dextran permeability assay and FITC permeability values of hITM-SIS and hITM-PET (n=2). Significance was calculated by unpaired t-test for D and E with ****= $P \leq 0.0001$, **= $P \leq 0.01$. Non-significant P-values are not displayed. SB = 10 µm. (Däullary et al., 2022, in review). **Abbreviations**: CHD1: Cadherin-1, CLDN: claudin, DSG3: Desmoglein 3, JAM: Junctional Adhesion molecule, OCLN: occludin, TRIC: Tricellulin, ZO: Zonula Occludens, FITC: Fluorescein-isothiocyanate, TEER: Transepithelial electrical resistance, hITM: human intestinal tissue model, SIS: small intestinal submucosa, PET: polyethylenterephthalate.

Overall, the culture of primary IECs on the decellularised SIS scaffold (= hITM-SIS) resulted in the development of an epithelial monolayer with *in vivo*-like characteristics in regard to cellular morphology and morphometry. In comparison, IECs on the synthetic PET scaffold (= hITM-PET) showed reduced cell polarisation and mucin expression values. Furthermore, the hITM-SIS recapitulated *in vivo*-like features such as barrier integrity to a higher degree as well as increased epithelial gene and protein expression patterns in comparison to the hITM-PET. In contrast, the hITM-PET developed a higher barrier integrity and function, but within non-physiological ranges. Taken together, the organ-specific SIS bioscaffold favours the tissue-specific development of an IEC monolayer in comparison to the analysed synthetic PET scaffold. Therefore, the hITM-SIS was examined for further cellular features of the small intestine.

4.1.3 Tissue-specific protein expression and structural features of the intestinal epithelium by the hITM-SIS

Besides morphometric and barrier functional features, the intestinal epithelium is characterised by tissue-specific protein expression profiles and ultrastructural components. To evaluate these key features, the hITM-SIS was examined for the expression pattern of MUC1, Villin-1 (VIL1), Lysozyme (LYS) and MUC2 as well as pan-Cytokeratin (pCK) and E-Cadherin (ECAD) by IHC staining. Ultrastructural features were investigated by transmission- and scanning electron microscopy (TEM/SEM).

As shown in Figure 14 A, MUC1, a transmembrane mucin expressed in the gut epithelium and other organs, was lining the apical side of the epithelial layer with spatial variances between individual IECs. Further, VIL-1, a main protein important for the formation of microvilli and the brush border cytoskeleton, was broadly expressed in the apical region of the cells. LYS, a defensive antimicrobial protein, was observed intracellularly with typical dot-like structures in individual cells. Finally, MUC2, a mucin secreted by Goblet cells, was located intracellularly in individual cells (Figure 14 A).

Ultrastructural analysis via TEM and SEM underlined the polarised characteristics of the epithelial cells as indicated by the basal localisation of the nucleus and the elongated morphology of individual IECs (Figure 14 B). In addition, the cells were decorated with microvilli (Figure 14 B), a typical feature of intestinal Enterocytes. Furthermore, varying shapes of microvilli were observed (Figure 14 B, right) as well as intracellular vesicular structures (Figure 14 B, star), which indicates different cell types. In addition, the presence of TJ proteins could be confirmed (Figure 14 B, right arrowheads).

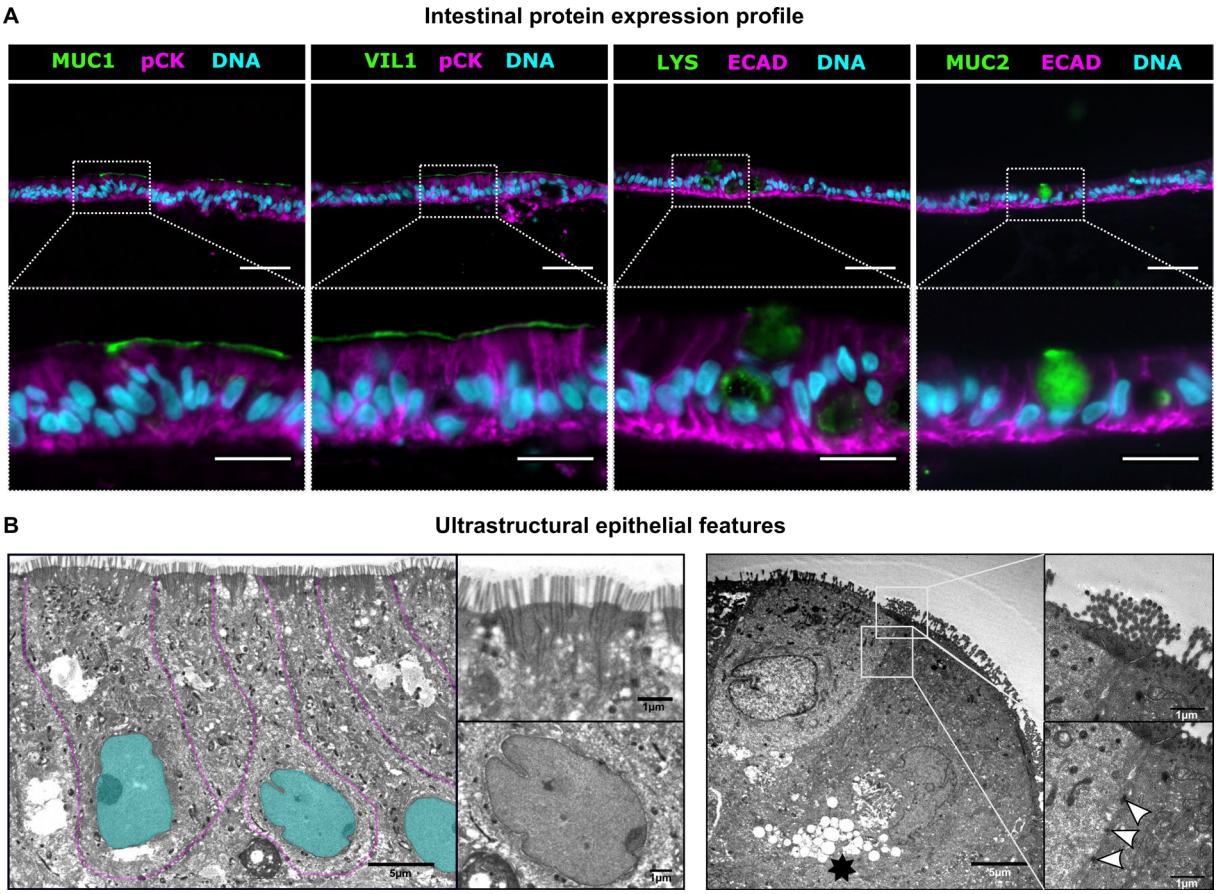

Figure 14. IECs of the hITM-SIS established an intestinal tissue-specific protein expression profile as well characteristic ultrastructural features. A Representative IHC-stained cross-sections of hITM-SIS displaying the expression of the tissue-specific proteins MUC1, VIL1, LYS, MUC2, pCK and ECAD. SB top row: 50µm, bottom row: 20µm **B left** Representative scanning electron microscope images of hITM-SIS displaying polarised cells with cell nuclei (cyan and enlargement bottom) separated by cell membrane (magenta) and decorated with microvilli (enlargement top). **B right** Representative transmission electron microscope image of hITM-SIS displaying vesicular structures (asterisk) as well microvilli (enlargement top) and typical TJ plates (enlargement bottom, arrowheads) SB = as indicated. (Däullary et al., 2022, in review). **Abbreviations**: ECAD: E-cadherin, LYS: Lysozyme, MUC: mucin, pCK: pan-Cytokeratin, VIL: Villin, hITM: human intestinal tissue model, SIS: small intestinal submucosa, TJ: Tight Junction.

4.1.4 The hITM-SIS represents major intestinal epithelial cell entities as shown by single cell transcriptomics

To gain deeper insights into the composition of the hITM-SIS in terms of cellular entities, single cell RNA-sequencing was applied. Therefore, the epithelial cell-layers of two individual hITM-SIS was gently dissociated into single cells and multiplexed by hash-tagging of the two samples. The single cells were subsequently pooled and processed for RNA sequencing based on droplet separation (Figure 15 4A), which was performed by Fabian Imdahl (working group of Dr. Antoine-Emmanuel Saliba, Helmholtz Institute for RNA-based Infection, Würzburg, Germany).

In total, 11727 individual single cells were sequenced with a median of 2424 genes per cell. After pre-processing and quality assessment (Appendix Figure 1A and B), a dataset of 3360 single cells with 33538 identified genes was further examined for unsupervised clustering (Appendix Figure 1C) and subsequent cell type identification (Figure 15 B). Of note, no variance between the two replicates was observed (Appendix Figure 1D). The bioinformatical processing was performed by Oliver Dietrich (working group of Dr. Antoine-Emmanuel Saliba, Helmholtz Institute for RNA-based Infection, Würzburg, Germany).

UMAP projection of unsupervised cell clustering resulted in distinct populations, which could be annotated to individual intestinal cells types by the expression of specific marker genes (Appendix Table 24, Figure 15B). Among them were proliferating TA cells (*NUSAP1*, *CCNA*, *MCM5*) with high expression values of proliferation markers (*PCNA*, *MKI67*, *TOP2A*) as well as stem cells (*LGR5*, *ASCL2*, *SOX4*) (Figure 15 C, blue and turquoise). Progenitor cells were defined by the expression of *FABP5*, *GPX2* and *CDK6* as well as by the relative absence or downregulation of other applied cell type-specific marker genes (Figure 15 C, grey). Additionally, members of the absorptive lineage such as mature (*RPB2*, *CYP3A4*, *APOA4*) and immature (*ALPI*, *FABP2*, *TMEM37*) Enterocytes (Figure 15 C, orange) were identified. Cells expressing secretory lineage-associated genes (*TFF1*, *RAB3B*, *DUOX2*, *HLA-E*) were annotated as secretory cells (Figure 15 C, green). Interestingly, expression of *MUC2*, a marker gene for differentiated Goblet cells, could not be detected. Furthermore, a cluster expressing immune-associated genes (*CCL20*, *CXCL3*) was classified as M-like cells (*LAMC2*, *TNFAIP2*, *TM4SF1*) (Figure 15 C, purple); however, canonical cell type markers like *SPIB* or *GP2* could not be detected. The expression of *HLA-G*, *APOL4*, *TRIP6*, and *SULT1C2* defined a distinct cluster, which did not express known cell marker genes and was thus classified as HLA-G+

cells (Figure 15 C, pink). Besides those, the high expression of the mitochondrial gene *MTRNR2L12* determined a dead/empty cell cluster (Figure 15 C, grey).

The largest population of cells was represented by the Progenitor cell cluster (31.01 %) followed by the Enterocytes (31.25 %), Secretory cells (12.32 %), Proliferating TA cells (6.75 %) and HLA-G+ cell cluster (10.10 %). Furthermore, the stem cell (2.82 %) and M-like cell cluster (4.73 %) represented only rare cell populations (Figure 15 E). Low quality cells were not considered, as they displayed dead cells or reflected empty droplets.

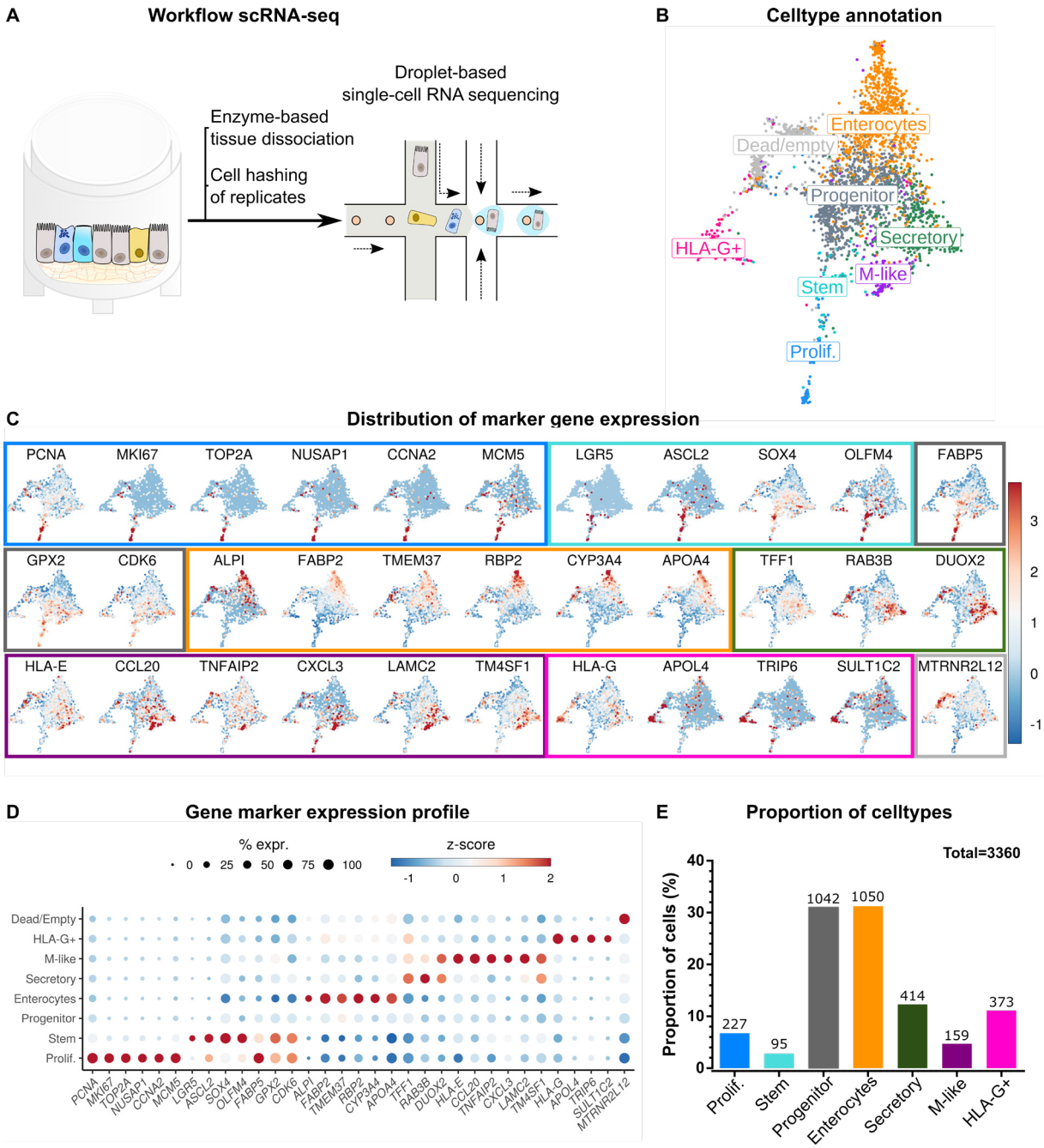

Figure 15. Single cell transcriptome analysis revealed distinct cellular entities of the native small intestine in the hITM-SIS. A Schematic experimental workflow of droplet-based cell separation and single cell RNA sequencing. **B** UMAP of unsupervised clustering of isolated IECs from hITM-SIS; two technical replicates. Colour annotation of identified cell types indicates the following cell clusters: Proliferating TA cells in blue, stem cells in turquoise, progenitor cells in orange, Enterocytes in red, Secretory cells in green, M-like cells in purple, HLA-G+ cells in pink and low-quality cells in grey. The determining marker genes are shown in C and in the Appendix Table 24. **C** UMAPs of applied cell type marker genes in scaled expression values, which were applied for the annotation in B. The colour frame represents the colour annotation in B. **D** Dot plot representation of marker genes sets displaying percentages of expressing cells and scaled expression values. **E** Proportion of identified cell types with colouring according to B. Representation of each cell type with indicated cell numbers as percentages of the total cell number of 3360. (Däullary et al., 2022, in review). **Abbreviations**: UMAP: Uniform Manifold Approximation and Projection, hITM: human intestinal tissue model, SIS: small intestinal submucosa.

4.1.5 IECs of the hITM-SIS display cell type-specific cytokine gene expression profiles

The scRNA dataset was applied to determine the cytokine expression profile of distinct cell types in the hITM-SIS. Therefore, the transcript levels of 43 cytokines (Table 25) including interleukins (IL), IL antagonists, and TNF-α, were evaluated in perspective of the annotated cell types from figure 4.

UMAP projection of the 43 cytokines revealed varying cytokine gene expression pattern in the IECs (Appendix Figure 2). Out of the 43 investigated cytokines, the gene expression for 22 pro- and anti-inflammatory cytokines was detected, whereas 21 cytokines were not expressed by the cells of the hITM-SIS (Appendix Figure 2, summarized in Figure 16 A). Of the 22 detected cytokines 8 cytokines *(IL5*, *IL10*, *IL11*, *IL13*, *IL16*, *IL19*, *IL20*, *IL34*, *IL36RN*) showed low expression levels and counts (Appendix Figure 2); they are further not expressed by epithelial cells according to published data (Akdis et al., 2016). The gene expression of the remaining 14 cytokines (*IL1A*, *IL1B*, *IL1RN*, *IL7*, *CXCL8*, *IL15*, *IL17C*, *IL17D*, *IL18*, *IL23A*, *IL32*, *IL33*, *IL37, TNF)* plus *IL6* are expressed by epithelial cells (Akdis et al., 2016) and were therefore investigated for cell type specific expression patterns (Figure 16 B and C).

Based on UMAP projection (Figure 16 B), the genes *IL1A*, *IL17C, IL17D, IL23A* and *TNF* seemed to be expressed by a low number of cells. In contrast the genes *IL1B*, *IL1RN*, *IL7*, *CXCL8, IL15, IL18, IL32, IL33,* and *IL37* seemed to be expressed by a higher number of cells; especially the genes *IL1RN, IL18,* and *IL32*, seemed most abundantly expressed. No cells expressing *IL6* transcripts were detected. The gene expression of *IL1B*, *IL1RN*, *IL7*, *IL15*, and *IL18* seemed further homogeneously distributed over all cells, whereas the gene expression of *CXCL8, IL23A* and *TNF* seemed to be specific in the earlier annotated M-like cell cluster (compare Figure 15 and Figure 16 B). In contrast, the expression of *IL37* appeared to be reduced in the M-like cell cluster and the expression of *CXCL8* and *IL33* seemed to be reduced in the Enterocyte cluster (Figure 15 and Figure 16 B), indicating cell type specific gene expression of the analysed cytokines.

Indeed, data representation as normalized gene expression within the individuals cell types displayed increased gene expression levels observed for *TNF*, *CXCL8* and *IL32*, as well as *IL1A*, *IL1B*, *IL18*, and *IL23A* in the M-like cell cluster (Figure 16 C). *IL33* expression was increased in the stem cell cluster and proliferating TA cell cluster (Prolif.). *IL1RN* was expressed in cells of the Secretory lineage-associated cluster (Secretory) (Figure 16 C). Overall, the expression profiling analysis indicated cell type-associated cytokine expression patterns in the hITM-SIS and revealed the M-like cell cluster, as cluster with the highest expression levels

and the most diverse expression profiles of the identified cytokines. Further, only a subset of investigated cytokines was expressed in hITM-SIS cells, indicating a potential restriction by the epithelial cell identity.

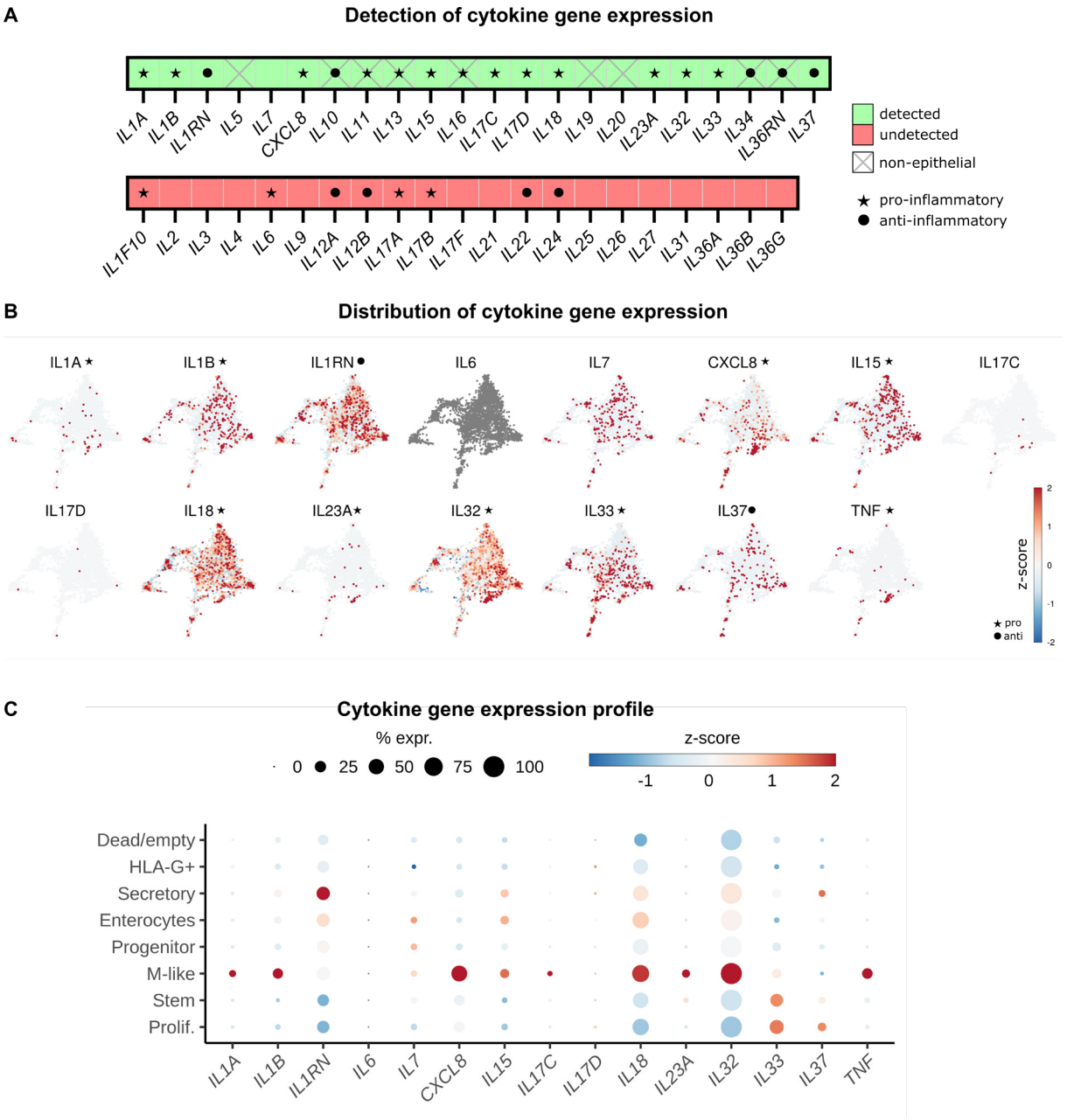

Figure 16. Cytokine expression profiling indicated cell type-associated cytokine expression in hITM-SIS cells. A Detected (green) and undetected (red) gene expression of cytokines, including interleukins, interleukin antagonists and TNF-α, displayed as graphical summary of the data in Table 25 and Appendix Figure 2. **B** UMAPs displaying scaled gene expression of cytokines, which were detected in hITM-SIS cells, plus IL6. **C** Dot plot representation of gene expression of cytokines of cells of the hITM-SIS, showing percentages and scaled expression values of B. According to Akdis et al., 2016,pro-inflammatory cytokines are marked with ●, anti-inflammatory cytokines are marked with ★. Bioinformatical analysis was performed by Oliver Dietrich (working group of Dr. Antoine-Emmanuel Saliba, Helmholtz Institute for RNA-based Infection, Würzburg, Germany). **Abbreviations**: UMAP: Uniform Manifold Approximation and Projection, hITM: human intestinal tissue model, SIS: small intestinal submucosa. IL: interleukin, IL1RN: interleukin antagonist 1, TNF: Tumour necrosis factor (= TNF-α).

Taken together, primary IECs cultured on decellularised porcine SIS bioscaffold showed a highly polarised monolayer with a native-like morphometry and barrier function. In addition, it recapitulates characteristic structural and ultrastructural features of the native tissue, such as microvilli and Tight Junction expression. RNA sequencing at the single cell level revealed a heterogeneous cell composition including multiple intestinal cell types that are found *in vivo*, such as stem cells, proliferating TA cells, progenitor cells, Enterocytes, M-like cells and Secretory cells. However, a distinct Paneth cell population, EE cells and *MUC2* expressing Goblet cells could not be identified. Furthermore, cytokine profiling revealed gene expression enrichment in distinct cell types, such as *CXCL8* and *TNF* in M-like cells. Conclusively, the hITM-SIS mimics the native tissue in multiple aspects and thus provides a platform for research of the human small intestinal epithelium in a tissue- and cell-specific manner.

4.2 Mimicking *Salmonella* Typhimurium infection in the hITM-SIS – characteristic hallmarks of the infection *in vitro* and heterogeneity of STm behaviour on single cell level

4.2.1 STm-infected hITM-SIS displays MOI- and time-dependent infection rates and LDH release

To investigate the cellular pathogenesis of STm infection *in vitro* on single cell level, hITM-SIS models were infected with a wild type STm (constitutively GFP expressing; GFP strain) or a proliferation reporter STm strain (constitutively mCherry expressing plus inducible GFP expression; reporter strain). First, a suitable infection workflow was established. In short, STm were inoculated in the apical compartment of the hITM-SIS and synchronised attachment of STm to the epithelium was achieved by centrifugation. After an attachment and invasion phase of 1h, extracellular STm were inactivated by a high dose Gentamicin treatment for 0.5h. Reinfection cycles were prevented by further incubation under Gentamicin protection conditions, further defined as time point 1.5h post application (p.a.). Over a timeframe of 24h p.a., samples were analysed by microscopy, flow cytometry, bead-based cytokine assay, FACS sorting and/or single cell RNA sequencing (Figure 17 A).

First, a suitable multiplicity of infection (MOI) value had to be determined to allow observations of intracellular STm dynamics overtime with low cytotoxicity and sufficient numbers of infected cells. Therefore, cytotoxic effects and the infection rate of the STm in the hITM-SIS were investigated after infection with a MOI of 5, 10 or 50 for 5.5h, 25.5h, or 49.5h p.a. (Figure 17 B and C). The LDH release, as a measure of cell death, was determined and flow cytometric analysis of GFP+ cells was performed to define the infection rate. In comparison to the uninfected hITM-SIS (mock) at 5.5h p.a., infection with a MOI5, MOI10 or MOI50 led to an increase of LDH release (MOI5: 1.7-fold; MOI10:1.9-fold; MOI50: 2.5-fold) (Figure 17 B). A similar trend was observed at 25.5h and 49.5h p.a. Comparable to LDH release levels, infection rates increased with the respective MOI from 1.0 % (± 0.4 %) for MOI5, 6.7 % (± 1.7 %) for MOI10, and 8.7 % (± 4.1 %) for MOI50 at 5.5h p.a. (Figure 17 C). Furthermore, infection rates raised overtime to 3.3 % (± 0.2 %) at 25.5h p.a. for MOI5, to 5.6 % (± 1.4 %) for MOI10, and to 6.9 % (± 1.1 %) for MOI50 as well as at to 5.8 % (± 0.87 %) at 49.5h p.a. for MOI5 and 6.3 % (± 1.1 %) for MOI10. At 49.5h p.a., no cells could be retrieved from the hITM-SIS infected at an MOI of 50 (Figure 17 C). Taken together, STm demonstrated MOI- and time-dependent LDH-release levels and infection rates.

Models infected with a MOI10 showed lower cytotoxicity compared to MOI5- or MOI50-infected hITM-SIS models, while maintaining stable numbers of infected cells. To this aim, further experiments were performed with a MOI of 10.

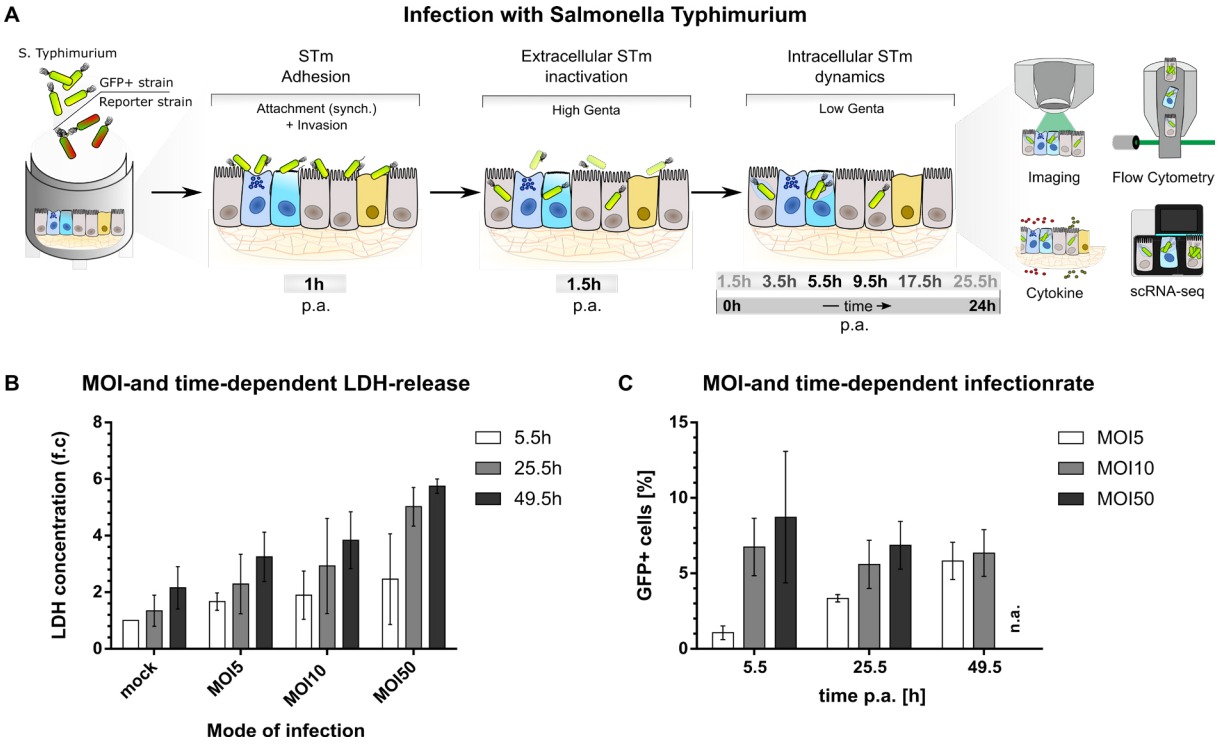

Figure 17. Infection of the hITM-SIS with STm revealed MOI- and time-dependent infection rates and respective LDH release. A Schematic depiction of the STm infection experimental workflow. hITMs were infected with GFP+ wt STm or the STm proliferation reporter strain. Bacteria were added to the apical compartment, followed by synchronised adhesion and invasion. Subsequently, extracellular STm were inactivated by High Gentamicin treatment and intracellular infection processes were investigated 1.5h, 3.5h, 5.5h, 9.5h, 17.5h, 25.5h after bacterial application to the model (referred to as post application: p.a.) via confocal imaging, flow cytometry, bead-based cytokine assay and single cell RNA sequencing. **B** Mean LDH concentration of the apical compartment of uninfected (mock) and infected hITMs (MOI5, MOI10, MOI50) at 5.5h, 25.5h or 49.5h p.a. indicated MOI- and time-dependent LDH release (n=2). **C** Percentages of STm infected epithelial cells in the hITM-SIS infected with MOI5, MOI10 or MOI50 for 5.5h, 25.5h and 48 p.a.. showed MOI-dependent infection rates with stable infection rates at MOI10 (n≥2). Infection rate was measured by flow cytometry determining GFP+ cells (n≥2). Non-significant P-values are not displayed. (Däullary et al., 2022, in review). **Abbreviations**: hITM: human intestinal tissue model, SIS: small intestinal submucosa, STm: *Salmonella* Typhimurium., LDH: Lactate Dehydrogenase, MOI: multiplicity of infection, GFP: green fluorescent protein, p.a.: post application, n.a.: not available.

4.2.2 STm adheres to IECs and invades the hITM-SIS via characteristic F-actin rearrangement

The STm invasion process is a sequential and well-studied mechanism including bacterial adhesion and internalisation, according to Larock et al., 2015 (schematically depicted in Figure 18 A). In order to investigate STm adhesion to the apical surface of the IECs within the hITM-SIS, SEM analyses were performed 1h post adhesion before Gentamicin treatment. As shown in Figure 18 B, the IECs displayed a characteristic brush border with microvilli decoration as well as established cell junctions between individual cells. STm (yellow) were observed on top of the IECs and seemed to interact with the cell brush border via their flagella (blue) (Fig 7B left + magnifications). Further, IECs showed membrane protuberances (red) in the vicinity of STm (Figure 18 B left and right) and STm were observed inside these protuberances (Figure 18 B right), indicating bacterial invasion by apical membrane rearrangements.

In order to investigate, if the observed membrane rearrangements were based on the typical remodelling of the underlining Actin cytoskeleton, the stereo spatial localisation of the STm and the F-actin was examined by confocal fluorescence microscopy. Focusing on the F-actin signal displayed at the apical surface of the infected hITM-SIS (Figure 18 B, Appendix Figure 3), several different steps of the invasion process could be visualized simultaneously: STm attached to the apical cell surface (I), which is followed by remodelling of the F-actin cytoskeleton to a “Donut”-shaped entry point (II). Subsequently, F-actin ruffling and further remodelling led to surrounding and enclosure of STm by the cell membrane (III). STm then migrated deeper into the cell and led to an F-actin reconstruction (IV) and finally to a completely restored F-actin cytoskeleton (V). This indicates STm invasion by actin-based membrane ruffling in the hITM-SIS.

Of note, STm seemed to invade the IECs as single bacterium or as pairs, indicating that no multiple infection events occurred during the invasion phase in the hITM-SIS *in vitro* model.

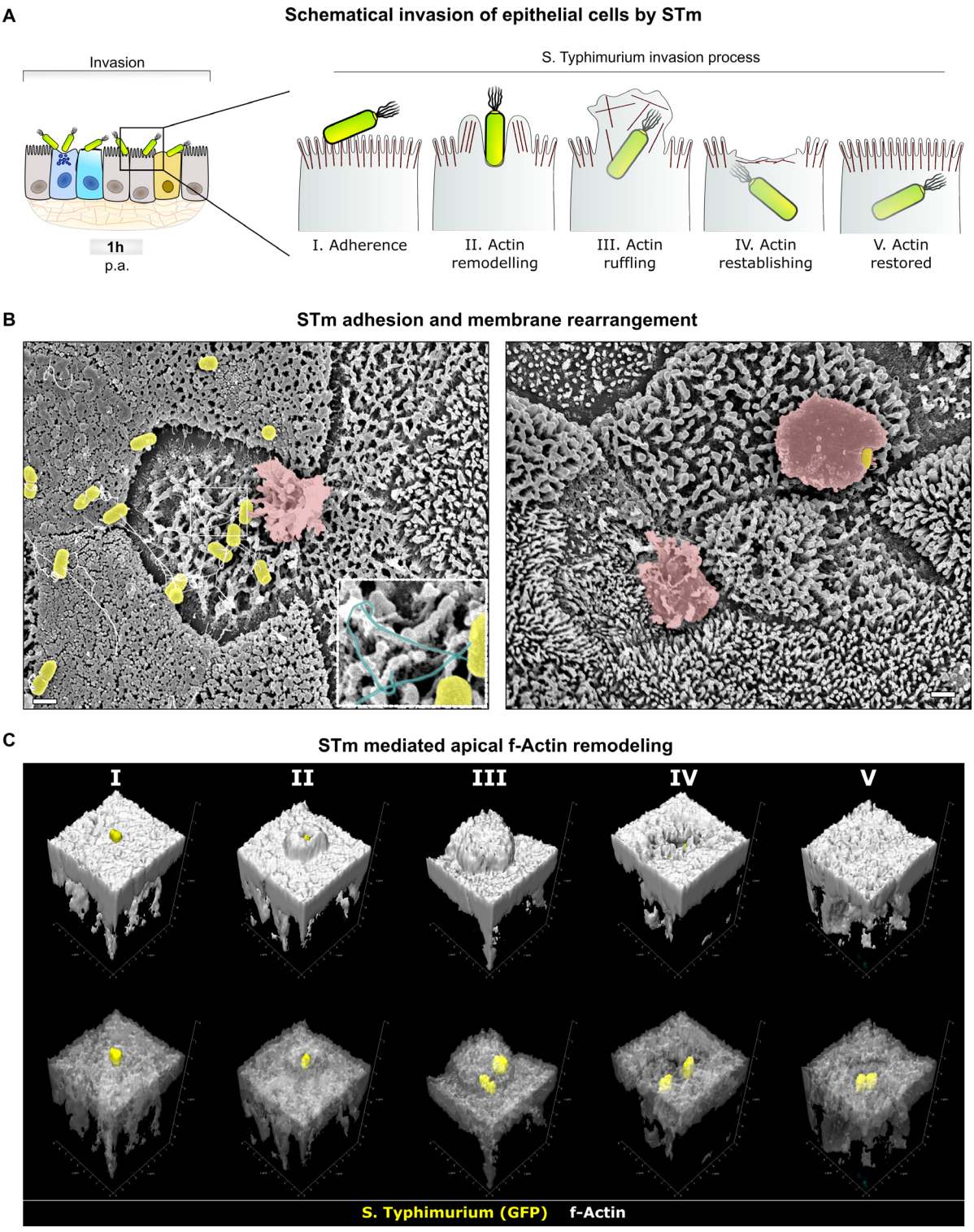

Figure 18. STm invasion of hITM-SIS reassembled hallmarks of STm infection by introducing typical actin ruffling events. A Schematic depiction of the STm invasion process according to Larock et al., 2015. After adhesion (I), STm introduces Actin remodelling (II) and further Actin ruffling (III), resulting in enclosing of the STm by the cellular membrane. After engulfment, the actin cytoskeleton is re-established (IV) and finally restored (V) **B** Representative scanning electron microscopy images of infected hITM-SIS 1h post adhesion. The left image shows IEC membrane protuberances (red) and STm (yellow), which adhered to the IEC brush border (left) and interacted with the microvilli via the bacterial flagellum (blue) (left magnification). On the right site, IEC membrane protuberances are depicted with a STm inside. (n=1). **C** Apical membrane area of STm infected hITM-SIS 1h post adhesion, displayed as 3D surface rendered images, reveal the individual invasion steps depicted in A (I-V). An overview of the infected hITM-SIS is depicted in the Appendix Figure 3. STm (GFP) are depicted in yellow and F-actin (Phalloidin) in grey (n=2). (Däullary et al., 2022, in review). **Abbreviations**: p.a.: post application, hITM: human intestinal tissue model, SIS: small intestinal submucosa, STm: *Salmonella* Typhimurium, IEC: intestinal epithelial cell, F-actin: filamentous Actin. SB: 1 µm

4.2.3 STm effectively infects the hITM-SIS epithelium and displays apical-basolateral migration within cells

In order to evaluate stereo spatial localisation of STm after infection, confocal microscopy and 3D projection of STm infected hITM-SIS was applied with spatial image analysis. The obtained data revealed effective STm infection and showed that STm localised intracellularly in the hITM-SIS monolayer in a scattered manner over the time course of 25.5h (Figure 19 A and B). Furthermore, the characteristic monolayer of hITM-SIS and the IECs cellular integrity were maintained, as indicated by the comparable distribution of cell nuclei within the infected hITM-SIS (Figure 19 A, top row).

The STm morphology, intracellular localisation, and STm cluster formation changed overtime within the infected hITM-SIS (Figure 19 A middle + bottom row). In detail, at 1.5h p.a., STm were observed either as single bacteria or as bacterial bundles that clustered within individual IECs. After 9.5h p.a., STm could be increasingly observed in cluster arrangements and as elongated STm structures with diffuse bacterial separation, indicating the formation of filamentous STm. After 25.5h p.a., the elongated structures seemed to be increased in number and in length and individual bacteria in these structures seemed to merge. However, IECs infected with a single STm or a pair of STm were also observed at each individual time point, indicating varying intracellular STm populations overtime (Figure 19 A middle row).

In addition, the intracellular localisation of STm changed overtime (Figure 19 B). At the initial analytical time point of 1.5h p.a., STm localised apically from the nuclei and close to the apical membrane of the monolayer. From 5.5h p.a. on, STm could be observed on the same horizontal positioning as the nucleus and from 9.5h p.a. on the basal side of the IECs. Simultaneously with increased SIT establishment at 17.5h p.a., the positioning of STm shifted to the basal region of the infected cells, suggesting an apical-basolateral migration of certain STm populations (Figure 19 B).

The intracellular migration behaviour of STm within the hITM-SIS was further characterized by quantification of the migrated distance of individual STm from the apical F-actin membrane surface (Figure 19 C), showing that the mean migration distance and the maximal migration distance increased overtime. In relation to the apical surface, STm migrated - 0.82 µm (± 0.99 µm, 0 – 3.64 µm) at 1.5h p.a., - 5.64 µm (± 3.44 µm, 1.59 – 18.15 µm) at 3.5h p.a., - 6.74 µm (± 5.34 µm, 0.42 – 24.07 µm) at 5.5h p.a., - 11.70 µm (± 7.232 µm, 3.02 – 28.51 µm) at 9.5h p.a., -16.34 µm (± 9.70 µm, 1.73 – 34.35 µm) at 17.5h p.a. and - 16.97 µm (± 7.271 µm, 1.36 – 31.20 µm) at 25.5h p.a. (Figure 19 C). As displayed in Figure 19 C, the mean migration

distance differed significantly between 1.5h and 5.5h, 9.5h, 17.5h, 25.5h p.a., between 3.5h and 9.5h, 17.5h, 25.5h p.a., between 5.5h and 17.5h, 25.5h p.a., and between 9.5h and 17.5h, 25.5h p.a.. Of note, the minimal distance of STm migration did not increase significantly overtime, indicating that individual STm did not migrate towards the basolateral side, but remained in the apical region.

In addition, flow cytometry of infected IECs (=GFP+ cells) proofed that STm infection of the IEC monolayer showed a stable infection rate and stable populations of infected IECs of 7.53 % (± 0.93 %) over the time course of 25.5h (Fig 8D). In detail, at 1.5h p.a. 7.20 % (± 3.21 %), at 3.5h p.a. 8.84 % (± 2.76 %), at 5.5h p.a. 8.07 % (± 1.4 %), at 9.5h p.a. 7.01 % (± 1.94 %), at 16 p.a. 8.13 % (± 2.97 %) and at 25.5h p.a. 5.96 % (± 1.75 %) infected cells were detected (Figure 19 D), with no significant variances.

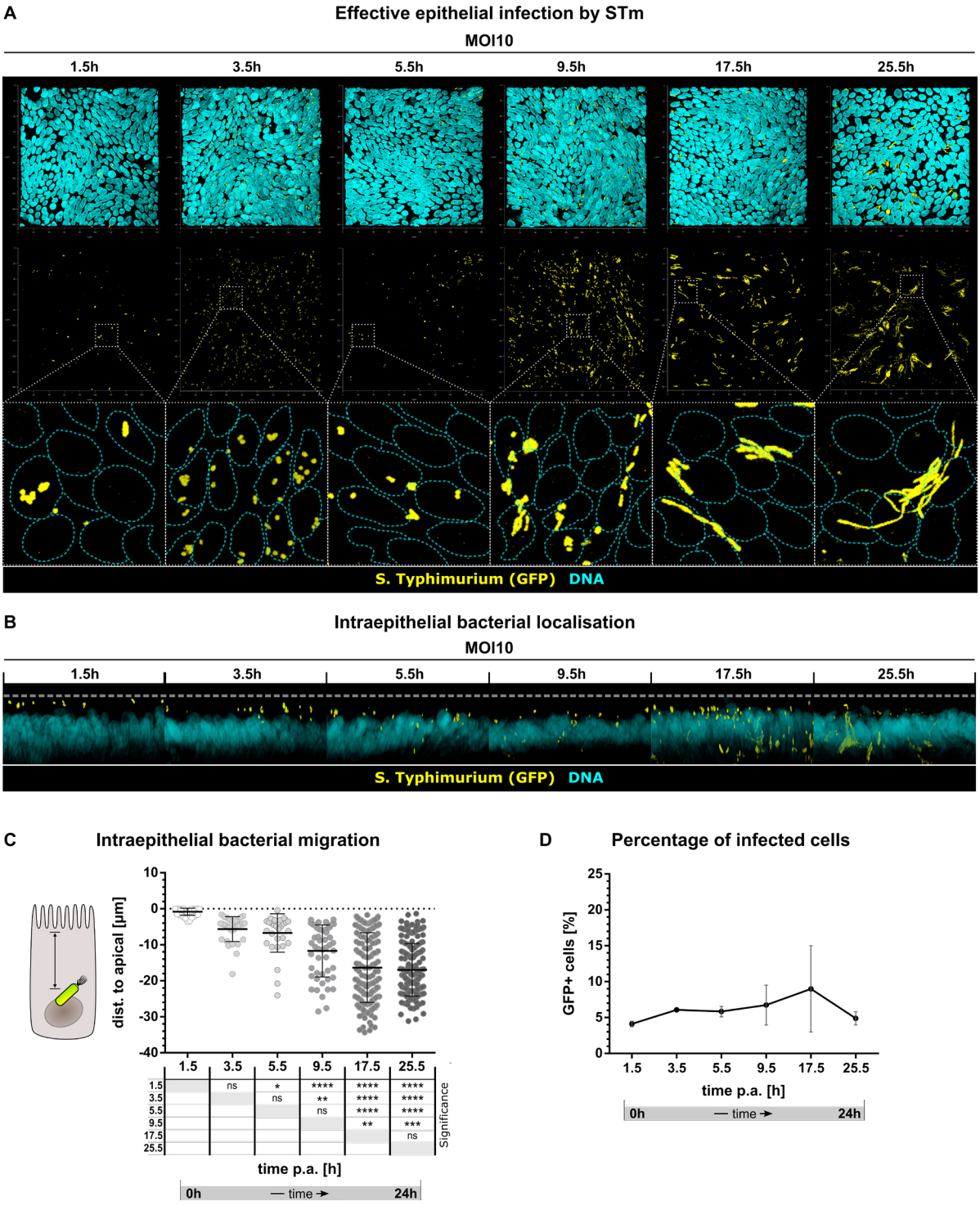

Figure 19. Application of STm to the hITM-SIS revealed effective infection of the IECs including STm morphism and intracellular migration. A Top view on 3D projection of fluorescent images of STm infected hITM-SIS after 1.5h, 3.5h, 5.5h, 9.5h, 17.5h, 25.5h p.a. with STm (GFP) in yellow and DNA (DAPI) in cyan. STm effectively infected epithelial cells as demonstrated by their intracellular localisation and typical STm morphology. Top panel displays merged images, middle STm only and bottom enlargements of STm with dotted cyan lines indicating nuclei. Images are representative images (n=3). **B** Side view on 3D projection of fluorescent images of STm infected hITM-SIS after 1.5h, 3.5h, 5.5h, 9.5h, 17.5h, 25.5h p.a. with STm (GFP) in yellow and DNA (DAPI) in cyan showing intracellular migration of STm overtime. Dotted line indicates the apical actin layer. Images are representative images (n=3). **C** Quantification of STm intracellular migration (1.5h: 43, 3.5h: 34, 5.5h: 32, 9.5h: 52, 17.5h: 204, 25.5h: 185) (n=1). **D** Percentages of infected epithelial cells at 1.5h, 3.5h, 5.5h, 9.5h, 17.5h, 25.5h p.a.. Infection rates were measured by flow cytometry of GFP+ cells (n=2). Significance was calculated by ordinary one-way ANOVA and Tukey's multiple comparisons test for C with ****= $P \leq 0.0001$, ***= $P \leq 0.001$, **= $P \leq 0.01$, *= $P \leq 0.05$, ns = $P > 0.05$. Non-significant P-values are not displayed in D. (Däullary et al., 2022, in review). **Abbreviations**: F-actin: filamentous actin, p.a.: post application, hITM: human intestinal tissue model, SIS: small intestinal submucosa, STm: *Salmonella* Typhimurium, MOI: multiplicity of infection, IEC: intestinal epithelial cell, ns: not significant.

4.2.4 STm develops a filamentous morphology and displays heterogeneous intracellular populations

Intracellular adaptation of STm is an important hallmark of STm infection progression. Therefore, intracellular STm populations in the hITM-SIS were investigated by spatial analysis via confocal fluorescence microscopy. After 17.5h p.a. and 25.5h p.a. STm developed elongated structures with continuous cytoplasmic GFP signals (Figure 20 B i), indicating filamentous STm. Co-staining for LPS revealed a continuous bacterial membrane in these filamentous STm with multiple chromosomal copies (Figure 20 C). Of note, the cell membrane and the F-actin cytoskeleton were not affected, indicating that infected cells harbouring filamentous STm were viable.

Furthermore, at 25.5 p.a., individual infected IECs contained varying numbers of bacteria. In addition to IECs infected with multiple or single STm, cells exhibiting STm without filament formation were also detected (Figure 20 B). This indicates heterogeneity of STm populations in the late phase of infection in the hITM-SIS.

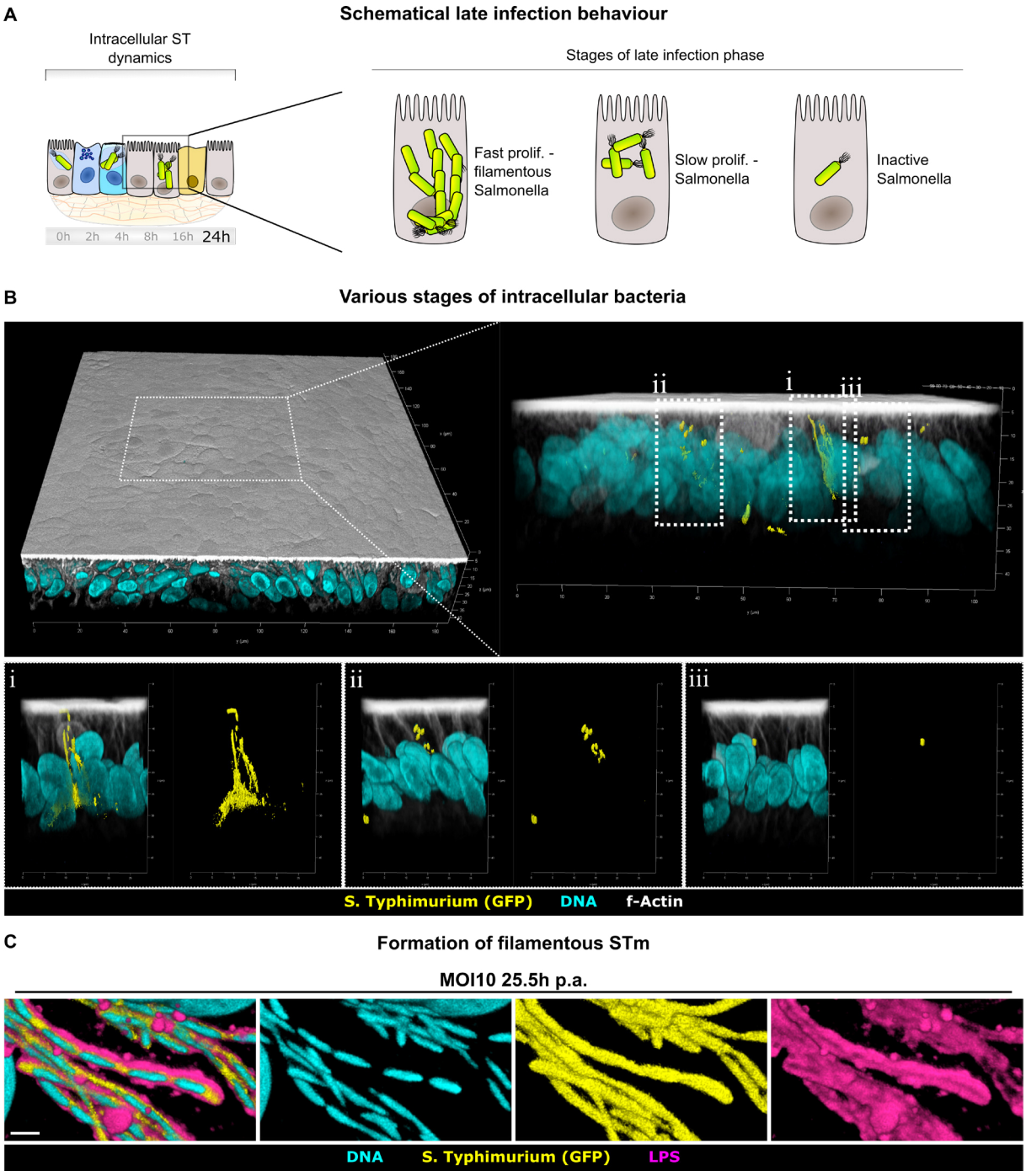

Figure 20. STm exhibited heterogeneous intracellular populations regarding morphology and bacterial burden in the late infection phase of the hITM-SIS. A Schematic depiction of the intracellular STm stages of the late infection phase: fast proliferating filamentous STm, slowly proliferating STm and non-proliferating STm. **B** Immunofluorescent-based 3D projection of STm infected hITM-SIS 25.5h p.a. with STm (GFP) in yellow, DNA (DAPI) in cyan and F-actin (Phalloidin) in grey. Magnification and side view of indicated area shows filamentous ST (i), multiple STm in single cells (ii) and single STm (iii) at the same point of time (n=2). **C** Representative images of intracellular filamentous STm depicting bacterial DNA (cyan), bacterial cytoplasm with GFP (yellow) and the continuous bacterial membrane with LPS (magenta). Scale bar: 1 µm (n = 3). (Däullary et al., 2022, in review). **Abbreviations**: F-actin: filamentous actin, p.a.: post application, hITM: human intestinal tissue model, SIS: small intestinal submucosa, MOI: multiplicity of infection, STm: *Salmonella* Typhimurium.

.

4.2.5 hITM-SIS displays a dynamic cytokine profile upon STm infection, while missing a characteristic IL-6 response

The first cellular response to infection can be the release of cytokines into the cell environment as an order of cell communication and defence regulation. In order the investigate the epithelial cytokine response to STm infection, the release of IL-8, IL-6, TNF-α, IL-10, IL-1β, and IL-12p70 was determined in the apical and the basolateral compartment of the STm infected hITM-SIS by flow cytometry-driven bead-array-based analysis of supernatants.

As shown in Figure 21 A, the infection of the hITM-SIS with STm, compared to the mock control, led to a general increase of IL-8 overtime (1.5h -25.5h) in the apical (from 2-fold to up to 5-fold) as well as in the basolateral compartment (from 2-fold to up to 11-fold) (detailed values in Table 26). This indicates a continuous IL-8 release of the IECs upon STm infection. Furthermore, after 3.5h p.a., the basolateral concentration of IL-8 was 2.8-fold higher than the apical concentration. After 9.5h p.a., IL-8 concentration was comparable in the apical and basolateral compartment; after 25.5h p.a., IL-8 was 1.5-fold higher in the apical than in the basolateral compartment. This indicates a trend of a basolateral-directed release of IL-8 in the early infection phase, with a potential inversion to apical-directed release overtime. Interestingly, the uninfected hITM-SIS (mock) showed no IL-8 release until 17.5h, but a rapid increase at 25.5h. However, IL-8 concentrations of the mock at 25.5h were 2-fold lower compared to the respective STm infected hITM-SIS. Of note, the concentration of IL-8 varied between replicates, leading to high standard deviations (SD) at later time points (17.5h and 25.5h p.a.).

In regard to TNF-α release, IECs secreted TNF-α upon STm infection in a time-dependent manner, whereas the uninfected hITM-SIS showed little to no release overtime (Figure 21 B, detailed values in Table 26). In detail, the TNF-α concentration in the STm infected hITM-SIS was increased after 3.5h p.a. to 8-fold apically and 7-fold basolaterally compared to the corresponding mock control. Overtime, the concentration of TNF-α decreased in both compartments to 1.9-fold apically and 2.1-fold basolaterally. These observations indicate an increased release during the early phase of the infection compared to later phases. Overall, similar to IL-8, also TNF-α concentrations showed high variations between replicates.

In addition to IL-8 and TNF-α, the levels of IL-10, IL-6, IL-1β, and IL-12p70 were also determined. However, these cytokines could not be detected, suggesting that STm does not trigger the release of IL-6, IL-10, IL-1β, and IL-12p70 in the hITM-SIS or that the IECs of the *in vitro* model are functionally unable to secrete IL-6, IL-10, IL-1β, and IL-12p70.

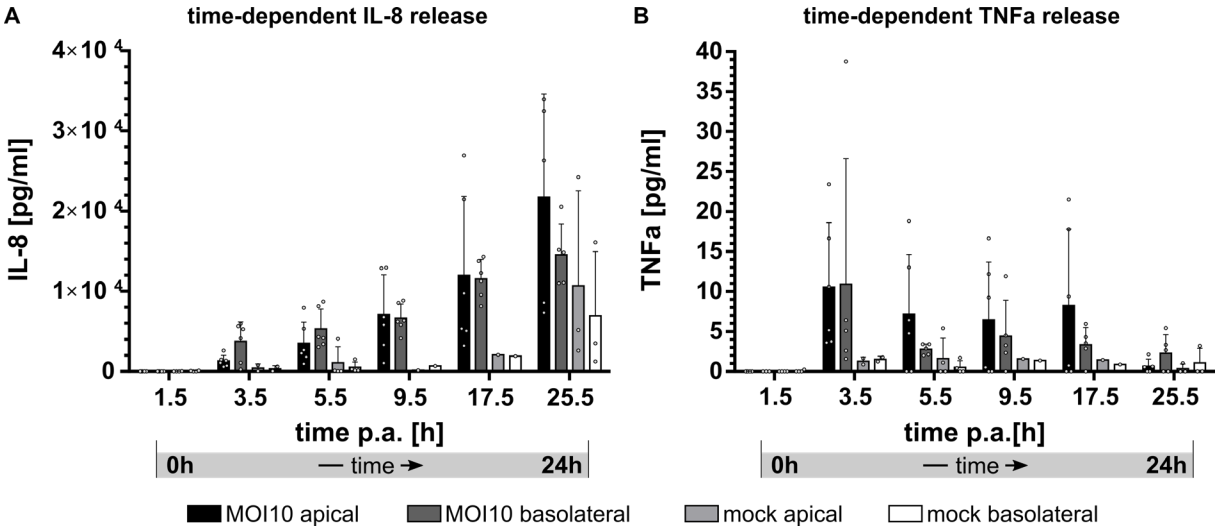

Figure 21. STm infection led to dynamic cytokine release by epithelial cells. A Mean IL-8 release in pg/ml in apical or basolateral compartment after STm infection (MOI10) or without (mock) at 1.5h, 3.5h, 5.5h, 9.5h, 17.5h, 25.5h p.a. revealed a trend of time-dependent and increasing IL-8 release in the STm infected hITM-SIS. Cytokine concentration was determined via cytometry-based bead array with n=3 for MOI10 and n=2 for mock 1.5h, 5.5h, 25.5h, and n=1 for mock 3.5h, 9.5h, 17.5h. **B** Mean TNF-α in pg/ml release in apical or basolateral compartment after STm infection (MOI10) or without (mock) at 1.5h, 3.5h, 5.5h, 9.5h, 17.5h, 25.5h p.a. revealed a trend for decreasing TNF-α release in STm infected hITM-SIS overtime. Cytokine concentration was determined via cytometry-based bead array with n=3 for MOI10 and n=2 for mock 1.5h, 5.5h, 25.5h, and n=1 for mock 3.5h, 9.5h, 17.5h. Non-significant P-values are not displayed. (Däullary et al., 2022, in review). **Abbreviations**: p.a.: post application, hITM: human intestinal tissue model, SIS: small intestinal submucosa, STm: *Salmonella* Typhimurium, IL-8: Interleukin 8, MOI: Multiplicity of infection, TNF-α: Tumour necrosis factor alpha.

In summary, the hITM-SIS represented important features of the native intestinal epithelium that enable its application as an alternative study model for STm-specific infection research. Indeed, after development of a suitable infection procedure, application of STm revealed effective epithelial infection with intracellular localisation and migration of the bacteria. Furthermore, hallmarks of the STm infection process were reflected, such as the early invasion process in terms of membrane-ruffling and pairwise infection as well as heterogeneous late infection phase stages of STm. As additional aspect, the systemic release of IL-8 and TNF-α represented a host reaction towards STm infection in epithelial cells. Interestingly, in all stages, a heterogeneous behaviour of STm was observed, such as the observation of filamentous STm and simultaneous single or multiple STm at 25.5h p.a. or the heterogeneous migration behaviour. This heterogeneity was further investigated on single cell level in regards of intracellular replication, cellular tropism, and transcriptomic adaption in the context of STm infection.

4.2.6 STm infected IECs show heterogeneity and diversity in terms of bacterial burden and spatial distribution

Individual IECs seemed to show varying intracellular bacterial burden as indicated in Figure 19 A and Figure 20 B, suggesting a differential STm behaviour on single cell level overtime. In order to address this heterogeneity in more detail, the STm infected hITM-SIS was investigated by confocal microscopy focusing on the individual bacterial burden. At 5.5h p.a., individual IECs could be observed, which showed a varying intracellular bacterial load (Figure 22 A). In detail, cells carried either low (i), medium (ii) or high bacterial (iii) loads as shown in Figure 22 A, with simultaneous uncompromised cell integrity.

In a quantitative approach, the STm infected hITM-SIS models were dissociated into single cells and subsequently sorted based on GFP fluorescence signal intensity via FACS (Figure 22 B). Infected cells were defined as GPF+/PerCP-Cy5.5- cells. Based on increasing GFP intensity, infected cells were classified as *low* (GPF+), *med* (GPF++) or *high* (GPF+++) infected cells. Each population (*low*, *med*, *high*) was further analysed via confocal microscopy for intracellular bacterial burden by counting of individual STm in single cells. The median STm count of the *low* population was 3 (1 - 4), of the *med* population 10 (8 - 22) and of the *high* population 56.50 (46 - 73) (Figure 22 C). One-way ANOVA analysis revealed further a significant difference regarding the bacterial load in all three populations.

Of note, flow cytometry revealed a GFP+/PerCP-Cy5.5+ population (Figure 22 B), which was also present in uninfected samples, later identified as MUC2+ cells by IHC (Appendix Figure 4). The signal of these cells in the GFP+/PerCP-Cy5.5+ channel seemed to rely on high auto fluorescence signals of vesicular cells.

In regards of total infected cells from 1.5h to 25.5h p.a., the *low* population represented the largest group with 70.66 % (± 9.12 %), followed by the *med* population with 25.55 % (± 6.04 %) and the *high* population of 3.79 % (± 3.59 %) (Figure 22 D). At each time point, there was a significant and distinct distribution between the individual populations, which seemed to change overtime. In detail, the *low* population decreased over time by 20.20 % (80.27 % at 1.5h to 60.07 % at 25.5h) with simultaneous increase of the *med* population by 11.68 % (18.39 % at 1.5h to 30.07 % at 25.5h) and the *high* population by 8.53 % (1.33 % at 1.5h to 9.86 % at 25.5h). Between 1.5h and 9.5h p.a., the proportions between all three populations appeared comparably stable, which seemed to change between 9.5h and 17.5h p.a. with an increase of the *med* and *high* populations. It indicates a shift of the *low* over *med* to *high* infected cells in a time-

dependent manner and potentially represents intracellular bacterial proliferation. However, due to a high standard deviation, the change was not significant.

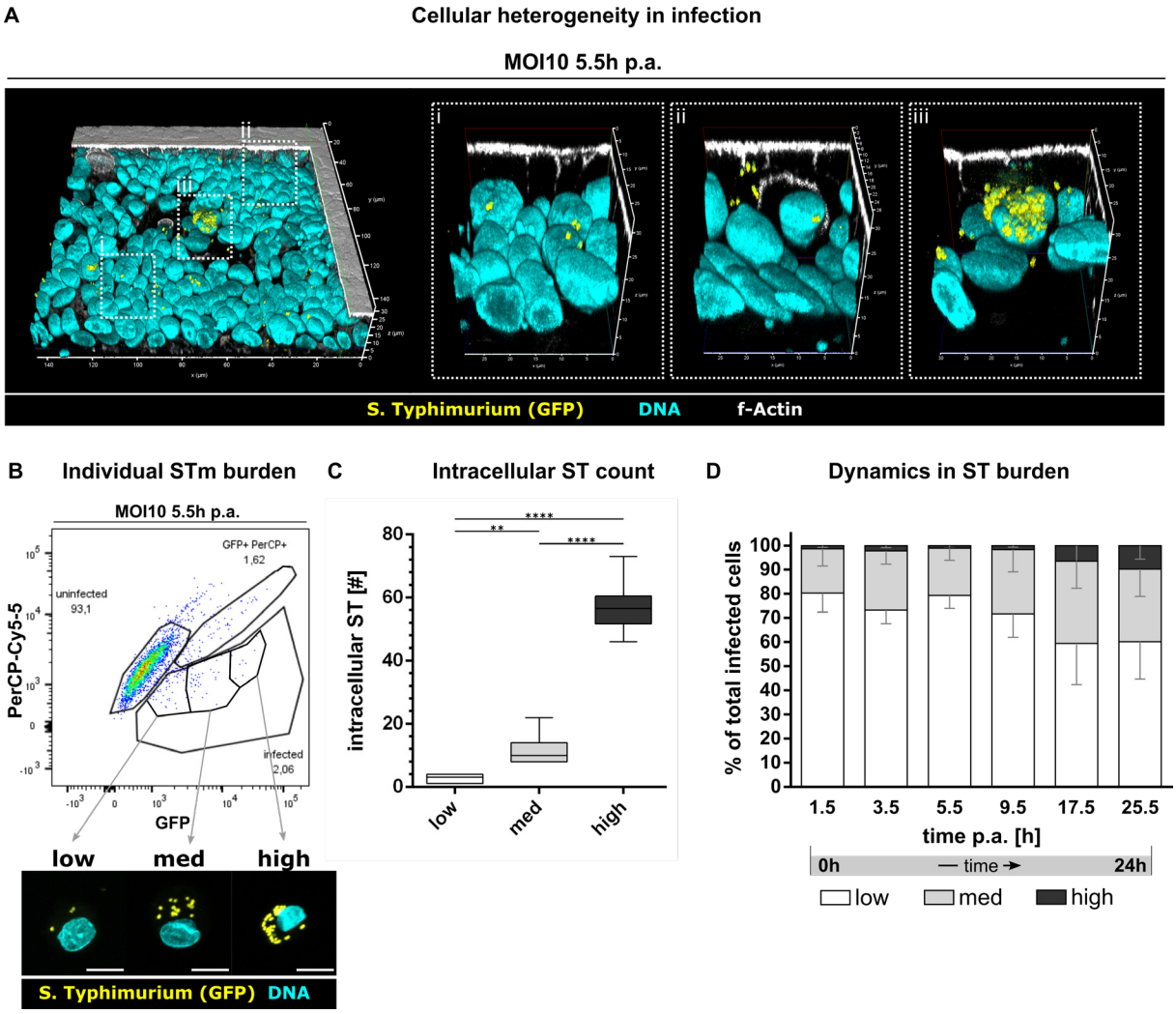

Figure 22. STm infection of the hITM-SIS led to heterogeneously infected epithelial cells in regards of the bacterial burden in the early infection phase. A Representative immunofluorescent-based 3D projection of STm infected hITM-SIS at 5.5h p.a. displays varying stages of cellular bacterial burden. Indicated magnifications show a *low* (i), *medium* (ii) and *high*-infected cell (iii). STm (GFP) is displayed in yellow, DNA (DAPI) in cyan and F-actin (Phalloidin) in white (n=3). **B** flow cytometry dot plot of single cells dissociated from infected hITM-SIS at 5.5h p.a.. Gates represent uninfected (GFP-, PerCP-Cy5.5-), infected (GFP+, PerCP-Cy5.5-) and goblet (GFP+, -Cy5.5+) cells. From the infected gate, the populations *low* (GFP+), *med* (GFP++) and *high* (GFP+++) were sorted and fluorescently imaged with STm (GFP) in yellow and DNA (DAPI) in cyan (bottom panel). **C** Median of intracellular STm burden per *low*, *med* and *high*-infected cells at 5.5h p.a. shows significant differences in STm burden per cell. Individual STm were counted in 9 cells for *low*, 11 cells for *med* and 10 cells for *high* (n=2). **D** Percentage of *low*, *med* and *high*-infected cells at 1.5h, 3.5h, 5.5h, 9.5h, 17.5h, and 25.5h p.a. of total infected cells. It displays a distinct distribution of *low*, *med* and *high*-infected cells at each time point and trends for increase of the *med* and *high* population overtime from17.5h p.a.. Significance was calculated by one-way ANOVA with statistically significant differences ($F(2,27) = 298.9$, $p < 0.0001$) with Tukey's test for multiple comparison for C with ****= $P \leq 0.0001$ p-Value, **= $P \leq 0.01$. Non-significant P-values are not displayed. (Däullary et al., 2022, in review). **Abbreviations**: F-actin: filamentous actin, p.a.: post application, hITM: human intestinal tissue model, SIS: small intestinal submucosa, STm: *Salmonella* Typhimurium, MOI: multiplicity of infection.

4.2.7 Variances in cellular bacterial burden are based on heterogeneous intracellular STm replication

In order to evaluate an increased bacterial proliferation within the infected IECs of the hITM-SIS as reason for the occurrence of the heterogeneous bacterial burden, a proliferation reporter STm strain (STm-rep) was used for hITM-SIS infection. This bacterial strain constitutively expresses the reporter protein mCherry and additionally allows Arabinose-inducible expression of the reporter gene GFP (Saliba et al., 2016). In the absence of Arabinose, GFP expression is therefore not induced, but is transferred to daughter bacterial cells during cellular division of STm and thus will be diluted. Accordingly, the ratio of GFP to mCherry signals indirectly indicates bacterial proliferation (Figure 23 A; Saliba et al., 2016). After hITM-SIS infection with STm-rep in absence of Arabinose, the infected cells were analysed regarding the mean fluorescence intensity (MFI) of the mCherry and the GFP signal (Figure 23 B). In detail, mCherry MFI increased by 1.98-fold and GFP MFI decreased by 0.59-fold after 25.5h p.a. in infected cells, indicating intracellular bacterial proliferation. Furthermore, the overall GFP/mCherry ratio of infected cells decreased overtime, but stayed above 0, meaning that cells still harboured GFP+ STm-rep after 25.5h.

In order to evaluate, if the decreasing GFP signal per cell derived from equal bacterial division, intracellular STm-rep were microscopically analysed for their corresponding mCherry and GFP fluorescence signals. For that, individual single infected IECs were classified as l*ow*, *med*, or *high* infected cells at 5.5h p.a. and sorted based on their mCherry expression. The intracellular STm-rep showed comparable phenotypes as depicted in Figure 22 B (Figure 23 C top). Further, STm-rep in *low* infected cells showed a high GFP intensity, whereas individual STm-rep of the *med* and *high*-infected cells displayed low or none GFP signals (Figure 23 C bottom). Therefore, indications of bacterial proliferation occurred in *med* and *high*-infected cells, but not in low infected cells.

Interestingly, the individual intracellular STm-rep populations consisted of heterogeneous populations regarding their individual GFP expression. Meaning, some STm-rep displayed none too little GFP signals, whereas other STm-rep in the same host cell displayed a high GFP signal intensity (Figure 23 C bottom). In a quantitative approach, STm-rep, derived from sorted *low*, *med* or *high*-infected cells 5.5h p.a. were analysed via flow cytometry for GFP expression and classified into GFP++, GFP+ and GFP- bacteria (Figure 23 D). STm-rep derived from the *low* population consisted of 80.50 % of GFP++ and 19.51 % of GFP+ bacteria. No GFP- bacteria were detected in the *low* population. The *med* population derived STm-rep consisted

of 59.41 % of GFP++, 34.34 % of GFP+, and 6.25 % of GFP- bacteria. Finally, the *high* population derived STm-rep consisted of 55.60 % of GFP++, 33.30 % of GFP+, and 55.60 % of GFP- bacteria. Together, these data confirmed the heterogeneous GFP expression of isolated STm-rep observed in Figure 23 C, especially in *med* and *high*-infected cells (Figure 23 D), which indicates that STm-rep populations proliferated differentially in individual single cells with higher proliferation rates in the *med* and *high* infected cell populations.

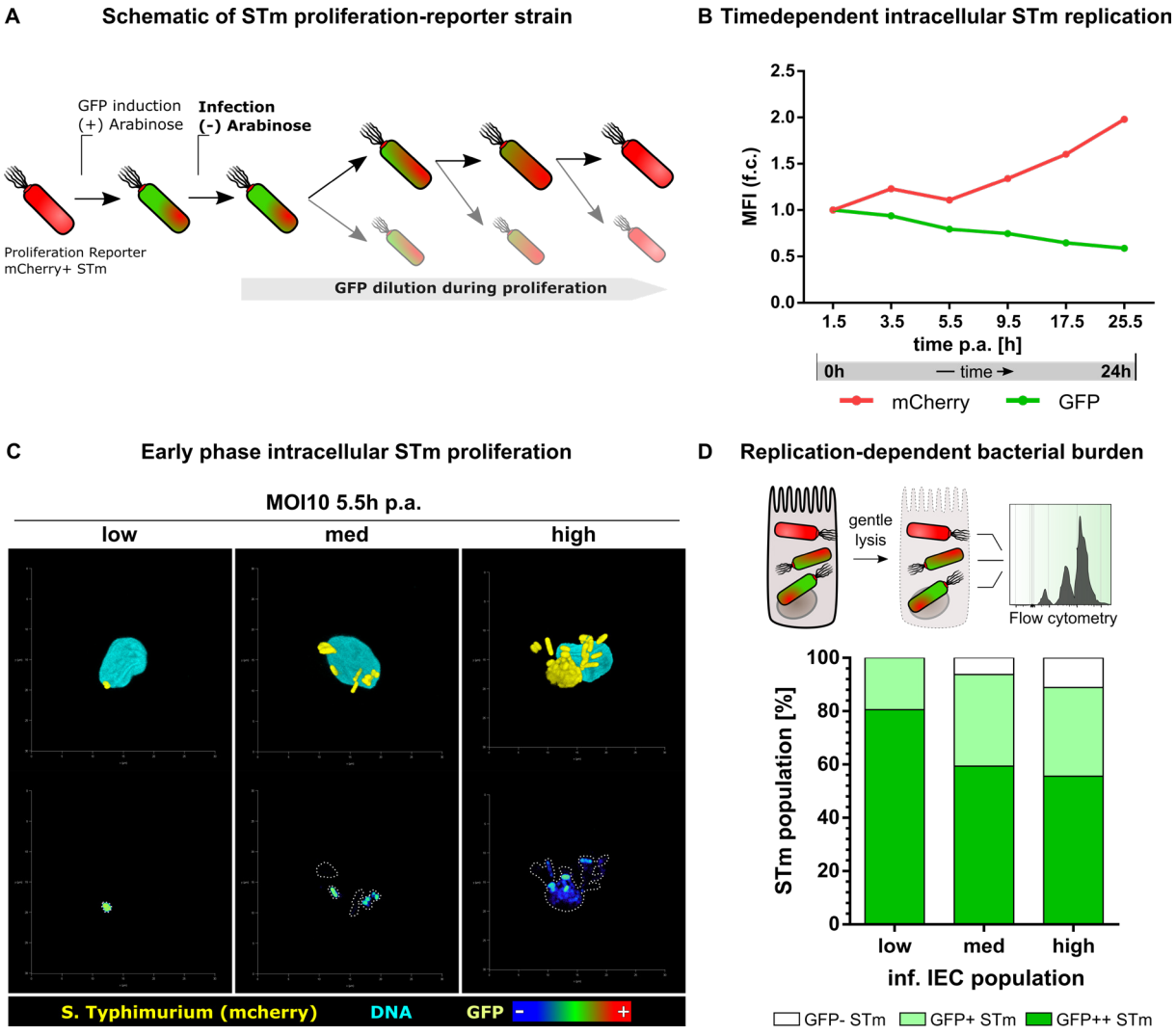

Figure 23. STm populations showed variances in intracellular proliferation in individual cells. A Schematic depiction of the STm proliferation reporter strain principle. Arabinose-dependent GFP expression is induced in constitutively mCherry expressing STm prior to infection, resulting in mCherry+/GFP+ STm. During infection, GFP expression is not induced and upon replication, GFP is divided and diluted between the daughter bacteria, resulting in reduced GFP in replicated STm. Therefore, low GFP signal indicates bacterial replication. **B** MFI of mCherry and GFP signals in infected cells at 1.5h, 3.5h, 5.5h, 9.5h, 17.5h, 25.5h p.a. showed increasing mCherry signals, while simultaneously decreasing GFP signals overtime, thereby indicating intracellular STm replication. flow cytometry data were obtained from single cells, which were dissociated from STm infected hITM-SIS. Values were normalised to 1.5h p.a. (n=1). **C** Representative 3D projection of fluorescent images of individual *low, med, high,* infected cells. Top panel displays STm (mCherry) in yellow, DNA (DAPI) in cyan and the bottom panel the GFP intensity range from blue (low) to red (high). The GFP intensity of individual STm in *low*-infected cells was high, whereas in *med* and *high*-infected cells heterogeneous populations of high and low GFP expression were observed. **D** Top: Schematic depiction of STm isolation with subsequent flow cytometry analysis. Infected cells were sorted according to

bacterial load (*low*, *med*, *high*), gently lysed and released STm were subsequently analysed. Bottom: proportional distribution of GFP-, GFP+ or GFP++ STm, which were obtained from the indicated cell population. STm derived from *low* proliferated to lower extend as seen by higher GFP intensity compared to STm derived from *med* or high, where proliferation was increased as seen by lower GFP intensities (n=1, analysed bacteria per population: *low*: 3890, *med*: 1997, *high*: 6858). Non-significant P-values are not displayed. (Däullary et al., 2022, in review). **Abbreviations**: p.a.: post application, hITM: human intestinal tissue model, SIS: small intestinal submucosa, STm: *Salmonella* Typhimurium, MFI: mean fluorescence intensity, MOI: multiplicity of infection.

4.2.8 Single-cell transcriptomic of STm infected IECs reveals infection of various cell types of the hITM-SIS

Infection of the hITM-SIS indicated a heterogeneous behaviour of STm, mainly in regards on the varying bacterial load in infected cells at distinct time points, diverse intracellular proliferation events and the differences regarding STm morphologies. Whether this heterogeneous behaviour is possibly-associated with a distinct infected cell type was investigated. By application of scRNA sequencing on infected cells with various bacterial burden, the type of the infected cell should be identified. In addition to the transcriptional definition of the cell type, the obtained data should also provide information on cellular responses to STm infection within the hITM-SIS

As shown in Figure 24 A, infected single cells were sorted as *low*, *med* or *high* cell populations based on their bacterial load (= GFP intensity) 1.5h, 3.5h, 5.5h, 8, 17.5h, and 25.5h after bacterial application to the hITM-SIS. Single cell RNA sequencing via SMARTseq was performed by Fabian Imdahl (working group of Dr. Antoine-Emmanuel Saliba, Helmholtz Institute for RNA-based Infection, Würzburg, Germany) (Figure 24 A). Per individual time point, 30 cells for *low*, 20 cells for *med* and 10 cells for *high* were analysed (Figure 24 A). Stable cell numbers were favoured for comparability and thus cell ratios do not represent the actual infection distribution. In total, 354 out of 360 cells were considered for further bioinformatical analysis and processed by Oliver Dietrich (working group of Dr. Antoine-Emmanuel Saliba, Helmholtz Institute for RNA-based Infection, Würzburg, Germany). The data set obtained thus not only provides information on transcriptional features of the infected cells, but also allows differentiation with respect to infection time and bacterial load.

As seen in Figure 24 B, unsupervised clustering of the scRNA data resulted in six populations of infected cells in the hITM-SIS defined as *'A'*, *'B'*, *'C'*, *'D'*, *'Prolif'*, and *'Low-quality'* cluster. Interestingly, cells of the *'Prolif'* cluster shown in blue were clearly separated from the other clusters. Instead, cells of the *'A'* (turquoise), *'B'* (purple), *'C'* (dark green) and *'D'* (orange) population showed a more homogeneous clustering (Figure 24 B). In addition, 'Low-

quality' cells shown in grey clustered separately; however, they were not considered for further analysis, as they represent dead or fragmented cells.

To gain insights into cellular characteristics that might underlie this clustering, the bacterial load of the infected cells was examined in more detail (Figure 24 C). As shown in Figure 22 C, the distribution of '*low'*, *'medium'*, and *'high'* infected cells appeared to be inconsistent and heterogeneous across the identified clusters. *'Low'* and *'medium'* infected cells were found in all clusters but occurred more in cluster *'A'*, *'C'* and *'D'* as well as in the *'Prolif'* cluster. *'High'* infected cells were mainly found in cluster *'B'*, indicating a specific population of cells within the hITM-SIS that were either predominantly infected by multiple STm or that provide a pro-proliferative environment for STm. Additionally, *'high'* infected cells were found in the *'Low-quality'* cluster, suggesting a possible correlation between a high bacterial load and cell quality or cellular survival after infection.

In addition to the bacterial load, the analysis time points were grouped into early (1.5h - 5.5h p.a.), middle (9.5h -17.5h p.a.) and late (25.5h p.a.) infection time points (Figure 24 D). While cells of the early analysis time points (1.5h and 3.5h after application to the hITM-SIS) are grouped in the *'A'* and *'B'* clusters, cells of the analysis time-points 5.5h and 9.5 h after application (middle infection time points) are predominantly found in cluster *'C'*. In addition to cluster *'C'*, mainly cluster *'D'* grouped cells analysed at late time points (17.5h and 25.5h after infection). The cluster *'Prolif'* contained cells from all time point, but enriched for the early infection time points.

In order to identify the types of the infected cells, a cell type specific gene expression analysis was conducted accordingly to the identified cell types in the uninfected hITM-SIS in Figure 15. Proliferative TA cells were characterized by the expression of *MKI67*, *TOP2A, NUSAP1* and *CCN2* and were predominantly assigned in the *'Prolif'* cluster. The proliferative gene markers *MKI67* and *TOP2A* were further not expressed in the cluster *'A'*, *'B'*, *'C',* '*D'* and *'Low-quality'*, thereby indicating that infected cells harbour different proliferative states or activities within the hITM-SIS. Furthermore, the *'Prolif'* cluster contained cells from all time points, indicating that throughout the whole infection phase proliferative infected cells are present and exhibit a TA profile.

Moderate to strong expression was found for *ALPI* and *RBP2* both classifying Enterocytes within the hITM-SIS. However, while *ALPI* expression was mainly found in the *'B'* and *'D'* cluster, *RBP2* was detected in all infected clusters except *'Low-quality'* cells. The gene

expression markers for Progenitor cells (*FAPB5*, *GPX2*), Secretory lineage-associated cells (*TFF1*, *RAB3B*), immune-associated M-like cells (*CCL20*, *CXCL3*, *TNFAIP2*, *LAMC2*) and HLA-G+ cells (*HLA-G*, *APOL4*) were not prominently expressed among the clusters (Figure 24 C); it indicates that these cell types were not predominantly infected in the hITM-SIS or that STm infection masks the expression of characteristic marker genes of those cellular entities.

Stem cells were identified on behalf of *LGR5* and *OLFM4* expression and were found in the *'A'* as well as in the *'Prolif'* cluster. LGR5 expressing stem cells were located only in the cluster *'A'*. This indicates that STm infected stem cells as well as that infected stem cells differ in their proliferative state/activity. Furthermore, the *LGR5* expressing infected stem cells seemed to be more abundant in the early phase of infection, as most of cells expressing *LGR5* derived from the 1.5h p.a. time point. Surprisingly, cells highly expressing *OLFM4* were further detected in the cell clusters *'C'* and *'D'*, which did not overlap with the gene expression of the canonical stem cell marker *LGR5*, thereby implying an *LGR5* independent expression of *OLFM4* in STm infected cells. Furthermore, the expression of *OLFM4* seemed to increase in cells obtained from later time points.

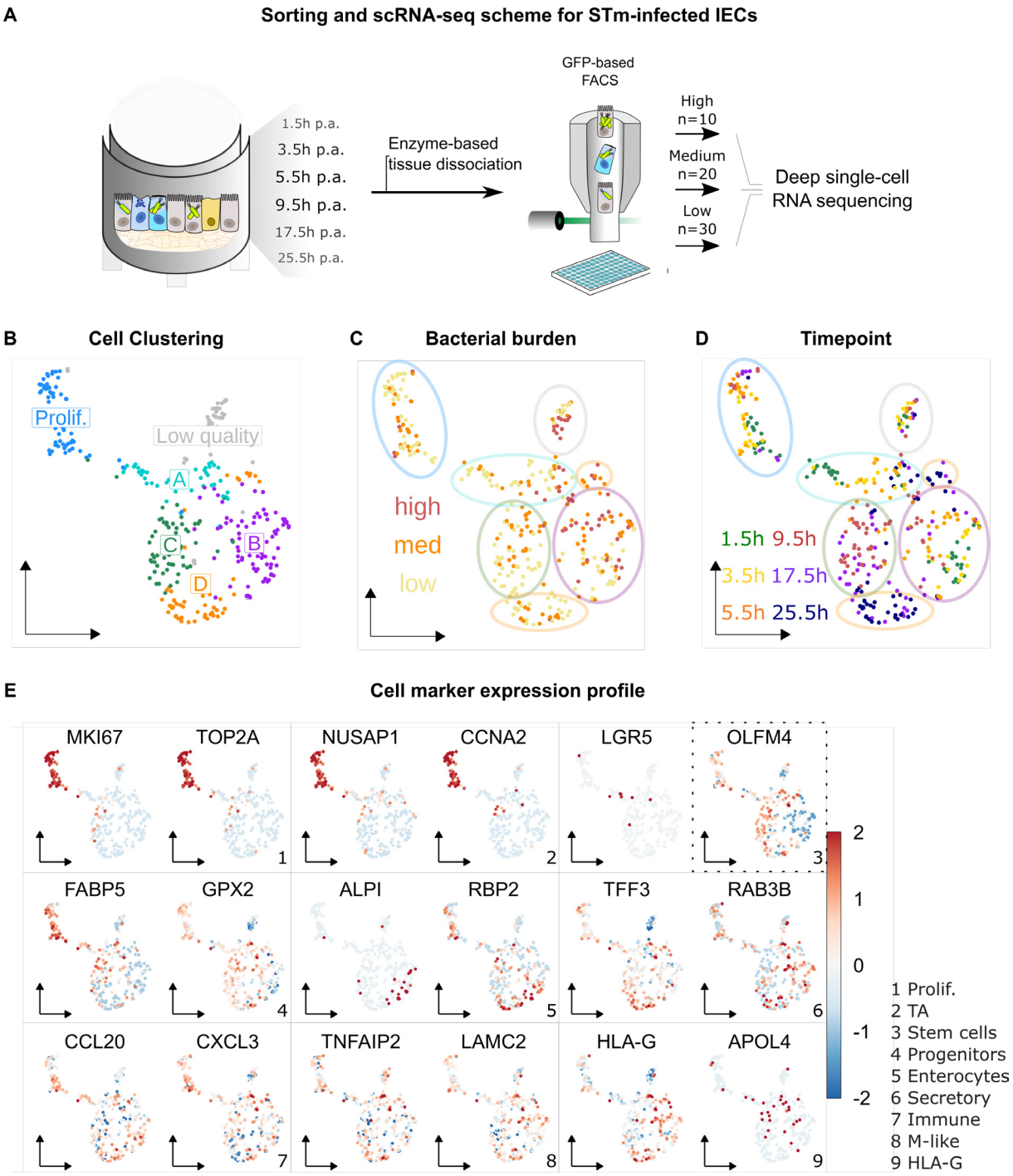

Figure 24. Single cell transcriptomic of STm-infected IECs of the hITM-SIS implied cell type independent infection tropism. A Schematic depiction of infected scRNA workflow. STm infected hITM-SIS was enzymatically dissociated into single cells at 1.5h, 3.5h, 5.5h, 9.5h, 17.5h, 25.5h p.a.. Cells were subsequently sorted according to their bacterial burden (=GFP signal: *low*, *med*, *high*). For each time point 30x *low*, 20x *med* and 10x *high* cells were collected and processed for single cell RNA sequencing. For each cell, the bacterial burden and the time point p.a. was recorded. **B** UMAP of unsupervised clustering of the infected scRNA data. Six clusters were identified and annotated: Prolif. (blue), Low quality (grey), A (turquoise), B (purple), C (dark green), D (orange). **C** UMAPs displaying clustering of B (circles indicates annotated clusters in the corresponding colours, manually encircled) with annotation of bacterial burden, revealing *low*, *med* and *high* infected cells in cluster A, B, and Low quality. Cluster Prolif, C, and D contained *low* and *med* infected cells with solitary *high* infected cells. **D** UMAP displaying clustering of B (circles indicate annotated clusters in the corresponding colours, manually encircled) with annotation for the time point of infection in h p.a.. Early (1.5h-5.5h), mid (9.5h-17.5h), and late (25.5h) infection time points clustered in cluster B, C, and D respectively. Cluster Low quality, Prolif., and A contained all time points of infection. **E** UMAPs displaying clustering of C with scaled expression of indicated cell marker genes. Gene sets defined cell types according to the gene sets used in Figure 15: 1 = Proliferating (*MKI67*, *TOPA2*), 2 = TA (*CCN2*, *NUSAP1*), 3 = stem cells (*LGR5*, *OLFM4*), 4 = Progenitor (*FABP5*, *GPX2*), 5 = Enterocytes (*ALPI*, *RP2*), 6 = Secretory-associated genes (*TFF1*, *RAB3B*), 7 = Immune-associated genes (*CCL20*, *CXCL3*), 8 = M-like (*TNFAIP2*, *LAMC1*), 9 = HLA-G (*HLA-G*, *APOL4*). Fabian Imdahl

MSc performed RNA processing for sequencing and Oliver Dietrich MSc performed bioinformatical data processing and analyses (both; Würzburg, HIRI, AG Dr. Saliba). Gene abbreviations are listed in Table 24. (Däullary et al., 2022, in review). **Abbreviations**: IEC: intestinal epithelial cell, TA: Transit amplifying cell, UMAP: Uniform Manifold Approximation and Projection, p.a.: post application, hITM: human intestinal tissue model, STm: *Salmonella* Typhimurium, MOI: multiplicity of infection.

4.2.9 Intracellular STm leads to induction of LGR5 independent OLFM4 gene expression in individual infected IECs with temporal dependence

The data obtained by single cell transcriptome analysis demonstrated high expression values for OLFM4 in infected hITM-SIS cells, which is a commonly known marker for intestinal stem cells (van der Flier et al., 2009). In detail, the expression of *OLFM4* seemed to increase in non-proliferative cells without gene expression of the canonical stem cell marker LGR5 from 1.5h to 25.5h p.a. (Figure 24 A).

In order to evaluate a STm mediated change in stem cell marker expression, the gene expression of *OLFM4* and the canonical stem cell marker *LGR5* of STm infected hITM-SIS were analysed via qPCR (Figure 25 A). *OLFM4* expression increased at 5.5h p.a. by 1.2-fold, at 9.5h p.a. by 1.9-fold, at 17.5h p.a. by 4.2-fold and at 25.5h p.a. by 2.7-fold compared to the initial time point 1.5h p.a.. On the other side, the expression of *LGR5* changed slightly at 5.5h p.a. by 1.1-fold, at 9.5h p.a. by 2-fold, at 17.5h p.a. by 1.3-fold and at 25.5h p.a. by 0.7-fold compared to 1.5h p.a.. Therefore, the expression *of OLFM4* and *LGR5* did not correlate during infection, indicating an upregulation of *OLFM4* independently of *LGR5.* Further qPCR analysis demonstrated a time-dependent and STm-related increase in *OLFM4* expression when comparing infected and uninfected models (Appendix Figure 5). In detail, the *OLFM4* expression increased in STm-infected models overtime, whereas *OLFM4* expression of uninfected models stayed on similar level.

In order to investigate the upregulation of *OLFM4* within the cells of the infected hITM-SIS, spatial gene expression analysis was applied by visualizing OLFM4-mRNA via HCR-FISH and subsequent confocal imaging. The DNA-probes for *OLFM4* detection were designed in collaboration with Tobias Krammer (working group of Dr. Antoine-Emmanuel Saliba, Helmholtz Institute for RNA-based Infection, Würzburg, Germany)

OLFM4-mRNA was observed in individual IECs in infected as well as uninfected models (Figure 25 A top) at all analysed time points, confirming the observation during scRNA and qPCR analysis. In detail, at 1.5h p.a. *OLFM4* expressing cells were rarely observed with no obvious differences between infected (MOI10) and uninfected models (mock), predominantly

identifying stem cell-like cells in both conditions. In contrast, from 9.5h to 25.5h p.a. on, the OLFM4 signal increased in the infected hITM-SIS regarding signal distribution and intensity, when compared to the initial time point and to the corresponding mock control. Further, OLFM4 expression signals seemed to overlap with GFP signals, indicating STm infected cells. In comparison, uninfected models of the corresponding time point showed expression in clustered cells with a comparable pattern to that detected at 1.5h p.a., which underlines a STm infection-related induction of *OLFM4* expression in a time-dependent manner and further a stable *OLFM4* expression in the uninfected models. The OLFM4-mRNA signal in infected cells seemed to accumulate in the individual infected cells (17.5h p.a.) and further to increase in intensity with ongoing infection time (25.5h p.a.). Additionally, the increased OLFM4-mRNA signals seemed to concentrate in areas with infected cells (Figure 25 A bottom left).

Taken together, *OLFM4* gene expression was induced in areas with STm infected IECs in a time-dependent manner, further individual infected cells seemed to accumulate OLFM4-mRNA. The uninfected hITM-SIS displayed OLFM4-mRNA signals in individual IECs as well, but expression patterns stayed stable overtime.

The OLFM4-mRNA accumulation seemed to be restricted to infected cells with 25.5h p.a. (Figure 25 B), whereas bystanding or neighbouring cells seemed to show no or only less signals for OLFM4-mRNA. Indeed, HCR-FISH combined with flow cytometry (FISH-Flow) for OLFM4-mRNA in infected (MOI10 infected) versus bystander (MOI10 bystander) IECs verified this observation and further demonstrated the OLFM4 gene induction in single infected IECs overtime (Figure 25 C, detailed values in Table 27). In the infected IECs population, the percentage of *OLFM4* expressing (OLFM4-mRNA+) cells increased from 2.28 % (± 0.45 %) at 1.5h p.a. to 31.50 % (± 8.01 %) at 24 h p.a.. In contrast, the percentage of OLFM4-mRNA+ bystander IECs stayed low, with only a minor increase from 2.08 % (± 1.32 %) at 1.5h p.a. to 3.42 % (± 0.53 %) at 24 h p.a., which were comparable with the percentage of OLFM4-mRNA+ uninfected IECs (mock, 1.32 % (± 0.30 %) at 1.5h p.a. and 3.44 % (± 1.00 %) at 24 h p.a.). OLFM4-mRNA+ IECs were significantly increased at 17.5h p.a. and 25.5h p.a. in the infected population in comparison with the bystander and mock populations. These observations indicate a restriction of the OLFM4 gene induction to a subpopulation of STm infected IECs.

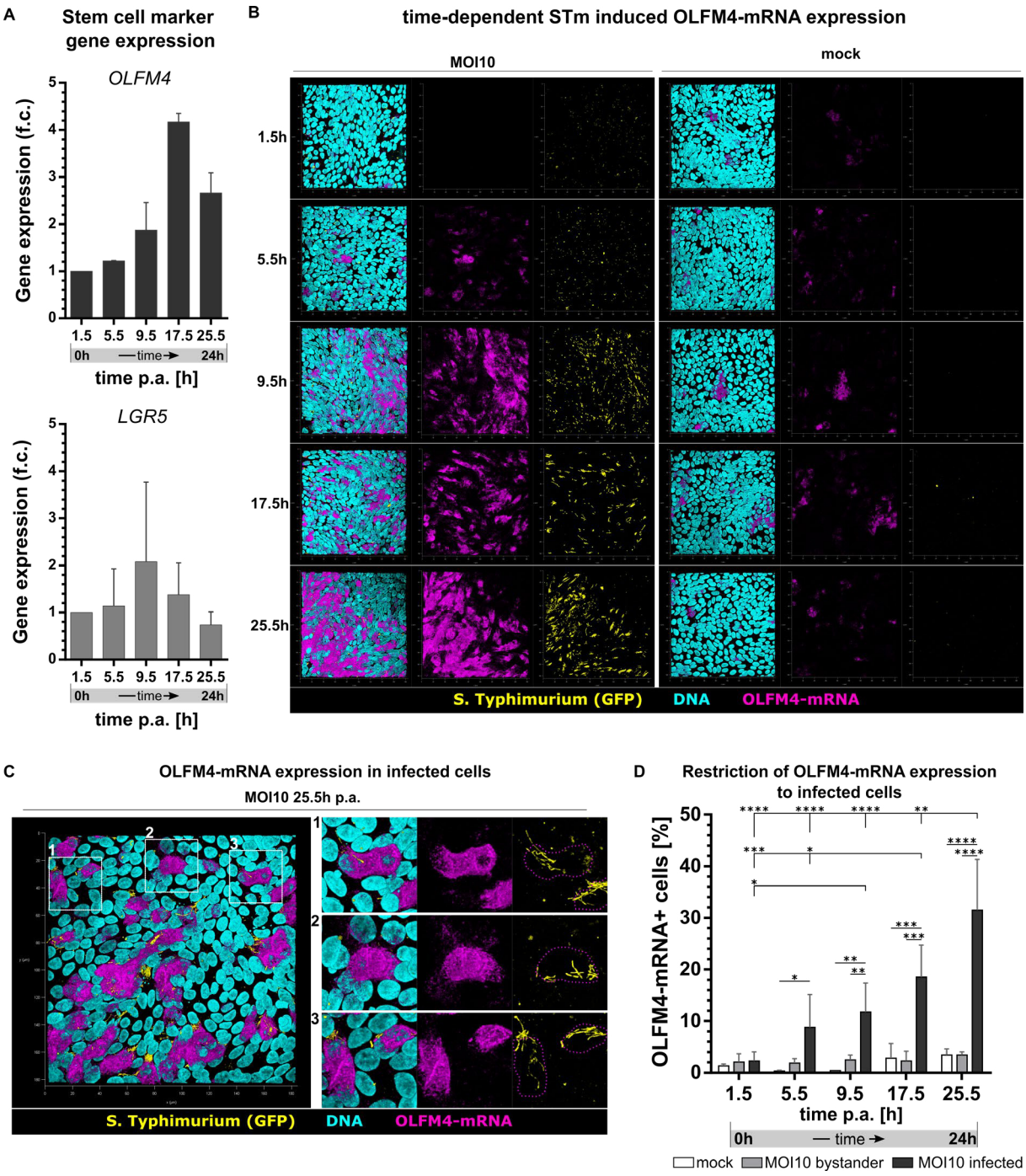

Figure 25. STm infection induced OLFM4 expression in individual cells in time-dependent manner. A Gene expression of stem cell marker genes *OLFM4* and *LGR5* of MOI10 infected hITM-SIS after 1.5h, 5.5h, 9.5h, 17.5h, 25.5h p.a. Values were normalised to 1.5h p.a. (n=2). **B** Top view on 3D projection of representative fluorescent images of STm infected hITM-SIS(MOI10, left) and uninfected hITM-SIS(mock, right) after 1.5h, 5.5h, 9.5h, 17.5h, 25.5h p.a. with STm (GFP) in yellow and DNA (DAPI) in cyan and OLFM4mRNA in magenta. OLFM4mRNA increases overtime after 5.5h p.a. in epithelial cells during STm infection in contrast to mock (n=3). OLFM4 was visualised with HCR-FISH. **B** Top view on 3D projection of representative fluorescent images of STm infected hITM-SIS(MOI10) at 25.5h p.a. Indicated magnification (1, 2, 3) show representative areas with restriction of increased OLFM4mRNA to infected cells and SIF formation (n=3). **C** Proportion of OLFM4mRNA+ cells of mock, non-infected bystander (MOI10 bystander) or infected cells (MOI10 infected) at 1.5h, 5.5h, 9.5h, 17.5h, 25.5h p.a. reveals restriction of OLFM4mRNA expression to infected cells (n=3). Significance was calculated via matching two-way ANOVA with statistically significant differences (Row F (4, 8) = 10.35, p = 0.0030; Column F (2, 4) =72.23, p = 0.0007) and Tukey's multiple comparisons test for C with ****= P ≤ 0.0001, ***= P ≤ 0.001, **= P ≤ 0.01, *= P ≤ 0.05. Non-significant P-values are not displayed. (Däullary et al., 2022, in review). **Abbreviations**: p.a.: post application, hITM: human intestinal tissue model, STm: *Salmonella* Typhimurium, MOI: multiplicity of infection, OLFM4: Olfactomedin 4, LGR5: Leucine-rich repeat-containing G-protein coupled receptor 5.

4.2.10 Upregulation of OLFM4 in STm infected hITM-SIS is not mediated by NFκB–pathway signalling

OLFM4 gene expression is known to be regulated by the NFκB–pathway (Chin et al., 2008). In general, upon activation of NFκB signalling cascade, the NFκB–p65 is transported into the nucleus, where it initiates transcriptionally the downstream target of the NFκB pathway (Figure 26 A). In order to elucidate STm-mediated NFκB-pathway activation, the nuclear accumulation of NFκB–p65 in perspective of the infection time point was microscopically assessed (Figure 26 B). In general, NFκB–p65 was observed mainly in the cytoplasm of cells regardless of STm infection and time. However, at 1.5h p.a. NFκB–p65 positive nuclei were identified in STm-infected models, but were absent in uninfected models (Figure 26 A left). At later time points, nuclear NFκB–p65 accumulation could not be observed (Figure 26 A right). Furthermore, the ratio of NFκB–p65 positive nuclei to NFκB–p65 negative nuclei was determined and revealed a 50-fold increase in infected models compared to the uninfected at 1.5h p.a. (Figure 26 C). After 5.5h p.a. on, the ratio was comparable small between infected and uninfected models at the corresponding time points. This indicates an early STm-mediated NFκB activation with subsequent restoration of the initial status after 5.5h.

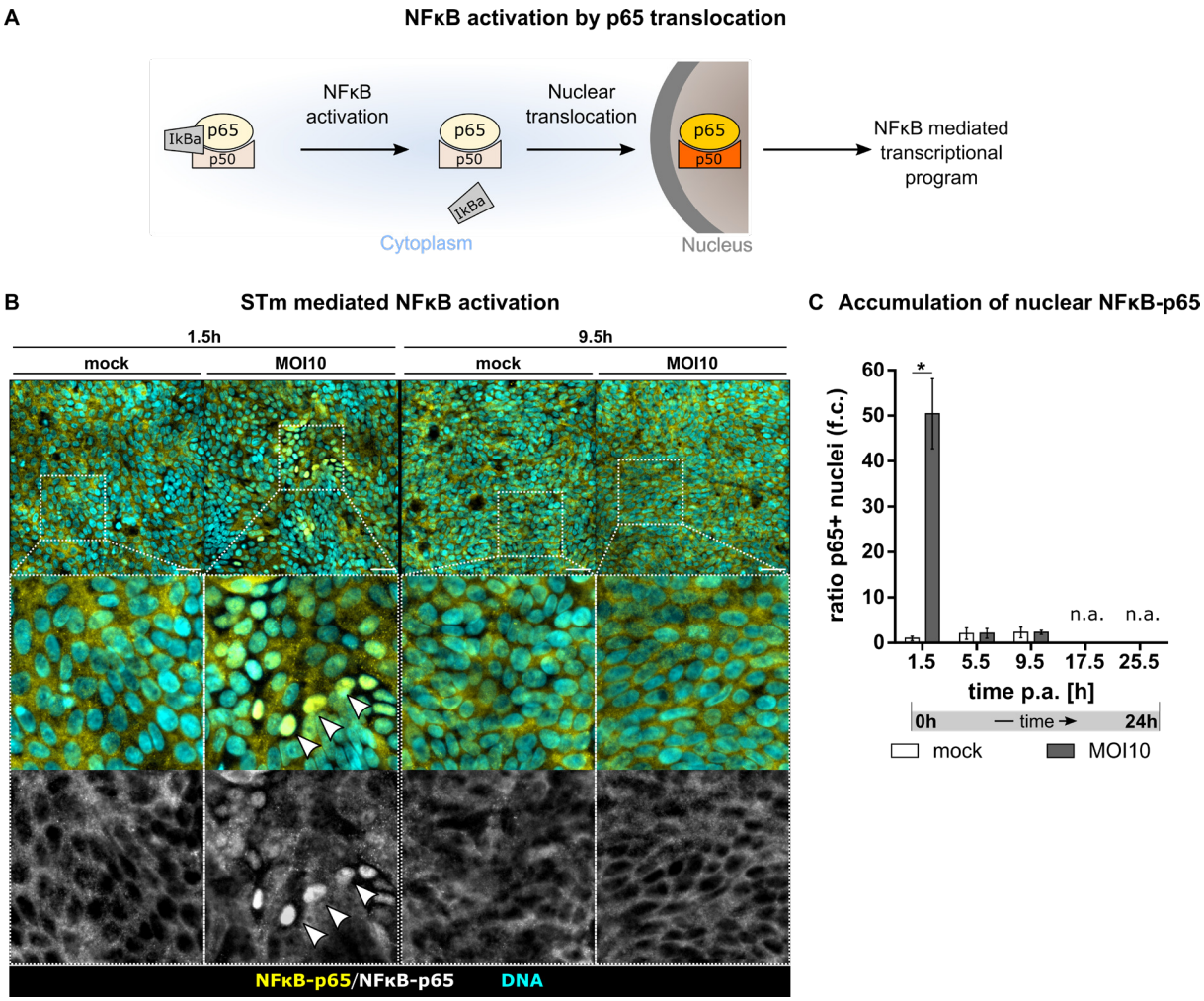

Figure 26. STm infection led to nuclear accumulation of NFκB-p65 in the initial phase of infection, which is reversed after 5.5h. A Schematic and simplified depiction of the NFκB-pathway activation. Activation leads to dissociation of IkBa from the p65-p50 in the cytoplasm with subsequent translocation of p65-p50 to the nucleus and thus transcriptional activation of downstream genes of the NFκB program. **B** Representative z-projection of immunofluorescent images of STm infected hITM-SIS(MOI10) and uninfected (mock) at 1.5h and 9.5h p.a. with NFκB-p65 in yellow or white and DNA (DAPI) in cyan. Enlargements of indicated areas show NFκB-p65 localisation in the cytoplasm in mock (1.5h and 9.5h) and in MOI10 (9.5h), but nuclear NFκB-p65 at MOI10 (1.5h) (n=2). **C** Ratio of NFκB-p65+ nuclei to NFκB-p65- nuclei normalized to mock 1.5h shows NFκB activation only in MOI10 at 1.5h p.a. (n=2).Significance was calculated by unpaired t-test between samples within the same time point for C with *= $P \leq 0.1$. Non-significant P-values are not displayed. SB = 50 µm. **Abbreviations**: p.a.: post application, hITM: human intestinal tissue model, STm: *Salmonella* Typhimurium, MOI: multiplicity of infection.

4.2.11 STm induced OLFM4 gene expression is reduced by Notch pathway inhibition.

OLFM4 expression can be regulated among others via the Delta-Notch-pathway (Kuno et al., 2021). In order to evaluate a Notch-mediated OLFM4 regulation during STm infection, the Notch pathway was inhibited by application of DAPT, a γ-secretase inhibitor (Feng et al., 2019), and subsequent microscopically analysis of the OLFM4-mRNA via HCR-FISH was applied (Figure 27 A).

In general, OLFM4-mRNA was detected in individual IECs of the hITM-SIS under infectious (MOI10), infectious + DAPT (MOI10+DAPT) and under uninfected conditions (mock) (Figure 27 A). At the early time point 1.5h p.a., the OLFM4-mRNA expression pattern did not differ between the specific conditions, thereby excluding an early effect of Notch inhibition on baseline OLFM4-mRNA expression and underlining the applicability of the assay. From 5.5h p.a. on, individual cells in MOI10 and MOI10+DAPT models displayed higher signals for cytoplasmic OLFM4-mRNA and a more defined pattern in comparison to mock OLFM4-mRNA+ cells. At 17h p.a. and at 25.5h p.a., the number cells expressing *OLFM4* as well as the OLFM4-mRNA signal intensity seemed to be increased in MOI10 models compared to MOI10+DAPT and the mock control, indicating a dampening effect of the DAPT treatment on OLFM4 transcription under infectious conditions. However, MOI10+DAPT models showed a similar pattern as MOI10 models in regards of the cellular localisation of the OLFM4-mRNA: sharp restriction to individual cells, whereas the signal in mock control seemed more diffuse. Taken together, DAPT treatment (=Notch inhibition) led to a decreased OLFM4-mRNA expression during STm infection, but with comparable spatial OLFM4 expression patterns.

The OLFM4-mRNA signal intensity was further quantified by automated image analysis and subsequent normalization to the number of nuclei, thereby giving a valid estimation of the OLFM4 signal intensity per cell in the field of view. The intensity of OLFM4 per nucleus increased up to 5.6-fold at 25.5h p.a. in MOI10 infected models compared to mock at 1.5h p.i, whereas in infected and DAPT treated as well as mock models the intensity increased up to 2.9-fold or 2.6-fold, respectively (Figure 27 B). Notch inhibition by DAPT led to a reduction of STm induced OLFM4-mRNA expression to similar ranges of the mock control, verifying a Notch-associated OLFM4 expression in STm infection. Similarly to *OLFM4*-mRNA levels the expression of OLFM4 was also reduced upon DAPT treatment on protein level, as revealed by IHC for OLFM4 (Figure 27 C). Furthermore, the bacterial morphology was influenced under DAPT treatment; in MOI10+DAPT models the formation of filamentous STm seemed to be reduced, when compared to the MOI10 models.

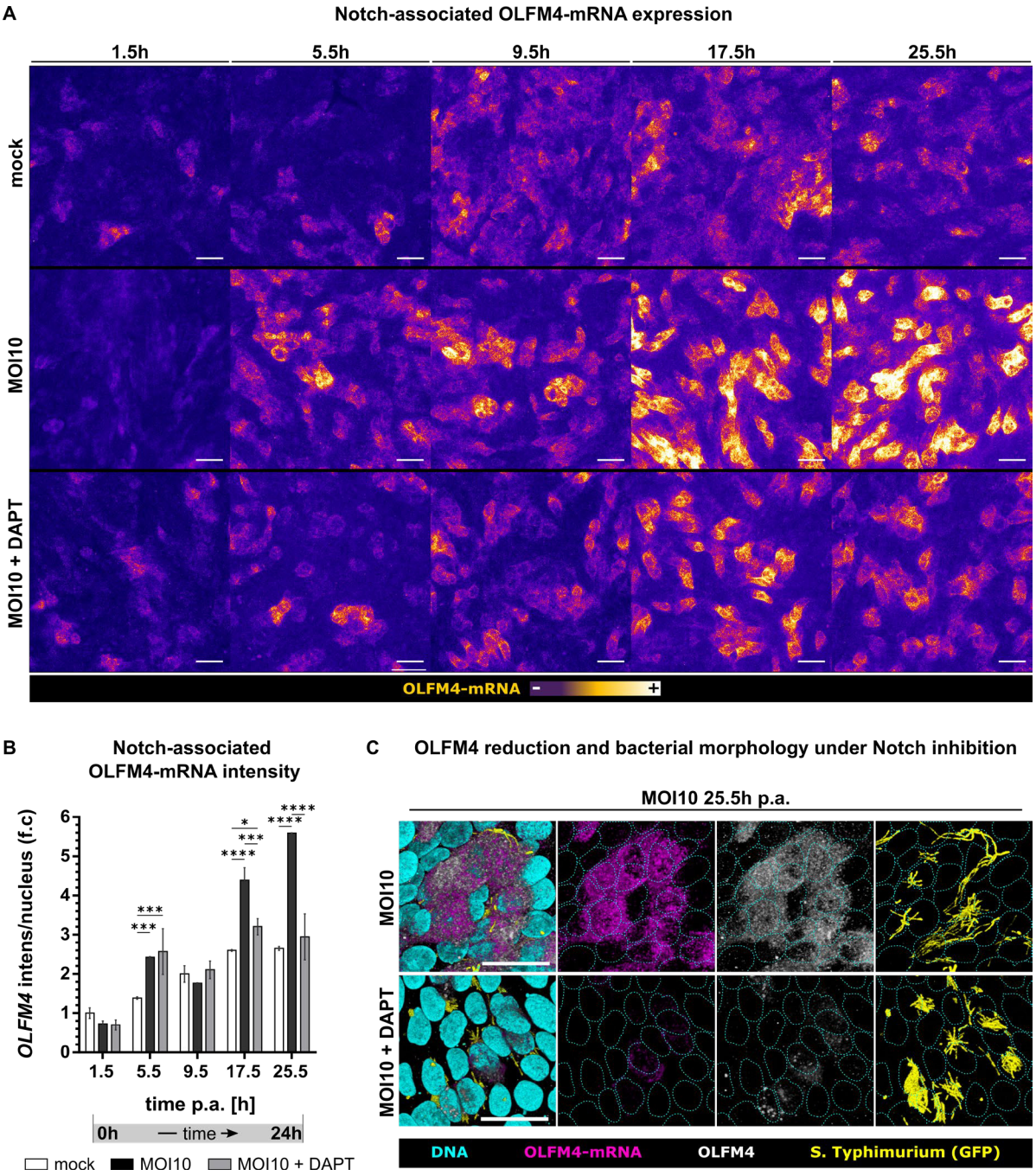

Figure 27. STm mediated OLFM4 expression is reduced and filamentous STm morphology is affected by Notch-pathway inhibition. A Representative fluorescent images of uninfected (mock), STm infected (MOI10) and STm infected with γ-Secretase-inhibitor treatment (MOI10+DAPT) at 1.5h, 5.5h, 9.5h, 17.5h, 25.5h p.a.. OLFM4mRNA was detected with HCR-FISH and visualised as intensity range in maximum projection images. OLFM4mRNA intensity increases in individual cells in MOI10 overtime but stagnate in MOI10+DAPT. (n=2). **B** OLFM4mRNA intensity per nucleus normalized to mock 1.5h p.a. reveals increase of OLFM4mRNA in MOI10 and similar levels in MOI+DAPT and mock (n=2). **C** 3D projection of representative fluorescent images of MOI10 and MOI10+DAPT at 25.5h p.a. with STm (GFP) in yellow, DNA (DAPI) in cyan, OLFM4 (Protein) in grey and OLFM4-mRNA (HCR-FISH) in magenta. Significance was calculated comparing the conditions within each time point via ordinary two-way ANOVA with statistically significant differences ($F(8,20) = 26.78$, $p < 0.0001$) and Tukey's multiple comparisons test for C with ****= $P \leq 0.0001$, ***= $P \leq 0.001$, **= $P \leq 0.01$, *= $P \leq 0.05$. Non-significant P-values are not displayed. A: SB = 20 µm, C: SB = 10 µm. (Däullary et al., 2022, in review). **Abbreviations**: p.a.: post application, hITM: human intestinal tissue model, STm: *Salmonella* Typhimurium, MOI: multiplicity of infection.

5 Discussion

5.1 Mimicking the intestinal epithelium *in vitro* – biological vs. synthetic membranes

In the recent years, fundamental breakthroughs in human gut biology research were achieved by using primary cell based model systems. With the identification of the LGR5 ISCs as well as with the protocols for their isolation and the *in vitro* cultivation as organoids, Sato et al. facilitated massive progress in the research field of human intestinal physiology and development (Sato et al., 2009). However, although being a revolutionizing methodology, organoid technology comes with distinct drawbacks. Among them is the accessibility of the luminal compartment, which is needed in order to properly investigate apical-basolateral polarised mechanisms or interactions; this includes directed cellular transport mechanisms and interactions between the epithelial cells and the various luminal content, such as nutrients, commensal bacteria of the microbiome or infectious enteric pathogens. Therefore, several methods have been developed to overcome these limitations of the organoid technology, such as by inverting the intestinal organoid polarisation or growing organoids as 2D monolayers (Co et al., 2019; Moon et al., 2014). Regarding the organoid-derived monolayers, IECs were typically applied on synthetic scaffolds – such as PET membranes – that require additional coating with ECM-like proteins to allow proper cell attachment and subsequent growth.

Next to synthetic scaffolds, biological scaffolds derived from e.g. decellularised tissue, such as the SIS, showed to be valuable carrier structures for organoid-derived cells; they provide important features of the *in vivo* microniche in an *in vitro* system with potential transplantation applications (Meran et al., 2020; Padhi and Nain, 2020; Schweinlin et al., 2016). In this context, Schweinlin et al. developed an intestinal tissue model based on ASC-derived organoids, stromal fibroblasts and the bioscaffold SIS combined with a dynamic luminal flow (Schweinlin et al., 2016); similarly to a Caco2 approach of Pusch et al (Pusch et al., 2011). The epithelial cells in the study of Schweinlin et al. developed the relevant cell types of the small intestine and showed increased barrier functionality when compared to static cultures. Insights of this work helped in the current study that focused on the epithelial component in a simplified setup.

The synthetic and the biological scaffold variants have their own benefits, but a comprehensive comparison in regards of their capability to recapitulate the biological features of the original tissue is missing. This is, however, an important aspect, which must be considered for the application of scaffold- and organoid-based monolayer models in infectious disease research.

Here, the relevance of an *in vitro* system is important for the translatability to the clinical situation and for receiving more reliable therapeutic predictions. In this context, the first part of the present study provides an in-depth comparison of an organoid-derived *in vitro* tissue model of the human small intestinal epithelium that was established either on the synthetic PET membrane (hITM-PET) or the biological SIS scaffold (hITM-SIS). As structure often determines function in biology (Abbot, 1916), the focus was on the cellular morphology, morphometry and barrier features of the IEC monolayer formed in both *in vitro* tissue models.

5.1.1 ECM-mediated cues of the biological SIS scaffold favour the formation of *in vivo*-like cellular characteristics in the hITM-SIS

In the native tissue, IECs of the SI display a highly polarized cell morphology with reported cell heights of ~37 µm (Crowe and Marsh, 1993). The epithelial cell polarization and height are therefore an important feature of a tissue model that mimics the small intestinal epithelium *in vitro*. Both parameters represent important indicators to allow a statement about the quality of cell development and functionality, especially, since defects regarding cellular polarity can significantly influence the quality of the model, such as the reliability of transport studies. In this context, the results obtained in this study showed that IECs grown on the SIS exhibited a cell height with similar values (approximately 40 µm) as the native tissue, whereas IECs cultured on the PET showed a 2.3-fold decreased cell height. In addition, the distance between the nucleus and the apical surface membrane was increased in the cells of the hITM-SIS. An important indicator for cell polarisation is the nucleus position. For instance in columnar polarised epithelial cells the nucleus is located in the basolateral region of the cell (Gundersen and Worman, 2013). Consequently, the relative position of the nucleus can give an estimation of the polarisation status of intestinal columnar epithelial cells: the closer the nucleus is to basolateral site or the further away from the apical side, the greater the polarisation status. With the following formula, the relative nucleus position can be determined:

$$[1] \qquad P_{r(nucleus)} = \frac{D_{(apical)}}{H_{(cell)}}$$

where $P_{r(nucleus)}$ is the relative position of the nucleus, D_{apical} is the distance of the nucleus from the apical surface, and H_{cell} is the height of the cell. If the nucleus is at the basolateral site of the cell then $P_{r(nucleus)} = 1$, if it is at the apical side then $P_{r(nucleus)} = 0$. Hence, the higher the number of the $P_{r(nucleus)}$, the closer is the nucleus to the basolateral site and the higher is the cell

polarisation status. When applying this formula [1] to the mean values for D_{apical} and H_{cell} hITM-SIS and hITM-PET, then $P_{r(nucleus)}$ is 0.44 for IECs of the hITM-SIS and 0.28 for IECs of the hITM-PET (for detailed values and calculation see Table 28). Therefore, the polarisation status of cells from the hITM-SIS is increased compared to the cells of the hITM-PET. Considering the importance of the ECM for tissue homeostasis, it is likely that the *in vivo*-like cell height and polarisation of IECs are driven by the biological scaffold and that extracellular cues mediated by the ECM-like scaffold drive these features.

Two major differences between the SIS and PET-based models regarding ECM features are the protein composition (native basal lamina composition of the SIS vs Matrigel® coating of the PET) and the stiffness/elasticity module of the two matrix. From a functional point of view, the preserved basal lamina of the SIS is equivalent to the Matrigel® coating on the PET membranes: both function as adhesion site for the IECs and thus influence cellular behaviour and development. The SIS basal lamina and the PET Matrigel® coating consist mainly of laminins, collagen IV, and entactin, which form a stable network, thereby enabling cellular adhesion (Arends and Lieleg, 2016; Hughes et al., 2010). Matrigel®; however, contains further factors, which that are connected to a broad range of functions (Hughes et al., 2010),and which might influence cell growth and behaviour. These proteins seem to be rather unlikely as critical factors for cell polarisation, as these would need to be stable over the culture period of up to 11 days.

What features might favour cell polarisation on the SIS? Recent studies emphasized the role of biomechanical cues mediated by the ECM (Berger et al., 2020; Gjorevski et al., 2022; Pérez-González et al., 2021), which can be transmitted via the cell skeleton in individual cells, thereby regulating cell morphology, differentiation and identity. For example, Gjorevski et al. showed in 2022 - with the help of intestinal organoids - that the geometrical shape of the intestinal crypt drives cell lineage differentiation into Paneth cells and subsequently the de novo formation of the stem cell niche (Gjorevski et al., 2022). Therefore, the varying stiffness/elasticity module of the underlying scaffold is likely to drive cell polarisation with softer material leading to greater cell polarity. In order to evaluate that finding, further investigation into the stiffness and elasticity of the SIS would be necessary. By that, the stiffness of the SIS could be mimicked on a PET membrane via adjustable hydrogels and the cell polarisation status could be re-evaluated.

Next to biophysical cues of the native ECM, JAM proteins expressed by tissue-specific cells are important factors in the regulation and development of cell polarity and polarisation. First, they recruit the Par3-aPKC-Par6 polarity protein complex and secondly they stabilise the built

complex by interaction with occludin and distinct claudins (Chen and Zhang, 2013). The increased expression of JAM-1 and JAM-3 observed in the hITM-SIS compared to the PET-based models suggests that the biological matrix supports the induction and maintenance of JAM proteins to a higher degree than the PET matrix. Therefore, the cells of the SIS-based models might have greater potential for the recruitment of the Par3-aPKC-Par6 polarity protein complex and associated downstream activities. In addition, cell polarity is thought to be established and maintained by cell-cell adhesion (CCA), mediated for instance by the JAM proteins and E-cadherin, as well as by cell-matrix anchoring (CMA), especially between integrins and the laminin/collagen networks (Burute and Thery, 2012; Chen and Zhang, 2013). In this context, Tseng et al. discovered the regulation of cell-cell junction (CCJ) by ECM-mediated intra- and extra-cellular forces, which indicates that the matrix biophysical properties contribute to the epithelial intercellular junction (EIJ) formation and thus to cell polarity and polarisation (Tseng et al., 2012).

The basal lamina plays an important role during polarisation, especially the correct orientation of the laminin and collagen fibres. This network is a stable and coordinated protein structure consisting mainly of laminin, collagen, entactin, perlecan complex in a certain orientation and is generated and modulated by epithelial cells (Arends and Lieleg, 2016; Padhi and Nain, 2020). According to Matlin et al. cells bind to the existing ECM network, which activates laminin secretion and further extracellular laminin accumulation. Due to the increased number of laminin the spatial orientation changes between the individual proteins, which leads to increased CMA by laminin/integrin interaction, thus favouring the cell polarisation by the PAR complexes and cytoskeleton remodelling (Matlin et al., 2017). In the current study, the physiological orientation of basal lamina of the bioscaffold could be better suitable for cell polarisation compared to the artificial network of Matrigel© ECM on the hITM-PET. In that regards, Berger et al demonstrated an intact basal lamina after decellularisation for the SIS scaffold, whereas the Matrigel© fibre networks seems rather irregular and chaotic (Aisenbrey and Murphy, 2020; Berger et al., 2020).

Mechanotransduction describes the processes that allow cells to convert biophysical information perceived by extracellular forces into a biological response; this includes cell fate determinations as well as migration behaviour. For example, Berger et al showed in 2020 that an organ-specific, biological ECM impacts the multi-lineage differentiation behavior of human iPSC cells (Berger et al., 2020) and Barriga et al proved in 2018 that tissue stiffening in *Xenopus laevis* triggers collective cell migration (Barriga et al., 2018; Berger et al., 2020). The integrin

superfamily are known to play a major role in the mechanotransduction of biophysical cues via a complex network of interaction partners from the extracellular domain of integrin to the F-actin-cytoskeleton via Talin and Tensins (Kechagia et al., 2019). By “pulling” forces on the individual integrins by the ECM and the intracellular F-actin filaments, the ECM properties are translated into intracellular signalling cascades (Oria et al., 2017; Swaminathan et al., 2017). Furthermore, the F-actin skeleton is among others connected to the EIJ and JAMs of epithelial cells, potentially transmitting forces directly to cell-cell connecting protein complexes. Conversely, JAM-1 was shown to modulate cell morphology by β1-integrin and RAP-1 activity (Mandell et al., 2005), which further indicates a direct connection between the ECM, integrins, F-actin, JAM-1 and cell polarity.

Taken together, when comparing the results of the present study to published data, it shows that the biological scaffold SIS drives cellular features to an *in vivo*-like phenotype regarding cellular morphology and morphometry; biophysical ECM properties are likely to contribute to this. In this context, signal transduction of the ECM mechanical stiffness or elasticity via integrin-cytoskeleton-IEJ connection contribute to the polarisation of cells. Similar observations were made by Lee et al. in 2021 in a cell-ECM contact approach with fibroblasts demonstrating that polarisation is mediated via cytoskeletal connections of the nucleus and extracellular laminins (Lee et al., 2021).

5.1.2 Transmembrane mucin expression and glycocalyx development might depend on ECM-cues

An important aspect of the small intestinal mucosa is the mucus expression and production. The intestinal mucus acts primarily as defensive barrier against exogenous reagents by physical separation, antimicrobial function and lubrication and contains of various mucins (Grondin et al., 2020; Hansson, 2012). It consists of the secreted, gel-forming mucus layer (mostly consisting of MUC2) and the transmembrane mucus layer (composed of MUC1, MUC3, MUC4, MUC12, MUC13, and MUC17) which contributes to the intestinal glycocalyx (Sun et al., 2020). In the present study, IECs grown on the SIS scaffold showed apical enrichment of glycosylated structures and MUC1 expression, thereby suggesting glycocalyx formation on the SIS, in contrast to PET based models. Microarray analysis of the glycocalyx-associated mucins confirmed these finding by demonstrating a lower gene expression value in IECs cultured on the synthetic scaffold. Therefore, glycocalyx formation seems to be impaired by the synthetic scaffold, which could be an indicator for incomplete cell differentiation or misregulation of

mucins gene expression. Further, the mucin layer could be an initial feature of the organoid derived IECs, which is maintained by the cells when grown on the SIS and lost when cultured on the PET membrane. Very little is known about transmembrane mucin regulation, but the present study provides first insights that the ECM contributes to formation or maintenance of the intestinal glycocalyx.

Interestingly, the expression of mucin 2 (MUC2), the major secreted mucin in the SI, which forms an adherent mucus layer on the epithelial surface, could not be detected in the Microarray analysis. However, hITM-SIS showed MUC2 protein expression in individual cells. This discrepancy indicates that MUC2 gene expression was too low for detection via the Microarray analysis, therefore deeper investigations in MUC2 expression using qPCR and Goblet cell differentiation by Immunofluorescence is required. Further, as seen by the scRNA analysis, cells expressing secretory lineage-associated genes missed *MUC2* expression as well. Overall, MUC2+ cells seem to be rarely distributed in the SIS based system, which might be due to applied cell culture conditions used for model set up, as high Wnt3A condition favours absorptive lineage differentiation (Pleguezuelos-manzano et al., 2020).

5.1.3 The bioscaffold SIS supports the formation of *in-vivo* like epithelial barrier formation.

The IE represents a tight barrier against the luminal content, but simultaneously provides the selective transport of nutrients and antigen representation to the immune system (Allaire et al., 2018; Greenwood-Van Meerveld et al., 2017). The barrier function is mainly mediated by the establishment of the tissue-specific epithelial junction complexes (JC) including tight junctions (TJ), adherens junctions (AJ) and desmosomes that are formed between individual cells (Van Itallie and Anderson, 2014). The JCs consist in general of extracellular protein-domains that are interlinked between cells and anchored intracellularly at the cytoskeleton; they usually consist of several distinct proteins (Fanning et al., 2012; Van Itallie and Anderson, 2014). By examining JC-associated protein and gene expression patterns, this study investigated the barrier integrity of hITM-SIS models compared with hITM-PET.

The TJ-complex establishes a tight connection between cells in their apical region and consists among others of the proteins ZO-1 and OCLN (Citi, 2019). The protein expression pattern of ZO-1 and OCLN was comparable between SIS- or PET-based models: signals for ZO-1 and OCLN detected by IHC could be localised in the apical region between individual cells. Further,

representative microscope pictures demonstrated a typical honey-comb-like protein expression pattern observed in polarised cell-layers, which was recently reported as characteristic for ZO-1 and OCLN in the IE (Fanning et al., 2012). On the gene expression level, however, *ZO-1* was increased in cells cultured on the SIS scaffold compared to cells grown on the PET-membrane. Besides *ZO-1,* other TJ-associated genes, such as representatives of the claudin superfamily (e.g. *CLDN4, CLDN7, CLDN12*), were upregulated in cells of the hITM-SIS, which indicates a possible regulatory role of the biological ECM variant. These observations are in line with a study of Haas et al. in 2020, which proved evidence for a link between the stiffness of the ECM scaffold and the ZO-1 TJ assembly; softer matrices thereby lead to differential positioning of JAM-1 within the cellular cytoskeleton, induced by mechanical forces of the ECM, and therefore stabilize TJ assembly.

Interestingly, although the gene expression of JC-associated proteins was increased, the barrier integrity and functionality were decreased in hITM-SIS models in comparison to the hITM-PET. The TEER value, as a measure of the barrier integrity, was lower for the hITM-SIS, but simultaneously in the physiological range of ~50 $\Omega*cm^2$ (Srinivasan et al., 2015). The TEER value of the hITM-PET on the other hand exceeded the physiological range by eight-fold. In general, the transepithelial electrical resistance is an indirect measure of the intercellular connection, mainly the JC, as the electric current flows through the paracellular route (Elbrecht et al., 2016). In short: the tighter the cell-cell contacts, the higher is the TEER value. However, the value is also influenced by additional parameters: the cell height (Chen et al., 2015) and the junctional length (Felix et al., 2021). The cell height, as a measure of polarisation, has been shown to be negatively correlated with the TEER value, meaning a higher polarisation degree implies lower TEER value (Chen et al., 2015). A potential explanation is a higher relative number of intercellular clefts per area in highly polarised layers compared in unpolarised layers. Hence, the electric current can transpass the epithelial barrier of the hITM-SIS more easily due to higher polarisation degree and the resulting increased number of clefts, which ultimately results in lower resistance.

A similar phenomenon could underlie the increased permeability observed for the hITM-SIS, as the FITC-dextran paracellular diffusion rate was higher for the hITM-SIS in comparison to the hITM-PET. Although with a low diffusion rate, the accumulative number of particles due to the increased number of clefts can lead to a higher final percentile diffusion in a given time.

Conclusively, TJ proteins seem to be expressed to a higher degree in IECs of the hITM-SIS compared to hITM-PET models, suggesting a more pronounced establishment of cell-cell

contacts. In regards of the epithelial barrier, the hITM-SIS displays a lower electrical resistance, but resembles the native characteristic, and shows a tight barrier against paracellular diffusion of small particles.

Taken together, an organ-specific biological scaffold favours the growth and development of IECs in comparison to the synthetic PET scaffold.

5.1.4 IECs of the hITM-SIS display characteristic protein expression profiles and ultrastructural features

Regarding cellular characteristics, the epithelial character of cells grown on the SIS was underlined by the expression of ECAD and pCK, two canonical epithelial proteins (Rajkovic et al., 2018; Xiao et al., 2015). The intestinal phenotype was further validated by the expression of key markers including the transmembrane located MUC1 and VIL1 that are expressed on the apical surface of intestinal epithelial cells (Khurana and George, 2008; Revenu et al., 2012). They play also important roles in the context of *Salmonella* infection: MUC1 is required for the STm-specific adhesion via SiiE (Li et al., 2019b) and the apical expression of VIL1 enables actin remodelling by the STm effectors SptP and SipA (Lhocine et al., 2015).

The structural features of the hITM-SIS epithelial cells resemble native physiological characteristics. Beside the distinct polygonal, cobblestone arrangement of the individual cells, the structural similarity of the hITM-SIS to the native intestinal epithelium is highlighted by apically expressed microvilli (Odenwald and Turner, 2016; Siddiqui and Chopra, 1984). Further, the length of the microvilli (~ 1 µm) in the hITM-SIS resembles the length of the native microvilli (BROWN, 1962; Crawley et al., 2014; Walton et al., 2016). In line with the observations of the ZO-1 and OCLN expression, tight junctions were established between individual cells of the hITM-SIS.

Vesicular structures in combination with MUC2 and LYZ protein expression indicated that different cell types of the epithelium developed in the hITM-SIS, which was further addressed by scRNA sequencing.

5.1.5 Transcriptomic profiling reveals distinct epithelial cell types on the hITM-SIS with cell specific cytokine expression

Cell types

Beside morphological and functional features, an important aspect in tissue engineering is the reflection of cellular entities of the respective native tissue, especially regarding cell type identity and their respective quantity. In this study, in depth investigation of the hITM-SIS in context of the formed cellular identities by scRNA-sequencing revealed a heterogeneous composition of different intestinal epithelial cell types, including proliferating TA cells, Progenitors, Enterocytes (mature and immature), cells with a secretory-associated gene expression profile, stem cells as well as M-like cells. In recent years, the technology of scRNA enabled the investigation of the cell types of a variety of organs, including the intestinal tract, and thus provided cell composition references for *in-vitro* models. Now it is possible to compare the *in-vitro* system to the native tissue in regards of cellular identities and more.

A current overview is given in Table 23 for the identified cell types that have been reported in native intestinal tissue and in 3D organoid systems with varying culture conditions as wells as in the hITM-SIS. The cell types were identified by scRNA-seq and/or IHC. Depending on the age and the analysed tissue region, the native intestinal epithelium consists of stem, Paneth, TA, Progenitor, Enterocytes, Goblet, Microfold, EE, and Tuft cells (Elmentaite et al., 2021; Fujii et al., 2018; Wang et al., 2020). When comparing the native cell type composition to the composition of the hITM-SIS, the hITM-SIS represents a majority of these cell types with the exception for Tuft cells and EE cells. In contrast, the common organoid model system from Sato et al. contains mainly stem cells, TA, and Enterocytes as well as a low number Goblet cells; it misses the development of Paneth, Microfold, Tuft and EE cells (Fujii et al., 2018; Holloway et al., 2021; Sato et al., 2009). By adaption of the culture condition, the diversity of cell types can be increased, including an increased number of Goblet cells, M-cells, and EE cells (Fujii et al., 2018) as well as Tuft cells (Holloway et al., 2021). Taking in consideration that the IECs of the hITM-SIS were cultured without a special adaption of the media, it resembles the native cell composition already with a simplified culture condition. When comparing the native, the organoid, and the hITM-SIS cellular composition, the hITM-SIS represents an intermediate state. With the adaption of the culture condition, e.g. by inclusion of IGF-1 and FGF-2, the cellular diversity of the hITM-SIS could be potentially further increased. Furthermore Schweinlin et al. demonstrated in a similar system the development of EE as well as Paneth cells, which could be attributed to the stromal cell compartment and/or the dynamic

luminal flow (Schweinlin et al., 2016). As stromal cells secrete protein and growth factors (Martini et al., 2017), a co-culture approach could benefit the cellular diversity.

Table 23: Overview of identified intestinal epithelial cell types via scRNA-seq in native tissue, hITM-SIS and ASC-derived organoids

System	native intestine			hITM	ASC-derived organoids		
Reference	Elmentaite et al. 2021	Wang et al. 2020	Fujii et al 2018	current study	Sato et al. 2009, Fujii et al. 2018, Holloway et al. 2021	Fujii et al. 2018	Holloway et al. 2021
Notes	Fetal + Adult	Adult	Crypts			+IGF-1, +FGF-2	+NRG-1
stem cell							
Paneth							
Transitory							
Progenitor							
Enterocyte							
Goblet cell							
Microfold cell							
Tuft							
Enteroendocrine							

Green: confirmed, yellow: ambiguous, red: not confirmed

Certain cell types such as Paneth cells, EEs and tuft cells could not be identified in the hITM-SIS. In addition, the gene expression of typical goblet cell markers including MUC2 and TFF3 could not be detected for the secretory cell cluster during scRNA analysis. In contradiction, the protein expression of MUC2 could be demonstrated in individual cells of the hITM-SIS via IHC and flow cytometry. It seems that the MUC2 positive goblet cells were lost during scRNA-Drop-Seq analysis, potentially due to technical difficulties that could have occurred during droplet-based separation. Thus cells could be excluded from downstream analysis due to the cell size or cell sensibility leading to no or low quality sequencing data. Paneth cells, EEs and tuft cells on the other hand represent rare cell types also in the native tissue, which could lead to a statistical underrepresentation in the hITM-SIS scRNA dataset. In order to evaluate the

"missing" cell types, a spatial transcriptomic approach could clarify whether this is due to a methodical error of the Drop-seq approach or to an impaired development of such cell type in the hITM-SIS.

In the *in vivo* studies of Wang et al. 2020, Enterocytes make up the largest population in the native IE, followed by Progenitor cells, TA, Goblet and stem cells, further followed by the rare cell types: Paneth, EEs, M-Cells, and Tuft cells. In comparison, the hITM-SIS demonstrates a similar ratio for the identified cell types, but with a relative larger Progenitor population. This discrepancy could indicate an incomplete differentiation of the IECs of the hITM-SIS. Similarly, Fujii et al. observed in 2018 a shift in the cellular composition of *in vitro* organoids towards stem cells, TA, and early Enterocytes, when comparing cultured organoids to freshly isolated human crypts (Fujii et al., 2018). They identified the applied medium conditions during *in-vitro* organoid cultivation, especially the growth factor composition, as main cause for an incomplete differentiation and thus the proportion of cell types. Intestinal organoid culture depends rigidly on the suppression of differentiation in order to maintain the stem cell population in the long term (Sato et al., 2011), which in turn impairs the development of terminal differentiated cell types. One of these factors commonly used in organoid culture is p38 mitogen-activated protein kinase (MAPK) inhibitors (p38i), which enables long term culture of intestinal organoids but simultaneously suppresses goblet cell differentiation (Sato et al., 2011). Fujii et al. were able to substitute p38i with the niche inspired factors insulin-like growth factor 1 (IGF-1) and fibroblast growth factor 2 (FGF-2), thereby achieving organoids with higher cellular diversity and similar growth behaviour. FGF-2 is a factor secreted among other by mesenchymal cells that are located underneath the epithelial cells in the native tissue; it supports cellular epithelial growth and the intestinal barrier homeostasis (Song et al., 2015). IGF-1 is present in the bloodstream and has been demonstrated to promote the proliferation of intestinal stem cells and epithelial cells under normal and injury-induced regenerative conditions (Zheng et al., 2018). These niche-inspired adaptions could be transferred to the hITM-SIS system, in order to potentially promote cell differentiation while maintaining the proliferative potential. Furthermore, the actual sources of IGF-1 and FGF-2 could be implemented by co-culture with mesenchymal cells and incorporation of a vascular system.

Interestingly, M-like cell development was observed in the hITM-SIS. These cells were characterised by the expression of *CCL20*, *TNFAIP2*, and *CXCL3*, which are genes expressed by M-cells according to Elmentaite et al. 2021, Haber et al. 2017, and Kanaya et al. 2018. However, according to Nakamura et al. mature M-cells express *SPIB* and *GP2* in addition to

TNFAIP2, indicating that M-like cells of the hITM-SIS mimic rather immature M-cells (Nakamura et al., 2018b). They further state that M-cell development is a stepwise process, which is mainly driven by the mesenchymal cell secreted Receptor Activator of NF-κB Ligand (RANKL) that is essential for M-cell differentiation *in vivo* and can be also used to induce M-cells *in vitro* (Haber et al., 2017; Knoop et al., 2009; Nagashima et al., 2017). As mesenchymal cell populations are not present in the hITM-SIS, the observed M-like cell development suggests that the initial onset of M-cell development could be independent of RANKL, but necessary during M-cell maturation. This initial steps could be meditated by ECM cues, as M-cell population are missing in intestinal organoids when cultured under the conditions of Sato et al. (Sato et al., 2009). By the addition of RANKL, full M-cell maturation could be eventually achieved. Furthermore, as immunocompetent cells (T-cell and dendritic cells (Walsh et al., 2013)) secrete RANKL and interact with M-cells *in vivo*, they potentially could guide M-cell maturation. Thus, M-cell maturation could be achieved by incorporation of these immune cells in the hITM-SIS system.

In contrast to Enterocytes or M-like cells, the secretory-like cell cluster showed rather a non-canonical gene expression profile lacking the expression of markers characterizing typical subtypes of secretory cells in the small intestine (Burclaff et al., 2022; Elmentaite et al., 2021). Among the canonical genes are *CHGA* (Chromogranin A) and *NEUROG3* (Neurogenin 3) expressed by EE cells, *DEFA5* (Defensin Alpha 5) and *REG3A* (Regenerating Family Member 3 Alpha) expressed by Paneth cells, *TFF3* (Trefoil Factor 3) and *SPINK4* (Serine Peptidase Inhibitor Kazal Type 4) expressed by mature Goblet cells. Instead, the secretory-like cell cluster based on non-canonical genes including *F3* or *RAB3B* expressed by EE cells (Rupnik et al., 2007; Ryu et al., 2018) and *DHSR9* or *TFF1*-associated with Goblet cell identity (Madsen et al., 2007; Parikh et al., 2019; Wang et al., 2020), according to the online intestinal cell atlas published by Elmentaite et al., in 2021. In general, the gene expression profile of the secretory-like cell cluster does not show specificity for a secretory subtype, but rather a mixture of gene expression patterns of all secretory cells. This suggests that possibly a precursor of the secretory lineage developed from the ISCs within the hITM-SIS by the applied differentiation protocol. During intestinal epithelial homeostasis absorptive and secretory progenitors derive from the stem cell population (Bonis et al., 2021). According to the literature, these populations are defined by the transcriptions factors HES1 (absorptive) or ATOH1 (secretory) and terminally differentiate into respective cell type (Bjerknes et al., 2012; Bonis et al., 2021; Lo et al., 2017). However, Böttcher et al. challenged this paradigm with the help of lineage tracing experiments conducted in mice, where they showed that Paneth and EE cells derive independently of Goblet

cells directly from the stem cell population without a common progenitor transition state (Böttcher et al., 2021). Whether differentiated secretory subtypes derive from a single multipotent precursor is therefore under debate and requires further investigation. In this context, the hITM-SIS could represent a suitable *in vitro* platform enabling secretory lineage differentiation studies involving a bioartificial cell niche represented by the native ECM component.

In addition to the secretory-like cell cluster, we defined a second, HLA-G+ cell cluster based on a non-canonical gene expression profile, characterized by elevated expression levels for the *HLA-G* gene. It encodes an immunomodulatory molecule expressed by intestinal epithelial cells (da Costa Ferreira et al., 2021; Onno et al., 1994). Next to the *HLA-G* gene, the cluster showed increased expression values for *APOL4* and *TRIP6*, which are expressed in intestinal epithelial cells. APOL4 is involved in lipid absorption as well as transport and TRIP6 is a protein involved in signalling for cytoskeletal organization (Ge et al., 2022; Yang et al., 2022).

Interleukins

Intestinal epithelial cells are in close contact with the microbial communities of the luminal microbiome and simultaneously with stromal cells and immune cells as part of the mucosal compartment. Intercellular communication can be ensured among others by secretion of cytokines; in case of immune-associated processes mostly Interleukins (ILs) that are released by a variety of cell types (Akdis et al., 2011). Upon external or internal stimulus, the release of intracellular ILs into the extracellular environment is triggered; the ILs bind subsequently to IL-receptors (ILR) on the recipient cell, such as epithelial cells or leukocytes, and lead mostly via signal transducers and activators of transcription (STAT) proteins to the activation of certain pro- or anti-inflammatory gene expression cascades. Especially in the context of infectious diseases, ILs play an important role regulating host defence mechanisms (Huang, 2021). The functions and origins of the individual ILs, particularly in epithelial cells, is under ongoing investigation, as they are often regulated in concert with immune cells. In the current study, the gene expression of common ILs in an epithelial-only context was examined in association with the cell identity; it revealed cell type-associated enrichments for IL gene expression. For example, M-like cells showed increased expression of *TNF* (= TNFa), *CXCL8* (= IL-8), *IL32*, *IL1A*, *IL1B*, *IL18* and *IL23A*. In comparison with the human gut cell atlas (see https://www.gutcellatlas.org/spacetime/epithelium/; Elmentaite et al., 2021; Teichmann et al., n.d.), also native M-cells seem to express specifically *IL23A,* which supports the M-like cell identity in the hITM-SIS. The human gut cell atlas also confirms the expression of *CXCL8*,

IL32, *IL1A*, *IL1B*, and *IL18*, but does not specifically represent the expression of *TNF* in M-cells; as TNFa is important in M-cell maturation (Wood et al., 2016), the expression of *TNF* in the hITM-SIS M-like cells underlines their immature state. Further, the lack of *TNF* in the gut cell atlas might be due to representation of mature M-cells (confirmed by the expression of *SPIB* and *GP2* (Teichmann et al., 2021)) and a potential external regulation or balancing by immune or stromal cells. Importantly, the gene expression of a certain IL does not equal their production or secretion; it only indicates the potential capability to produce it. In that regard, there was interestingly no *IL6* gene expression detectable. Although, former studies have shown IL6 secretion of intestinal epithelial cells in *in vitro* settings with increasing levels when co-cultured with macrophages (Noel et al., 2017b), also the human gut cell atlas confirmed no *IL6* expression in native intestinal epithelial cells. Hence, IL6 signalling in the human intestinal epithelium is mediated rather by exocrine sources such as immune and/or stromal cells, than by the epithelial cells themselves. As IL6 is an important factor in intestinal homeostasis (Jeffery et al., 2017) and during bacterial infection (Wang et al., 2016b), the hITM-SIS model might help in future to investigate the regulatory aspects of IL6 gene expression in more detail.

Taken together, the hITM-SIS mimics the native tissue in multiple key aspects and thus provides a platform for research of the human small intestinal epithelium in a tissue- and cell-specific manner.

5.2 Recapitulating the infection process of the enteric pathogen STm and investigation of the host-cell response

For decades, infection studies of the enteric pathogen *Salmonella* Typhimurium (STm) were mainly carried out using either cancer cell lines or animal studies - predominantly murine - and fundamental findings were achieved with these valuable tools (Collazo and Galán, 1997; Galan and Curtiss, 1989a; Ibarra et al., 2010). However, the translation to human *in vivo* pathology is still challenging as cell lines of cancerous origin or animal models do not represent the human native tissue in an adequate way. Thus, the cancer cell-derived cultures, which are frequently applied in STm research, derived originally not from small intestinal tissue. For instance, HeLa cells derived from cervical cancer (Scherer et al., 1953) and Caco-2 derived from colon carcinoma (Meunier et al., 1995), thereby inadequately representing the site of the natural infection. Furthermore, the native cellular diversity is not represented as cancer cell-derived cultures mostly exhibit one particular cell type; for instance Caco-2 cells show only Enterocyte-

like phenotypes (Meunier et al., 1995). The STm infection in murine models on the other hand shows a pathogenesis similar to the *Salmonella* Typhi in humans, which implies differential pathogenesis between human and mice (Keestra-Gounder et al., 2015). Therefore, the translatability of STm infection studies in mice is debatable. Human primary cell based approaches can overcome those aforementioned limitations, as the cell material can be isolated from the natural infection site - the intestine - and it preserves *in vitro* the cellular diversity to a certain degree when cultured as organoids. The organoid technology, however, has one important drawback in the application for infectious disease research: the luminal accessibility is restricted. The hITM-SIS system could circumvent these limitations due to its human and tissue-specific cell origin, accessibility of the luminal content, and overall representation of the native intestine.

In the second part of this study, the hITM-SIS was therefore applied in STm infections study, one of the best studied enteric pathogens, in order to evaluate its applicability as a new platform for infectious disease research. The observations of this study showed that the hITM-SIS indeed is applicable, as it recapitulates the infection process of STm as it is described in the literature in regards of bacterial adhesion, invasion, and intracellular proliferation as well as host cell cytokine release. Furthermore, by application of scRNA sequencing of infected cells, *OLFM4* upregulation as a potential new host cell response could be identified. The *OLFM4* expression was upregulated solely in infected cells and could be reduced by Notch inhibition. Thus, with the application of the hITM-SIS system it was possible to examine a new host cell response during STm infection.

5.2.1 The characteristics of the hITM-SIS promise successful and relevant infection with STm

The hITM-SIS properties promise successful adhesion and invasion of STm. For instance, the cells of the hITM-SIS were shown to express VIL-1 and MUC-1, which both facilitate adhesion and attachment of STm; this was demonstrated by knockdown studies that verified a decreased STm invasion capacity after VIL or MUC-1 depletion in Caco-2 cells or HTX29 cells respectively (Lhocine et al., 2015; Li et al., 2019a). An additional important aspect during STm infection process is the broad range of infected cell types. In particular, STm can infect Enterocytes and M-cells, whereas M-cells seemed to preferentially infected as intracellular STm was more observed in M-cells of STm infected mice (B. Jones et al., 1994) and in RANKL induced M-cells of primary cell-derived monolayer (Rouch et al., 2016). Moreover, Fattinger

et al. demonstrated with by comparison of cell line versus *in vivo* infection the importance of a polarised cell layer and multiple cell types for adequate recapitulation of the *in vivo* infection process. They showed that STm infected polarised cells *in vivo* at the cell-cell junction in close proximity of Goblet cells with a different infection mechanism than in cell lines (Fattinger et al., 2020). Taken together, the hITM-SIS platform combines these features as it exhibits as different cell types, especially Enterocytes and M-cells, as well highly polarized cells with defined cell junction. In combination with the human primary cell background, it could give new insights in the cellular pathogenesis of STm.

5.2.2 A controlled methodical approach enables investigation of extra- and intracellular processes during STm infection

Studying STm infection in an *in vitro* model requires suitable culturing conditions and protocols. The current study aimed for the establishment of a representative STm infection model with the possibility to investigate the single infected cell pathogenesis in a human tissue context. For that, it was important to control and validate the infection process at its best. In regards of the methodical approach, important aspects in the infection protocol were considered. First, the applied MOI has to be balanced between *in vivo* representation, cytotoxic effects and downstream analysis applicability. As a measure of infectivity, the infective dose of *Salmonella enterica* in humans varies between 10^5 – 10^{10} bacteria per dose (Kothary and Babu, 2001), which is hardly translatable to *in vitro* conditions due to factors, such as the gastric bypassing , patient condition and simple cell numbers. Commonly used MOI in *in vitro* models range from 5 to 50, with most studies applying a MOI of 10 (Fulde et al., 2021; Kusters et al., 1993; Roche et al., 2018). Until recently the MOI application in *in vivo* studies was hardly comparable with *in vitro* approaches, then Fattinger et al in 2020 determined the effective MOI in a mouse infection model with an MOI of ~90 (Fattinger et al., 2020). However, in that approach the mouse microbiome was suppressed by antibiotic treatment pre-infection in order to support terminal saturation with STm bacteria, therefore the determined MOI of 91 is potentially overestimating the natural bacterial to cell ratio. In the current study, a high cytotoxic effect was observed at MOI 50 overtime and with MOI 5 only a low number of cells were infected. Therefore, a MOI of 10 was applied in further experiments, thereby more closely representing the *in vitro* approaches.

Beside the MOI, controlling the initial bacterial contact to the IECs is important to secure a synchronised infection process. Therefore, the hITM-SIS models were centrifuged after

application of STm to achieve temporal synchronisation. Furthermore, STm multiplies, spreads and re-infects the IE after infection (Chong et al., 2021). Reinfection events should be prevented in the present study by application of an initial high Gentamicin dose with subsequent low Gentamicin concentration throughout the infection course. This Gentamicin protection assay inactivates extracellular STm and ensures that the observed intracellular bacterial dynamics were based on the initial infection event (Tabrizi and Robins-Browne, 1993). Indeed, the stable infection rate overtime indicated successful prevention of reinfection events and hence ensured downstream observations. Taken together, the established infection protocol is suitable to investigate STm dynamics-associated with infection of IECs at the cellular level from the initial adhesion event to late phase effects.

5.2.3 Recapitulating the STm infection process in primary polarised human cells – from adhesion to intracellular progression

After successful establishment of a suitable infection protocol, the bacterial infection process during STm infection of the hITM-SIS was examined, especially with perspective of the literature. For that, the infection process was divided in: (1) adhesion, (2) invasion, (3) intracellular migration and (4) intracellular progression (Larock et al., 2015). In addition, the epithelial cytokine release, as an important hallmark of STm infection, was examined in context of published data.

5.2.3.1 Bacterial adhesion to the apical site of the human IECs occurs in STm typical manner

In regards of bacterial adhesion, this initial step could be observed in the first hour after STm application to the hITM-SIS. STm showed successful adhesion to the epithelial surface of the hITM-SIS, because non-adhesive STm would have been removed due to washing. Mechanistically, the flagellum seems to support anchoring of the bacterial corpus to the cellular surface, as it exhibits a stretched and oriented morphology. These observations are consistent with former published data that the STm flagellum is essential as adhesion and invasion is impaired upon fliC/fliB deletion (Olsen et al., 2013). Furthermore, STm adhered and interacted with the microvilli of IECs, which is consistent with early observations in Caco-2 cultures (Finlay and Falkow, 1990). Although microvilli are able to establish an electrostatical barrier against bacterial adhesion, as shown by Bennett et al in 2014, this adverse effect might be

compensated by distinct adhesive mechanisms of the bacteria. Several are known for STm and are well described (Wagner and Hensel, 2011). Among them are the fimbrial adhesins of STm; for example the Mannose-binding Fim protein, which could bind to the glycosylated structures of the glycocalyx, similar to observations during human immunodeficiency virus (HIV) infection studies (Spillings et al., 2022). Additionally, Li et al. proved that MUC1, a mucin of glycocalyx, is receptor for STm SiiE and facilitates STm adhesion (Li et al., 2019a). Furthermore, STm can degrade the host glycocalyx by glycosyl hydrolases (GH) (Arabyan et al., 2016), eventually in order to the establish physical contact between the cellular membrane and the T3SS. With the application of the hITM-SIS, this potential mechanism and other influences of the glycocalyx during STm infection can be investigated in a human primary cell context. For that, the application of cryogenic electron microscopy in combination with super resolution imaging of glycosylated structure via IHC could enable deeper insights in glycocalyx and STm interaction.

5.2.3.2 STm enters human IECs pairwise via discreet invasion mechanism

Recent studies showed that after adhesion, STm invades IECs by two distinct mechanisms: ruffle-induced (RI) or discreet (DI) invasion (Fattinger et al., 2020). In short, both require a complex concert of the SPI-1 effector proteins (SopB, SopE, SopE2, SipA, SipC), which are injected into IECs by the T3SS-1, and lead to rapid actin and membrane remodelling, facilitating bacterial uptake (Larock et al., 2015). RI, however, is mostly observed during invasion of unpolarised cells, independent of SipA and displays large membrane perturbation, whereas DI seems to occur mostly in polarised IECs during *in vivo* infection with smaller "discreet" perturbations and is driven by SipA (Fattinger et al., 2021; Lhocine et al., 2015). The results of the present study indicate that invasion process of IECS the hITM-SIS by STm recapitulates the steps that has been described formerly in the literature (Fattinger et al., 2021; Larock et al., 2015). In detail, key steps of STm invasion of cells in the hITM-SIS could be observed and divided in different states based on visual classification: (I) STm adhered and localised at the brush border and at the F-actin skeleton, (II) rapid Actin polymerisation was induced which led to proturbance of the cell membrane and "donut" shape surrounding of the bacteria, (III) Actin polymerisation continued and STms were encapsulated by the membrane leading to typical ruffling structure, (IV) STm were endocytosed in vacuoles and the F-actin was re-established, (V) finally the Actin skeleton is completely restored. Overall, the membrane proturbances recapitulated rather the DI-like phenotype of polarised cells then the RI

mechanism in cell lines, hence it reassembled the *in vivo* observations of Fattinger et al. in 2020, but in a human context. Off note, an exact definition of membrane ruffling and hence invasion phenotypes of STm on structural approaches is not clear determined, therefore the interpretation of the invasion mechanism must be seen in the context of former and future publications.

Furthermore, STm invaded IECs in the hITM-SIS mostly in pairwise manner and not as single bacteria, which is in line with a previous finding in canine and human polarised cells *in vitro* (Lorkowski et al., 2014). However, *in vivo* data from mouse models do not support the pairwise infection mode of action, but rather appoints that phenomenon to the extensive membrane ruffling of the RI invasion observed in unpolarised *in vitro* cells (Fattinger et al., 2020). Contradictory, in the present study pairwise infection in polarised cells were indeed observed with DI-like invasion mechanism. A possible explanation for this discrepancy could be a species-specific invasion mechanism, which could be addressed by comparing murine and human polarised IECs in an *in vitro* infection approach. Nevertheless, it seems that the polarisation of IECs and thus cellular morphometry are important features in the STm pathogenesis.

Taken together, in combination with the expression of Villin and Muc1 as well as the presence of microvilli structures, the infection of hITM-SIS with STm reassembles the adhesion and invasion process to the current scientific state and opens new implications in regards of supportive pairwise invasion of STm. With the help of the hITM-SIS platform, future studies can evaluate and investigate these processes now in a primary polarised cell and human background.

5.2.3.3 STm migrates intracellularly from apical to basolateral in human polarised IECs

The established hITM-SIS infection model was not only able to mimic bacterial invasion into intestinal epithelial cells, but it was further demonstrated that STm shows distinct time-dependent behaviours regarding its intracellular migration from the apical entry site towards the basolateral region of the IEC. Interestingly, only subpopulations of the bacteria reached the basolateral site of the cells after 24h, whereas individual STm seemed migratory non-active and remained at the intracellular apical region. How is this bacterial intracellular migration or trafficking behaviour controlled and why does it occur?

Under physiological conditions, transmigration of STm in IECs is a natural process that aims to overcome the intestinal mucosal barrier, in order to ultimately spreading systemically in the host. For that, STm resides first in SCV after internalisation and establishes an intracellular niche as *Salmonella* induced tubules (SIT), which are found in close contact to specific cell organelles such as the nucleus or the Golgi apparatus (Salcedo and Holden, 2003). The Golgi is canonically located next to the nucleus and thus is closer to the intracellular basolateral site in polarised cells (Gundersen and Worman, 2013). As STm in SCV interferes with intracellular trafficking in order to avoid lysosomal fusion, it shows the ability to initiate a directional transport towards specific cellular compartments in the infected cell (D'Costa et al., 2015; Uchiya et al., 1999). In addition, Fulde et al. demonstrated in a recent study published in 2021 that SPI-2 T3SS effector proteins (including sseB), which are released from the SCV, are essential for apical-basolateral transmigration. Typically, intracellular trafficking of vesicles and organelles is mediated by the microtubule network and its-associated motor proteins Kinesin and Dynein (Alberts et al., 2015). *Salmonella* containing vacuoles (SCV) could therefore be transported via Dynein towards the nucleus and the Golgi apparatus. However, underlying regulatory mechanisms are yet to be elucidated. Furthermore, these processes might vary between distinct cell types, for example between Enterocytes and M-cell. In order to investigate these complex mechanisms, adequate polarized cell and different cell types must be represented in the applied model system.

Interestingly, although the majority of individual STm migrated to the basolateral site, some STm were observed in the apical region of the IECs over the time course of 24h. These findings are consistent with observations in a neonatal mouse model reported by Fulde et al. in 2021; they observed an increase of basolateral STms in IECs overtime, but up to 50 % of the STm stayed in the apical compartments. The authors demonstrated that the persistence of some of the SCVs in the apical region is related to the expression of sseB, as deletion of this SPI-2 effector impaired successful trafficking and decreased basolateral egression. Furthermore, as sseB is translocated by the SPI-2 T3SS from the SCV into the cell cytoplasm, the authors concluded that the expression of SPI-2 T3SS is essential for this specific bacterial transport behaviour. These findings, in combination with the observations made on behalf of the hITM-SIS infection model, suggest a similar mechanism in human IECs and further might indicate migratory non-active STm populations inside SCVs. One hast to consider that Fulde et al. measured the relative localisation of STm to the nucleus, whereas the present study related to the apical actin membrane. However, in consideration of the mean height of the cells and the migration distance, the results and conclusions are comparable. In order to further elucidate

these mechanisms, it would be interesting to apply STm sseB mutants in the hITM-SIS as well as to investigate the SCV composition. Furthermore, the trafficking mechanism differs from the apical site to the nucleus (with Dynein) and further from the nucleus to the basolateral site (with Kinesin) and it would be interesting to investigate regulatory principles in this context: how STm senses the localisation of the SCV and how it switches the localisation signal. Whether the non-migrating SCV are connected to bacterial persistence will be an interesting point to address in the future.

5.2.3.4 Intracellular bacterial progression – STm develops distinct morphologies inside human IECs

Interestingly the intracellular STm morphology changed over time. While in the early infection phase (0h – 8h p.i.) STm showed typical rod-shape morphologies, in the late stage of the infection (24h p.i.) STm formed elongated filaments. These structures could potentially represent SI), which are considered as the replicative niche of intracellular STm facilitating nutrient and membrane uptake (Knuff and Finlay, 2017). Although there are several SIT types described, SIF represent the most abundant form (Mota et al., 2009; Schroeder et al., 2011, 2010). In contrast to bacteria in SIF, the intracellular STm observed in the hITM-SIS showed a rather filamentous morphology. Bacterial filamentation can be an effect of interrupted bacterial division and occurs in a variety of bacterial species, when bacterial growth continues without subsequent division, leading to the elongated morphology and multiple chromosomal copies (Justice et al., 2008). Several *Salmonella enterica* serovars form this specialised filamentous morphology extracellularly in response to environmental factors, including osmotic stress or temperature variations (Lensmire et al., 2018; Mattick et al., 2003). However, the significance of intracellular filamentous STm in pathophysiological conditions is currently poorly understood. The intracellular STm filamentation was first described by Martínez-Lorenzo et al., in 2001 using the STm strain SL1344 for infecting MelJuSo cells, a human melanoma cell line; subsequent work then showed that filamentation is SulA-mediated, related to histidine metabolism, and occurs exclusively in vacuolar STm (Henry et al., 2005; Humphrey et al., 2011). Recently, filamentous STm were also observed inside macrophages under transcription factor EB (TFEB) induced high vacuolar concentrations of the immunometabolite itaconate (Schuster et al., 2022); the authors concluded a restrictive function of the itaconate on the STm proliferation upon successful transfer in the SCV, which in turn led to the formation of filamentous STm. The filamentous STm were hence a sign of stress exhibited by itaconate. The

results of the present study indicate that the formation of filamentous STm also occurs in human epithelial cells; however if a similar mechanism as observed by Schuster et al. is responsible, needs to be further evaluated. In addition, these morphologies were not yet described *in vivo* studies, neither in mice nor in human, and could therefore represent either *in vitro* artefacts or so far overseen phenomena. Both aspects need to be investigated in more detail in future studies.

5.2.3.5 STm infection induces epithelial specific secretion of pro-inflammatory cytokines IL-8 and TNF-α in human IECs, without IL-6 or IL-1β release

Cytokines are important effectors of the host cellular defence mechanism in immune and inflammatory responses. They are released by various kind of cells types (including immune cells or epithelial cells (Sansonetti, 2004)) upon the encounter with a pathogen- or damage-associated molecular pattern (PAMP and DAMP) (Kelso, 1998). Intra- and extracellular *Salmonella*-associated PAMPs, such as LPS or flaggelin-1, are detected by Pattern recognition receptors (PRR) and Nod like receptors (NLRs), resulting in the activation of signal transduction pathways regulating the expression and the release of cytokines (Wemyss and Pearson, 2019). During STm infection, many different cytokines inducing pro-inflammatory processes are involved in the mucosal immune response, including IL-1α/β, IL-6, IL-8, IL-10, IL12/23, IL-15, IL-17A, IL-18, IL-25, IL-27, TNF-α, chemokine ligand 2 (CCL2), IFN-γ (Huang, 2021). Although this host cell defence mechanism is commonly thought to support bacterial clearance due to recruitment of immune cells, Stecher et al showed in 2007 that the pro-inflammatory processes facilitate STm colonisation in mice as they suppress the commensal microbiota more efficiently then the STm, thereby giving STm a growth advantage (Stecher et al., 2007).

In the present study, the release of a defined set of pro-inflammatory cytokines (IL-1β, IL-6, IL-8, IL-10, IL-12p70, TNF-α) was investigated, which are especially involved in the epithelial cellular response against STm infection. Of those cytokines, IL-1β, IL-6, IL-10, and IL-12p70 secretion could not be detected. IL-10 and IL-12p70 are known to be secreted by cells of the innate and adaptive immune system (Akdis et al., 2016) and not by epithelial cells. Hence, no secretion in this study is consistent as the hITM-SIS cells are only epithelial cells. The other cytokines (IL-1β, IL-6, IL-8, and TNF-α), however, can be secreted by epithelial cells (Akdis et al., 2016). Interestingly, of those only IL-8 and TNF-α were detectable in sufficient concentrations in the hITM-SIS infection setup.

Generally, IL-8 is a pro-inflammatory chemokine that recruits innate immune cells to the infection site and is known to be induced by NOD2 and Toll-like receptor (TLR) 5 recognition of STm flagellin-1 (Eckmann et al., 1993; Huang, 2012). It is a common reaction of the intestinal epithelium upon enteric pathogen encounter. The observed IL-8 release in this study is hence consistent with earlier reports, stating IL-8 release of human intestinal epithelial cells during STm infection (Gewirtz et al., 2000). However, it implies that IL-8 secretion is further induced during intracellular localisation of STm as extracellular STm are inactivated by the Gentamicin protection assay. Besides that, the IL-8 release demonstrates the capability of the hITM-SIS IECs to induce pro-inflammatory and phagocyte-recruiting signals

TNF-α is an early pro-inflammatory cytokine that exhibits a wide range of pleiotropic activities in epithelial tissues including production of pro-survival cytokines and anti-apoptotic factors via nuclear factor kappa B (NF-κB) or mitogen-activated protein kinase (MAPK) signalling cascades (Delgado and Brunner, 2019; Wemyss and Pearson, 2019). Next to IL-8, the release of TNF-α is also an well-studied early mucosal response towards STm infection, also induced by flagellin-1 (Ciacci-Woolwine et al., 1998). Early reports suggest a constant release of TNF-α during infection with STm in mice, with low concentrations in the early (~ 6h) and high in the late phase (~ 20h) (Arnold et al., 1993). The results of the present study are contrary as TNF-α was released in the early phase of infection and stagnated overtime. A possible explanation could be that reinfection events occurred in the animal, whereas that was inhibited during the infection of the hITM-SIS model by the Gentamicin protection assay. This would further imply that TNF-α is induced during adhesion and/or entry by STm while flaggelin-1 is expressed, but intracellular STm does not lead to TNF-α reaction.

Notably, no release of the cytokines IL-1β and IL-6 could be detected in the hITM-SIS model, not under STm challenge or control conditions. This observation is contradictory to previous reports that state IL-6 is as a cytokine, which is released by epithelial cells during STm infection in Caco-2 cells (Huang, 2009). In contrast, the IECs of the hITM-SIS showed no IL-6 secretion under infectious conditions. In line with this, no *IL-6* expression was detectable during the scRNA-seq analysis in this study, which was further confirmed by recently published data in context of the online intestinal cell atlas (Elmentaite et al. 2021). Furthermore, Roodsant et al. could not detect IL-6 secretion in a similar monolayer system with human primary intestinal epithelial cells, under control conditions or when they challenged the cells with viral particles (Roodsant et al., 2020). This indicates that intestinal epithelial cells alone cannot secrete IL-6, not under physiological not pathogenic conditions. It further seems that the initial observation

of Huang in 2009 represents an artefact of the Caco-2 cells and is therefore a good example, why the primary based model systems should be preferred.

IL-1β on the other site was expressed indeed by the epithelial cells of the hITM-SIS as seen by the scRNA analysis, which was in line with the data of the online intestinal cell atlas (Elmentaite et al. 2021). However, no IL-1β release could be detected after challenging the IECs of hITM-SIS with STm. This is consistent as STm related IL-1β gene expression or secretion was mainly observed *ex vivo* studies or isolated immune cells. In detail, human PBMC-derived macrophages secreted IL-1β upon challenge with STm as rapid response (Diamond et al., 2017) and *ex vivo* human intestine sample released IL-1β after infection with STm (Nickerson et al., 2018). Only one report stated epithelial *IL-1β* mRNA expression as response towards STm infection in a Caco-2 system (Huang, 2016). Together this indicates that the human intestinal epithelium does not secrete IL-1β, and that rather immune cells (e.g. macrophages) are the source of IL-1β during STm infection. By implementation of an immune component in the hITM-SIS platform, this question could be ultimately addressed by localising IL-1β under STm infection conditions.

5.2.4 Multi-layered heterogeneity during STm infection

Due to the development of experimental techniques with focus on single cell analysis, in the past years a phenotypical heterogeneity of STm population was more and more often observed in STm infection studies, as nicely summarized by C. N. Tsai and Coombes in 2019 and Ackermann in 2015. For example Malik-Kale and colleagues described already in 2012 that two populations of intracellular STm account together to net bacterial burden of a system, namely cytosolic and vacuolar STm. Already then, they emphasized the importance of single cell resolution in STm infection studies.

5.2.4.1 Heterogeneity in intracellular STm populations results in individual bacterial burden

Also, in the current study, intracellular STm populations demonstrated heterogeneous phenotypes at various stages of infection on a single cell level: (1) STm invaded IECs by DI or RI mechanism, (2) intracellular STm migrated either to the basolateral site or stayed in the apical region, (3) intracellular STm were observed as single bacterium, as clusters or as

filamentous STm in late phase infection stage. Furthermore, already at an early stage of infection (4h p.a.), STm developed distinct intracellular populations (low, med, high) in regards of number of bacteria per cell. These observations are consistent with findings of the Steele-Mortimer group, as they describe similar phenotypes in cultured HeLa and polarized Caco-2 cells with a similar timing and proportion (Finn et al., 2017; Knodler et al., 2010). They concluded that a small sub-population of STm escapes the SCV by a not-well understood mechanism and replicates rapidly in the cytosol (cytosolic STm), which is SPI-1 induced, T3SS1 effector mediated and dependent on SopB Akt-phosphorylation (Finn et al., 2017; Malik-Kale et al., 2012). These hyper-replicating STm account for up to half of the total bacterial load after 7h p.a. in *in vitro* infection assays with Caco-2 or Hela cells, according to Knodler et al in 2014. On the other hand, STm remaining in the SCV (vacuolar STm) are reported to replicate slowly with SPI-2 T3SS activity to deploy f SPI-2 effector proteins gene (Finn et al., 2017).

In the current study, the high-infected cells could represent hyper-replicating cytosolic STms; further, the med infected population could represent cells containing slowly replicating vacuolar STms and the low infected cells could contain non-replicating STm. Indeed, the application of a Proliferation-reporter strain in hITM-SIS infection demonstrated that the higher number of STm in highly infected cells was due to an increased replication rate, whereas med and low populations contained STm with lower replication rates. Interestingly, also non-replicating STm were observed in med and high infected cells. The results of the current study indicate therefore on the one hand that the replication rate of intracellular STm differs between infected epithelial cells and furthermore between individual STm within a single infected cell. This is consistent with observations in macrophages (Helaine et al., 2014), but was not yet observed in primary epithelial cells. On the other hand it also indicates the existence of hyper replicating STm population in human primary epithelial cells, an observation, which was so far discussed as potential cell line artefact (Castanheira and García-Del Portillo, 2017).

An important next aspect is to evaluate if these hyperreplicative STm are also cytosolic populations. For that the STm localisation in regards of cytosolic and vacuolar should be clarified via immunofluorescent analysis of the SCV marker Lysosomal-associated membrane protein 1 (LAMP-1) and subsequent co-localisation with the different populations.

According to Tsai and Coombes in 2019, the cytosolic STm population derive from early SCV escape and due to accessibility of cytosolic nutrients the STm can massively replicate, whereas the vacuolar STm are restricted by nutrient diffusion into the vacuole. In later stages, the SIT

formation facilitates nutrient uptake of vacuolar STm then allowing rapid bacterial division (Larock et al., 2015). Therefore, a potential trigger of SCV escape could be a reduced accessibility of nutrients leading to stress induced escape. However, the limited nutrient supply would be present to all STm in one individual cell, which should lead to SCV escape and massive cytosolic replication of a majority of the STms, which is not the case as non-replicating and replicating STm populations were observed in one individual cell. It seems that the mechanism is rather multifactorial and still under debate. Therefore, further research is needed and the hITM-SIS represents an ideal platform for the investigation of intracellular replication of STm in a human epithelial *in vivo*-like background.

5.2.4.2 STm infects a heterogeneous range of cell types and might induce transcriptomic changes to individual cell type populations

An additional factor to the nutrient supply driving STm heterogeneity could be the identity of the infected cell. Early studies reported targeted infection of M-cells in mice, which are used as transition vehicle to the underlying phagocytizing cells (Clark et al., 1996; B. D. Jones et al., 1994). Later, also Enterocytes were reported to be infected and that they are used as spreading tool by faecal shedding (Chong et al., 2021; Fattinger et al., 2020; Sellin et al., 2014). Further, STm is capable of triggering M-cell trans-differentiation of Enterocytes by inducing RANK receptor and ligand expression (Tahoun et al., 2012). These findings suggest cell type mediated mechanisms and adaptions of STm. As the hITM-SIS represents the major cell types of the human intestinal epithelium *in vivo*, analysis of the identity of infected cells could reveal insights into underlying mechanisms in different cellular entities.

Therefore, STm infected cells were sorted based on their bacterial burden and subsequently analysed via scRNA sequencing for their respective cell type. In general, cell type identification based on canonical cell marker expression resulted in ambiguous cell type annotation for the terminal differentiated cells (Enterocytes, Secretory cells, M-like cells), but with definitive annotation for TA and stem cells, meaning that STm is capable of infecting a broad range of cell types including, TA cells as well as stem cells. The stem cells showed the expression of the canonical cell marker *LGR5* (Sato et al., 2009) and interestingly a deviating expression of *OLFM4*, a protein with various function that is often used as intestinal stem cell marker (Elmentaite et al., 2021; van der Flier et al., 2009). The infected *LGR5*+ stem cells of the hITM-SIS were especially enriched in the early phase of infection but vanished in later time points. This observation could imply that STm indeed initially infects LGR5 stem cells, but the infected

stem cell die overtime or lose their transcriptomic footprint. So far, stem cell infection by STm has not been described in the human context; Liu et al., however, demonstrated an increase Wnt/β-catenin pathway signalling as well as an increase of stem cell number in murine crypts upon STm infection (X. Liu et al., 2010). Although the number of stem cells in this study could have been increased due to repair mechanisms and without a direct stem cell infection by STm, together with the result of the current study it shows that STm can affect directly or indirectly stem cell fate. stem cell infection might be rare occurrence *in vivo*, as they reside in the crypt niche under physiological conditions, where they are protected from infection by spatial separation and antimicrobial peptide secretion. Therefore, stem cell infection by STm could be a secondary effect upon bacterial induced tissue damage or after loss of the tissue structure when the protective function of crypt is lost. This would be of special interest in the context of chronical diseases, such as inflammatory bowel disease (IBD) that result in lesion and partial structural loss of the intestinal epithelium (Guan, 2019). By the application IBD-hITM-SIS, a potential increased susceptibility of the damaged tissue to STm infection could be investigated.

Next to the observation of *LGR5* and *OLFM4*, the cell type gene markers for Enterocytes, *ALPI* and *RBP2*, were deviating in between individual infected cells. Here, the expression of *ALPI* seemed to be enriched in infected cells during the early phase, whereas *RBP2* appeared to be expressed in other cell types as well and during all time points of infection. Similar ambiguous gene expression pattern were observed for the canonical markers of the other differentiated cell types. These observations could be a result of transcriptomic interference by the STm infection, which might indicate an on setting transdifferentiation. However, due to the low number of cells in combination with the complexity of the dataset, further interpretation in this regards is difficult. As it combined the information for the parameters of the infection (time point) as wells as the bacterial burden (high, med, low) in a heterogeneous cell system and in combination with the already discussed heterogeneity of the STm dynamics, the interpretation of the dataset should be taken carefully and further experimental validation is needed.

However, the scRNA analysis revealed interestingly an unexpected massively high expression of *OLFM4* in infected cells, especially in later time points.

5.2.5 OLFM4, a new cellular response during STm infection

STm infection has a variety of effects on the infected epithelial host cells. For example, STm infection led to increased epithelial gene expression of the cytokine regulator suppressor of cytokine signalling 3 (SOCS3) in infected Hela cells as shown in a dual RNA-seq approach (Westermann et al., 2016). Westermann et al. showed further that PinT, a non-coding RNA of STm, was modulating indirectly the SOCS3 gene expression by regulation of SPI-2 genes. This observations were then confirmed by Schulte et al. in 2020 in a co-culture setup of Caco-2, endothelial and immune cells (Schulte et al., 2020). These findings prove that STm infection affects gene expression of the host epithelial cell, which can result in alternated protein activity. Furthermore, STm infection can affect FAE-associated epithelial cells in a way that leads ultimately to transdifferentiation towards a M-like cell phenotype; Tahoun et al. showed that the induction of M-cell like phenotypes in primary murine FAE-associated epithelial cells is modulated by endocrinal signalling of RANKL upon SopB administration by STm (Tahoun et al., 2012). It means that STm can induce severe transcriptomic changes to its host epithelial cell. These fundamental findings were obtained from mice or cell line based systems and hence are limited in their translatability to humans, as discussed before. Furthermore as shown in this study and others (Bumann and Cunrath, 2017; Castanheira and García-Del Portillo, 2017; Staes et al., 2019), intracellular STm populations exhibit high degree of heterogeneity in individual cells and tissues, which therefore also requires the analytical methods for individual cells.

In the current study, the transcriptome of STM-infected IECs of the hITM-SIS was investigated in a scRNA-seq approach. As discussed in 5.2.4.1, STm infected a broad range of cell types including *LGR5* and *OLFM4* expressing stem cells. Interestingly, the expression of *OLFM4* deviated from expression of *LGR5*, indicating an increase of *OLFM4* gene expression by multiple individual IECs during the infection and overtime. Furthermore, *OLFM4* expression overlapped the gene expression of other cell markers thereby implying that *OLFM4* expression is not restricted to canonical *LGR5* stem cells and hence not necessarily a factor determining stemness of a stem cell. According to the literature, OLFM4 is a diverse protein that is connected to several cellular functions (Liu and Rodgers, 2022a, 2022b, 2016), among them are cell proliferation in epithelial cells as well as innate immunity and inflammation in myeloid cells. In particular, OLFM4 seems to be involved in the regulation of cell proliferation as shown in a study in 2016, which demonstrated that OLFM4 deletion led to increased intestinal crypt proliferation and inflammation in an $APC^{Min/-}$ mouse model, resulting ultimately in colon adenocarcinoma (Liu et al., 2016). This proliferative regulatory function is potentially responsible for the common use of OLFM4 as stem cell marker; according to study of van der

Flier et al. in 2009, OLFM4 is a robust marker gene for intestinal stem cells in mice and is therefore often used together with *LGR5* and *ASCL2* in stem cell annotation in scRNA-seq analysis (Burclaff et al., 2022; Elmentaite et al., 2021). This is in line with the results of the present study that indicate OLFM4 is indeed expressed by *LGR5* and *ASCL2* expressing stem cells of IECs in the uninfected hITM-SIS, as shown during scRNA based cell profiling.

However, the *OLFM4* expression of STm-infected cells seemed not to correlate with the *LGR5* expression in the scRNA-seq analysis, which was also confirmed by qPCR analysis that demonstrated OLFM4 gene expression increased during STm infection but independently of *LGR5* expression. This suggests that *OLFM4* exhibits additional functions in intestinal epithelial cells besides the regulation of cell proliferation in the intestinal stem cell population. Increasing evidence accumulate over the past years, which state the involvement of OLFM4 in additional pathways and processes, such as inflammation. For instance Liu et al. connected OLFM4 with a regulatory function in the NFκB pathway in addition to the Wnt/β-catenin pathway in a murine adenocarcinoma model (Liu et al., 2016). Further, OLFM4 was upregulated in intestinal epithelial cells of patients with inflammatory bowel disease (IBD), as shown in patient material (Gersemann et al., 2012; Shinozaki et al., 2001). The upregulation in inflammatory processes could be further ascribed to a synergistic effect of TNF-α and Notch signalling that leads to cytoplasmic accumulation of OLFM4 and exhibits ultimately an anti-apoptotic effect of OLFM4 in IBD (Kuno et al., 2021).

5.2.5.1 The role of OLFM4 in infectious disease

Next to this cell-protective role in IBD, OLFM4 appears to be an important factor in modulating host innate immunity to bacterial infections. Thus OLFM4 expression levels were elevated in gastric mucosa of patients infected with *Helicobacter (H.) pylori* (Mannick et al., 2009) and it was later revealed that *H. pylori* colonization was reduced under OLFM4 depletion, as shown in an Olfm4-deficient mouse model (W. Liu et al., 2010). Furthermore, *OLFM4* was significantly increased in intestinal crypts as a regenerative response towards infection with *Lawsonia (L.) intracellularis* in a porcine infection model, (Huan et al., 2017). OLFM4 was also connected to migration, proliferation and the inflammatory response against *Porphyromonas gingivalis* (Fitzsimonds et al., 2021). The bacterial infection with *Staphylococcus (S.) aureus* led to upregulated level of *OLFM4* in children (Ramilo et al., 2007) and Olfm4-deficient neutrophils showed increased killing capability of *S. aureus* (Liu et al., 2012). Together, these reports indicate that OLFM4 plays a variety of important roles in

immunomodulation-associated with bacterial infections. However, the exact mechanism or function in this context is not clear and could rely on the pathogen species as well as site of infection.

In the context of STm infection of intestinal epithelial cells, OLFM4 was so far not described. The results of the current study however demonstrate clearly that *OLFM4* is upregulated on transcriptomic and protein level in individual infected IECs of the hITM-SIS upon STm infection as shown by HCR-FISH and IHC. In this context, STm infection in hITM-SIS reveals a previously unknown upregulation of OLFM4 as an epithelial response to STm infection. Although extensively studied, this upregulation during STm infection might have been overseen or the model systems were not able to recapitulate this feature. For instance, Westermann et al. did not detect OLFM4 upregulation in a transcriptomic approach of STm infected Hela cells, probably due to fact that baseline OLFM4 in uninfected Hela cells is not expressed (Westermann et al., 2016). This underlines the importance of primary cell based model systems and the hITM-SIS in infectious disease research.

In addition, the results of the current study demonstrated that the observed OLFM4 upregulation was restricted to the STm-infected cells and thus a direct consequence of the intracellular STm. If this processes is actively induced by STm and hence beneficial for the bacteria or if it is a host defence mechanism as a response towards intracellular STm remains to be clarified. In consideration of the reported anti-apoptotic and cell-protective function of OLFM4 in the context of other bacterial or viral infections, the STm mediated OLFM4 expression might indicate a cellular survival mechanism and/or a STm controlled hijacking of the cellular immune response. Similarly, *H. pylori* infection in OLFM4 deficient mice showed that OLFM4 protects against severe gastritis and exhibits anti-inflammatory effects (W. Liu et al., 2010). However, this function is hijacked by *H. pylori* to reduce the inflammatory response and to ultimately establish persistent colonization. The host inflammatory cascade is also controlled by STm in order to establish its replicative niche (Galán, 2021). A similar mechanism could underlie the STm mediated OLFM4 expression, meaning that STm might induce OLFM4 to control and regulate pro-inflammatory and anti-inflammatory effects in order to establish the replicative niche in later stages (Däullary et al., 2022, in review). In order to elucidate the function of OLFM4 in this context, a time wise controllable conditional Knockout of OLFM4 in primary organoids with subsequent STm infection could give insight in a direct effect of OLFM4 on the bacteria.

5.2.5.2 How is OLFM4 regulated during infection? Indications for Notch dependency

By investigation of the STm mediated regulation of OLFM4, the potential function during STm infection could be determined. As mentioned before, the regulation of OLFM4 is a complex system with various components; among them are the NFκB pathway (Chin et al., 2008) and the Notch pathway (VanDussen et al., 2012).

Regarding the first, Chin et al. 2008 demonstrated that OLFM4 is a target gene of the NFκB pathway in myeloid precursor cells. It was further reported that OLFM4 influences NFκB signalling negatively via direct association with the intracellular pattern recognition receptors (PRR) nucleotide binding oligomerisation domain containing (NOD) 1 and 2; which was observed in a cancer cell line infected with *H. pylori* (W. Liu et al., 2010). OLFM4 might therefore interact in negative feedback loop with the NFκB pathway. NFκB activation is also a first defensive cellular response in STm infection biology as shown in previous reports (Pinaud et al., 2018). STm is further known to actively modulate the cellular innate response, including the regulation of the NFκB signalling, in order to establish its niche (Larock et al., 2015). The OLFM4 upregulation during STm infection could rely on NFκB pathway activation. The result of the present study demonstrated that NFκB signalling was active in the early STm infection phase in the IECs of the hITM-SIS, but diminished quickly after the first 4h. The induction of OLFM4 gene expression on the other site started at 8h, hence additional 4h later. A correlation between NFκB activation and OLFM4 induction is therefore rather unlike due to a time discrepancy of 8h. However, in order to validate this finding, a conditional and time controlled NFκB pathway inhibition during STm infection with subsequent OLFM4 detection should be applied.

While the NFκB pathway mediated OLFM4 regulation seems to be more prominent in myeloid cells (Chin et al., 2008; Kuno et al., 2021), in epithelial cells the Notch signalling pathway seems to be more dominant (Kawamato et al. 2018; Kuno et al. 2021). Thus previous reports demonstrated a direct binding of the Notch intracellular domain (NICD) to the RBP-J consensus site of OLFM4 and thus a direct downstream regulation of OLFM4 by Notch activation (Kuno et al., 2021; VanDussen et al., 2012). Notably, Notch and TNF-α are regulating OLFM4 expression synergistically, as shown in IEC cells lines and IBD patients (Kuno et al., 2021). The current study addressed therefore Notch signalling as a potential initiator of the OLFM4 expression in a STm infection context and could show that OLFM4 expression is significantly reduced under Notch inhibition via application of the γ-secretase inhibitor DAPT (De Strooper et al., 1999). As TNF-α is a well-known cytokine that is induced during STm infection (Arnold

et al. 1993) and was also secreted by the IECs of the hITM-SIS, it could also contribute to the observed OLFM4 upregulation. Based on these observations STm-associated OLFM4 gene and protein expression is regulated via the Notch pathway, a fact that was not described so far in STm infection context. Furthermore, the observation in this study (increased OLFM4 expression) indicates indirectly an activation of the Notch pathway during STm infection in epithelial cells. In future studies, the implication of the Notch pathway in STm infection biology should be further investigated; with application of additional Notch pathway inhibitor, such as DBZ, or with the application of conditional Notch-knockout IECs, the importance and relevance of Notch mediated OLFM4 expression in this context could be underlined.

So far, Notch signalling in the intestinal epithelial tissue was mostly under investigation with the prospective of cell lineage development. Thus, it is important in concert with Wnt/β-catenin signalling in the cell fate determination in the intestinal cell composition. The development of an intestinal stem cell into the absorptive lineage is regulated via Notch activation and subsequent HES1 activation, which inhibits ATOH1 and hence secretory lineage differentiation (Figure 28) (Quach et al., 2022; VanDussen et al., 2012). By interfering with the Notch signalling via DAPT application, the cell development towards the secretory lineage is favoured as previous studies reported a Notch dependent secretory cell hyperplasia in mice (VanDussen et al., 2012). In addition, the Notch pathway regulates OLFM4 and LGR5 expression and hence contribute to the maintenance of the stem cell population (Carulli et al., 2015; VanDussen et al., 2012). However, just recently the involvement of Notch signalling in the context of infection diseases was reviewed with the conclusion that Notch signalling contributes to immune modulation of the innate and adaptive immune response (Castro et al., 2021). The authors pointed out that further investigation, especially on the functional level is needed. In the present study, a time-dependent Notch pathway activation in STm infected cells is indirectly indicated by the increased OLFM4 expression. This implications are in contrast of a study by Quach et al. in 2022, which states a Notch inhibition by STm infection of murine organoid derived monolayers. They further observed a shift in gene expression towards the secretory lineage and a downregulation of Enterocyte specific genes; the expression of OLFM4 or LGR5 as stem cell gene expression marker was unfortunately not addressed. The authors concluded from their results a directed shift in cellular identity towards the secretory lineage by the infection with STm. Other pathogens lead to activation of the Notch signalling: *Desulfovibrio vulgaris* l in epithelial cell lines and in the mouse intestine (Singh et al., 2021), *L. intracellularis* in the porcine intestine (Huan et al., 2017), and *Ehrlichia chaffeensis* in monocyte cell lines (Lina et al., 2016). The observed discrepancy could be a manner of species specificity of STm infection

biology. In order to elucidate this observation, the Notch activation luciferase reporter system of Kuno et al. 2021 should be applied in a mouse versus human cell line during STm infection, which would allow insight species dependent Notch activation mechanism during STm infection.

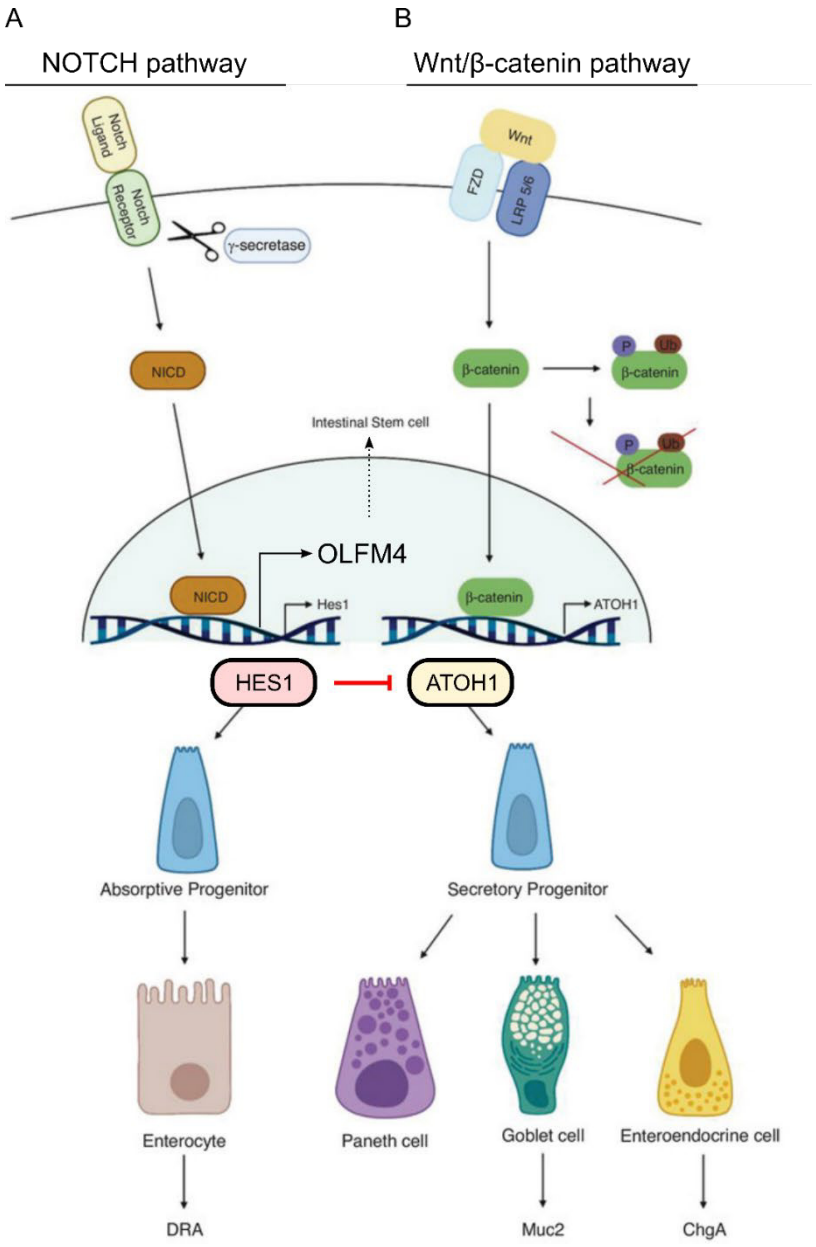

Figure 28. Schematic depiction of intestinal cell fate determination by Notch and Wnt/β-catenin signalling. Adapted from Quach et al. 2022

In addition to the reduction of OLFM4 by Notch pathway inhibition, a morphological change of the intracellular STm was observed: the filamentous STm showed shorter filaments and compact cluster formation under Notch inhibition. The mechanisms behind the formation of

intracellular filamentous. STm are poorly understood, but filamentous STm are generally considered as environmentally stressed bacteria (Lensmire et al., 2018). Hence, the observed morphological change indicated a transition from “stressed” to “less-stressed” intracellular bacteria during OLFM4 reduction by Notch inhibition. This could indicate that the reduction of OLFM4 leads to a more beneficial intracellular environment for the STm and would therefore assign a role of OLFM4 in antimicrobial intracellular processes. However, one has to consider that the DAPT based Notch inhibition might influence other antimicrobial processes or the bacteria activity directly. In order to further investigate these mechanisms, the application of IECs with a conditional Knockout for OLFM4 in the hITM-SIS would give insights in function of OLFM4 during STm infection.

5.3 Limitations of the study

In this study, we demonstrated the use of the hITM-SIS system in infectious research and its potential in basic research; however, there are also limitations of the model. First, although representing several important intestinal cell types, the hITM-SIS epithelium does not represent all mature intestinal cell types that are found in the native tissue; such as mature canonical Goblet cells (Kim and Ho, 2010), mature Paneth cells (Clevers and Bevins, 2013), EE cells; including I-, K-, L-, M-, N-, D-, Entorochromaffin cells) (Worthington et al., 2018) or Tuft cells (Gerbe and Jay, 2016). Thus, Goblet and Paneth cells secrete antimicrobial peptides and/or a barrier mucus under physiological conditions, which could impair the bacterial adherence or the invasion to the epithelial layer *in vivo*. However, this aspect would presumably affect the initial invasion processes, but would rather not affect the observed upregulation of OLFM4 and its downstream activity during intracellular STm progression. Further refinement of the differentiation protocol could increase the cellular diversity, for example by application of MAPK inhibitor and BMP4 the EE population can be induced (Beumer et al., 2018; Pleguezuelos-manzano et al., 2020).

Furthermore, the study focused on the isolated epithelial reaction to the encountered pathogen; by the incorporation of a stromal, endothelial and/or immune component, we could improve the translatability to the human pathology. In the case of STm for example it is known that macrophages are actively infected after crossing the epithelial barrier, followed by a systemic dissemination to the spleen and liver (Kurtz et al., 2017). By implementing macrophages in the hITM-SIS and connecting the basolateral compartment to a tissue engineered spleen and or liver (Broutier et al., 2016; Zanardo et al., 2020), the dissemination process could be addressed. Finally, our model relies on adult stem cell derived enteroids, which inherently represents the specific background of their donor origin. By application of various alternative donors in the hITM-SIS system with, could exclude donor specific effects for general scientific assumptions, but more importantly we could also investigate potential risk factors of specific patients. Finally, Notch inhibition is addressed broadly with the y-secretase inhibitor DAPT, therefore potential site-effects of that specific substance cannot be excluded.

5.4 Outlook

In the future, the field of intestinal tissue engineering must aim to increase the functional and physiological relevance in terms of mimicking the native tissue with highest standards. To achieve this, the focus must be on the native tissue and its properties

The hITM-SIS can provide a valid representation of the cellular properties of the intestinal epithelium in combination with a methodologically applicable approach for infection studies. The next generation of intestinal *in vitro* tissue models must include parameters that are more sophisticated. As summarised in Figure 29, a multitude of native characteristics have to be addressed in this context, especially micro environmental factors and structures, as these have to be shown recently to play a fundamental role for tissue homeostasis and function. For example, Gjorevski et al. demonstrated the importance of a proper 3D structure by showing that crypt geometry contributes massively to the regulation of cell development *in vivo* (Gjorevski et al., 2022). This is an important issue that could be addressed in the future by the development of hydrogel based printing/moulding/stamping approaches to generate the crypt-villus structure of the intestine. Of note, the characteristics of such a hydrogel itself are extremely important as the biophysical parameters of the scaffold are crucial for its function *in vivo* and, consequently, *in vitro*. These include biocompatibility, biostability, stiffness, elasticity, nanostructure organisation and functionality as well as balanced fabrication characteristics (Aisenbrey and Murphy, 2020; Gjorevski et al., 2016; Heo et al., 2022; Padhi and Nain, 2020).

In addition, bioscaffold-based approaches with sustained 3D structure were interesting, but unfortunately failed so far. Beside the structural component, biomechanical stimuli such as dynamic flow were already proven to be important (Schweinlin et al., 2016), but could be further extended by the application of passive contraction and contractile fibres, thereby simulating the gut peristaltic. Further, important gradients, such as the oxygen (O_2) distribution, should be considered, as the O_2 concentration is 8-fold higher in the crypt region compared to the villus region (Zheng et al., 2015); an aspect, which has been mostly neglected so far in most model systems. In this context also vascularisation is an important criteria of future *in vitro* models, which provides the mucosa with O_2, but also with nutrients and in the end with cells of the immune system. The immune system in concert with microbial community plays an important role in disease development, for instance the development of IBD was connected to a cross-talk of epithelial and immune cells and the microbiome (Al-Ghadban et al., 2016). These aspects and more should be considered in the future in order to develop an adequate *in vitro*

representation of the intestinal tissue (Däullary et al., 2020). Promising approaches are organ-on-chip systems and hydrogel-based recapitulation of the gut (Bein et al., 2018; Nikolaev et al., 2020)

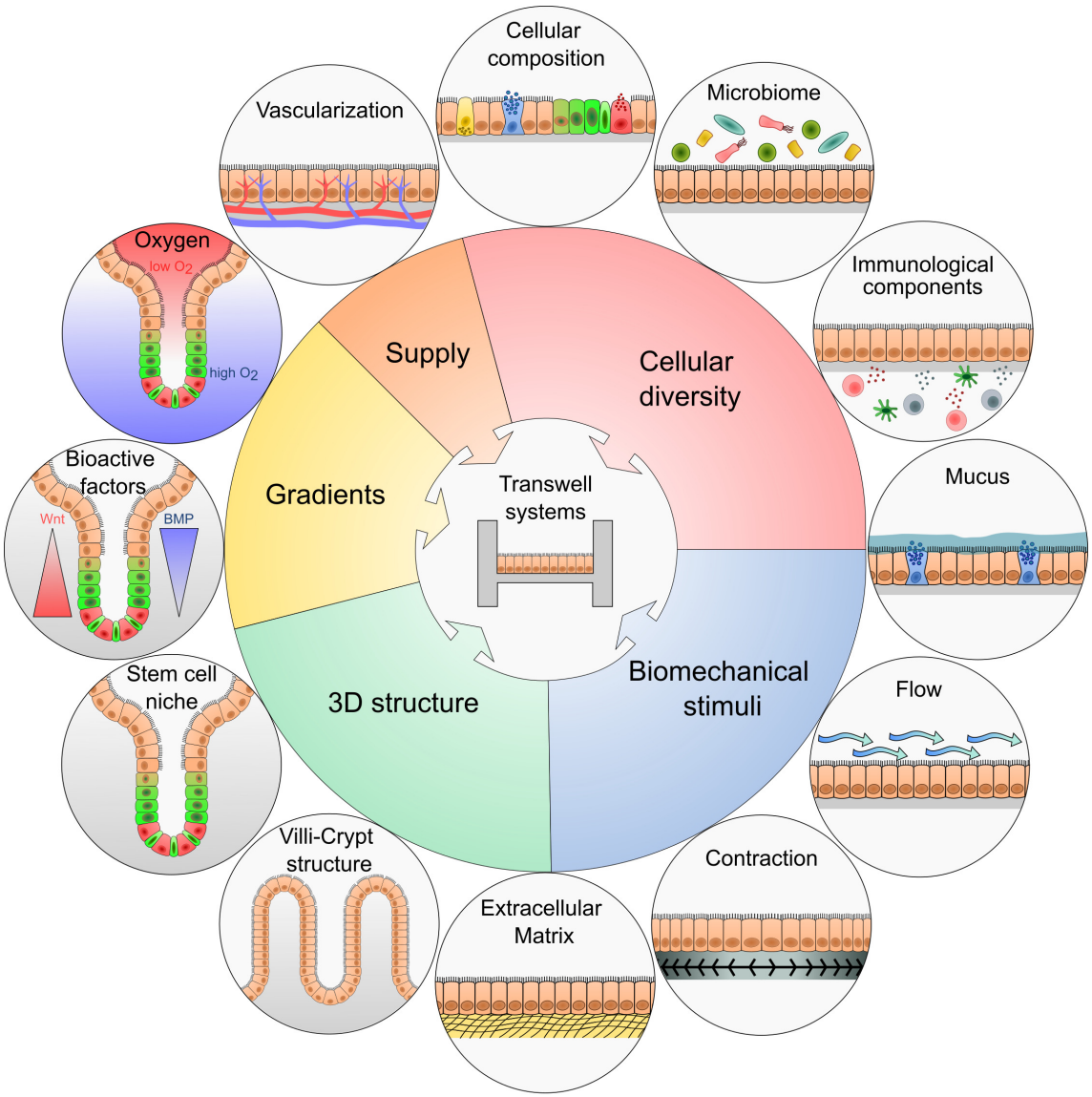

Figure 29. Outlook of characteristics for future intestinal *in vitro* modelling. Schematic depiction of the parameters that could and should considered when developing next generation intestinal tissue models. Adapted from Däullary et al., 2020.

With the platform technology of the current study, the STm infection biology of epithelial cells could be adequately represented, which led to the identification of OLFM4 as potential cellular response against intracellular STm. In future studies, the concrete function of that protein needs to be investigated and clarified. With that also the controversy of OLFM4 as stem cell marker (Liu and Rodgers, 2022b) might be concluded when the canonical cellular function in epithelial cells is finally determined. In order to investigate a potential antimicrobial function without the

bias of an unspecific inhibitor, the generation of an OLFM-4 specific conditional Knock-out organoid line would be beneficial. Until recently, genomic editing in organoids was inefficient and laborious, but Sun et al. published a straight forward toolbox for gene-editing in ASC-derived organoids (Sun et al., 2021). With the use of a conditional OLFM4 knockout organoid line in the hITM-SIS setup, the expression of OLFM4 could be inhibited in dependency of STm infectious condition with subsequent evaluation of the STm pathogenicity.

Furthermore, the upregulation of OLFM4 expression was identified by the application of scRNA-seq to infected cells. Unfortunately, was the significance and the interpretation impeded by the complexity of the dataset. For example, the identification of some cell types was difficult as the gene expression was unclear, which could have been induced by STm. Therefore, the original cell marker expression was masked by the newly induced genes upon infection. In order to circumvent this issue, the application of a time-resolved measurement of newly synthesized and existing RNA, so called SLAMseq, could dissect the STm infection induced transcripts from the original cell type on single cell level (Herzog et al., 2017). By that, specific cellular responses could be addressed in a time-dependent manner and in combination with prior sorting of the differently burdened cells also in a bacterial load-dependent manner. Furthermore, an orchestra of mechanisms between host and pathogen might underlie the heterogeneous behaviour of intracellular STm. In order to resolve such phenomenon, bacterial and simultaneously the host transcriptomic changes could be addressed by single-cell-dual-RNA sequencing (scDual-Seq) (Avital et al., 2017). With the representation of the native cellular characteristics as well as of the STm infection biology and in combination with the potential technological approaches, the hITM-SIS platform fulfils the ideal requirements to gain insights into fundamental questions regarding epithelial host and STm biology with human relevance. Taken together, the hITM-SIS model system represents an additional tool in the application box for enteric infectious research that will help to support fundamental findings in the field.

6 Appendix

Table 24. List of genes applied for cell type identification, including abbreviation

Gene Abbreviation	Gene name	Reference	Cell type	
PCNA	proliferating cell nuclear antigen	1), 2)	Proliferating Transit-Amplifying (TA)	
MKI67	marker of proliferation Ki-67	1), 2)		
TOP2A	DNA topoisomerase II alpha	1), 2)		
NUSAP1	nucleolar and spindle-associated protein 1	1)		
CCNA2	cyclin A2	1)		
MCM5	minichromosome maintenance complex component 5	1), 3)		
LGR5	leucine rich repeat containing G protein-coupled receptor 5	1), 2)	stem Cells	
ASCL2	achaete-scute family bHLH transcription factor 2	2), 4)		
SOX4	SRY-box transcription factor 4	1), 2)		
(OLFM4)	olfactomedin 4	2), 5), 6)		
FABP5	fatty acid binding protein 5	1), 7)	Progenitor	
GPX2	glutathione peroxidase 2	8)		
CDK6	cyclin dependent kinase 6	1)		
ALPI	alkaline phosphatase, intestinal	9)	Enterocytes	immature
FABP2	fatty acid binding protein 2	2)		
TMEM37	transmembrane protein 37	1)		
RBP2	retinol binding protein 2	2)		mature
CYP3A4	cytochrome P450 family 3 subfamily A member 4			
APOA4	apolipoprotein A4	2), 10)		
TFF1	trefoil factor 1	11)	Secretory	
RAB3B	RAB3B, member RAS oncogene family			
DUOX2	dual oxidase 2			
HLA-E	major histocompatibility complex, class I, E			
CCL20	C-C motif chemokine ligand 20	2)	M-like	
TNFAIP2	TNF alpha induced protein 2	7), 12)		
CXCL3	C-X-C motif chemokine ligand 3			
LAMC2	laminin subunit gamma 2	13)		
TM4SF1	transmembrane 4 L six family member 1	13)		
HLA-G	major histocompatibility complex, class I, G		HLA-G+	
APOL4	apolipoprotein L4			
TRIP6	thyroid hormone receptor interactor 6			
SULT1C2	sulfotransferase family 1C member 2			
MTRNR2L12	MT-RNR2 like 12 (pseudogene)		Dead/Empty	

1) (Wang et al., 2020), 2) (Elmentaite et al., 2021), 3) (Ayyaz et al., 2019), 4) (Murata et al., 2020), 5) (van der Flier et al., 2009), 6) (Suzuki et al., 2018), 7) (Haber et al., 2017), 8) (Andreas E Moor et al., 2018), 9) (Tetteh et al., 2016), 10) (Yu et al., 2021), 11) (Shaoul et al., 2004), 12) (Kanaya et al., 2018), 13) (Anderle et al., 2005)

Table 25. List of Cytokines including function

#	Gene	Function		#	Gene	Function		#	Gene	Function
1.	*IL1A*	Pro		**16.**	*IL12B*	anti		**31.**	*IL24*	anti
2.	*IL1B*	pro		**17.**	*IL13*	pro		**32.**	*IL25*	adaptiv
3.	*IL1F10*	pro		**18.**	*IL15*	pro		**33.**	*IL26*	pro
4.	*IL1RN*	anti		**19.**	*IL16*	pro		**34.**	*IL27*	adaptiv
5.	*IL2*	adaptiv		**20.**	*IL17A*	pro		**35.**	*IL31*	pro
6.	*IL3*	adaptiv		**21.**	*IL17B*	pro		**36.**	*IL32*	pro
7.	*IL4*	adaptiv		**22.**	*IL17C*	pro		**37.**	*IL33*	pro
8.	*IL5*	adaptiv		**23.**	*IL17D*	pro		**38.**	*IL34*	anti
9.	*IL6*	pro		**24.**	*IL17F*	pro		**39.**	*IL36A*	pro
10.	*IL7*	adaptiv		**25.**	*IL18*	pro		**40.**	*IL36B*	pro
11.	*CXCL8*	pro		**26.**	*IL19*	unknown		**41.**	*IL36G*	pro
12.	*IL9*	adaptiv		**27.**	*IL20*	unknown		**42.**	*IL36RN*	anti
13.	*IL10*	anti		**28.**	*IL21*	adaptiv		**43.**	*IL37*	anti
14.	*IL11*	pro		**29.**	*IL22*	anti				
15.	*IL12A*	anti		**30.**	*IL23A*	pro				

Table 26. IL-8 and TNF concentration in pg/ml

IL-8	**Mean**	**SD**		**TNFa**	**Mean**	**SD**
	MOI10 apical				MOI10 apical	
1.5h	0	0		**1.5h**	0,015	0,03354102
3.5h	1303,81333	664,47831		**3.5h**	10,54	7,36354308
5.5h	3505,02833	2408,33818		**5.5h**	7,17333333	6,81935888
9.5h	7133,30333	4473,91272		**9.5h**	6,435	6,61982817
17.5h	11975,26	9016,37809		**17.5h**	8,23333333	8,75840866
25.5h	21740,962	11528,8609		**25.5h**	0,658	0,78466298
	MOI10 basolateral				MOI10 basolateral	
1.5h	0	0		**1.5h**	0	0
3.5h	3735,40667	2249,59421		**3.5h**	10,906	14,0385948
5.5h	5307,99667	2260,76251		**5.5h**	2,77	0,60099917
9.5h	6652,215	1608,8902		**9.5h**	4,41	4,03106438
17.5h	11560,4333	2197,37186		**17.5h**	3,34	1,95653776
25.5h	14536,79	3485,06241		**25.5h**	2,298	2,0886589
	mock apical				mock apical	
1.5h	16,2975	20,620078		**1.5h**	0	0
3.5h	413,905	380,305		**3.5h**	1,28	0,38
5.5h	1073,59	1740,80483		**5.5h**	1,6275	2,2246952
9.5h	156,14	0		**9.5h**	1,59	0
17.5h	2070,18	0		**17.5h**	1,46	0
25.5h	10685,1033	9656,57939		**25.5h**	0,34666667	0,4902607
	mock basolateral				mock basolateral	
1.5h	47,9925	49,8289682		**1.5h**	0,0625	0,10825318
3.5h	330,65	271,81		**3.5h**	1,525	0,275
5.5h	519,77	584,849474		**5.5h**	0,5325	0,71040042
9.5h	694,71	0		**9.5h**	1,39	0
17.5h	1911,83	0		**17.5h**	0,9	0
25.5h	6959,33	6532,40058		**25.5h**	1,07333333	1,51792256

Table 27. Percentage of OLFM4mRNA+ cells

	mock		MOI10 bystander		MOI10 infected	
	Mean	**SD**	**Mean**	**SD**	**Mean**	**SD**
1.5h	1.32	0.30	2.08	1.32	2.28	1.45
5.5h	0.34	0.13	1.86	0.71	8.81	5.18
9.5h	0.42	0.02	2.46	0.78	11.76	4.60
17.5h	2.81	2.32	2.26	1.57	18.50	5.08
25.5h	3.44	1.00	3.42	0.53	31.50	8.01

Table 28. Values for calculation of the relative nucleus position

	D_{apical} **Distance of nucleus from apical surface (mean)**	**H_{cell}** **Cell height (mean)**	**$P_{r(nucleus)}$** **Relative nucleus position (basolateral: $P_{r(nucleus)} = 1$, apical: $P_{r(nucleus)} = 0$)**
hITM-SIS	17.91	40.82	0.44
hITM-PET	4.917	17.35	0.28

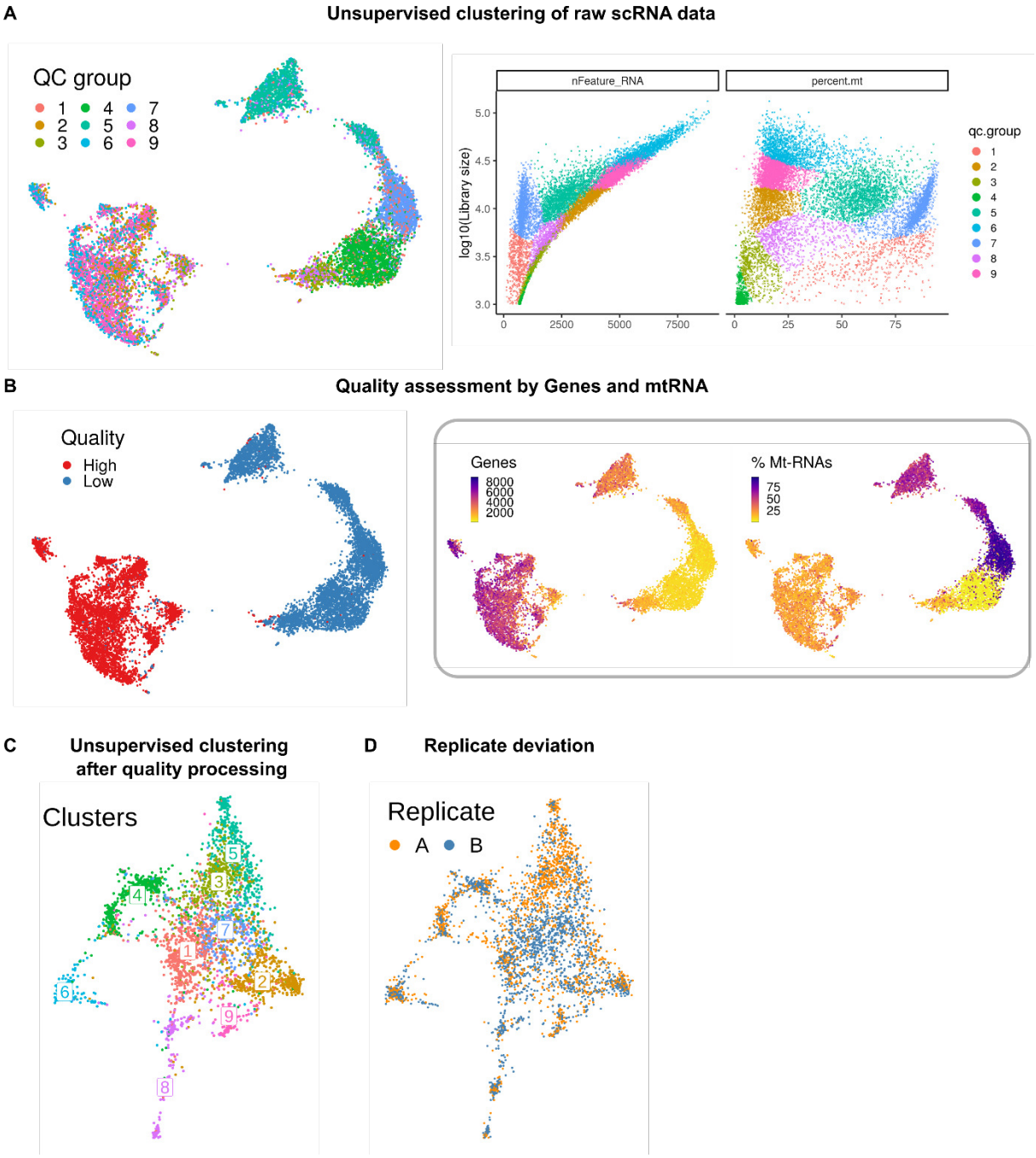

Appendix Figure 1. scRNA quality processing of hITM-SIS. A left UMAP of unsupervised clustering of the raw scRNA sequencing data the hITM-SIS for Quality control (QC). In total, 11727 IECs resulted in 9 clusters. **A right** Depiction of detected number of genes (=nfeature_RNA) and percentage of detected mitochondrial RNA (percent.mt) per single data point. **B left** UMAP of quality classification in high quality with high number of detected genes (Genes) and low percentage of mitochondrial RNA (Mt-RNA) and low quality with low number of genes and high percentage of Mt-RNA according to **B right. C** UMAP of unsupervised clustering of high quality cells (3360) from B, resulting in 9 distinct clusters, which were annotated in figure 4B. **F** UMAP representing distribution of two replicates over the clustering.

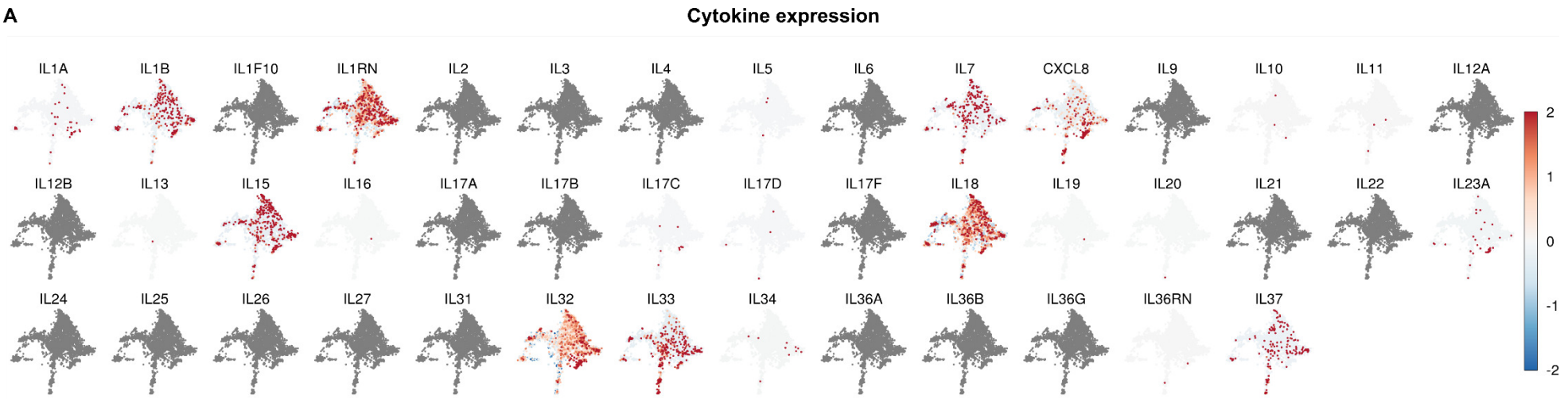

Appendix Figure 2. Cytokine expression of IECs from the hITM. A UMAPs of scaled expression of Cytokines (Table 25) of the hITM-SIS. Grey UMAPs indicated no detected RNAs for the indicated Cytokine

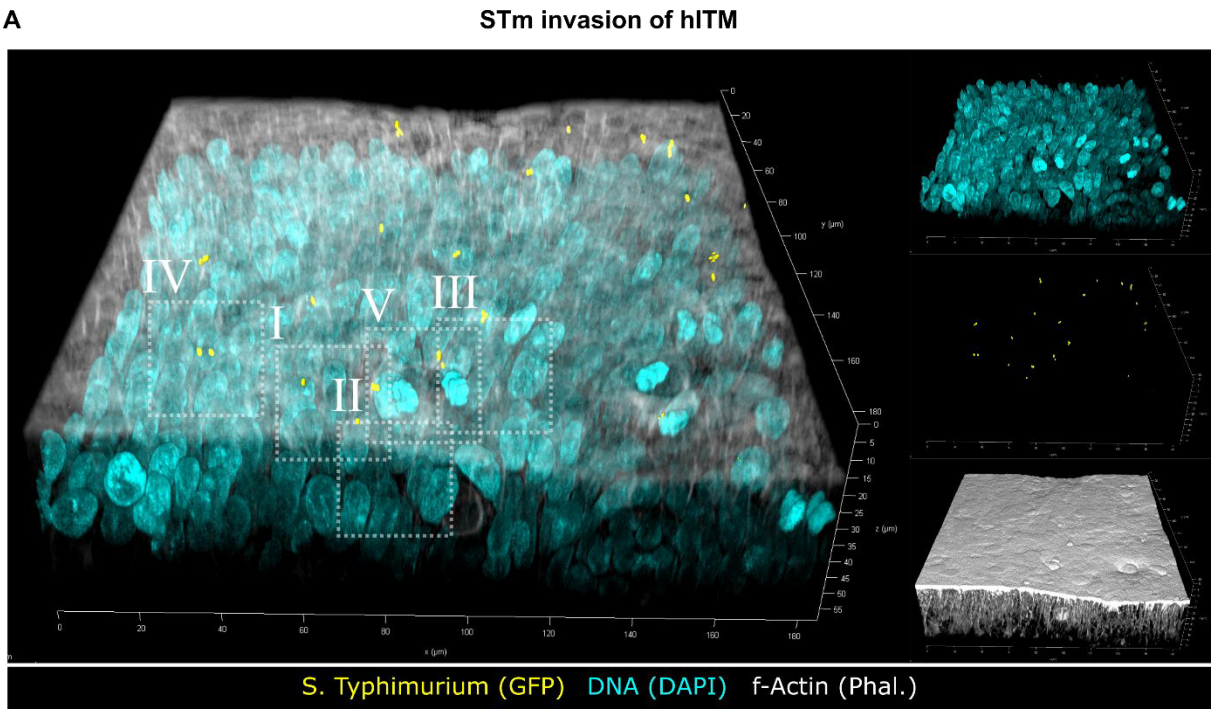

Appendix Figure 3. Invasion of STm into hITM-SIS cells by actin remodelling. A Immunofluorescent based 3D projection of STm infected hITM-SIS at 1h post adhesion with STm (GFP) in yellow, DNA (DAPI) in cyan and F-actin (Phalloidin) in grey. The left side displays the merged image of the individual channels on the right with reduction in opacity of the F-actin channel (top: DNA, mid: STm, bot: F-actin). Numbers indicate the regions, which are depicted in Fig. 7C. (n=1)

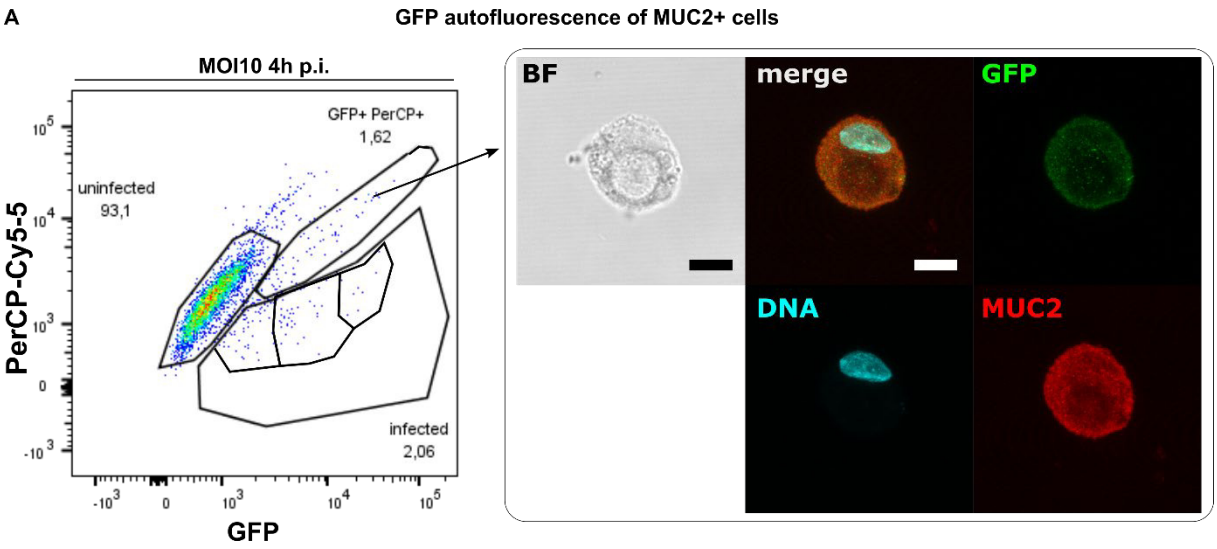

Appendix Figure 4. MUC2+ cells show auto fluorescence in GFP and PerCP-Cy5-5. A Left flow cytometry for plot revealed cells with autofluorescence in GFP and PerCP-Cy5-5 channel, which were positively stained for MUC2 in immunohistochemistry after sorting (right).(n=1)

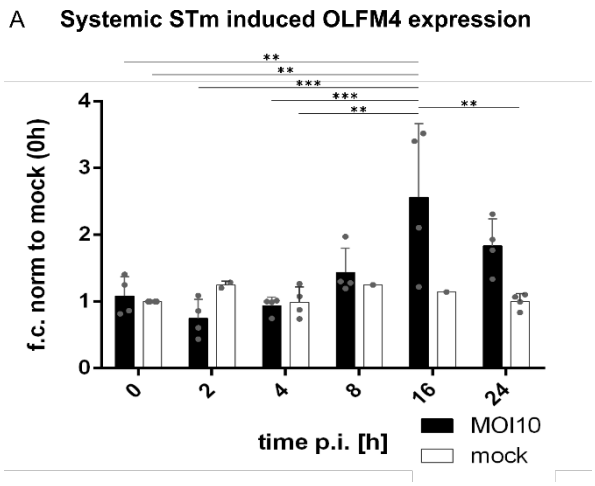

Appendix Figure 5. STm induces OLFM4 gene expression in time-dependent manner. A Systemic gene expression of OLFM4 of MOI10 and mock at 1.5h, 5.5h, 9.5h, 17.5h, and 25.5h p.a. shows STm induced and time-dependent increase of OLFM4 expression. Values are normalised to mock 1.5h. (n=3 for MOI10 and mock 1.5h, 5.5h and 25.5h p.a., n=1 for mock 9.5h, 17.5h p.a.) Significance was calculated comparing the conditions within each time point via ordinary two-way ANOVA with statistically significant differences ($F(5, 28) = 2.945$, $p = 0.0293$) and Tukey's multiple comparisons test for C with ***= $P \leq 0.001$, **= $P \leq 0.01$. Non-significant P-values are not displayed.

7 List of figures

Main figures

Appendix figures

8 List of tables

9 List of abbreviations

AJ	adherens junction
ASC	adult stem cells
ATOH1	atonal homolog 1
BMI1	polycomb complex protein 1
BMP	bone morphogenic proteins
CCA	cell-cell adhesion
CCJ	cell-cell junction
CMA	cell-matrix anchoring
CRB	Crumbs
DALY	Disability-Adjusted Life Years
DAMP	damage-associated molecular pattern
DAP	d-glutamyl-meso-diaminopimelic acid
DI	discreet invasion
Dkk1	Dickkopf-1
Dll	Delta-like
DNA	Deoxyribonucleic acid
ECAD	Ecadherin
ECM	Extra cellular matrix
EE	Enteroendocrine
EIJ	epithelial intercellular junction
EPHB	ephrin
EPP	epithelial polarity programme
ESC	embryonic stem cells
FACS	fluorescent activated cell sorting
F-actin	filamentous actin
FAE	follicle-associated epithelium
FGF-2	fibroblast growth factor 2
GI	gastrointestinal
GJ	gap junction
HG	high Gentamicin
HH	hedgehog
hITM	human intestinal epithelial tissue model
HIV	human immunodeficiency
IBD	inflammatory bowel disease
ICH	Immunohistochemistry
IEC	intestinal epithelial cell
IGF-1	insulin-like growth factor 1
IL	Interleukin
ILR	Interleukin receptor
ISC	intestinal stem cell
LAMP	Lysosomal-associated membrane protein
LB	Lennox broth
LG	low Gentamicin
LI	large intestine

LYS	Lysozyme
MAPK	mitogen-activated protein kinase
M-cells	microfold cells
MDP	muramyl dipeptide
MOI	multiplicity of infection
MUC	mucin
NLRs	Nod like receptors
NOD	nucleotide binding oligomerization domain containing 1
NOG	Noggin
NTS	non-typhoidal
OD	optical density
OD 600	OD at 600 nm
OLFM4	Olfactomedin 4
PAMP	pathogen-associated molecular pattern
PAR	partitioning defective
PC	polycarbonate
pCK	pan Cytokeratin
PE	polyester
PET	polyethylene terephthalate
PP	Peyers Patches
PRR	Pattern recognition receptors
PSC	pluripotent stem cells
RANKL	Receptor Activator of NF-κB Ligand
RI	ruffle-induced invasion
RNA	Ribonucleic acid
rpm	rounds per minute
RSPO	R-Spondin
RT	room temperature
SC	stem cell
SCRIB	Scribble
scRNA	single cell RNA
SCV	*Salmonella* containing vacuole
SEM	scanning electron microscopy
seq	sequencing
SI	small intestine
SIF	*Salmonella* induced filaments
SIS	small intestinal submucosa
SIT	*Salmonella* induced tubules
SMAD	Mothers against decapentaplegic homolog
SOCS3	Suppressor of Cytokine Signalling 3
SPI	*Salmonella* pathogenicity island
STAT	signal transducers and activators of transcription
STm	*Salmonella* Typhimurium
T3SS	Type three secretion system

TA	transit amplifying
TEER	transepithelial electrical resistance
TEM	transmission electron microscopy
TJ	tight junction
TNF	tumour necrosis factor
VIL1	Vilin-1
WNT3a	Wnt3a
ZO	Zona Occludens

10 References

Abbot, E.S., 1916. The Causal Relations between Structure and Function in Biology. Am. J. Psychol. 27, 245. https://doi.org/10.2307/1413176

Ackermann, M., 2015. A functional perspective on phenotypic heterogeneity in microorganisms. Nat. Rev. Microbiol. 2015 138 13, 497–508. https://doi.org/10.1038/nrmicro3491

Aguilar, C., Alves da Silva, M., Saraiva, M., Neyazi, M., Olsson, I.A.S., Bartfeld, S., 2021. Organoids as host models for infection biology – a review of methods. Exp. Mol. Med. 2021 5310 53, 1471–1482. https://doi.org/10.1038/s12276-021-00629-4

Aguilar, C., Pauzuolis, M., Pompaiah, M., Vafadarnejad, E., Arampatzi, P., Fischer, M., Narres, D., Neyazi, M., Kayisoglu, Ö., Sell, T., Blüthgen, N., Morkel, M., Wiegering, A., Germer, C.-T., Kircher, S., Rosenwald, A., Saliba, A.-E., Bartfeld, S., 2022. Helicobacter pylori shows tropism to gastric differentiated pit cells dependent on urea chemotaxis. Nat. Commun. 13, 5878. https://doi.org/10.1038/s41467-022-33165-4

Aisenbrey, E.A., Murphy, W.L., 2020. Synthetic alternatives to Matrigel. Nat. Rev. Mater. 2020 57 5, 539–551. https://doi.org/10.1038/s41578-020-0199-8

Akdis, M., Aab, A., Altunbulakli, C., Azkur, K., Costa, R.A., Crameri, R., Duan, S., Eiwegger, T., Eljaszewicz, A., Ferstl, R., Frei, R., Garbani, M., Globinska, A., Hess, L., Huitema, C., Kubo, T., Komlosi, Z., Konieczna, P., Kovacs, N., Kucuksezer, U.C., Meyer, N., Morita, H., Olzhausen, J., O'Mahony, L., Pezer, M., Prati, M., Rebane, A., Rhyner, C., Rinaldi, A., Sokolowska, M., Stanic, B., Sugita, K., Treis, A., van de Veen, W., Wanke, K., Wawrzyniak, M., Wawrzyniak, P., Wirz, O.F., Zakzuk, J.S., Akdis, C.A., 2016. Interleukins (from IL-1 to IL-38), interferons, transforming growth factor β, and TNF-α: Receptors, functions, and roles in diseases. J. Allergy Clin. Immunol. 138, 984–1010. https://doi.org/10.1016/J.JACI.2016.06.033/ATTACHMENT/37979BDC-86F0-44E4-BF67-9792F020AE14/MMC4.DOCX

Akdis, M., Burgler, S., Crameri, R., Eiwegger, T., Fujita, H., Gomez, E., Klunker, S., Meyer, N., O'Mahony, L., Palomares, O., Rhyner, C., Ouaked, N., Quaked, N., Schaffartzik, A., Van De Veen, W., Zeller, S., Zimmermann, M., Akdis, C.A., 2011. Interleukins, from 1 to 37, and interferon-γ: receptors, functions, and roles in diseases. J. Allergy Clin. Immunol. 127, 701-21.e1-70. https://doi.org/10.1016/j.jaci.2010.11.050

Al-Ghadban, S., Kaissi, S., Homaidan, F.R., Naim, H.Y., El-Sabban, M.E., 2016. Cross-talk between intestinal epithelial cells and immune cells in inflammatory bowel disease. Sci. Reports 2016 61 6, 1–13. https://doi.org/10.1038/srep29783

Alberts, B., Johnson, A., Lewis, J., Morgan, D., Raff, M., Roberts, K., Walter, P., 2015. Molecular biology of THE CELL, 6. ed. Garland Science, New York, NY.

Allaire, J.M., Crowley, S.M., Law, H.T., Chang, S.-Y., Ko, H.-J., Vallance, B.A., 2018. The Intestinal Epithelium: Central Coordinator of Mucosal Immunity. Trends Immunol. 39, 677–696. https://doi.org/10.1016/j.it.2018.04.002

Altay, G., Larrañaga, E., Tosi, S., Barriga, F.M., Batlle, E., Fernández-Majada, V., Martínez, E., 2019. Self-

organized intestinal epithelial monolayers in crypt and villus-like domains show effective barrier function. Sci. Rep. 9, 10140. https://doi.org/10.1038/s41598-019-46497-x

Álvarez-Ordóñez, A., Begley, M., Prieto, M., Messens, W., López, M., Bernardo, A., Hill, C., 2011. Salmonella spp. survival strategies within the host gastrointestinal tract. Microbiology 157, 3268–3281. https://doi.org/10.1099/mic.0.050351-0

Anderle, P., Rumbo, M., Sierro, F., Mansourian, R., Michetti, P., Roberts, M.A., Kraehenbuhl, J.P., 2005. Novel markers of the human follicle-associated epithelium identified by genomic profiling and microdissection. Gastroenterology 129, 321–327. https://doi.org/10.1053/J.GASTRO.2005.03.044/ATTACHMENT/7756F669-EB87-439F-BF7F-A8D6675FA66D/MMC6.DOC

Andrée, B., Bär, A., Haverich, A., Hilfiker, A., 2013. Small Intestinal Submucosa Segments as Matrix for Tissue Engineering: Review. Tissue Eng. Part B Rev. 19, 279–291. https://doi.org/10.1089/ten.teb.2012.0583

Apodaca, G., 2001. Endocytic Traffic in Polarized Epithelial Cells: Role of the Actin and Microtubule Cytoskeleton. Traffic 2, 149–159. https://doi.org/10.1034/J.1600-0854.2001.020301.X

Arabyan, N., Park, D., Foutouhi, S., Weis, A.M., Huang, B.C., Williams, C.C., Desai, P., Shah, J., Jeannotte, R., Kong, N., Lebrilla, C.B., Weimer, B.C., 2016. Salmonella Degrades the Host Glycocalyx Leading to Altered Infection and Glycan Remodeling. Sci. Reports 2016 61 6, 1–11. https://doi.org/10.1038/srep29525

Arends, F., Lieleg, O., 2016. Biophysical Properties of the Basal Lamina: A Highly Selective Extracellular Matrix, in: Composition and Function of the Extracellular Matrix in the Human Body. InTech. https://doi.org/10.5772/62519

Arnold, J.W., Niesel, D.W., Annable, C.R., Hess, C.B., Asuncion, M., Cho, Y.J., Peterson, J.W., Klimpel, G.R., 1993. Tumor necrosis factor-α mediates the early pathology in Salmonella infection of the gastrointestinal tract. Microb. Pathog. 14, 217–227. https://doi.org/10.1006/MPAT.1993.1021

Auclair, B.A., Benoit, Y.D., Rivard, N., Mishina, Y., Perreault, N., 2007. Bone Morphogenetic Protein Signaling Is Essential for Terminal Differentiation of the Intestinal Secretory Cell Lineage. Gastroenterology 133, 887–896. https://doi.org/10.1053/J.GASTRO.2007.06.066

Avital, G., Avraham, R., Fan, A., Hashimshony, T., Hung, D.T., Yanai, I., 2017. scDual-Seq: Mapping the gene regulatory program of Salmonella infection by host and pathogen single-cell RNA-sequencing. Genome Biol. 18, 1–8. https://doi.org/10.1186/S13059-017-1340-X/FIGURES/4

Ayyaz, A., Kumar, S., Sangiorgi, B., Ghoshal, B., Gosio, J., Ouladan, S., Fink, M., Barutcu, S., Trcka, D., Shen, J., Chan, K., Wrana, J.L., Gregorieff, A., 2019. Single-cell transcriptomes of the regenerating intestine reveal a revival stem cell. Nature (in press). https://doi.org/10.1038/s41586-019-1154-y

Barker, N., 2013. Adult intestinal stem cells: critical drivers of epithelial homeostasis and regeneration. Nat. Rev. Mol. Cell Biol. 15, 19–33. https://doi.org/10.1038/nrm3721

Barker, N., van Es, J.H., Kuipers, J., Kujala, P., van den Born, M., Cozijnsen, M., Haegebarth, A., Korving, J., Begthel, H., Peters, P.J., Clevers, H., 2007. Identification of stem cells in small intestine and colon by marker

gene Lgr5. Nature 449, 1003–7. https://doi.org/10.1038/nature06196

Barker, N., van Oudenaarden, A., Clevers, H., 2012. Identifying the stem cell of the intestinal crypt: strategies and pitfalls. Cell Stem Cell 11, 452–60. https://doi.org/10.1016/j.stem.2012.09.009

Barriga, E.H., Franze, K., Charras, G., Mayor, R., 2018. Tissue stiffening coordinates morphogenesis by triggering collective cell migration in vivo. Nat. 2018 5547693 554, 523–527. https://doi.org/10.1038/nature25742

Basak, O., Born, M. van de, Korving, J., Beumer, J., Elst, S. van der, Es, J.H. van, Clevers, H., 2014. Mapping early fate determination in Lgr5+ crypt stem cells using a novel Ki67-RFP allele. EMBO J. 33, 2057–2068. https://doi.org/10.15252/EMBJ.201488017

Batlle, E., Henderson, J.T., Beghtel, H., Born, M.M.W. Van Den, Sancho, E., Huls, G., Meeldijk, J., Robertson, J., Wetering, M. Van De, Pawson, T., Clevers, H., 2002. Beta-Catenin and TCF Mediate Cell Positioning in the Intestinal Epithelium by Controlling the Expression of EphB / EphrinB Leslie Dan Faculty of Pharmacy. Cell 111, 251–263.

Behrens, I., Kissel, T., 2003. Do cell culture conditions influence the carrier-mediated transport of peptides in Caco-2 cell monolayers? Eur. J. Pharm. Sci. 19, 433–42. https://doi.org/10.1016/S0928-0987(03)00146-5

Bein, A., Shin, W., Jalili-Firoozinezhad, S., Park, M.H., Sontheimer-Phelps, A., Tovaglieri, A., Chalkiadaki, A., Kim, H.J., Ingber, D.E., 2018. Microfluidic Organ-on-a-Chip Models of Human Intestine. Cell. Mol. Gastroenterol. Hepatol. 5, 659–668. https://doi.org/10.1016/j.jcmgh.2017.12.010

Bennett, K.M., Walker, S.L., Lo, D.D., 2014. Epithelial microvilli establish an electrostatic barrier to microbial adhesion. Infect. Immun. 82, 2860–2871. https://doi.org/10.1128/IAI.01681-14/SUPPL_FILE/ZII999090752SO1.PDF

Berger, C., Bjørlykke, Y., Hahn, L., Mühlemann, M., Kress, S., Walles, H., Luxenhofer, R., Ræder, H., Metzger, M., Zdzieblo, D., 2020. Matrix decoded - A pancreatic extracellular matrix with organ specific cues guiding human iPSC differentiation. Biomaterials 244, 119766. https://doi.org/10.1016/j.biomaterials.2020.119766

Beumer, J., Artegiani, B., Post, Y., Reimann, F., Gribble, F., Nguyen, T.N., Zeng, H., Van den Born, M., Van Es, J.H., Clevers, H., 2018. Enteroendocrine cells switch hormone expression along the crypt-to-villus BMP signalling gradient. Nat. Cell Biol. 2018 208 20, 909–916. https://doi.org/10.1038/s41556-018-0143-y

Beumer, J., Clevers, H., 2020. Cell fate specification and differentiation in the adult mammalian intestine. Nat. Rev. Mol. Cell Biol. 2020 221 22, 39–53. https://doi.org/10.1038/s41580-020-0278-0

Beumer, J., Gehart, H., Clevers, H., 2020. Enteroendocrine Dynamics – New Tools Reveal Hormonal Plasticity in the Gut. Endocr. Rev. 41. https://doi.org/10.1210/ENDREV/BNAA018

Birchenough, G.M.H., Nyström, E.E.L., Johansson, M.E. V, Hansson, G.C., 2016. A sentinel goblet cell guards the colonic crypt by triggering Nlrp6-dependent Muc2 secretion. Science 352, 1535–42. https://doi.org/10.1126/science.aaf7419

Biteau, B., Jasper, H., 2011. EGF signaling regulates the proliferation of intestinal stem cells in Drosophila. Development 138, 1045–1055. https://doi.org/10.1242/DEV.056671

Bjerknes, M., Khandanpour, C., Möröy, T., Fujiyama, T., Hoshino, M., Klisch, T.J., Ding, Q., Gan, L., Wang, J., Martín, M.G., Cheng, H., 2012. Origin of the brush cell lineage in the mouse intestinal epithelium. Dev. Biol. 362, 194–218. https://doi.org/10.1016/j.ydbio.2011.12.009

Bonis, V., Rossell, C., Gehart, H., 2021. The Intestinal Epithelium - Fluid Fate and Rigid Structure From Crypt Bottom to Villus Tip. Front. cell Dev. Biol. 9, 661931. https://doi.org/10.3389/fcell.2021.661931

Böttcher, A., Büttner, M., Tritschler, S., Sterr, M., Aliluev, A., Oppenländer, L., Burtscher, I., Sass, S., Irmler, M., Beckers, J., Ziegenhain, C., Enard, W., Schamberger, A.C., Verhamme, F.M., Eickelberg, O., Theis, F.J., Lickert, H., 2021. Non-canonical Wnt/PCP signalling regulates intestinal stem cell lineage priming towards enteroendocrine and Paneth cell fates. Nat. Cell Biol. 23, 23–31. https://doi.org/10.1038/s41556-020-00617-2

Breau, K.A., Ok, M.T., Gomez-Martinez, I., Burclaff, J., Kohn, N.P., Magness, S.T., 2022. Efficient transgenesis and homology-directed gene targeting in monolayers of primary human small intestinal and colonic epithelial stem cells. Stem cell reports 17, 1493–1506. https://doi.org/10.1016/j.stemcr.2022.04.005

Brenner, F.W., Villar, R.G., Angulo, F.J., Tauxe, R., Swaminathan, B., 2000. Salmonella nomenclature. J. Clin. Microbiol. 38, 2465–2467. https://doi.org/10.1128/JCM.38.7.2465-2467.2000

Broutier, L., Andersson-Rolf, A., Hindley, C.J., Boj, S.F., Clevers, H., Koo, B.-K., Huch, M., 2016. Culture and establishment of self-renewing human and mouse adult liver and pancreas 3D organoids and their genetic manipulation. Nat. Protoc. 11, 1724–1743. https://doi.org/10.1038/nprot.2016.097

BROWN, A.L., 1962. Microvilli of the human jejunal epithelial cell. J. Cell Biol. 12, 623–7.

Brunet, A., Goodell, M.A., Rando, T.A., 2022. Ageing and rejuvenation of tissue stem cells and their niches. Nat. Rev. Mol. Cell Biol. 2022 241 24, 45–62. https://doi.org/10.1038/s41580-022-00510-w

Bumann, D., Cunrath, O., 2017. Heterogeneity of Salmonella-host interactions in infected host tissues. Curr. Opin. Microbiol. 39, 57–63. https://doi.org/10.1016/J.MIB.2017.09.008

Burclaff, J., Bliton, R.J., Breau, K.A., Ok, M.T., Gomez-Martinez, I., Ranek, J.S., Bhatt, A.P., Purvis, J.E., Woosley, J.T., Magness, S.T., 2022. A Proximal-to-Distal Survey of Healthy Adult Human Small Intestine and Colon Epithelium by Single-Cell Transcriptomics. Cell. Mol. Gastroenterol. Hepatol. 13, 1554–1589. https://doi.org/10.1016/J.JCMGH.2022.02.007

Burute, M., Thery, M., 2012. Spatial segregation between cell–cell and cell–matrix adhesions. Curr. Opin. Cell Biol. 24, 628–636. https://doi.org/10.1016/J.CEB.2012.07.003

Carulli, A.J., Keeley, T.M., Demitrack, E.S., Chung, J., Maillard, I., Samuelson, L.C., 2015. Notch receptor regulation of intestinal stem cell homeostasis and crypt regeneration. Dev. Biol. 402, 98–108. https://doi.org/10.1016/J.YDBIO.2015.03.012

Castanheira, S., García-Del Portillo, F., 2017. Salmonella Populations inside Host Cells. Front. Cell. Infect. Microbiol. 7, 432. https://doi.org/10.3389/fcimb.2017.00432

Castro, R.C., Gonçales, R.A., Zambuzi, F.A., Frantz, F.G., 2021. Notch signaling pathway in infectious diseases: role in the regulation of immune response. Inflamm. Res. 70, 261–274. https://doi.org/10.1007/S00011-021-

01442-5/FIGURES/3

Chabin-Brion, K., Marceiller, J., Perez, F., Settegrana, C., Drechou, A., Durand, G., Poüs, C., 2001. The Golgi complex is a microtubule-organizing organelle. Mol. Biol. Cell 12, 2047–2060. https://doi.org/10.1091/MBC.12.7.2047/ASSET/IMAGES/LARGE/MK0711545008.JPEG

Chaffer, C.L., San Juan, B.P., Lim, E., Weinberg, R.A., 2016. EMT, cell plasticity and metastasis. Cancer Metastasis Rev. 35, 645–654. https://doi.org/10.1007/S10555-016-9648-7/TABLES/1

Chantret, I., Barbat, A., Dussaulx, E., Brattain, M.G., Zweibaum, A., 1988. Epithelial polarity, villin expression, and enterocytic differentiation of cultured human colon carcinoma cells: a survey of twenty cell lines. Cancer Res. 48, 1936–42.

Chelakkot, C., Ghim, J., Ryu, S.H., 2018. Mechanisms regulating intestinal barrier integrity and its pathological implications. Exp. Mol. Med. 50, 1–9. https://doi.org/10.1038/s12276-018-0126-x

Chen, J., Zhang, M., 2013. The Par3/Par6/aPKC complex and epithelial cell polarity. Exp. Cell Res. 319, 1357–64. https://doi.org/10.1016/j.yexcr.2013.03.021

Chen, L., Lu, X., Liang, X., Hong, D., Guan, Z., Guan, Y., Zhu, W., 2016. Mechanistic studies of the transport of peimine in the Caco-2 cell model. Acta Pharm. Sin. B 6, 125–131. https://doi.org/10.1016/J.APSB.2016.01.006

Chen, S., Einspanier, R., Schoen, J., 2015. Transepithelial electrical resistance (TEER): a functional parameter to monitor the quality of oviduct epithelial cells cultured on filter supports. Histochem. Cell Biol. 144, 509–515. https://doi.org/10.1007/S00418-015-1351-1/FIGURES/4

Chin, K.L., Aerbajinai, W., Zhu, J., Drew, L.S., Chen, L., Liu, W., Rodgers, G.P., 2008. The regulation of OLFM4 expression in myeloid precursor cells relies on NF-κB transcription factor. Br. J. Haematol. 143, 421–432. https://doi.org/10.1111/J.1365-2141.2008.07368.X

Choi, H.M.T., Schwarzkopf, M., Fornace, M.E., Acharya, A., Artavanis, G., Stegmaier, J., Cunha, A., Pierce, N.A., 2018. Third-generation in situ hybridization chain reaction: Multiplexed, quantitative, sensitive, versatile, robust. Dev. 145. https://doi.org/10.1242/DEV.165753/48466

Chong, A., Cooper, K.G., Kari, L., Nilsson, O.R., Hillman, C., Fleming, B.A., Wang, Q., Nair, V., Steele-Mortimer, O., 2021. Cytosolic replication in epithelial cells fuels intestinal expansion and chronic fecal shedding of Salmonella Typhimurium. Cell Host Microbe 29, 1177-1185.e6. https://doi.org/10.1016/j.chom.2021.04.017

Ciacci-Woolwine, F., Blomfield, I.C., Richardson, S.H., Mizel, S.B., 1998. Salmonella Flagellin Induces Tumor Necrosis Factor Alpha in a Human Promonocytic Cell Line. Infect. Immun. 66, 1127. https://doi.org/10.1128/IAI.66.3.1127-1134.1998

Citi, S., 2019. The mechanobiology of tight junctions. Biophys. Rev. 11, 783. https://doi.org/10.1007/S12551-019-00582-7

Clark, M.A., Reed, K.A., Lodge, J., Stephen, J., Hirst, B.H., Jepson, M.A., 1996. Invasion of murine intestinal M cells by Salmonella typhimurium inv mutants severely deficient for invasion of cultured cells. Infect. Immun.

64, 4363–8. https://doi.org/10.1128/iai.64.10.4363-4368.1996

Clevers, H., Nusse, R., 2012. Wnt/β-catenin signaling and disease. Cell 149, 1192–205. https://doi.org/10.1016/j.cell.2012.05.012

Clevers, H.C., Bevins, C.L., 2013. Paneth cells: maestros of the small intestinal crypts. Annu. Rev. Physiol. 75, 289–311. https://doi.org/10.1146/annurev-physiol-030212-183744

Co, J.Y., Margalef-Català, M., Li, X., Mah, A.T., Kuo, C.J., Monack, D.M., Amieva, M.R., 2019. Controlling Epithelial Polarity: A Human Enteroid Model for Host-Pathogen Interactions. Cell Rep. 26, 2509-2520.e4. https://doi.org/10.1016/j.celrep.2019.01.108

Collazo, C.M., Galán, J.E., 1997. The invasion-associated type III system of Salmonella typhimurium directs the translocation of Sip proteins into the host cell. Mol. Microbiol. 24, 747–756. https://doi.org/10.1046/J.1365-2958.1997.3781740.X

Collins, J.T., Nguyen, A., Badireddy, M., 2021. Anatomy, Abdomen and Pelvis, Small Intestine [WWW Document]. StatPearls. URL https://www.ncbi.nlm.nih.gov/books/NBK459366/ (accessed 4.4.22).

Cornes, J.S., 1965. Number, size, and distribution of Peyer's patches in the human small intestine: Part I The development of Peyer's patches. Gut 6, 225–9. https://doi.org/10.1136/gut.6.3.225

Crawley, S.W., Mooseker, M.S., Tyska, M.J., 2014. Shaping the intestinal brush border. J. Cell Biol. 207, 441. https://doi.org/10.1083/JCB.201407015

Criss, A.K., Ahlgren, D.M., Jou, T.S., McCormick, B.A., Casanova, J.E., 2001. The GTPase Rac1 selectively regulates Salmonella invasion at the apical plasma membrane of polarized epithelial cells. J. Cell Sci. 114, 1331–1341. https://doi.org/10.1242/JCS.114.7.1331

Cronin, C.G., Delappe, E., Lohan, D.G., Roche, C., Murphy, J.M., 2010. Normal small bowel wall characteristics on MR enterography. Eur. J. Radiol. 75, 207–11. https://doi.org/10.1016/j.ejrad.2009.04.066

Crowe, P., Marsh, M., 1993. Morphometric analysis of small intestinal mucosa. IV. Determining cell volumes. Virchows Arch. A. Pathol. Anat. Histopathol. 422, 459–466. https://doi.org/10.1007/BF01606454

D'Costa, V.M., Braun, V., Landekic, M., Shi, R., Proteau, A., McDonald, L., Cygler, M., Grinstein, S., Brumell, J.H., 2015. Salmonella Disrupts Host Endocytic Trafficking by SopD2-Mediated Inhibition of Rab7. Cell Rep. 12, 1508–18. https://doi.org/10.1016/j.celrep.2015.07.063

da Costa Ferreira, S., Sadissou, I.A., Parra, R.S., Feitosa, M.R., Neto, F.S.L., Pretti da Cunha Tirapelli, D., Ramalho, L.N.Z., Féres, O., da Rocha, J.J.R., Donadi, E.A., de Almeida Troncon, L.E., 2021. Increased HLA-G Expression in Tissue-Infiltrating Cells in Inflammatory Bowel Diseases. Dig. Dis. Sci. 66, 2610–2618. https://doi.org/10.1007/S10620-020-06561-3/FIGURES/3

Darwich, A.S., Aslam, U., Ashcroft, D.M., Rostami-Hodjegan, A., 2014. Meta-analysis of the turnover of intestinal epithelia in preclinical animal species and humans. Drug Metab. Dispos. 42, 2016–2022. https://doi.org/10.1124/dmd.114.058404

Date, S., Sato, T., 2015. Mini-gut organoids: reconstitution of the stem cell niche. Annu. Rev. Cell Dev. Biol. 31,

269–89. https://doi.org/10.1146/annurev-cellbio-100814-125218

Däullary, T., Fey, C., Berger, C., Metzger, M., Zdzieblo, D., 2020. Bioartificial gut—current state of small intestinal tissue engineering, in: Vrana, N.E., Knopf-Marques, H., Barthes, J. (Eds.), Biomaterials for Organ and Tissue Regeneration. Elsevier, pp. 273–297. https://doi.org/10.1016/B978-0-08-102906-0.00025-8

Däullary, T., Imdahl, F., Dietrich, O., Hepp, L., Krammer, T., Fey, C., Neuhaus, W., Metzger, M., Vogel, J., Westermann, A., Saliba, A.-E., Zdzieblo, D., 2022. A primary cell-based in vitro model of the human small intestine reveals the induction of OLFM4 expression as host cell response during Salmonella Typhimurium infection. Gut Microbes. In review.

De Strooper, B., Annaert, W., Cupers, P., Saftig, P., Craessaerts, K., Mumm, J.S., Schroeter, E.H., Schrijvers, V., Wolfe, M.S., Ray, W.J., Goate, A., Kopan, R., 1999. A presenilin-1-dependent γ-secretase-like protease mediates release of Notch intracellular domain. Nat. 1999 3986727 398, 518–522. https://doi.org/10.1038/19083

Delgado, M.E., Brunner, T., 2019. The many faces of tumor necrosis factor signaling in the intestinal epithelium. Genes Immun. 2019 208 20, 609–626. https://doi.org/10.1038/s41435-019-0057-0

Diamond, C.E., Leong, K.W.K., Vacca, M., Rivers-Auty, J., Brough, D., Mortellaro, A., 2017. Salmonella typhimurium-induced IL-1 release from primary human monocytes requires NLRP3 and can occur in the absence of pyroptosis. Sci. Rep. 7. https://doi.org/10.1038/S41598-017-07081-3

Drenckhahn, D., Benninghoff, A., 2008. Anatomie: Makroskopische Anatomie, Histologie, Embryologie, Zellbiologie. Band 1.

Duncan, J.T., 1924. A “New” Salmonella from a Case of Enteric Fever. J. Hyg. (Lond). 22, 402. https://doi.org/10.1017/S0022172400008354

Dupin, I., Camand, E., Etienne-Manneville, S., 2009. Classical cadherins control nucleus and centrosome position and cell polarity. J. Cell Biol. 185, 779–86. https://doi.org/10.1083/jcb.200812034

Eckmann, L., Kagnoff, M.F., Fierer, J., 1993. Epithelial cells secrete the chemokine interleukin-8 in response to bacterial entry. Infect. Immun. 61, 4569–4574. https://doi.org/10.1128/IAI.61.11.4569-4574.1993

Elbrecht, D.H., Long, C.J., Hickman, J.J., 2016. Transepithelial/endothelial Electrical Resistance (TEER) theory and applications for microfluidic body-on-a-chip devices. J. Rare Dis. Res. Treat. 1, 46–52. https://doi.org/10.29245/2572-9411/2016/3.1026

Elmentaite, R., Kumasaka, N., Roberts, K., Fleming, A., Dann, E., King, H.W., Kleshchevnikov, V., Dabrowska, M., Pritchard, S., Bolt, L., Vieira, S.F., Mamanova, L., Huang, N., Perrone, F., Goh Kai’En, I., Lisgo, S.N., Katan, M., Leonard, S., Oliver, T.R.W., Hook, C.E., Nayak, K., Campos, L.S., Domínguez Conde, C., Stephenson, E., Engelbert, J., Botting, R.A., Polanski, K., van Dongen, S., Patel, M., Morgan, M.D., Marioni, J.C., Bayraktar, O.A., Meyer, K.B., He, X., Barker, R.A., Uhlig, H.H., Mahbubani, K.T., Saeb-Parsy, K., Zilbauer, M., Clatworthy, M.R., Haniffa, M., James, K.R., Teichmann, S.A., 2021. Cells of the human intestinal tract mapped across space and time. Nature 597, 250–255. https://doi.org/10.1038/s41586-021-03852-1

Engelmann, B., Massberg, S., 2012. Thrombosis as an intravascular effector of innate immunity. Nat. Rev. Immunol. 13, 34–45. https://doi.org/10.1038/nri3345

Engle, M.J., Goetz, G.S., Alpers, D.H., 1998. Caco-2 Cells Express a Combination of Colonocyte and Enterocyte Phenotypes. J. Cell. Physiol. 174, 362–369. https://doi.org/10.1002/(SICI)1097-4652(199803)174:3

Fang, Z., Méresse, S., 2021. Endomembrane remodeling and dynamics in *Salmonella* infection. Microb. Cell 9, 24. https://doi.org/10.15698/MIC2022.02.769

Fanning, A.S., Van Itallie, C.M., Anderson, J.M., 2012. Zonula occludens-1 and -2 regulate apical cell structure and the zonula adherens cytoskeleton in polarized epithelia. Mol. Biol. Cell 23, 577–90. https://doi.org/10.1091/mbc.E11-09-0791

Farin, H.F., Jordens, I., Mosa, M.H., Basak, O., Korving, J., Tauriello, D.V.F., De Punder, K., Angers, S., Peters, P.J., Maurice, M.M., Clevers, H., 2016. Visualization of a short-range Wnt gradient in the intestinal stem-cell niche. Nat. 2016 5307590 530, 340–343. https://doi.org/10.1038/nature16937

Fattinger, S.A., Böck, D., Di Martino, M.L., Deuring, S., Samperio Ventayol, P., Ek, V., Furter, M., Kreibich, S., Bosia, F., Müller-Hauser, A.A., Nguyen, B.D., Rohde, M., Pilhofer, M., Hardt, W.-D., Sellin, M.E., 2020. Salmonella Typhimurium discreet-invasion of the murine gut absorptive epithelium. PLoS Pathog. 16, e1008503. https://doi.org/10.1371/journal.ppat.1008503

Fattinger, S.A., Sellin, M.E., Hardt, W.D., 2021. Salmonella effector driven invasion of the gut epithelium: breaking in and setting the house on fire. Curr. Opin. Microbiol. 64, 9–18. https://doi.org/10.1016/J.MIB.2021.08.007

Feasey, N.A., Dougan, G., Kingsley, R.A., Heyderman, R.S., Gordon, M.A., 2012. Invasive non-typhoidal salmonella disease: an emerging and neglected tropical disease in Africa. Lancet 379, 2489–2499. https://doi.org/10.1016/S0140-6736(11)61752-2

Fedi, A., Vitale, C., Ponschin, G., Ayehunie, S., Fato, M., Scaglione, S., 2021. In vitro models replicating the human intestinal epithelium for absorption and metabolism studies: A systematic review. J. Control. Release 335, 247–268. https://doi.org/10.1016/J.JCONREL.2021.05.028

Felix, K., Tobias, S., Jan, H., Nicolas, S., Michael, M., 2021. Measurements of transepithelial electrical resistance (TEER) are affected by junctional length in immature epithelial monolayers. Histochem. Cell Biol. 156, 609–616. https://doi.org/10.1007/S00418-021-02026-4/FIGURES/4

Feng, J., Wang, J., Liu, Q., Li, J., Zhang, Q., Zhuang, Z., Yao, X., Liu, C., Li, Y., Cao, L., Li, C., Gong, L., Li, D., Zhang, Y., Gao, H., 2019. DAPT, a γ-secretase inhibitor, suppresses tumorigenesis, and progression of growth hormone-producing adenomas by targeting notch signaling. Front. Oncol. 9, 809. https://doi.org/10.3389/FONC.2019.00809/BIBTEX

Ferraretto, A., Bottani, M., De Luca, P., Cornaghi, L., Arnaboldi, F., Maggioni, M., Fiorilli, A., Donetti, E., 2018. Morphofunctional properties of a differentiated Caco2/HT-29 co-culture as an in vitro model of human intestinal epithelium. Biosci. Rep. 38. https://doi.org/10.1042/BSR20171497

Finlay, B.B., Falkow, S., 1990. Salmonella Interactions with Polarized Human Intestinal Caco-2 Epithelial Cells.

J. Infect. Dis. 162, 1096–1106. https://doi.org/10.1093/INFDIS/162.5.1096

Finn, C.E., Chong, A., Cooper, K.G., Starr, T., Steele-Mortimer, O., 2017. A second wave of Salmonella T3SS1 activity prolongs the lifespan of infected epithelial cells. PLOS Pathog. 13, e1006354. https://doi.org/10.1371/JOURNAL.PPAT.1006354

Fitzsimonds, Z.R., Liu, C., Stocke, K.S., Yakoumatos, L., Shumway, B., Miller, D.P., Artyomov, M.N., Bagaitkar, J., Lamont, R.J., 2021. Regulation of olfactomedin 4 by Porphyromonas gingivalis in a community context. ISME J. 2021 159 15, 2627–2642. https://doi.org/10.1038/s41396-021-00956-4

Forbester, J.L., Goulding, D., Vallier, L., Hannan, N., Hale, C., Pickard, D., Mukhopadhyay, S., Dougan, G., 2015. Interaction of salmonella enterica serovar Typhimurium with intestinal organoids derived from human induced pluripotent stem cells. Infect. Immun. 83, 2926–2934. https://doi.org/10.1128/IAI.00161-15/SUPPL_FILE/ZII999091303SD1.XLSX

Frisch, S.M., Francis, H., 1994. Disruption of epithelial cell-matrix interactions induces apoptosis. J. Cell Biol. 124, 619–26. https://doi.org/10.1083/jcb.124.4.619

Fujii, M., Matano, M., Toshimitsu, K., Takano, A., Mikami, Y., Nishikori, S., Sugimoto, S., Sato, T., 2018. Human Intestinal Organoids Maintain Self-Renewal Capacity and Cellular Diversity in Niche-Inspired Culture Condition. Cell Stem Cell 23, 787-793.e6. https://doi.org/10.1016/j.stem.2018.11.016

Fulde, M., van Vorst, K., Zhang, K., Westermann, A.J., Busche, T., Huei, Y.C., Welitschanski, K., Froh, I., Pägelow, D., Plendl, J., Pfarrer, C., Kalinowski, J., Vogel, J., Valentin-Weigand, P., Hensel, M., Tedin, K., Repnik, U., Hornef, M.W., 2021. SPI2 T3SS effectors facilitate enterocyte apical to basolateral transmigration of Salmonella-containing vacuoles in vivo. Gut Microbes 13. https://doi.org/10.1080/19490976.2021.1973836

Galán, J.E., 2021. Salmonella Typhimurium and inflammation: a pathogen-centric affair. Nat. Rev. Microbiol. 2021 1911 19, 716–725. https://doi.org/10.1038/s41579-021-00561-4

Galan, J.E., Curtiss, R., 1989a. Cloning and molecular characterization of genes whose products allow Salmonella typhimurium to penetrate tissue culture cells. Proc. Natl. Acad. Sci. 86, 6383–6387. https://doi.org/10.1073/PNAS.86.16.6383

Galan, J.E., Curtiss, R., 1989b. Cloning and molecular characterization of genes whose products allow Salmonella typhimurium to penetrate tissue culture cells. Proc. Natl. Acad. Sci. 86, 6383–6387. https://doi.org/10.1073/PNAS.86.16.6383

Galán, J.E., Zhou, D., 2000. Striking a balance: Modulation of the actin cytoskeleton by Salmonella. Proc. Natl. Acad. Sci. 97, 8754–8761. https://doi.org/10.1073/PNAS.97.16.8754

Garcia, M.A., Nelson, W.J., Chavez, N., 2018. Cell-Cell Junctions Organize Structural and Signaling Networks. Cold Spring Harb. Perspect. Biol. 10. https://doi.org/10.1101/cshperspect.a029181

GBD 2017 Non-Typhoidal Salmonella Invasive Disease Collaborators, 2019. The global burden of non-typhoidal salmonella invasive disease: a systematic analysis for the Global Burden of Disease Study 2017. Lancet. Infect. Dis. 19, 1312–1324. https://doi.org/10.1016/S1473-3099(19)30418-9

Ge, Y., Zadeh, M., Mohamadzadeh, M., 2022. Vitamin B12 Regulates the Transcriptional, Metabolic, and Epigenetic Programing in Human Ileal Epithelial Cells. Nutr. 2022, Vol. 14, Page 2825 14, 2825. https://doi.org/10.3390/NU14142825

Gebert, A., 1997. The role of M cells in the protection of mucosal membranes. Histochem. Cell Biol. 108, 455–70. https://doi.org/10.1007/s004180050186

Gerbe, F., Jay, P., 2016. Intestinal tuft cells: epithelial sentinels linking luminal cues to the immune system. Mucosal Immunol. 9, 1353–1359. https://doi.org/10.1038/mi.2016.68

Gerhartl, A., Pracser, N., Vladetic, A., Hendrikx, S., Friedl, H.P., Neuhaus, W., 2020. The pivotal role of micro-environmental cells in a human blood-brain barrier in vitro model of cerebral ischemia: Functional and transcriptomic analysis. Fluids Barriers CNS 17, 1–17. https://doi.org/10.1186/S12987-020-00179-3/TABLES/2

Gersemann, M., Becker, S., Nuding, S., Antoni, L., Ott, G., Fritz, P., Oue, N., Yasui, W., Wehkamp, J., Stange, E.F., 2012. Olfactomedin-4 is a glycoprotein secreted into mucus in active IBD. J. Crohn's Colitis 6, 425–434. https://doi.org/10.1016/J.CROHNS.2011.09.013/2/6-4-FIG014.JPEG

Gewirtz, A.T., Rao, A.S., Simon, P.O., Merlin, D., Carnes, D., Madara, J.L., Neish, A.S., 2000. Salmonella typhimurium induces epithelial IL-8 expression via Ca2+-mediated activation of the NF-κB pathway. J. Clin. Invest. 105, 79–92. https://doi.org/10.1172/JCI8066

Gilchrist, J.J., MaClennan, C.A., Hill, A.V.S., 2015. Genetic susceptibility to invasive Salmonella disease. Nat. Rev. Immunol. 2015 157 15, 452–463. https://doi.org/10.1038/nri3858

Gjorevski, N., Nikolaev, M., Brown, T.E., Mitrofanova, O., Brandenberg, N., DelRio, F.W., Yavitt, F.M., Liberali, P., Anseth, K.S., Lutolf, M.P., 2022. Tissue geometry drives deterministic organoid patterning. Science (80-.). 375.

Gjorevski, N., Sachs, N., Manfrin, A., Giger, S., Bragina, M.E., Ordóñez-Morán, P., Clevers, H., Lutolf, M.P., 2016. Designer matrices for intestinal stem cell and organoid culture. Nature 539, 560–564. https://doi.org/10.1038/nature20168

Gog, J.R., Murcia, A., Osterman, N., Restif, O., McKinley, T.J., Sheppard, M., Achouri, S., Wei, B., Mastroeni, P., Wood, J.L.N., Maskell, D.J., Cicuta, P., Bryant, C.E., 2012. Dynamics of Salmonella infection of macrophages at the single cell level. J. R. Soc. Interface 9, 2696. https://doi.org/10.1098/RSIF.2012.0163

Goodman, B.E., 2010. Insights into digestion and absorption of major nutrients in humans. Am. J. Physiol. - Adv. Physiol. Educ. 34, 44–53. https://doi.org/10.1152/ADVAN.00094.2009/ASSET/IMAGES/LARGE/ZU10021025780006.JPEG

Goulas, S., Conder, R., Knoblich, J.A., 2012. The Par Complex and Integrins Direct Asymmetric Cell Division in Adult Intestinal Stem Cells. Cell Stem Cell 11, 529–540. https://doi.org/10.1016/J.STEM.2012.06.017

Gracz, A.D., Samsa, L.A., Fordham, M.J., Trotier, D.C., Zwarycz, B., Lo, Y.H., Bao, K., Starmer, J., Raab, J.R., Shroyer, N.F., Reinhardt, R.L., Magness, S.T., 2018. Sox4 Promotes Atoh1-Independent Intestinal Secretory Differentiation Toward Tuft and Enteroendocrine Fates. Gastroenterology 155, 1508-1523.e10.

https://doi.org/10.1053/j.gastro.2018.07.023

Green, K.J., Jaiganesh, A., Broussard, J.A., 2019. Desmosomes: Essential contributors to an integrated intercellular junction network. F1000Research 8. https://doi.org/10.12688/F1000RESEARCH.20942.1

Greenwood-Van Meerveld, B., Johnson, A.C., Grundy, D., 2017. Gastrointestinal Physiology and Function. Handb. Exp. Pharmacol. 239, 1–16. https://doi.org/10.1007/164_2016_118

Grondin, J.A., Kwon, Y.H., Far, P.M., Haq, S., Khan, W.I., 2020. Mucins in Intestinal Mucosal Defense and Inflammation: Learning From Clinical and Experimental Studies. Front. Immunol. 0, 2054. https://doi.org/10.3389/FIMMU.2020.02054

Guan, Q., 2019. A Comprehensive Review and Update on the Pathogenesis of Inflammatory Bowel Disease. J. Immunol. Res. 2019, 7247238. https://doi.org/10.1155/2019/7247238

Gundersen, G.G., Worman, H.J., 2013. Nuclear Positioning. Cell 152, 1376–1389. https://doi.org/10.1016/J.CELL.2013.02.031

Gunn, J.S., Marshall, J.M., Baker, S., Dongol, S., Charles, R.C., Ryan, E.T., 2014. Salmonella chronic carriage: epidemiology, diagnosis, and gallbladder persistence. Trends Microbiol. 22, 648–655. https://doi.org/10.1016/J.TIM.2014.06.007

Haas, A.J., Zihni, C., Ruppel, A., Hartmann, C., Ebnet, K., Tada, M., Balda, M.S., Matter, K., 2020. Interplay between Extracellular Matrix Stiffness and JAM-A Regulates Mechanical Load on ZO-1 and Tight Junction Assembly. Cell Rep. 32. https://doi.org/10.1016/j.celrep.2020.107924

Haber, A.L., Biton, M., Rogel, N., Herbst, R.H., Shekhar, K., Smillie, C., Burgin, G., Delorey, T.M., Howitt, M.R., Katz, Y., Tirosh, I., Beyaz, S., Dionne, D., Zhang, M., Raychowdhury, R., Garrett, W.S., Rozenblatt-Rosen, O., Shi, H.N., Yilmaz, O., Xavier, R.J., Regev, A., 2017. A single-cell survey of the small intestinal epithelium. Nature 551, 333–339. https://doi.org/10.1038/nature24489

Hansson, G.C., 2012. Role of mucus layers in gut infection and inflammation. Curr. Opin. Microbiol. 15, 57–62. https://doi.org/10.1016/j.mib.2011.11.002

Haramis, A.G., Begthel, H., van den Born, M., van Es, J., Jonkheer, S., Offerhaus, G.J.A., Clevers, H., 2004. De novo crypt formation and juvenile polyposis on BMP inhibition in mouse intestine. Science 303, 1684–6. https://doi.org/10.1126/science.1093587

Hartmann, C., Schwietzer, Y.A., Otani, T., Furuse, M., Ebnet, K., 2020. Physiological functions of junctional adhesion molecules (JAMs) in tight junctions. Biochim. Biophys. Acta - Biomembr. 1862, 183299. https://doi.org/10.1016/J.BBAMEM.2020.183299

He, X.C., Zhang, J., Tong, W.G., Tawfik, O., Ross, J., Scoville, D.H., Tian, Q., Zeng, X., He, X., Wiedemann, L.M., Mishina, Y., Li, L., 2004. BMP signaling inhibits intestinal stem cell self-renewal through suppression of Wnt–β-catenin signaling. Nat. Genet. 2004 3610 36, 1117–1121. https://doi.org/10.1038/ng1430

Helaine, S., Cheverton, A.M., Watson, K.G., Faure, L.M., Matthews, S.A., Holden, D.W., 2014. Internalization of salmonella by macrophages induces formation of nonreplicating persisters. Science (80-.). 343, 204–208. https://doi.org/10.1126/SCIENCE.1244705/SUPPL_FILE/HELAINE-SM.PDF

Helaine, S., Thompson, J.A., Watson, K.G., Liu, M., Boyle, C., Holden, D.W., 2010. Dynamics of intracellular bacterial replication at the single cell level. Proc. Natl. Acad. Sci. U. S. A. 107, 3746–3751. https://doi.org/10.1073/PNAS.1000041107/SUPPL_FILE/SM01.MOV

Helander, H.F., Fändriks, L., 2014. Surface area of the digestive tract - revisited. Scand. J. Gastroenterol. 49, 681–9. https://doi.org/10.3109/00365521.2014.898326

Henry, T., Garcia-Del Portillo, F., Gorvel, J.P., 2005. Identification of Salmonella functions critical for bacterial cell division within eukaryotic cells. Mol. Microbiol. 56, 252–267. https://doi.org/10.1111/J.1365-2958.2005.04540.X

Heo, J.H., Kang, D., Seo, S.J., Jin, Y., 2022. Engineering the Extracellular Matrix for Organoid Culture. Int. J. Stem Cells 15, 60–69. https://doi.org/10.15283/IJSC21190

Herath, M., Hosie, S., Bornstein, J.C., Franks, A.E., Hill-Yardin, E.L., 2020. The Role of the Gastrointestinal Mucus System in Intestinal Homeostasis: Implications for Neurological Disorders. Front. Cell. Infect. Microbiol. 10, 248. https://doi.org/10.3389/FCIMB.2020.00248/BIBTEX

Herzog, V.A., Reichholf, B., Neumann, T., Rescheneder, P., Bhat, P., Burkard, T.R., Wlotzka, W., Von Haeseler, A., Zuber, J., Ameres, S.L., 2017. Thiol-linked alkylation of RNA to assess expression dynamics. Nat. Methods 2017 1412 14, 1198–1204. https://doi.org/10.1038/nmeth.4435

Hill, D.R., Spence, J.R., 2017. Gastrointestinal Organoids: Understanding the Molecular Basis of the Host-Microbe Interface. Cell. Mol. Gastroenterol. Hepatol. 3, 138–149. https://doi.org/10.1016/j.jcmgh.2016.11.007

Hoffmann, P., Schnepel, N., Langeheine, M., Kunnemann, K., Grassl, G.A., Brehm, R., Seeger, B., Mazzuoli-Weber, G., Breves, G., 2021. Intestinal organoid-based 2D monolayers mimic physiological and pathophysiological properties of the pig intestine. PLoS One 16. https://doi.org/10.1371/JOURNAL.PONE.0256143

Hohmann, E.L., 2001. Nontyphoidal salmonellosis. Clin. Infect. Dis. 32, 263–269. https://doi.org/10.1086/318457

Holloway, E.M., Czerwinski, M., Tsai, Y.-H., Wu, J.H., Wu, A., Childs, C.J., Walton, K.D., Sweet, C.W., Yu, Q., Glass, I., Treutlein, B., Camp, J.G., Spence, J.R., 2021. Mapping Development of the Human Intestinal Niche at Single-Cell Resolution. Cell Stem Cell 28, 568-580.e4. https://doi.org/10.1016/j.stem.2020.11.008

House, D., Bishop, A., Parry, C., Dougan, G., Wain, J., 2001. Typhoid fever: pathogenesis and disease. Curr. Opin. Infect. Dis. 14, 573–578. https://doi.org/10.1097/00001432-200110000-00011

Huan, Y.W., Bengtsson, R.J., MacIntyre, N., Guthrie, J., Finlayson, H., Smith, S.H., Archibald, A.L., Ait-Ali, T., 2017. Lawsonia intracellularis exploits β-catenin/Wnt and Notch signalling pathways during infection of intestinal crypt to alter cell homeostasis and promote cell proliferation. PLoS One 12, e0173782. https://doi.org/10.1371/JOURNAL.PONE.0173782

Huang, F.-C., 2021. The Interleukins Orchestrate Mucosal Immune Responses to Salmonella Infection in the Intestine. Cells 10, 3492. https://doi.org/10.3390/cells10123492

Huang, F.C., 2016. Vitamin D differentially regulates Salmonella -induced intestine epithelial autophagy and

interleukin-1β expression. World J. Gastroenterol. 22, 10353–10363. https://doi.org/10.3748/wjg.v22.i47.10353

Huang, F.C., 2012. Regulation of Salmonella flagellin-induced interleukin-8 in intestinal epithelial cells by muramyl dipeptide. Cell. Immunol. 278, 1–9. https://doi.org/10.1016/J.CELLIMM.2012.06.013

Huang, F.C., 2009. Upregulation of salmonella-induced IL-6 production in caco-2 cells by PJ-34, parp-1 inhibitor: Involvement of PI3K, p38 MAPK, ERK, JNK, and NF- B. Mediators Inflamm. 2009. https://doi.org/10.1155/2009/103890

Hughes, C.S., Postovit, L.M., Lajoie, G.A., 2010. Matrigel: a complex protein mixture required for optimal growth of cell culture. Proteomics 10, 1886–90. https://doi.org/10.1002/pmic.200900758

Humphrey, S., Macvicar, T., Stevenson, A., Roberts, M., Humphrey, T.J., Jepson, M.A., 2011. SulA-induced filamentation in Salmonella enterica serovar Typhimurium: effects on SPI-1 expression and epithelial infection. J. Appl. Microbiol. 111, 185–196. https://doi.org/10.1111/J.1365-2672.2011.05022.X

Hyeon, J.-Y., Chon, J.-W., Hwang, I.-G., Kwak, H.-S., Kim, M.-S., Kim, S.-K., Choi, I.-S., Song, C.-S., Park, C., Seo, K.-H., 2011. Prevalence, antibiotic resistance, and molecular characterization of Salmonella serovars in retail meat products. J. Food Prot. 74, 161–6. https://doi.org/10.4315/0362-028X.JFP-10-327

Ibarra, J.A., Knodler, L.A., Sturdevant, D.E., Virtaneva, K., Carmody, A.B., Fischer, E.R., Porcella, S.F., Steele-Mortimer, O., 2010. Induction of Salmonella pathogenicity island 1 under different growth conditions can affect Salmonella-host cell interactions in vitro. Microbiology 156, 1120–1133. https://doi.org/10.1099/mic.0.032896-0

Iden, S., Misselwitz, S., Peddibhotla, S.S.D., Tuncay, H., Rehder, D., Gerke, V., Robenek, H., Suzuki, A., Ebnet, K., 2012. aPKC phosphorylates JAM-A at Ser285 to promote cell contact maturation and tight junction formation. J. Cell Biol. 196, 623–39. https://doi.org/10.1083/jcb.201104143

Ivanov, A.I., 2013. Structure and Regulation of Intestinal Epithelial Tight Junctions. Adv. Exp. Med. Biol. 763, 132–148. https://doi.org/10.1007/978-1-4614-4711-5_6

Jannasch, M., Groeber, F., Brattig, N.W., Unger, C., Walles, H., Hansmann, J., 2015. Development and application of three-dimensional skin equivalents for the investigation of percutaneous worm invasion. Exp. Parasitol. 150, 22–30. https://doi.org/10.1016/J.EXPPARA.2015.01.005

Jeffery, V., Goldson, A.J., Dainty, J.R., Chieppa, M., Sobolewski, A., 2017. IL-6 Signaling Regulates Small Intestinal Crypt Homeostasis. J. Immunol. 199, 304–311. https://doi.org/10.4049/JIMMUNOL.1600960/-/DCSUPPLEMENTAL

Jochems, P.G.M., Garssen, J., Van Keulen, A.M., Masereeuw, R., Jeurink, P. V., 2018. Evaluating Human Intestinal Cell Lines for Studying Dietary Protein Absorption. Nutrients 10. https://doi.org/10.3390/NU10030322

Jones, B., Ghori, N., Falkow, S., 1994. Salmonella typhimurium initiates murine infection by penetrating and destroying the specialized epithelial M cells of the Peyer's patches. J. Exp. Med. 180, 15–23. https://doi.org/10.1084/jem.180.1.15

Jones, B.D., Ghori, N., Falkow, S., 1994. Salmonella typhimurium initiates murine infection by penetrating and destroying the specialized epithelial M cells of the Peyer's patches. J. Exp. Med. 180, 15–23. https://doi.org/10.1084/jem.180.1.15

Justice, S.S., Hunstad, D.A., Cegelski, L., Hultgren, S.J., 2008. Morphological plasticity as a bacterial survival strategy. Nat. Rev. Microbiol. 2008 62 6, 162–168. https://doi.org/10.1038/nrmicro1820

Kämpfer, A.A.M., Urbán, P., Gioria, S., Kanase, N., Stone, V., Kinsner-Ovaskainen, A., 2017. Development of an in vitro co-culture model to mimic the human intestine in healthy and diseased state. Toxicol. In Vitro 45, 31–43. https://doi.org/10.1016/J.TIV.2017.08.011

Kanaya, T., Sakakibara, S., Jinnohara, T., Hachisuka, M., Tachibana, N., Hidano, S., Kobayashi, T., Kimura, S., Iwanaga, T., Nakagawa, T., Katsuno, T., Kato, N., Akiyama, T., Sato, T., Williams, I.R., Ohno, H., 2018. Development of intestinal M cells and follicle-associated epithelium is regulated by TRAF6-mediated NF-κB signaling. J. Exp. Med. 215, 501–519. https://doi.org/10.1084/jem.20160659

Kannaiyan, D.J., Chhabra, D.H., M, D.P., B, D.M.R., Narayanan S, D.M.S., Pandey, D.A., 2016. Biological and synthetic scaffold: an extra cellular matrix for constructive tissue engineering. Int. J. Med. Res. Rev. 4, 1882–1896. https://doi.org/10.17511/IJMRR.2016.I10.27

Kauffmann, F., 1973. [The classification and nomenclature of salmonella-species]. Zentralbl. Bakteriol. Orig. A. 223, 508–12.

Kechagia, J.Z., Ivaska, J., Roca-Cusachs, P., 2019. Integrins as biomechanical sensors of the microenvironment. Nat. Rev. Mol. Cell Biol. 20, 457–473. https://doi.org/10.1038/s41580-019-0134-2

Keestra-Gounder, A.M., Tsolis, R.M., Bäumler, A.J., 2015. Now you see me, now you don't: the interaction of Salmonella with innate immune receptors. Nat. Rev. Microbiol. 13, 206–216. https://doi.org/10.1038/NRMICRO3428

Keithlin, J., Sargeant, J.M., Thomas, M.K., Fazil, A., 2015. Systematic review and meta-analysis of the proportion of non-typhoidal Salmonella cases that develop chronic sequelae. Epidemiol. Infect. 143, 1333–1351. https://doi.org/10.1017/S0950268814002829

Kelsall, B.L., Strober, W., 1996. Distinct populations of dendritic cells are present in the subepithelial dome and T cell regions of the murine Peyer's patch. J. Exp. Med. 183, 237–247. https://doi.org/10.1084/JEM.183.1.237

Kelso, A., 1998. Cytokines: Principles and prospects. Immunol. Cell Biol. 76, 300–317. https://doi.org/10.1046/J.1440-1711.1998.00757.X

Khurana, S., George, S.P., 2008. Regulation of cell structure and function by actin-binding proteins: villin's perspective. FEBS Lett. 582, 2128–39. https://doi.org/10.1016/j.febslet.2008.02.040

Kim, S., Min, S., Choi, Y.S., Jo, S.H., Jung, J.H., Han, K., Kim, J., An, S., Ji, Y.W., Kim, Y.G., Cho, S.W., 2022. Tissue extracellular matrix hydrogels as alternatives to Matrigel for culturing gastrointestinal organoids. Nat. Commun. 2022 131 13, 1–21. https://doi.org/10.1038/s41467-022-29279-4

Kim, T.H., Li, F., Ferreiro-Neira, I., Ho, L.L., Luyten, A., Nalapareddy, K., Long, H., Verzi, M., Shivdasani, R.A.,

2014a. Broadly permissive intestinal chromatin underlies lateral inhibition and cell plasticity. Nature 506, 511–515. https://doi.org/10.1038/NATURE12903

Kim, T.H., Li, F., Ferreiro-Neira, I., Ho, L.L., Luyten, A., Nalapareddy, K., Long, H., Verzi, M., Shivdasani, R.A., 2014b. Broadly permissive intestinal chromatin underlies lateral inhibition and cell plasticity. Nat. 2014 5067489 506, 511–515. https://doi.org/10.1038/nature12903

Kim, Y.S., Ho, S.B., 2010. Intestinal goblet cells and mucins in health and disease: Recent insights and progress. Curr. Gastroenterol. Rep. 12, 319–330. https://doi.org/10.1007/s11894-010-0131-2

Kirk, M.D., Pires, S.M., Black, R.E., Caipo, M., Crump, J.A., Devleesschauwer, B., Döpfer, D., Fazil, A., Fischer-Walker, C.L., Hald, T., Hall, A.J., Keddy, K.H., Lake, R.J., Lanata, C.F., Torgerson, P.R., Havelaar, A.H., Angulo, F.J., 2015. World Health Organization Estimates of the Global and Regional Disease Burden of 22 Foodborne Bacterial, Protozoal, and Viral Diseases, 2010: A Data Synthesis. PLoS Med. 12, e1001921. https://doi.org/10.1371/journal.pmed.1001921

Kitano, K., Schwartz, D.M., Zhou, H., Gilpin, S.E., Wojtkiewicz, G.R., Ren, X., Sommer, C.A., Capilla, A. V., Mathisen, D.J., Goldstein, A.M., Mostoslavsky, G., Ott, H.C., 2017. Bioengineering of functional human induced pluripotent stem cell-derived intestinal grafts. Nat. Commun. 8, 765. https://doi.org/10.1038/s41467-017-00779-y

Knodler, L.A., Crowley, S.M., Sham, H.P., Yang, H., Wrande, M., Ma, C., Ernst, R.K., Steele-Mortimer, O., Celli, J., Vallance, B.A., 2014a. Noncanonical Inflammasome Activation of Caspase-4/Caspase-11 Mediates Epithelial Defenses against Enteric Bacterial Pathogens. Cell Host Microbe 16, 249–256. https://doi.org/10.1016/J.CHOM.2014.07.002

Knodler, L.A., Nair, V., Steele-Mortimer, O., 2014b. Quantitative Assessment of Cytosolic Salmonella in Epithelial Cells. PLoS One 9, e84681. https://doi.org/10.1371/JOURNAL.PONE.0084681

Knodler, L.A., Vallance, B.A., Celli, J., Winfree, S., Hansen, B., Montero, M., Steele-Mortimer, O., 2010. Dissemination of invasive Salmonella via bacterial-induced extrusion of mucosal epithelia. Proc. Natl. Acad. Sci. U. S. A. 107, 17733–8. https://doi.org/10.1073/pnas.1006098107

Knoop, K.A., Kumar, N., Butler, B.R., Sakthivel, S.K., Taylor, R.T., Nochi, T., Akiba, H., Yagita, H., Kiyono, H., Williams, I.R., 2009. RANKL is necessary and sufficient to initiate development of antigen-sampling M cells in the intestinal epithelium. J. Immunol. 183, 5738–5747. https://doi.org/10.4049/JIMMUNOL.0901563

Knuff-Janzen, K., Tupin, A., Yurist-Doutsch, S., Rowland, J.L., Finlay, B.B., 2020. Multiple Salmonella-pathogenicity island 2 effectors are required to facilitate bacterial establishment of its intracellular niche and virulence. PLoS One 15, e0235020. https://doi.org/10.1371/JOURNAL.PONE.0235020

Knuff, K., Finlay, B.B., 2017. What the SIF Is happening—The role of intracellular Salmonella-induced filaments. Front. Cell. Infect. Microbiol. 7, 335. https://doi.org/10.3389/fcimb.2017.00335

Kolling, G., Wu, M., Guerrant, R.L., 2012. Enteric pathogens through life stages. Front. Cell. Infect. Microbiol. 2, 114. https://doi.org/10.3389/FCIMB.2012.00114

Kothary, M.H., Babu, U.S., 2001. INFECTIVE DOSE OF FOODBORNE PATHOGENS IN VOLUNTEERS: A REVIEW. J. Food Saf. 21, 49–68. https://doi.org/10.1111/J.1745-4565.2001.TB00307.X

Kraehenbuhl, J.P., Neutra, M.R., 2000. Epithelial M cells: differentiation and function. Annu. Rev. Cell Dev. Biol. 16, 301–32. https://doi.org/10.1146/annurev.cellbio.16.1.301

Krasemann, S., Haferkamp, U., Pfefferle, S., Woo, M.S., Heinrich, F., Schweizer, M., Appelt-Menzel, A., Cubukova, A., Barenberg, J., Leu, J., Hartmann, K., Thies, E., Littau, J.L., Sepulveda-Falla, D., Zhang, L., Ton, K., Liang, Y., Matschke, J., Ricklefs, F., Sauvigny, T., Sperhake, J., Fitzek, A., Gerhartl, A., Brachner, A., Geiger, N., König, E.M., Bodem, J., Franzenburg, S., Franke, A., Moese, S., Müller, F.J., Geisslinger, G., Claussen, C., Kannt, A., Zaliani, A., Gribbon, P., Ondruschka, B., Neuhaus, W., Friese, M.A., Glatzel, M., Pless, O., 2022. The blood-brain barrier is dysregulated in COVID-19 and serves as a CNS entry route for SARS-CoV-2. Stem cell reports 17, 307–320. https://doi.org/10.1016/J.STEMCR.2021.12.011

Krndija, D., Marjou, F. El, Guirao, B., Richon, S., Leroy, O., Bellaiche, Y., Hannezo, E., Vignjevic, D.M., 2019. Active cell migration is critical for steady-state epithelial turnover in the gut. Science (80-.). 365, 705–710. https://doi.org/10.1126/science.aau3429

Kucharzik, T., Lügering, N., Schmid, K.W., Schmidt, M.A., Stoll, R., Domschke, W., 1998. Human intestinal M cells exhibit enterocyte-like intermediate filaments. Gut 42, 54–62. https://doi.org/10.1136/GUT.42.1.54

Kuhnert, F., Davis, C.R., Wang, H.T., Chu, P., Lee, M., Yuan, J., Nusse, R., Kuo, C.J., 2004. Essential requirement for Wnt signaling in proliferation of adult small intestine and colon revealed by adenoviral expression of Dickkopf-1. Proc. Natl. Acad. Sci. U. S. A. 101, 266–271. https://doi.org/10.1073/PNAS.2536800100/SUPPL_FILE/6800FIG7.JPG

Kuno, R., Ito, G., Kawamoto, A., Hiraguri, Y., Sugihara, H.Y., Takeoka, S., Nagata, S., Takahashi, J., Tsuchiya, M., Anzai, S., Mizutani, T., Shimizu, H., Yui, S., Oshima, S., Tsuchiya, K., Watanabe, M., Okamoto, R., 2021. Notch and TNF-α signaling promote cytoplasmic accumulation of OLFM4 in intestinal epithelium cells and exhibit a cell protective role in the inflamed mucosa of IBD patients. Biochem. Biophys. Reports 25, 100906. https://doi.org/10.1016/J.BBREP.2020.100906

Kurtz, J.R., Goggins, J.A., McLachlan, J.B., 2017. Salmonella infection: Interplay between the bacteria and host immune system. Immunol. Lett. 190, 42–50. https://doi.org/10.1016/j.imlet.2017.07.006

Kusters, J.G., Mulders-Kremers, G.A.W.M., Van Doornik, C.E.M., Van der Zeijst, B.A.M., 1993. Effects of multiplicity of infection, bacterial protein synthesis, and growth phase on adhesion to and invasion of human cell lines by Salmonella typhimurium. Infect. Immun. 61, 5013. https://doi.org/10.1128/IAI.61.12.5013-5020.1993

Larock, D.L., Chaudhary, A., Miller, S.I., 2015. Salmonellae interactions with host processes. Nat. Rev. Microbiol. 2015 134 13, 191–205. https://doi.org/10.1038/nrmicro3420

Lee, G., Han, S.B., Kim, D.H., 2021. Cell-ECM contact-guided intracellular polarization is mediated via lamin A/C dependent nucleus-cytoskeletal connection. Biomaterials 268, 120548. https://doi.org/10.1016/J.BIOMATERIALS.2020.120548

Lensmire, J.M., Pratt, Z.L., Wong, A.C.L., Kaspar, C.W., 2018. Phosphate and carbohydrate facilitate the

formation of filamentous salmonella Enterica during osmotic stress. Microbiol. (United Kingdom) 164, 1503–1513. https://doi.org/10.1099/MIC.0.000731/CITE/REFWORKS

Leoni Swart, A., Hensel, M., 2012. Interactions of Salmonella enterica with dendritic cells. Virulence 3, 660. https://doi.org/10.4161/VIRU.22761

Lhocine, N., Arena, E.T., Bomme, P., Ubelmann, F., Prévost, M.C., Robine, S., Sansonetti, P.J., 2015. Apical Invasion of Intestinal Epithelial Cells by Salmonella typhimurium Requires Villin to Remodel the Brush Border Actin Cytoskeleton. Cell Host Microbe 17, 164–177. https://doi.org/10.1016/J.CHOM.2014.12.003

Li, X., Bleumink-Pluym, N.M.C., Luijkx, Y.M.C.A., Wubbolts, R.W., van Putten, J.P.M., Strijbis, K., 2019a. MUC1 is a receptor for the Salmonella SiiE adhesin that enables apical invasion into enterocytes. PLoS Pathog. 15, e1007566. https://doi.org/10.1371/journal.ppat.1007566

Li, X., Bleumink-Pluym, N.M.C., Luijkx, Y.M.C.A., Wubbolts, R.W., van Putten, J.P.M., Strijbis, K., 2019b. MUC1 is a receptor for the Salmonella SiiE adhesin that enables apical invasion into enterocytes. PLOS Pathog. 15, e1007566. https://doi.org/10.1371/JOURNAL.PPAT.1007566

Liang, G., Zhang, Y., 2012. Embryonic stem cell and induced pluripotent stem cell: an epigenetic perspective. Cell Res. 2013 231 23, 49–69. https://doi.org/10.1038/cr.2012.175

Lin, G.C., Leitgeb, T., Vladetic, A., Friedl, H.P., Rhodes, N., Rossi, A., Roblegg, E., Neuhaus, W., 2020. Optimization of an oral mucosa in vitro model based on cell line TR146. Tissue Barriers. https://doi.org/10.1080/21688370.2020.1748459/SUPPL_FILE/KTIB_A_1748459_SM4220.ZIP

Lina, T.T., Dunphy, P.S., Luo, T., McBride, J.W., 2016. Ehrlichia chaffeensis TRP120 activates canonical notch signaling to downregulate TLR2/4 expression and promote intracellular survival. MBio 7. https://doi.org/10.1128/MBIO.00672-16/ASSET/75A54524-7300-4E33-8C94-97FA1E3BC3AB/ASSETS/GRAPHIC/MBO0031628840010.JPEG

Liu, G., David, B.T., Trawczynski, M., Fessler, R.G., 2019. Advances in Pluripotent Stem Cells: History, Mechanisms, Technologies, and Applications. Stem Cell Rev. Reports 2019 161 16, 3–32. https://doi.org/10.1007/S12015-019-09935-X

Liu, W., Li, H., Hong, S.H., Piszczek, G.P., Chen, W., Rodgers, G.P., 2016. Olfactomedin 4 deletion induces colon adenocarcinoma in ApcMin/+ mice. Oncogene 2016 3540 35, 5237–5247. https://doi.org/10.1038/onc.2016.58

Liu, W., Rodgers, G.P., 2022a. Olfactomedin 4 Is a Biomarker for the Severity of Infectious Diseases. Open Forum Infect. Dis. 9. https://doi.org/10.1093/OFID/OFAC061

Liu, W., Rodgers, G.P., 2022b. Olfactomedin 4 Is Not a Precise Marker for Human Intestinal Stem Cells, But Is Involved in Intestinal Carcinogenesis. Gastroenterology 162, 1001–1004. https://doi.org/10.1053/j.gastro.2021.11.041

Liu, W., Rodgers, G.P., 2016. Olfactomedin 4 expression and functions in innate immunity, inflammation, and cancer. Cancer Metastasis Rev. 35, 201–12. https://doi.org/10.1007/s10555-016-9624-2

Liu, W., Yan, M., Liu, Y., McLeish, K.R., Coleman, W.G., Rodgers, G.P., 2012. Olfactomedin 4 Inhibits

Cathepsin C-Mediated Protease Activities, Thereby Modulating Neutrophil Killing of Staphylococcus aureus and Escherichia coli in Mice. J. Immunol. 189, 2460–2467. https://doi.org/10.4049/JIMMUNOL.1103179

Liu, W., Yan, M., Liu, Y., Wang, R., Li, C., Deng, C., Singh, A., Coleman, W.G., Rodgers, G.P., 2010. Olfactomedin 4 down-regulates innate immunity against Helicobacter pylori infection. Proc. Natl. Acad. Sci. U. S. A. 107, 11056–11061. https://doi.org/10.1073/pnas.1001269107

Liu, X., Lu, R., Wu, S., Sun, J., 2010. Salmonella regulation of intestinal stem cells through the Wnt/β-catenin pathway. FEBS Lett. 584, 911. https://doi.org/10.1016/J.FEBSLET.2010.01.024

Lo, Y.H., Chung, E., Li, Z., Wan, Y.W., Mahe, M.M., Chen, M.S., Noah, T.K., Bell, K.N., Yalamanchili, H.K., Klisch, T.J., Liu, Z., Park, J.S., Shroyer, N.F., 2017. Transcriptional Regulation by ATOH1 and its Target SPDEF in the Intestine. Cell. Mol. Gastroenterol. Hepatol. 3, 51–71. https://doi.org/10.1016/J.JCMGH.2016.10.001

Lorkowski, M., Felipe-López, A., Danzer, C.A., Hansmeier, N., Hensel, M., 2014. Salmonella enterica invasion of polarized epithelial cells is a highly cooperative effort. Infect. Immun. 82, 2657–67. https://doi.org/10.1128/IAI.00023-14

Lu, R., Wu, S., Zhang, Y.G., Xia, Y., Liu, X., Zheng, Y., Chen, H., Schaefer, K.L., Zhou, Z., Bissonnette, M., Li, L., Sun, J., 2014. Enteric bacterial protein AvrA promotes colonic tumorigenesis and activates colonic beta-catenin signaling pathway. Oncog. 2014 36 3, e105–e105. https://doi.org/10.1038/oncsis.2014.20

Mabbott, N.A., Donaldson, D.S., Ohno, H., Williams, I.R., Mahajan, A., 2013. Microfold (M) cells: important immunosurveillance posts in the intestinal epithelium. Mucosal Immunol. 2013 64 6, 666–677. https://doi.org/10.1038/mi.2013.30

Macara, I.G., 2004. Parsing the polarity code. Nat. Rev. Mol. Cell Biol. 5, 220–31. https://doi.org/10.1038/nrm1332

Macdonald, T.T., Monteleone, G., 2005. Immunity, inflammation, and allergy in the gut. Science 307, 1920–5. https://doi.org/10.1126/science.1106442

Macosko, E.Z., Basu, A., Satija, R., Nemesh, J., Shekhar, K., Goldman, M., Tirosh, I., Bialas, A.R., Kamitaki, N., Martersteck, E.M., Trombetta, J.J., Weitz, D.A., Sanes, J.R., Shalek, A.K., Regev, A., McCarroll, S.A., 2015. Highly parallel genome-wide expression profiling of individual cells using nanoliter droplets. Cell 161, 1202–1214. https://doi.org/10.1016/J.CELL.2015.05.002/ATTACHMENT/4A61AA26-CCB0-48AC-9D09-485C9571EDBD/MMC6.ZIP

Madison, B.B., Braunstein, K., Kuizon, E., Portman, K., Qiao, X.T., Gumucio, D.L., 2005. Epithelial hedgehog signals pattern the intestinal crypt-villus axis. Development 132, 279–289. https://doi.org/10.1242/DEV.01576

Madison, K.C., 2003. Barrier function of the skin: “la raison d’être” of the epidermis. J. Invest. Dermatol. 121, 231–41. https://doi.org/10.1046/j.1523-1747.2003.12359.x

Madsen, J., Nielsen, O., Tornøe, I., Thim, L., Holmskov, U., 2007. Tissue localization of human trefoil factors 1,

2, and 3. J. Histochem. Cytochem. 55, 505–513. https://doi.org/10.1369/JHC.6A7100.2007/ASSET/IMAGES/LARGE/10.1369_JHC.6A7100.2007-FIG3.JPEG

Mah, A.T., Yan, K.S., Kuo, C.J., 2016. Wnt pathway regulation of intestinal stem cells. J. Physiol. 594, 4837–47. https://doi.org/10.1113/JP271754

Malik-Kale, P., Jolly, C.E., Lathrop, S., Winfree, S., Luterbach, C., Steele-Mortimer, O., 2011. Salmonella- at home in the host cell. Front. Microbiol. 2, 125. https://doi.org/10.3389/FMICB.2011.00125/BIBTEX

Malik-Kale, P., Winfree, S., Steele-Mortimer, O., 2012. The bimodal lifestyle of intracellular Salmonella in epithelial cells: replication in the cytosol obscures defects in vacuolar replication. PLoS One 7, e38732. https://doi.org/10.1371/journal.pone.0038732

Mandel, L.J., Bacallao, R., Zampighi, G., 1993. Uncoupling of the molecular "fence" and paracellular "gate" functions in epithelial tight junctions. Nat. 1993 3616412 361, 552–555. https://doi.org/10.1038/361552a0

Mandell, K.J., Babbin, B.A., Nusrat, A., Parkos, C.A., 2005. Junctional Adhesion Molecule 1 Regulates Epithelial Cell Morphology through Effects on β1 Integrins and Rap1 Activity. J. Biol. Chem. 280, 11665–11674. https://doi.org/10.1074/JBC.M412650200

Mannick, E.E., Schurr, J.R., Zapata, A., Lentz, J.J., Gastanaduy, M., Cote, R.L., Delgado, A., Correa, P., Correa, H., 2009. Gene expression in gastric biopsies from patients infected with Helicobacter pylori. http://dx.doi.org/10.1080/00365520410003588 39, 1192–1200. https://doi.org/10.1080/00365520410003588

Marc Erhardt lab - Humboldt-Universität zu Berlin, AG Bakterienphysiologie [WWW Document], n.d. URL https://www.baktphys.hu-berlin.de/projects.html (accessed 12.7.22).

Martínez-Lorenzo, M.J., Méresse, S., De Chastellier, C., Gorvel, J.P., 2001. Unusual intracellular trafficking of Salmonella typhimurium in human melanoma cells. Cell. Microbiol. 3, 407–416. https://doi.org/10.1046/J.1462-5822.2001.00123.X

Martini, E., Krug, S.M., Siegmund, B., Neurath, M.F., Becker, C., 2017. Mend Your Fences: The Epithelial Barrier and its Relationship With Mucosal Immunity in Inflammatory Bowel Disease. Cell. Mol. Gastroenterol. Hepatol. 4, 33–46. https://doi.org/10.1016/j.jcmgh.2017.03.007

Matlin, K.S., Myllymäki, S.M., Manninen, A., 2017. Laminins in Epithelial Cell Polarization: Old Questions in Search of New Answers. Cold Spring Harb. Perspect. Biol. 9. https://doi.org/10.1101/CSHPERSPECT.A027920

Mattick, K.L., Phillips, L.E., Jørgensen, F., Lappin-Scott, H.M., Humphrey, T.J., 2003. Filament Formation by Salmonella spp. Inoculated into Liquid Food Matrices at Refrigeration Temperatures, and Growth Patterns When Warmed. J. Food Prot. 66, 215–219. https://doi.org/10.4315/0362-028X-66.2.215

McCauley, H.A., Guasch, G., 2015. Three cheers for the goblet cell: maintaining homeostasis in mucosal epithelia. Trends Mol. Med. 21, 492–503. https://doi.org/10.1016/J.MOLMED.2015.06.003

McCracken, K.W., Catá, E.M., Crawford, C.M., Sinagoga, K.L., Schumacher, M., Rockich, B.E., Tsai, Y.H.,

Mayhew, C.N., Spence, J.R., Zavros, Y., Wells, J.M., 2014. Modelling human development and disease in pluripotent stem-cell-derived gastric organoids. Nat. 2014 5167531 516, 400–404. https://doi.org/10.1038/nature13863

McCrary, M.W., Bousalis, D., Mobini, S., Song, Y.H., Schmidt, C.E., 2020. Decellularized tissues as platforms for in vitro modeling of healthy and diseased tissues. Acta Biomater. 111, 1–19. https://doi.org/10.1016/j.actbio.2020.05.031

Meran, L., Massie, I., Campinoti, S., Weston, A.E., Gaifulina, R., Tullie, L., Faull, P., Orford, M., Kucharska, A., Baulies, A., Novellasdemunt, L., Angelis, N., Hirst, E., König, J., Tedeschi, A.M., Pellegata, A.F., Eli, S., Snijders, A.P., Collinson, L., Thapar, N., Thomas, G.M.H.H., Eaton, S., Bonfanti, P., De Coppi, P., Li, V.S.W.W., 2020. Engineering transplantable jejunal mucosal grafts using patient-derived organoids from children with intestinal failure. Nat. Med. 26, 1593–1601. https://doi.org/10.1038/s41591-020-1024-z

Meunier, V., Bourrié, M., Berger, Y., Fabre, G., 1995. The human intestinal epithelial cell line Caco-2; pharmacological and pharmacokinetic applications. Cell Biol. Toxicol. 11, 187–194. https://doi.org/10.1007/BF00756522

Mian, M.F., Pek, E.A., Chenoweth, M.J., Ashkar, A.A., 2010. Humanized mice are susceptible to Salmonella typhi infection. Cell. Mol. Immunol. 2010 81 8, 83–87. https://doi.org/10.1038/cmi.2010.52

Min, S., Kim, S., Cho, S.W., 2020. Gastrointestinal tract modeling using organoids engineered with cellular and microbiota niches. Exp. Mol. Med. 2020 522 52, 227–237. https://doi.org/10.1038/s12276-020-0386-0

Moest, T.P., Méresse, S., 2013. Salmonella T3SSs: successful mission of the secret(ion) agents. Curr. Opin. Microbiol. 16, 38–44. https://doi.org/10.1016/J.MIB.2012.11.006

Moon, C., VanDussen, K.L., Miyoshi, H., Stappenbeck, T.S., 2014. Development of a primary mouse intestinal epithelial cell monolayer culture system to evaluate factors that modulate IgA transcytosis. Mucosal Immunol. 7, 818–28. https://doi.org/10.1038/mi.2013.98

Moor, Andreas E., Harnik, Y., Ben-Moshe, S., Massasa, E.E., Rozenberg, M., Eilam, R., Bahar Halpern, K., Itzkovitz, S., 2018. Spatial Reconstruction of Single Enterocytes Uncovers Broad Zonation along the Intestinal Villus Axis. Cell 175, 1156-1167.e15. https://doi.org/10.1016/J.CELL.2018.08.063

Moor, Andreas E, Harnik, Y., Ben-Moshe, S., Massasa, E.E., Rozenberg, M., Eilam, R., Bahar Halpern, K., Itzkovitz, S., 2018. Spatial Reconstruction of Single Enterocytes Uncovers Broad Zonation along the Intestinal Villus Axis. Cell 175, 1156-1167.e15. https://doi.org/10.1016/j.cell.2018.08.063

Moorefield, E.C., Blue, R.E., Quinney, N.L., Gentzsch, M., Ding, S., 2018. Generation of renewable mouse intestinal epithelial cell monolayers and organoids for functional analyses. BMC Cell Biol. 19, 1–11. https://doi.org/10.1186/S12860-018-0165-0/FIGURES/5

Mota, L.J., Ramsden, A.E., Liu, M., Castle, J.D., Holden, D.W., 2009. SCAMP3 is a component of the Salmonella-induced tubular network and reveals an interaction between bacterial effectors and post-Golgi trafficking. Cell. Microbiol. 11, 1236–1253. https://doi.org/10.1111/J.1462-5822.2009.01329.X

Mowat, A.M., Agace, W.W., 2014. Regional specialization within the intestinal immune system. Nat. Rev.

Immunol. 14, 667–85. https://doi.org/10.1038/nri3738

Müller, J., Spriewald, S., Stecher, B., Stadler, E., Fuchs, T.M., 2019. Evolutionary Stability of Salmonella Competition with the Gut Microbiota: How the Environment Fosters Heterogeneity in Exploitative and Interference Competition. J. Mol. Biol. 431, 4732–4748. https://doi.org/10.1016/j.jmb.2019.06.027

Murata, K., Jadhav, U., Madha, S., Es, J. Van, Dean, J., Cavazza, A., Wucherpfennig, K., Michor, F., Clevers, H., Shivdasani, R.A., 2020. Ascl2-Dependent Cell Dedifferentiation Drives Regeneration of Ablated Intestinal Stem Cells Article Ascl2-Dependent Cell Dedifferentiation Drives Regeneration of Ablated Intestinal Stem Cells. Cell Stem Cell TnQ, 1–14. https://doi.org/10.1016/j.stem.2019.12.011

Nagashima, K., Sawa, S., Nitta, T., Tsutsumi, M., Okamura, T., Penninger, J.M., Nakashima, T., Takayanagi, H., 2017. Identification of subepithelial mesenchymal cells that induce IgA and diversify gut microbiota. Nat. Immunol. 2017 186 18, 675–682. https://doi.org/10.1038/ni.3732

Nakamura, Y., Kimura, S., Hase, K., 2018a. M cell-dependent antigen uptake on follicle-associated epithelium for mucosal immune surveillance. Inflamm. Regen. 38, 15. https://doi.org/10.1186/s41232-018-0072-y

Nakamura, Y., Kimura, S., Hase, K., 2018b. M cell-dependent antigen uptake on follicle-associated epithelium for mucosal immune surveillance. Inflamm. Regen. 38, 1–9. https://doi.org/10.1186/S41232-018-0072-Y/FIGURES/3

Neutra, M.R., Mantis, N.J., Kraehenbuhl, J.P., 2001. Collaboration of epithelial cells with organized mucosal lymphoid tissues. Nat. Immunol. 2001 211 2, 1004–1009. https://doi.org/10.1038/ni1101-1004

Nicholl, C.G., Polak, J.M., Bloom, S.R., 1985. The hormonal regulation of food intake, digestion, and absorption. Annu. Rev. Nutr. 5, 213–39. https://doi.org/10.1146/annurev.nu.05.070185.001241

Nickerson, K.P., Senger, S., Zhang, Y., Lima, R., Patel, S., Ingano, L., Flavahan, W.A., Kumar, D.K.V., Fraser, C.M., Faherty, C.S., Sztein, M.B., Fiorentino, M., Fasano, A., 2018. Salmonella Typhi Colonization Provokes Extensive Transcriptional Changes Aimed at Evading Host Mucosal Immune Defense During Early Infection of Human Intestinal Tissue. EBioMedicine 31, 92–109. https://doi.org/10.1016/J.EBIOM.2018.04.005/ATTACHMENT/BF710F69-6203-49BB-AE51-385289D024EC/MMC4.DOCX

Niess, J.H., Reinecker, H.C., 2006. Dendritic cells in the recognition of intestinal microbiota. Cell. Microbiol. 8, 558–564. https://doi.org/10.1111/J.1462-5822.2006.00694.X

Nikolaev, M., Mitrofanova, O., Broguiere, N., Geraldo, S., Dutta, D., Tabata, Y., Elci, B., Brandenberg, N., Kolotuev, I., Gjorevski, N., Clevers, H., Lutolf, M.P., 2020. Homeostatic mini-intestines through scaffold-guided organoid morphogenesis. Nat. 2020 5857826 585, 574–578. https://doi.org/10.1038/s41586-020-2724-8

Noel, G., Baetz, N.W., Staab, J.F., Donowitz, M., Kovbasnjuk, O., Pasetti, M.F., Zachos, N.C., 2017a. A primary human macrophage-enteroid co-culture model to investigate mucosal gut physiology and host-pathogen interactions. Sci. Reports 2017 71 7, 1–14. https://doi.org/10.1038/srep45270

Noel, G., Baetz, N.W., Staab, J.F., Donowitz, M., Kovbasnjuk, O., Pasetti, M.F., Zachos, N.C., 2017b. A primary

human macrophage-enteroid co-culture model to investigate mucosal gut physiology and host-pathogen interactions. Sci. Reports 2017 71 7, 1–14. https://doi.org/10.1038/srep45270

Odenwald, M.A., Turner, J.R., 2016. The intestinal epithelial barrier: a therapeutic target? Nat. Rev. Gastroenterol. Hepatol. 14, 9–21. https://doi.org/10.1038/nrgastro.2016.169

Olsen, J.E., Hoegh-Andersen, K.H., Casadesús, J., Rosenkranzt, J., Chadfield, M.S., Thomsen, L.E., 2013. The role of flagella and chemotaxis genes in host pathogen interaction of the host adapted Salmonella enterica serovar Dublin compared to the broad host range serovar S. Typhimurium. BMC Microbiol. 13, 1–11. https://doi.org/10.1186/1471-2180-13-67/TABLES/4

Onno, M., Guillaudeux, T., Amiot, L., Renard, I., Drenou, B., Hirel, B., Girr, M., Semana, G., Le Bouteiller, P., Fauchet, R., 1994. The HLA-G gene is expressed at a low mRNA level in different human cells and tissues. Hum. Immunol. 41, 79–86. https://doi.org/10.1016/0198-8859(94)90089-2

Oria, R., Wiegand, T., Escribano, J., Elosegui-Artola, A., Uriarte, J.J., Moreno-Pulido, C., Platzman, I., Delcanale, P., Albertazzi, L., Navajas, D., Trepat, X., García-Aznar, J.M., Cavalcanti-Adam, E.A., Roca-Cusachs, P., 2017. Force loading explains spatial sensing of ligands by cells. Nat. 2017 5527684 552, 219–224. https://doi.org/10.1038/nature24662

Orr, S.E., Gokulan, K., Boudreau, M., Cerniglia, C.E., Khare, S., 2019. Alteration in the mRNA expression of genes associated with gastrointestinal permeability and ileal TNF-α secretion due to the exposure of silver nanoparticles in Sprague-Dawley rats. J. Nanobiotechnology 17, 1–10. https://doi.org/10.1186/S12951-019-0499-6/TABLES/1

Padhi, A., Nain, A.S., 2020. ECM in Differentiation: A Review of Matrix Structure, Composition and Mechanical Properties. Ann. Biomed. Eng. 48, 1071–1089. https://doi.org/10.1007/s10439-019-02337-7

Pagel, M., Beck-Sickinger, A.G., 2017. Multifunctional biomaterial coatings: Synthetic challenges and biological activity. Biol. Chem. 398, 3–22. https://doi.org/10.1515/HSZ-2016-0204/ASSET/GRAPHIC/J_HSZ-2016-0204_FIG_003.JPG

Papenfort, K., Said, N., Welsink, T., Lucchini, S., Hinton, J.C.D., Vogel, J., 2009. Specific and pleiotropic patterns of mRNA regulation by ArcZ, a conserved, Hfq-dependent small RNA. Mol. Microbiol. 74, 139–158. https://doi.org/10.1111/J.1365-2958.2009.06857.X

Parikh, K., Antanaviciute, A., Fawkner-Corbett, D., Jagielowicz, M., Aulicino, A., Lagerholm, C., Davis, S., Kinchen, J., Chen, H.H., Alham, N.K., Ashley, N., Johnson, E., Hublitz, P., Bao, L., Lukomska, J., Andev, R.S., Björklund, E., Kessler, B.M., Fischer, R., Goldin, R., Koohy, H., Simmons, A., 2019. Colonic epithelial cell diversity in health and inflammatory bowel disease. Nature 567, 49–55. https://doi.org/10.1038/s41586-019-0992-y

Pelaseyed, T., Hansson, G.C., 2020. Membrane mucins of the intestine at a glance. J. Cell Sci. 133. https://doi.org/10.1242/JCS.240929/225013

Pellegrinet, L., Rodilla, V., Liu, Z., Chen, S., Koch, U., Espinosa, L., Kaestner, K.H., Kopan, R., Lewis, J., Radtke, F., 2011. Dll1- and dll4-mediated notch signaling are required for homeostasis of intestinal stem cells. Gastroenterology 140, 1230-1240.e1–7. https://doi.org/10.1053/j.gastro.2011.01.005

Pérez-González, C., Ceada, G., Greco, F., Matejčić, M., Gómez-González, M., Castro, N., Menendez, A., Kale, S., Krndija, D., Clark, A.G., Gannavarapu, V.R., Álvarez-Varela, A., Roca-Cusachs, P., Batlle, E., Vignjevic, D.M., Arroyo, M., Trepat, X., 2021. Mechanical compartmentalization of the intestinal organoid enables crypt folding and collective cell migration. Nat. Cell Biol. 23, 745–757. https://doi.org/10.1038/s41556-021-00699-6

Picelli, S., Faridani, O.R., Björklund, A.K., Winberg, G., Sagasser, S., Sandberg, R., 2014. Full-length RNA-seq from single cells using Smart-seq2. Nat. Protoc. 9, 171–81. https://doi.org/10.1038/nprot.2014.006

Pinaud, L., Sansonetti, P.J., Phalipon, A., 2018. Host Cell Targeting by Enteropathogenic Bacteria T3SS Effectors. Trends Microbiol. 26, 266–283. https://doi.org/10.1016/J.TIM.2018.01.010

Pleguezuelos-manzano, C., Puschhof, J., Brink, S. Van Den, van den Brink, S., Geurts, V., Beumer, J., Clevers, H., 2020. Establishment and Culture of Human Intestinal Organoids Derived from Adult Stem Cells. Curr. Protoc. Immunol. 130, e106. https://doi.org/10.1002/cpim.106

Potten, C.S., Loeffler, M., 1990. Stem cells: attributes, cycles, spirals, pitfalls and uncertainties. Lessons for and from the crypt. Development 110, 1001–20. https://doi.org/10.1002/pola.1991.080290905

Pusch, J., Votteler, M., Göhler, S., Engl, J., Hampel, M., Walles, H., Schenke-Layland, K., 2011. The physiological performance of a three-dimensional model that mimics the microenvironment of the small intestine. Biomaterials 32, 7469–7478. https://doi.org/10.1016/j.biomaterials.2011.06.035

Qi, Z., Li, Y., Zhao, B., Xu, C., Liu, Y., Li, H., Zhang, B., Wang, X., Yang, X., Xie, W., Li, B., Han, J.D.J., Chen, Y.G., 2017. BMP restricts stemness of intestinal Lgr5+ stem cells by directly suppressing their signature genes. Nat. Commun. 2017 81 8, 1–14. https://doi.org/10.1038/ncomms13824

Quach, A., Jayaratne, R.R., Lee, B.J., Ibeawuchi, S.R., Lim, E., Das, S., Barrett, K.E., 2022. Diarrhoeal pathogenesis in Salmonella infection may result from an imbalance in intestinal epithelial differentiation through reduced Notch signalling. J. Physiol. 600, 1851–1865. https://doi.org/10.1113/JP282585

Rahmani, S., Breyner, N.M., Su, H., Verdu, E.F., Didar, T.F., 2019. Intestinal organoids: A new paradigm for engineering intestinal epithelium in vitro. Biomaterials 194, 195–214. https://doi.org/10.1016/j.biomaterials.2018.12.006

Rajkovic, N., Li, X., Plataniotis, K.N., Kanjer, K., Radulovic, M., Miloševic, N.T., 2018. The Pan-Cytokeratin staining intensity and fractal computational analysis of breast tumor malignant growth patterns prognosticate the occurrence of distant metastasis. Front. Oncol. 8, 348. https://doi.org/10.3389/FONC.2018.00348/BIBTEX

Ramilo, O., Allman, W., Chung, W., Mejias, A., Ardura, M., Glaser, C., Wittkowski, K.M., Piqueras, B., Banchereau, J., Palucka, A.K., Chaussabel, D., 2007. Gene expression patterns in blood leukocytes discriminate patients with acute infections. Blood 109, 2066–2077. https://doi.org/10.1182/BLOOD-2006-02-002477

Ramme, A.P., Koenig, L., Hasenberg, T., Schwenk, C., Magauer, C., Faust, D., Lorenz, A.K., Krebs, A.C., Drewell, C., Schirrmann, K., Vladetic, A., Lin, G.C., Pabinger, S., Neuhaus, W., Bois, F., Lauster, R., Marx, U., Dehne, E.M., 2019. Autologous induced pluripotent stem cell-derived four-organ-chip. Futur. Sci. OA

5, 413–2056. https://doi.org/10.2144/FSOA-2019-0065/ASSET/IMAGES/LARGE/FIGURE5.JPEG

Revenu, C., Ubelmann, F., Hurbain, I., El-Marjou, F., Dingli, F., Loew, D., Delacour, D., Gilet, J., Brot-Laroche, E., Rivero, F., Louvard, D., Robine, S., 2012. A Highlights from MBoC Selection: A new role for the architecture of microvillar actin bundles in apical retention of membrane proteins. Mol. Biol. Cell 23, 324. https://doi.org/10.1091/MBC.E11-09-0765

REYNOLDS, E.S., 1963. THE USE OF LEAD CITRATE AT HIGH pH AS AN ELECTRON-OPAQUE STAIN IN ELECTRON MICROSCOPY. J. Cell Biol. 17, 208. https://doi.org/10.1083/JCB.17.1.208

Ritsma, L., Ellenbroek, S.I.J., Zomer, A., Snippert, H.J., de Sauvage, F.J., Simons, B.D., Clevers, H., van Rheenen, J., 2014. Intestinal crypt homeostasis revealed at single-stem-cell level by in vivo live imaging. Nature 507, 362–365. https://doi.org/10.1038/nature12972

Roche, S.M., Holbert, S., Trotereau, J., Schaeffer, S., Georgeault, S., Virlogeux-Payant, I., Velge, P., 2018. Salmonella Typhimurium invalidated for the three currently known invasion factors keeps its ability to invade several cell models. Front. Cell. Infect. Microbiol. 8, 273. https://doi.org/10.3389/FCIMB.2018.00273/BIBTEX

Rodriguez-Boulan, E., Macara, I.G., 2014. Organization and execution of the epithelial polarity programme. Nat. Rev. Mol. Cell Biol. 15, 225. https://doi.org/10.1038/NRM3775

Rogers, A.P., Mileto, S.J., Lyras, D., 2022. Impact of enteric bacterial infections at and beyond the epithelial barrier. Nat. Rev. Microbiol. 2022 1–15. https://doi.org/10.1038/s41579-022-00794-x

Roodsant, T., Navis, M., Aknouch, I., Renes, I.B., van Elburg, R.M., Pajkrt, D., Wolthers, K.C., Schultsz, C., van der Ark, K.C.H., Sridhar, A., Muncan, V., 2020. A Human 2D Primary Organoid-Derived Epithelial Monolayer Model to Study Host-Pathogen Interaction in the Small Intestine. Front. Cell. Infect. Microbiol. 10, 1–14. https://doi.org/10.3389/fcimb.2020.00272

Roser, M., Ritchie, H., Spooner, F., 2021. Burden of disease [WWW Document]. Our World Data. URL https://ourworldindata.org/burden-of-disease (accessed 11.6.22).

Rouch, J.D., Scott, A., Lei, N.Y., Solorzano-Vargas, R.S., Wang, J., Hanson, E.M., Kobayashi, M., Lewis, M., Stelzner, M.G., Dunn, J.C.Y., Eckmann, L., Martín, M.G., 2016. Development of functional microfold (M) cells from intestinal stem cells in primary human enteroids. PLoS One 11. https://doi.org/10.1371/journal.pone.0148216

Rumsey, D., 2005. SMALL INTESTINE | Structure and Function, in: Caballero, B. (Ed.), Encyclopedia of Human Nutrition. Elsevier, pp. 126–133. https://doi.org/10.1016/B0-12-226694-3/02255-9

Rupnik, M., Kreft, M., Nothias, F., Grilc, S., Bobanovic, L.K., Johannes, L., Kiauta, T., Vernier, P., Darchen, F., Zorec, R., 2007. Distinct role of Rab3A and Rab3B in secretory activity of rat melanotrophs. Am. J. Physiol. - Cell Physiol. 292, 98–105. https://doi.org/10.1152/AJPCELL.00005.2006/ASSET/IMAGES/LARGE/ZH00120650070006.JPEG

Ryu, G.R., Lee, E., Kim, J.J., Moon, S.D., Ko, S.H., Ahn, Y.B., Song, K.H., 2018. Comparison of enteroendocrine cells and pancreatic β-cells using gene expression profiling and insulin gene methylation. PLoS One 13.

https://doi.org/10.1371/JOURNAL.PONE.0206401

Salcedo, S.P., Holden, D.W., 2003. SseG, a virulence protein that targets Salmonella to the Golgi network. EMBO J. 22, 5003–5014. https://doi.org/10.1093/EMBOJ/CDG517

Saliba, A.-E., Li, L., Westermann, A.J., Appenzeller, S., Stapels, D.A.C., Schulte, L.N., Helaine, S., Vogel, J., 2016. Single-cell RNA-seq ties macrophage polarization to growth rate of intracellular Salmonella. Nat. Microbiol. 2, 16206. https://doi.org/10.1038/nmicrobiol.2016.206

Sancho, R., Cremona, C.A., Behrens, A., 2015. Stem cell and progenitor fate in the mammalian intestine: Notch and lateral inhibition in homeostasis and disease. EMBO Rep. 16, 571–581. https://doi.org/10.15252/EMBR.201540188

Sansonetti, P.J., 2004. War and peace at mucosal surfaces. Nat. Rev. Immunol. 4, 953–64. https://doi.org/10.1038/nri1499

Sato, T., Clevers, H., 2013. Growing self-organizing mini-guts from a single intestinal stem cell: Mechanism and applications. Science (80-.). 340, 1190–1194. https://doi.org/10.1126/SCIENCE.1234852/SUPPL_FILE/SATO.SM.COVER.PAGE.PDF

Sato, T., Stange, D.E., Ferrante, M., Vries, R.G.J., Van Es, J.H., Van Den Brink, S., Van Houdt, W.J., Pronk, A., Van Gorp, J., Siersema, P.D., Clevers, H., 2011. Long-term expansion of epithelial organoids from human colon, adenoma, adenocarcinoma, and Barrett's epithelium. Gastroenterology 141, 1762–72. https://doi.org/10.1053/j.gastro.2011.07.050

Sato, T., Vries, R.G., Snippert, H.J., van de Wetering, M., Barker, N., Stange, D.E., van Es, J.H., Abo, A., Kujala, P., Peters, P.J., Clevers, H., 2009. Single Lgr5 stem cells build crypt-villus structures in vitro without a mesenchymal niche. Nature 459, 262–5. https://doi.org/10.1038/nature07935

Scanu, T., Spaapen, R.M., Bakker, J.M., Pratap, C.B., Wu, L. en, Hofland, I., Broeks, A., Shukla, V.K., Kumar, M., Janssen, H., Song, J.Y., Neefjes-Borst, E.A., te Riele, H., Holden, D.W., Nath, G., Neefjes, J., 2015. Salmonella Manipulation of Host Signaling Pathways Provokes Cellular Transformation Associated with Gallbladder Carcinoma. Cell Host Microbe 17, 763–774. https://doi.org/10.1016/J.CHOM.2015.05.002

Scherer, W.F., Syverton, J.T., Gey, G.O., 1953. Studies on the propagation in vitro of poliomyelitis viruses. IV. Viral multiplication in a stable strain of human malignant epithelial cells (strain HeLa) derived from an epidermoid carcinoma of the cervix. J. Exp. Med. 97, 695–710. https://doi.org/10.1084/JEM.97.5.695

Schroeder, N., Henry, T., de Chastellier, C., Zhao, W., Aude-Agnés, G., Gorvel, J.P., Méresse, S., 2010. The Virulence Protein SopD2 Regulates Membrane Dynamics of Salmonella-Containing Vacuoles. PLOS Pathog. 6, e1001002. https://doi.org/10.1371/JOURNAL.PPAT.1001002

Schroeder, N., Mota, L.J., Méresse, S., 2011. Salmonella-induced tubular networks. Trends Microbiol. 19, 268–277. https://doi.org/10.1016/J.TIM.2011.01.006

Schulte, L.N., Schweinlin, M., Westermann, A.J., Janga, H., Santos, S.C., Appenzeller, S., Walles, H., Vogel, J., Metzger, M., 2020. An Advanced Human Intestinal Coculture Model Reveals Compartmentalized Host and Pathogen Strategies during Salmonella Infection. MBio 11. https://doi.org/10.1128/mBio.03348-19

Schultz, B.M., Melo-Gonzalez, F., Salazar, G.A., Porto, B.N., Riedel, C.A., Kalergis, A.M., Bueno, S.M., 2021. New Insights on the Early Interaction Between Typhoid and Non-typhoid Salmonella Serovars and the Host Cells. Front. Microbiol. 12, 1772. https://doi.org/10.3389/FMICB.2021.647044/BIBTEX

Schuster, E.M., Epple, M.W., Glaser, K.M., Mihlan, M., Lucht, K., Zimmermann, J.A., Bremser, A., Polyzou, A., Obier, N., Cabezas-Wallscheid, N., Trompouki, E., Ballabio, A., Vogel, J., Buescher, J.M., Westermann, A.J., Rambold, A.S., 2022. TFEB induces mitochondrial itaconate synthesis to suppress bacterial growth in macrophages. Nat. Metab. 4, 856–866. https://doi.org/10.1038/s42255-022-00605-w

Schweinlin, M., Wilhelm, S., Schwedhelm, I., Hansmann, J., Rietscher, R., Jurowich, C., Walles, H., Metzger, M., 2016. Development of an Advanced Primary Human In Vitro Model of the Small Intestine. Tissue Eng. Part C. Methods 22, 873–83. https://doi.org/10.1089/ten.TEC.2016.0101

Sellin, M.E., Müller, A.A., Felmy, B., Dolowschiak, T., Diard, M., Tardivel, A., Maslowski, K.M., Hardt, W.D., 2014. Epithelium-Intrinsic NAIP/NLRC4 Inflammasome Drives Infected Enterocyte Expulsion to Restrict Salmonella Replication in the Intestinal Mucosa. Cell Host Microbe 16, 237–248. https://doi.org/10.1016/J.CHOM.2014.07.001

Shaoul, R., Okada, Y., Cutz, E., Marcon, M.A., 2004. Colonic expression of MUC2, MUC5AC, and TFF1 in inflammatory bowel disease in children. J. Pediatr. Gastroenterol. Nutr. 38, 488–93. https://doi.org/10.1097/00005176-200405000-00006

Shinozaki, S., Nakamura, T., Iimura, M., Kato, Y., Iizuka, B., Kobayashi, M., Hayashi, N., 2001. Upregulation of Reg 1alpha and GW112 in the epithelium of inflamed colonic mucosa. Gut 48, 623–629. https://doi.org/10.1136/GUT.48.5.623

Shoshkes-Carmel, M., Wang, Y.J., Wangensteen, K.J., Tóth, B., Kondo, A., Massasa, E.E., Itzkovitz, S., Kaestner, K.H., 2018. Subepithelial telocytes are an important source of Wnts that supports intestinal crypts. Nature 557, 242–246. https://doi.org/10.1038/s41586-018-0084-4

Siddiqui, K.M., Chopra, D.P., 1984. Primary and long term epithelial cell cultures from human fetal normal colonic mucosa. In Vitro 20, 859–868. https://doi.org/10.1007/BF02619632

Silva, J., Leite, D., Fernandes, M., Mena, C., Gibbs, P.A., Teixeira, P., 2011. Campylobacter spp. As a foodborne pathogen: A review. Front. Microbiol. 2, 200. https://doi.org/10.3389/FMICB.2011.00200/BIBTEX

Singh, S.B., Coffman, C.N., Carroll-Portillo, A., Varga, M.G., Lin, H.C., 2021. Notch Signaling Pathway Is Activated by Sulfate Reducing Bacteria. Front. Cell. Infect. Microbiol. 11, 643. https://doi.org/10.3389/FCIMB.2021.695299/BIBTEX

Smith, J.L., 2003. The role of gastric acid in preventing foodborne disease and how bacteria overcome acid conditions. J. Food Prot. 66, 1292–1303. https://doi.org/10.4315/0362-028X-66.7.1292

Smith, M.E., Morton, D.G., 2010. THE SMALL INTESTINE. Dig. Syst. 107–127. https://doi.org/10.1016/B978-0-7020-3367-4.00007-4

Song, X., Dai, D., He, X., Zhu, S., Yao, Y., Gao, H., Wang, J., Qu, F., Qiu, J., Wang, H., Li, X., Shen, N., Qian, Y., 2015. Growth Factor FGF2 Cooperates with Interleukin-17 to Repair Intestinal Epithelial Damage.

Immunity 43, 488–501. https://doi.org/10.1016/J.IMMUNI.2015.06.024

Spence, J.R., Mayhew, C.N., Rankin, S.A., Kuhar, M.F., Vallance, J.E., Tolle, K., Hoskins, E.E., Kalinichenko, V. V., Wells, S.I., Zorn, A.M., Shroyer, N.F., Wells, J.M., 2011. Directed differentiation of human pluripotent stem cells into intestinal tissue in vitro. Nature 470, 105–109. https://doi.org/10.1038/nature09691

Spillings, B.L., Day, C.J., Garcia-Minambres, A., Aggarwal, A., Condon, N.D., Haselhorst, T., Purcell, D.F.J., Turville, S.G., Stow, J.L., Jennings, M.P., Mak, J., 2022. Host glycocalyx captures HIV proximal to the cell surface via oligomannose-GlcNAc glycan-glycan interactions to support viral entry. Cell Rep. 38. https://doi.org/10.1016/J.CELREP.2022.110296

Srinivasan, B., Kolli, A.R., Esch, M.B., Abaci, H.E., Shuler, M.L., Hickman, J.J., 2015. TEER measurement techniques for in vitro barrier model systems. J. Lab. Autom. 20, 107–26. https://doi.org/10.1177/2211068214561025

Staes, I., Passaris, I., Cambré, A., Aertsen, A., 2019. Population heterogeneity tactics as driving force in Salmonella virulence and survival. Food Res. Int. 125, 108560. https://doi.org/10.1016/J.FOODRES.2019.108560

Stapels, D.A.C., Hill, P.W.S., Westermann, A.J., Fisher, R.A., Thurston, T.L., Saliba, A.-E., Blommestein, I., Vogel, J., Helaine, S., 2018. Salmonella persisters undermine host immune defenses during antibiotic treatment. Science 362, 1156–1160. https://doi.org/10.1126/science.aat7148

Stecher, B., Robbiani, R., Walker, A.W., Westendorf, A.M., Barthel, M., Kremer, M., Chaffron, S., Macpherson, A.J., Buer, J., Parkhill, J., Dougan, G., Von Mering, C., Hardt, W.D., 2007. Salmonella enterica Serovar Typhimurium Exploits Inflammation to Compete with the Intestinal Microbiota. PLOS Biol. 5, e244. https://doi.org/10.1371/JOURNAL.PBIO.0050244

Sun, D., Evans, L., Perrone, F., Sokleva, V., Lim, K., Rezakhani, S., Lutolf, M., Zilbauer, M., Rawlins, E.L., 2021. A functional genetic toolbox for human tissue-derived organoids. Elife 10. https://doi.org/10.7554/ELIFE.67886

Sun, W.W., Krystofiak, E.S., Leo-Macias, A., Cui, R., Sesso, A., Weigert, R., Ebrahim, S., Kachar, B., 2020. Nanoarchitecture and dynamics of the mouse enteric glycocalyx examined by freeze-etching electron tomography and intravital microscopy. Commun. Biol. 2020 31 3, 1–10. https://doi.org/10.1038/s42003-019-0735-5

Suzuki, A., Sekiya, S., Gunshima, E., Fujii, S., Taniguchi, H., 2010. EGF signaling activates proliferation and blocks apoptosis of mouse and human intestinal stem/progenitor cells in long-term monolayer cell culture. Lab. Investig. 2010 9010 90, 1425–1436. https://doi.org/10.1038/labinvest.2010.150

Suzuki, K., Murano, T., Shimizu, H., Ito, G., Nakata, T., Fujii, S., Ishibashi, F., Kawamoto, A., Anzai, S., Kuno, R., Kuwabara, K., Takahashi, J., Hama, M., Nagata, S., Hiraguri, Y., Takenaka, K., Yui, S., Tsuchiya, K., Nakamura, T., Ohtsuka, K., Watanabe, M., Okamoto, R., 2018. Single cell analysis of Crohn's disease patient-derived small intestinal organoids reveals disease activity-dependent modification of stem cell properties. J. Gastroenterol. 53, 1035–1047. https://doi.org/10.1007/s00535-018-1437-3

Swaminathan, V., Kalappurakkal, J.M., Mehta, S.B., Nordenfelt, P., Moore, T.I., Koga, N., Baker, D.A., Oldenbourg, R., Tani, T., Mayor, S., Springer, T.A., Waterman, C.M., 2017. Actin retrograde flow actively aligns and orients ligand-engaged integrins in focal adhesions. Proc. Natl. Acad. Sci. U. S. A. 114, 10648–10653. https://doi.org/10.1073/PNAS.1701136114/SUPPL_FILE/PNAS.1701136114.SM02.AVI

Tabrizi, S.N., Robins-Browne, R.M., 1993. Elimination of extracellular bacteria by antibiotics in quantitative assays of bacterial ingestion and killing by phagocytes. J. Immunol. Methods 158, 201–206. https://doi.org/10.1016/0022-1759(93)90215-S

Tahoun, A., Mahajan, S., Paxton, E., Malterer, G., Donaldson, D.S., Wang, D., Tan, A., Gillespie, T.L., O'Shea, M., Roe, A.J., Shaw, D.J., Gally, D.L., Lengeling, A., Mabbott, N.A., Haas, J., Mahajan, A., 2012. Salmonella transforms follicle-associated epithelial cells into M cells to promote intestinal invasion. Cell Host Microbe 12, 645–56. https://doi.org/10.1016/j.chom.2012.10.009

Takahashi, K., Tanabe, K., Ohnuki, M., Narita, M., Ichisaka, T., Tomoda, K., Yamanaka, S., 2007. Induction of pluripotent stem cells from adult human fibroblasts by defined factors. Cell 131, 861–872. https://doi.org/10.1016/J.CELL.2007.11.019

Takahashi, T., Shiraishi, A., 2020. Stem Cell Signaling Pathways in the Small Intestine. Int. J. Mol. Sci. 21, 1–18. https://doi.org/10.3390/ijms21062032

Tan, D.W.-M., Barker, N., 2014. Intestinal stem cells and their defining niche. Curr. Top. Dev. Biol. 107, 77–107. https://doi.org/10.1016/B978-0-12-416022-4.00003-2

Teichmann, S., Zilbauer, M., James, K., Elmentaite, R., Ross, A., 2021. Human gut cell atlas - Epithelium [WWW Document]. URL https://www.gutcellatlas.org/spacetime/epithelium/ (accessed 12.15.22).

Tetteh, P.W., Basak, O., Farin, H.F., Wiebrands, K., Kretzschmar, K., Begthel, H., van den Born, M., Korving, J., de Sauvage, F., van Es, J.H., van Oudenaarden, A., Clevers, H., 2016. Replacement of Lost Lgr5-Positive Stem Cells through Plasticity of Their Enterocyte-Lineage Daughters. Cell Stem Cell 18, 203–13. https://doi.org/10.1016/j.stem.2016.01.001

Tian, H., Biehs, B., Warming, S., Leong, K.G., Rangell, L., Klein, O.D., De Sauvage, F.J., 2011. A reserve stem cell population in small intestine renders Lgr5-positive cells dispensable. Nat. 2011 4787368 478, 255–259. https://doi.org/10.1038/nature10408

Tsai, C.N., Coombes, B.K., 2019. The Role of the Host in Driving Phenotypic Heterogeneity in Salmonella. Trends Microbiol. 27, 508–523. https://doi.org/10.1016/j.tim.2019.01.004

Tseng, Q., Duchemin-Pelletier, E., Deshiere, A., Balland, M., Guilloud, H., Filhol, O., Theŕy, M., 2012. Spatial organization of the extracellular matrix regulates cell-cell junction positioning. Proc. Natl. Acad. Sci. U. S. A. 109, 1506–1511. https://doi.org/10.1073/PNAS.1106377109/SUPPL_FILE/SM03.MOV

Uchiya, K.I., Barbieri, M.A., Funato, K., Shah, A.H., Stahl, P.D., Groisman, E.A., 1999. A Salmonella virulence protein that inhibits cellular trafficking. EMBO J. 18, 3924–3933. https://doi.org/10.1093/EMBOJ/18.14.3924

van der Flier, L.G., Clevers, H., 2009. Stem Cells, Self-Renewal, and Differentiation in the Intestinal Epithelium.

Annu. Rev. Physiol. 71, 241–260. https://doi.org/10.1146/annurev.physiol.010908.163145

van der Flier, L.G., Haegebarth, A., Stange, D.E., van de Wetering, M., Clevers, H., 2009. OLFM4 Is a Robust Marker for Stem Cells in Human Intestine and Marks a Subset of Colorectal Cancer Cells. Gastroenterology 137, 15–17. https://doi.org/10.1053/j.gastro.2009.05.035

van Dop, W.A., Uhmann, A., Wijgerde, M., Sleddens-Linkels, E., Heijmans, J., Offerhaus, G.J., van den Bergh Weerman, M.A., Boeckxstaens, G.E., Hommes, D.W., Hardwick, J.C., Hahn, H., van den Brink, G.R., 2009. Depletion of the Colonic Epithelial Precursor Cell Compartment Upon Conditional Activation of the Hedgehog Pathway. Gastroenterology 136, 2195-2203.e7. https://doi.org/10.1053/J.GASTRO.2009.02.068

Van Es, J.H., Sato, T., Van De Wetering, M., Lyubimova, A., Yee Nee, A.N., Gregorieff, A., Sasaki, N., Zeinstra, L., Van Den Born, M., Korving, J., Martens, A.C.M., Barker, N., Van Oudenaarden, A., Clevers, H., 2012. Dll1+ secretory progenitor cells revert to stem cells upon crypt damage. Nat. Cell Biol. 2012 1410 14, 1099–1104. https://doi.org/10.1038/ncb2581

Van Itallie, C.M., Anderson, J.M., 2014. Architecture of tight junctions and principles of molecular composition. Semin. Cell Dev. Biol. 36, 157–65. https://doi.org/10.1016/j.semcdb.2014.08.011

VanDussen, K.L., Carulli, A.J., Keeley, T.M., Patel, S.R., Puthoff, B.J., Magness, S.T., Tran, I.T., Maillard, I., Siebel, C., Kolterud, Å., Grosse, A.S., Gumucio, D.L., Ernst, S.A., Tsai, Y.-H.H., Dempsey, P.J., Samuelson, L.C., 2012. Notch signaling modulates proliferation and differentiation of intestinal crypt base columnar stem cells. Development 139, 488–97. https://doi.org/10.1242/dev.070763

Ventola, C.L., 2015. The Antibiotic Resistance Crisis: Part 1: Causes and Threats. Pharm. Ther. 40, 277. https://doi.org/Article

Volk, N., Lacy, B., 2017. Anatomy and Physiology of the Small Bowel. Gastrointest. Endosc. Clin. N. Am. 27, 1–13. https://doi.org/10.1016/j.giec.2016.08.001

Wagner, C., Hensel, M., 2011. Adhesive mechanisms of Salmonella enterica. Adv. Exp. Med. Biol. 715, 17–34. https://doi.org/10.1007/978-94-007-0940-9_2

Walsh, N.C., Alexander, K.A., Manning, C.A., Karmakar, S.K., Wang, J.F., Weyand, C.M., Pettit, A.R., Gravallese, E.M., 2013. Activated human T cells express alternative mRNA transcripts encoding a secreted form of RANKL. Genes Immun. 2013 145 14, 336–345. https://doi.org/10.1038/gene.2013.29

Walton, K.D., Freddo, A.M., Wang, S., Gumucio, D.L., 2016. Generation of intestinal surface: an absorbing tale. Development 143, 2261. https://doi.org/10.1242/DEV.135400

Wang, K.C., Huang, C.H., Ding, S.M., Chen, C.K., Fang, H.W., Huang, M. Te, Fang, S. Bin, 2016a. Role of yqiC in the pathogenicity of salmonella and innate immune responses of human intestinal epithelium. Front. Microbiol. 7, 1614. https://doi.org/10.3389/FMICB.2016.01614/BIBTEX

Wang, K.C., Huang, C.H., Huang, C.J., Fang, S. Bin, 2016b. Impacts of Salmonella enterica serovar typhimurium and its speG gene on the transcriptomes of in vitro M cells and Caco-2 cells. PLoS One 11, 1–22. https://doi.org/10.1371/journal.pone.0153444

Wang, Y., Kim, R., Hinman, S.S., Zwarycz, B., Magness, S.T., Allbritton, N.L., 2018. Bioengineered Systems and

Designer Matrices That Recapitulate the Intestinal Stem Cell Niche. Cell. Mol. Gastroenterol. Hepatol. 5, 440-453.e1. https://doi.org/10.1016/j.jcmgh.2018.01.008

Wang, Y., Song, W., Wang, J., Wang, T., Xiong, X., Qi, Z., Fu, W., Yang, X., Chen, Y.-G., 2020. Single-cell transcriptome analysis reveals differential nutrient absorption functions in human intestine. J. Exp. Med. 217, 1–15. https://doi.org/10.1084/jem.20191130

Waterman, S.R., Small, P.L.C., 1998. Acid-Sensitive Enteric Pathogens Are Protected from Killing under Extremely Acidic Conditions of pH 2.5 when They Are Inoculated onto Certain Solid Food Sources. Appl. Environ. Microbiol. 64, 3882. https://doi.org/10.1128/AEM.64.10.3882-3886.1998

Weigel, Tobias, Malkmus, Christoph, Weigel, Verena, Wußmann, Maximiliane, Berger, Constantin, Brennecke, Julian, Groeber-Becker, Florian, Hansmann, Jan, Weigel, T, Weigel, V, Wußmann, M, Groeber-Becker, F, Malkmus, C, Berger, C, Brennecke, J, Hansmann, J, 2022. Fully Synthetic 3D Fibrous Scaffolds for Stromal Tissues—Replacement of Animal-Derived Scaffold Materials Demonstrated by Multilayered Skin. Adv. Mater. 34, 2106780. https://doi.org/10.1002/ADMA.202106780

Wemyss, M.A., Pearson, J.S., 2019. Host Cell Death Responses to Non-typhoidal Salmonella Infection. Front. Immunol. 10, 1758. https://doi.org/10.3389/fimmu.2019.01758

Westermann, A.J., Förstner, K.U., Amman, F., Barquist, L., Chao, Y., Schulte, L.N., Müller, L., Reinhardt, R., Stadler, P.F., Vogel, J., 2016. Dual RNA-seq unveils noncoding RNA functions in host-pathogen interactions. Nature 529, 496–501. https://doi.org/10.1038/nature16547

Winter, S.E., Thiennimitr, P., Winter, M.G., Butler, B.P., Huseby, D.L., Crawford, R.W., Russell, J.M., Bevins, C.L., Adams, L.G., Tsolis, R.M., Roth, J.R., Bäumler, A.J., 2010. Gut inflammation provides a respiratory electron acceptor for Salmonella. Nature 467, 426–429. https://doi.org/10.1038/NATURE09415

Wood, M.B., Rios, D., Williams, I.R., 2016. TNF-α augments RANKL-dependent intestinal M cell differentiation in enteroid cultures. Am. J. Physiol. - Cell Physiol. 311, C498–C507. https://doi.org/10.1152/AJPCELL.00108.2016/ASSET/IMAGES/LARGE/ZH00141679970009.JPEG

Worthington, J.J., Reimann, F., Gribble, F.M., 2018. Enteroendocrine cells-sensory sentinels of the intestinal environment and orchestrators of mucosal immunity. Mucosal Immunol. 11, 3–20. https://doi.org/10.1038/mi.2017.73

Xiao, S., Liu, L., Lu, X., Long, J., Zhou, X., Fang, M., 2015. The prognostic significance of bromodomain PHD-finger transcription factor in colorectal carcinoma and association with vimentin and E-cadherin. J. Cancer Res. Clin. Oncol. 141, 1465–1474. https://doi.org/10.1007/S00432-015-1937-Y

Yang, Y., Li, X.M., Wang, J.R., Li, Y., Ye, W.L., Wang, Y., Liu, Y.X., Deng, Z.Y., Gan, W.J., Wu, H., 2022. TRIP6 promotes inflammatory damage via the activation of TRAF6 signaling in a murine model of DSS-induced colitis. J. Inflamm. (Lond). 19. https://doi.org/10.1186/S12950-021-00298-0

Yin, X., Farin, H.F., Van Es, J.H., Clevers, H., Langer, R., Karp, J.M., 2013. Niche-independent high-purity cultures of Lgr5+ intestinal stem cells and their progeny. Nat. Methods 2013 111 11, 106–112. https://doi.org/10.1038/nmeth.2737

Yu, Q., Kilik, U., Holloway, E.M., Tsai, Y.H., Harmel, C., Wu, A., Wu, J.H., Czerwinski, M., Childs, C.J., He, Z., Capeling, M.M., Huang, S., Glass, I.A., Higgins, P.D.R., Treutlein, B., Spence, J.R., Camp, J.G., 2021. Charting human development using a multi-endodermal organ atlas and organoid models. Cell 184, 3281-3298.e22. https://doi.org/10.1016/J.CELL.2021.04.028

Zanardo, T.É.C., Amorim, F.G., Taufner, G.H., Pereira, R.H.A., Baiense, I.M., Destefani, A.C., Iwai, L.K., Maranhão, R.C., Nogueira, B.V., 2020. Decellularized Splenic Matrix as a Scaffold for Spleen Bioengineering. Front. Bioeng. Biotechnol. 8. https://doi.org/10.3389/FBIOE.2020.573461/FULL

Zha, L., Garrett, S., Sun, J., 2019. Salmonella Infection in Chronic Inflammation and Gastrointestinal Cancer. Dis. 2019, Vol. 7, Page 28 7, 28. https://doi.org/10.3390/DISEASES7010028

Zhang, Y., He, Y., Bharadwaj, S., Hammam, N., Carnagey, K., Myers, R., Atala, A., Van Dyke, M., 2009. Tissue-Specific Extracellular Matrix Coatings Promote Cell Proliferation and Maintain Cell Phenotypes. Biomaterials 30, 4021. https://doi.org/10.1016/J.BIOMATERIALS.2009.04.005

Zhao, Z., Chen, X., Dowbaj, A.M., Sljukic, A., Bratlie, K., Lin, L., Fong, E.L.S., Balachander, G.M., Chen, Z., Soragni, A., Huch, M., Zeng, Y.A., Wang, Q., Yu, H., 2022. Organoids. Nat. Rev. Methods Prim. 2, 1–21. https://doi.org/10.1038/s43586-022-00174-y

Zheng, L., Kelly, C.J., Colgan, S.P., 2015. Physiologic hypoxia and oxygen homeostasis in the healthy intestine. A review in the theme: Cellular responses to hypoxia. Am. J. Physiol. - Cell Physiol. 309, C350–C360. https://doi.org/10.1152/AJPCELL.00191.2015/ASSET/IMAGES/LARGE/ZH00181578000003.JPEG

Zheng, Y., Song, Y., Han, Q., Liu, W., Xu, J., Yu, Z., Zhang, R., Li, N., 2018. Intestinal epithelial cell-specific IGF1 promotes the expansion of intestinal stem cells during epithelial regeneration and functions on the intestinal immune homeostasis. Am. J. Physiol. Endocrinol. Metab. 315, E638–E649. https://doi.org/10.1152/AJPENDO.00022.2018

Zhou, D., Mooseker, M.S., Galán, J.E., 1999. Role of the S. typhimurium Actin-binding protein SipA in bacterial internalization. Science (80-.). 283, 2092–2095. https://doi.org/10.1126/SCIENCE.283.5410.2092/ASSET/0E2091AA-90D5-46CA-B5E1-99A690F6F0A0/ASSETS/GRAPHIC/SE1297364004.JPEG

11 Acknowledgment

With the document, you are holding at this very moment, you have a summary of the most intensive time of my life in your hands. In a few days (when I will hopefully have submitted successfully), it will be in total 1906 days or five years, two months, two weeks and two days that I will have spent on finally producing this text. It was a long and exciting time, with a lot of high highs and deep lows, with happiness and sadness, with times of motivation and frustration; a mixture of all of them which would not have been possible without the help of so many good people. Here is the right chapter and the right moment to say “thank you”:

First of all, I would like to thank my doctoral supervisors and my doctoral committee: My greatest gratitude goes to you, Dr. Daniela Zdzieblo, for your supervision and guidance over all these years. I thank you in particular for your support and understanding in difficult times and for your intensive help and patience during the final corrections.

Furthermore, I would like to thank Dr Marco Metzger for your tireless support, especially in the early years, and for your commitment up to the last second. I would also like to thank Prof. Dr. Cynthia Sharma for her fruitful comments during our meetings and Prof. Dr. Alexander Westermann for his valuable input, advice, expertise and laughter.

I would also like to thank Prof. Dr. Dandekar who is willing to take over the position of chairperson and who will ensure the proper conduct of the thesis defence.

Further, I want to further thank my academic and professional collaborators: Dr. Emmanuel-Antoine Saliba, Oliver Dietrich, Tobias Krammer, Prof. Dr. Christian Stigloher and Daniela Bunsen, Prof. Dr. Winfried Neuhaus, and Prof. Dr. Jörg Vogel.

Thank you to all the members of the Department of Tissue Engineering and Regenerative Medicine, current and former ones, who made every day special. I had a wonderful time with you and was made very welcome in this group of very friendly and kind people. Honestly, the atmosphere here is particularly heart-warming.

My special thanks go to my closest and dearest colleagues: to Consti, for all the scientific discussion, the fun time with Schafkopfen, Fussball or Billy Talent as well as for being an idol in science and a really good friend; to Christina, for all the conversations in the past years as well as for the help and support in lab and life questions; to Marion, for Trailerpark during organoid splitting and the one cigarette; to Marie, Anna-Lena, Laura and Gohar, for being the best students I was allowed to accompany for a piece of their lives and their final theses; and to

Anna-Kristina, for an open ear for all dark and bright things in life and for the nice moments with coffee and laughter.

I want to especially mention and thank Christoph, Lukas and Dr. Fabi who became really really really good friends and Brotzeit companions in these years. Thank you for having one supportive hand on my shoulder and in the other always a freshly opened “Pils” (not Würzburger); you are the best!

A big thank you to all the nice people I met in the years and who became friends: Laura, Franzi, Pino, Ronja, Johannes and the Stammtisch. Moreover, to the friends who have been there since the beginning: Louisa, Ludwig, Jakob, Vogel, Tilman, Sophie und Oskar.

Near the end, but most important I want to thank my family from the bottom of my heart: my mother Birgit, for being my mother with never-ending love and support and thus gave me the opportunity to do all this in the first place; my brother Basti, who was always there whenever needed and who told me what I needed to hear; and my Gigi, for supporting me with affection and stability. Thank you also to my uncle Uli, for supporting me in difficult decisions and sponsoring a lot of my study books over the years; to Micha for your kind words; to Kathi for understanding; and to Pauli, for being the best niece!

Thank you, Judi, for coming into my life with your laughter and airiness and for being so kind and so tremendously patient with me.

13 List of Publications

Articles:

Däullary T. & Imdahl F., Dietrich O. , Hepp L. , Krammer T., Fey C., Neuhaus W., Metzger M., Vogel J., Westermann A., Saliba AE., Zdzieblo D. (2022). A primary cell-based in vitro model of the human small intestine reveals the induction of OLFM4 expression as host cell response during Salmonella Typhimurium infection. **In revision (Gut microbes)**

Hell L., **Däullary T.**, Burghart V., Mauracher LM, Grilz E., Moser B., Kramer G. , Schmid J. , Ay C. , Pabinger I., Thaler J. (2021). Extracellular Vesicle-Associated Tissue Factor Activity in Prostate Cancer Patients with Disseminated Intravascular Coagulation. Cancers (Basel). 2021 Mar 24;13(7):1487. doi: 10.3390/cancers13071487.

Däullary T., Fey C., Berger C., Metzger M., Zdzieblo D. (2020) Bioartificial gut—current state of small intestinal tissue engineering. In Nihal Vrana, Helena Knopf-Marques, Julien Barthes (Eds). Biomaterials for Organ and Tissue Regeneration. 1 st ed. (p 273 -298) Elsevier. doi.org/10.1016/C2018-0-02069-1

Moeller S., Patan-Zugaj B., **Däullary T**., Tichy A., Licka TF. (2019) The influence of trimming of the hoof wall on the damage of laminar tissue after loading: An in vitro study. Vet J. 2019;250:63 - 70. doi:10.1016/j.tvjl.2019.07.002

Mauracher LM., Posch F., Martinod K., **Däullary T**.,et al. (2018) Citrullinated histone H3, a biomarker of neutrophil extracellular trap formation, predicts the risk of venous thromboembolism in cancer patients. J Thromb Haemost. 2018;16(3):508 - 518. doi:10.1111/jth.13951

Oral presentations:

Däullary T. & Imdahl F., Dietrich O. , Hepp L. , Krammer T., Fey C., Neuhaus W., Metzger M., Vogel J., Westermann A., Saliba AE., Zdzieblo D. (2022, Würzburg, Germany). Salmonella Typhimurium infection in a primary in vitro model of the human small intestine reveals the induction of OLFM4 expression as host cell response. (Biofabrication meets infection on 25th of November 2022)

14 Contributions by others

The work presented here was conducted under the supervision of PD Dr. Marco Metzger and Dr. Daniela Zdzieblo at the Chair of Tissue Engineering and Regenerative Medicine, University Hospital Würzburg, Germany. Several experiments were conducted by colleagues and collaborators want to name here:

- Method high-throughput qPCR chip was conducted in the group of Dr. Prof. Winfried Neuhaus (Austrian Institute of Technology, Vienna, Austria).

- Fabian Imdahl (working group of Dr. Antoine-Emmanuel Saliba, Helmholtz Institute for RNA-based Infection, Würzburg, Germany) performed single sorting and processing for scRNA sequencing (Drop-seq and SMART-seq).

- Bioinformatical analysis of single-cell RNA sequencing conducted by Oliver Dietrich (working group of Dr. Antoine-Emmanuel Saliba, Helmholtz Institute for RNA-based Infection, Würzburg, Germany).

- Tobias Krammer (working group of Dr. Antoine-Emmanuel Saliba, Helmholtz Institute for RNA-based Infection, Würzburg, Germany) performed Method establishment of HCR-Fish and probe design for HCR-FISH.

15 Affidavit

I hereby confirm that my thesis entitled "***Establishment of an infection model of the human intestinal epithelium to study host and pathogen determinants during the Salmonella Typhimurium infection process***" is the result of my own work. I did not receive any help or support from commercial consultants. All sources and / or material applied are listed and specified in the thesis.

Furthermore, I confirm that this thesis has not been submitted as part of another examination process neither in identical nor in similar form.

Place, Date Signature

16 Eidesstattliche Erklärung

Hiermit erkläre ich an Eides statt, die Dissertation „***Etablierung eines Infektionsmodells des menschlichen Darmepithels zur Untersuchung von Wirts- und Erregerdeterminanten während des Salmonella Typhimurium-Infektion***" eigenständig, d.h. insbesondere selbständig und ohne Hilfe eines kommerziellen Promotionsberaters, angefertigt und keine anderen als die von mir angegebenen Quellen und Hilfsmittel verwendet zu haben.

Ich erkläre außerdem, dass die Dissertation weder in gleicher noch in ähnlicher Form bereits in einem anderen Prüfungsverfahren vorgelegen hat.

Ort, Datum Unterschrift